Ultraluminous Infrared Galaxies: Power Sources and Ages Along the Merger Sequence

Thesis by

Thomas W. Murphy, Jr.

In Partial Fulfillment of the Requirements
for the Degree of
Doctor of Philosophy

California Institute of Technology
Pasadena, California

2000
(Defended May 17, 2000)

Dedicated to Casey and Dana

Acknowledgements

Naturally, a graduate career does not take place in a vacuum. Through the years I have benefitted greatly from my relationships with a number of people, both professionally and personally. But rather than catalog all of the significant people with whom I've shared my life these past (how many?!) years, I'll keep the list brief.

First and foremost, I owe many thanks to my advisor, Tom Soifer. Tom was always 100% behind my desire to build astronomical instrumentation, and worked hard to create the opportunity for me to do so. Perhaps most importantly, Tom was always considerate of what I wanted to get out of my graduate experience, rather than deciding himself what should be important to me. At the same time, he looked out for my interests by making sure I spent time on things that would serve me later, though I may not have wanted to focus on those things at that time. Tom has been a truly generous advisor, and I appreciate the extent to which he has thought about my future. I have had a great experience working with Tom, and always enjoy and look forward to our interactions.

Gerry Neugebauer was always available to discuss issues ranging from life philosophy and career choices to using modes vs. medians, or subtleties of pixel sampling. I have enjoyed knowing Gerry these past years—he has always taken an interest in the things I've done, and gave me countless valuable pieces of advice along the way. I suppose the most concise way to state what I have learned from him is the following: "Don't get all wound up in the details until you understand the very basic fundamentals of what is going on."

Keith Matthews rounds out the Caltech infrared "triumvirate," and has been a delightful acquaintance during my time at Caltech—even though he's a New Yorker. Keith has taught me a great deal about how to get things done. I've learned to adopt a healthy mixture of cleverness and practicality. I've learned that whenever possible, find what you're looking for commercially before trying to re-invent it yourself. I have

also learned through Keith what the future holds for astronomical instrumentation. My raised awareness has and will continue to serve me well as I stumble into the future.

Rob Knop and James Larkin deserve mention as they paved the way for my thesis in a number of substantial ways. Rob and James were fourth-year graduate students when I arrived at Caltech, and in the thick of bulding a spectrograph for the Palomar 200-inch Telescope. This spectrograph—which never acquired a suitable acronym—came to be known as the HNA, or Has No Acronym, spectrograph. The HNA spectrograph has been of tremendous importance to me. Firstly, the data presented in Chapters 2 and 3 were obtained with this spectrograph. I have in fact observed with their spectrograph more than have both of them combined. In addition to this obvious benefit, their spectrograph also provided a baseline for the PIFS design. In fact, had funding not become available for the PIFS, I would have used the dewar from the HNA spectrograph. I am endebted (though not financially, I should make clear to James) to both Rob and James for their efforts from which I so directly benefitted.

I thank Lee Armus for teaching me all about data reduction, ULIRGs, observing, and astronomy in general when I first started working with the infrared group. He and I worked together extensively preparing the ULIRG imaging survey that appeared in our 1996 *Astronomical Journal* article. Lee also played a big role in formulating the near-infrared spectroscopic survey of ULIRGs with the HNA spectrograph. Lee's extensive knowledge of current astronomy has been a real asset over the years.

Finally, with the professional acknowledgements out of the way, I owe a great deal of thanks to Babra, who has been my companion for most of my time at Caltech. Babra has dealt with many episodes of playing second fiddle to the thesis work, which too often involved spending very few waking hours at home each week. I am grateful for her companionship, her support, and the perspective she has given me on life. Babra constantly challenges me to think about humanity, the meaning of life, and cleaning out the cat box. For most of these things she deserves my deepest gratitude.

Abstract

Ultraluminous infrared galaxies (ULIRGs) are the most luminous galaxies in the local universe, with power outputs above 10^{12} times that of our sun. Almost all ULIRGs are found to be associated with collisions between large, gas-rich galaxies. With most of the energy output emerging at far-infrared wavelengths, these galaxies are understood to be extremely dusty. As such, the nature of the power source within the dust shroud is not clearly understood. The two most likely explanations involve either a massive burst of star formation or the presence of an active galactic nucleus (AGN) in the form of a dust-enshrouded quasar.

This work presents two separate approaches to investigating the nature of ultraluminous infrared galaxies. The first is a spectrosciopic survey of 33 ULIRGs in the near-infrared band around a wavelength of 2 microns, where dust extinction is much less severe than in visible light. The aim of this study is to search for evidence of buried AGN, as indicated by velocity-broadened hydrogen recombination lines as well as the presence of the high excitation [Si VI] emission line. This survey finds that signs of AGN are rare in ULIRGs, with the most natural conclusion being that the majority of ULIRGs are powered by starburst phenomena.

The second approach presented involves the design, construction, and use of a novel instrument built specifically to study the spatial and kinematical properties of gas within the morphologically complex ULIRGs. A single long slit is generally not capable of capturing the rich phenomenology found in the complex environments of ULIRGs. Data from the Palomar Integral Field Spectrograph reveals that several ULIRGs are found to exist at times very early in the galaxy encounter process. The possibility that ultraluminous activity may develop so early in the merger history suggests a non-trivial luminosity evolution among galaxy mergers, wherein the less powerful class of luminous infrared galaxies may represent a different phase of the same overall phenomenon.

Contents

List of Figures

List of Tables

Chapter 1 Introduction

This introduction is meant to serve a number of purposes, and as such does not follow a single logical thread. First, a brief overview of the scientific background is given. Because each of the principal chapters in this thesis represent self-contained articles—each with its own introduction to the scientific background—the introduction that follows has been kept basic and minimal. Following this background section is an account of the history of the integral field spectrograph project, which aims to place the instrumentation effort in the context of the larger goals represented in this thesis. Finally, an outline of the thesis is presented, detailing the state of publication of each chapter, as well as my personal contribution to each of these collective efforts.

1.1 Scientific Background

Ultraluminous infrared galaxies (hereafter ULIRGs) are the most luminous class of galaxies in the local universe. Their power output of $10^{12} L_{\odot}$ is rivaled only by quasars—or more generally quasi-stellar objects (QSOs). ULIRGs were recognized as a class of galaxies following the *Infrared Astronomical Satellite*—or *IRAS*—mission in the mid 1980s. The reason for their late discovery is a result of the fact that the bulk of the energy emitted from these galaxies emerges in the far-infrared, where ground-based observations are impossible. The nature of the far-infrared emission can be characterized as thermal radiation at a temperature of ~ 60 K. The extreme far-infrared luminosity of these galaxies is understood to be the result of an optically obscured energy source with its energy output reprocessed via dust heating. In other words, whatever is responsible for generating the immense power is buried behind vast quantities of dust, and we only see the second-hand product of the dust that is heated by this power source.

As a result of the thick obscuration, it is very difficult to determine the nature of

the central power source. The two most viable candidates include a major burst of star formation—termed "starburst"—or a buried QSO, often referred to as an active galactic nucleus (AGN—also refers to active galactic nuclei). The luminosity from the starburst originates primarily from the most massive young stars produced in the burst. The luminosity in the AGN scenario originates from viscous dissipation of gravitational energy released by gas falling onto a super-massive black hole. These processes have very different characteristics that would be easily distinguished in the absence of the dust obscuration. Starbursts are characterized by moderate spatial extent of a few hundred parsecs, blackbody energy distributions with little or no far-ultraviolet emission, and moderate velocities typically not exceeding $\sim$ 500 km s^{-1}. AGN, on the other hand, have power-law spectral energy distributions extending into the far-ultraviolet/soft-X-ray wavelengths, very compact spatial extents of perhaps a few parsecs, and very high velocities well over 1000 km s^{-1} resulting from gas orbiting the black hole at close range.

Light at near-infrared wavelengths is much less susceptible to attenuation by dust than is visible light, with almost a factor of ten-thousand difference in transmitted energy. Therefore, attempts to probe the internal processes in ULIRGs are best performed at longer wavelengths. This thesis presents a number of observations of ULIRGs in the 2 μm atmospheric window, some of which are directed at searching for evidence of AGN phenomena hidden from view in visible light observations. The primary diagnostics employed for this purpose are Doppler-broadening of the emission lines due to high velocity orbital motions, and the presence of the [Si VI] emission line, which cannot be produced by the relatively low energy photons emitted from stars. Very little evidence is seen in this work for AGN activity in ULIRGs, with the vast majority appearing to be powered by starburst phenomena.

Besides their unusually high levels of luminosity, ULIRGs share another common trait, which is that almost all ULIRGs appear to be associated with major mergers between massive galaxies. Nearly half of all ULIRGs are seen as close, overlapping pairs of galaxies in the process of merging. The other half appear to be single objects, but surrounded by tidal debris that was ripped out of the progenitor galaxies during

a very recent violent merger process. A direct connection can be made between the merging process and the high luminosity. In short, the orbits of gaseous material within the galaxies is disrupted by the merger process, and is funneled into the central regions where the resulting high concentrations of gas provide the means to ignite a massive starburst or fuel an AGN. The dust that rides along with the gas provides a natural screen, hiding the internal fireworks from direct view.

The latter half of the thesis concentrates on investigating the geometries of ULIRGs, both looking at the subtle character of the nuclear line emission in a ULIRG suspected to harbor an AGN, and trying to understand the merger geometry and its connection to the ultraluminous activity. The former work finds evidence that both AGN and starburst components contribute to the total observed luminosity of this particular ULIRG. The latter work finds a surprising population of ULIRGs believed to be viewed just after their first major encounter. It was previously assumed that double-nucleus ULIRGs were in the end-stages of the merger process. This finding has implications for the rate at which fuel can be gathered and concentrated, as well as on the nature of the luminosity evolution during the merger process.

1.2 History of the PIFS Project

A very major part of my graduate student effort was the design and construction of the Palomar Integral Field Spectrograph (PIFS). The treatment of this enterprise is very much abbreviated in the present work, as the focus of the written thesis is on the scientific results of the ULIRG observations. Due to its minor coverage in the thesis, despite its great importance in the big picture, I should say a few words about the history of this project that were not appropriate for the published article on the instrument, found in Chapter 5.

I knew very early in my graduate career that I wanted to build a significant piece of astronomical instrumentation. Because I was working on a project involving ULIRGS, my thoughts were naturally bent towards a device that would enable unique observations of these twisted, complex, train-wreck galaxies. I thought about building an

infrared Fabry Perot device, though it became clear that the right way to implement such a device would be to use an off-the-shelf etalon from the highly successful Queensgate line of products. The act of simply placing a commercially available component in the train of an existing infrared camera lacked the substance I was seeking in a project.

Sometime during this period, probably early 1995, Tom Soifer showed me an article from Reinhard Genzel's group at the Max Plank Institute in Garching that described a novel sort of infrared spectrograph built by Lothar Weitzel, and capable of delivering simultaneous spectra across a two-dimensional field. This article went into very little detail about the instrument itself, focusing primarily on some early results. But I saw a schematic of the focal plane assembly of the image slicer, which was enough to tell me how the device worked. I thought it was a clever idea, but the rumored $1M price tag (with $100k for the image slicer alone) discouraged me from thinking seriously about an integral field spectrograph as an option for my thesis project.

In 1995, some months before the three-year NSF group proposal was due, it was decided that I could dismantle one of our existing imaging cameras and use its 256×256 HgCdTe (NICMOS 3) array for whatever instrument I might want to build. With this option available, I began thinking seriously about building an integral field spectrograph. The use of a pre-existing array and electronics brought this goal into range, not only due to the financial savings, but also from an infrastructure standpoint—this system was already in use at Palomar. The group proposal contained a two-page description and figure of the very earliest rendition of the spectrograph design.

Unfortunately, our group did not receive the funding support from NSF that had fueled the group's activities for decades. This unexpected lack of funding changed my plans a bit. We planned to submit new proposals specifically for the instrument project both to NASA and to the NSF in the summer of 1996. A month or two before the first proposal was due, I sat down with Tom Soifer to discuss our strategy, and expressed my hesitation to embark on what was still a rather large scale project. A few sticky technical problems, compounded with uncertainty of funding, caused me to reconsider pushing forward with this plan. I convinced Tom that the integral

field project was too ambitious given our resources, and we started thinking about alternative instrument projects. Just then, a key idea hit me, which in retrospect was so painfully obvious that it was downright alarming it had not occurred to us before. The idea was to follow the approach of my fellow graduate students—James Larkin and Rob Knop—and build the spectrograph to feed the existing imaging cameras by adopting a two-dewar approach (Larkin et al., 1996; Knop, 1997; Larkin, 1996, see the bibliography in Chapter 5). This approach, successfully demonstrated by the longslit spectrograph, was a proven concept with minimal losses at wavelengths shortward of about 2.3 microns. Additionally, I realized that a design tailored to fit within the current spectrograph dewar would allow a contingency plan in the event that funding did not become available. Tom and I were both immediately revitalized in our enthusiasm for the project. This was the critical design approach that brought the project within the reach of a single graduate student's effort.

A design conforming to the dimensional constraints imposed by the longslit spectrograph dewar quickly converged into a compact arrangement of optics, setting the dimensions and optical properties for the image slicer. With a relatively mature design in the proposals, and a contingency plan in the event of zero funding, I was able to begin concentrating on the real physical issues of the design—the most important of which was the image slicer. Unlike the German integral field spectrograph, with its warm image slicer, the Palomar instrument was to have a cryogenic slicer in order to more effectively work in the K band without the pernicious baffling problems encountered in the German instrument. This suggested an all aluminum design, such that differential contraction between, for example, glass and metal, would not compromise cryogenic alignment and performance. Aluminum optics were attractive because diamond fly cutting techniques could very easily create optical-quality surfaces on aluminum. My insistence that no fiddling should be necessary for alignment of the eight optical paths demanded a fabrication process that guaranteed alignment upon assembly. An approach using precision pinholes arose from a series of brainstorming sessions with Keith Matthews. Beginning work in November of 1996, I had a precision "prototype" image slicer assembled by February, which ended up being the final

version. Full funding from the NSF arrived in April, with a total budget of $240k. The project then hit full speed.

Unfortunately, or perhaps fortunately for me, a variety of factors made the resources I had planned on utilizing (e.g., mechanical engineer, all of the machining labor) either unavailable or too slow for my needs. As a result, I ended up doing all of the optical/mechanical design work, which resulted in about 150 machine drawings (made to ANSI standards, no less). I performed the majority of the machine work, fabricating almost half of the 350 machined pieces—typically machining the most challenging pieces, with compound angles or high precision requirements. The project demanded an unjustifiably large amount of metrology—especially on the dewar—for which my personal theodolite was an invaluable tool. The theodolite was also a highly useful item in the optical alignment process.

Because of my underutilization of resources, the instrument was built in total for less than $70k, not including my own salary, which came from an external fellowship. The total time commitment on my part was approximately two years, with first light on 3 September 1998—one year and a half after funding commenced.

From its very first hour under dark skies on its first scheduled night at the telescope, PIFS has been ready to perform. The weather, unfortunately, did not cooperate until March of 1999. In those first few runs, though, enough time was spent on the sky to verify its fully functional performance. However, a few incidents have temporarily compromised full observing efficiency in its 7–8 runs to date. In the July 1999 run, an internal setscrew became loose on one of the two grating shafts, requiring manual tuning prior to each observation. That problem was soon remedied in a permanent manner. On one occasion, during the November 1999 run, small bits of black-painted aluminum foil with double-stick tape on one side—used to baffle small cracks—came loose and partially obscured a small portion of the light path. Apparently the tape does not stick very well in cryogenic environments, even though it was supposedly specialized for this purpose. These fragments have since been removed, and all is presently in tip-top shape. PIFS continues to be used by other investigators, with 12 nights scheduled in the current semester, none of which are for my own use.

I have written an extensive 100-plus page manual for PIFS, also covering operations of some of the auxiliary infrared equipment setup. This manual can currently be accessed via the web, at http://www.its.caltech.edu/~tmurphy/pifs/pifs.html.

1.3 Thesis Outline

This thesis is arranged primarily in two sections. The first deals with a spectroscopic survey of a sample of 33 ULIRGs, with the primary goal of searching for buried AGN, and also understanding the physical conditions of typical ULIRGs. The second phase of the thesis treats the construction and use of the Palomar Integral Field Spectrograph toward the understanding of ULIRG kinematics and how the present state of the galaxy merger relates to the ultraluminous activity.

This is essentially a "staple" thesis in that it is comprised of papers that have either already been published in refereed journals, or will soon be published, or submitted. I am not the sole author on any of these papers, and as such I am required by Institute guidelines to clarify my contribution to each of the works in order to justify its appearance in the thesis. One ill effect of this "paper thesis" approach is that introductory information to each chapter is often repetitious. Each chapter contains its own bibliography, with some references repeated among the various chapters.

Chapter 2 presents the results of the spectroscopic survey, displaying the individual spectra for each ULIRG and exploring the range of properties observed among the sample. This is a work in preparation for journal submission, with an author list: T. W. Murphy, Jr., B. T. Soifer, K. Matthews, L. Armus, and J. R. Kiger. My contribution to this program has been substantial, with the great majority of the work and analysis performed by me. J. Kiger wrote a significant portion of the data reduction procedures. The observing program lasted 2.5 years, and resulted in a dataset rich enough to warrant a full thesis by itself. Because I divide my attention between this and the integral field data, this data set is not exploited to its full capacity.

Chapter 3 is from a published article that summarizes the results of the AGN search component of the spectroscopic survey. This paper appeared in *Astrophysical Jour-*

nal Letters, 1999, **525**, L85, titled "Near-Infrared Spectra of Ultraluminous Infrared Galaxies," with an author list: T. W. Murphy, Jr., B. T. Soifer, K. Matthews, J. R. Kiger, and L. Armus. This too was largely my effort, though B. T. Soifer contributed substantially to the co-authoring of this paper.

Chapter 4 provides a logical transition from the longslit survey in Chapters 2 and 3 to the integral field work that follows. An introduction to the concept of integral field spectroscopy is offered, followed by a description of the scientific issues one may explore with an integral field device. This chapter preserves to a great extent the original motivation for moving in this direction, as well as some supplementary examples indicating the potential utility of an integral field instrument. This chapter serves as glue for the thesis, and does not appear outside of this work.

Chapter 5 describes the Palomar Integral Field Spectrograph (PIFS), and provides sample data to illustrate its versatility and effectiveness. This chapter is published in the *Publications of the Astronomical Society of the Pacific*, 1999, **111**, 1176, titled "A Cryogenic Integral Field Spectrograph for the Palomar 200-Inch Telescope" with authors: T. W. Murphy, Jr., K. Matthews, and B. T. Soifer. The construction of the spectrograph was a major part of my effort as a graduate student, which is disproportionately represented in the chapters to follow. Because of this special circumstance, and to illustrate my personal involvement in this project, I have included a history of the project above, in Section 1.2. This, I believe, helps place the instrument effort in context.

Chapter 6 presents integral field data from the PIFS on IRAS 08311−2459—one of the two ULIRGs out of 33 that show signs of AGN activity (as detailed in Chapter 3). This work demonstrates the power of subtlety that is available with integral field spectroscopic techniques by differentiating the various morphologies among various line species or velocity regimes. This chapter is a paper that has recently (March 2000) been submitted to the *Astronomical Journal*, titled "The Active Nucleus in the Ultraluminous Infrared Galaxy IRAS 08311−2459," with authors T. W. Murphy, Jr., B. T. Soifer, K. Matthews, and L. Armus. This paper represents work that again is largely my own.

The final chapter before the conclusions, Chapter 7, presents a rather diverse set of morphologically challenged ULIRGs, as observed with PIFS. These galaxies showcase the wealth of information available via integral field techniques. The merger geometry for three of the four galaxies presented in Chapter 7 has been elucidated, through which it is seen that ULIRGs may be found at very early times in the encounter process. This chapter represents a work in progress, to be submitted in the near future with an author list similar to that for the paper on IRAS 08311−2459. The efforts presented in this chapter are mostly my own, with B. T. Soifer actively participating in the discussions of issues surrounding the effort to understand the data and their implications.

A chapter presenting the overall conclusions from this diverse body of observations is found at the end. Most of the data chapters contain their own summary, some of which is repeated in Chapter 8. A few overarching principles learned from the integrated effort are presented here as well.

Chapter 2 Near-Infrared Spectroscopic Survey of ULIRGs

2.1 Chapter Overview

We present near-infrared spectroscopy for a complete sample of 33 ultraluminous infrared galaxies at a resolution of $R \approx 1000$. Most of the wavelength range from 1.80–2.20 μm in the rest frame is covered, capturing the Paα and Brγ hydrogen recombination lines, and the molecular hydrogen vibration-rotation 1–0 S(1) and S(3) lines. Other species, such as He I, [Fe II], and [Si VI] appear in the spectra as well, in addition to a number of lesser molecular hydrogen lines. Nuclear extractions for each of the individual galaxies are presented here, along with spectra of secondary nuclei, where available.

This survey was carried out primarily to search for signatures of active nuclei via velocity-broadened hydrogen recombination or by the presence of the [Si VI] coronal line, with a 167 eV excitation potential. These signatures are rare in the present sample, occurring in only two of the 33 galaxies. The extinction to the hydrogen recombination lines is investigated via ratios of Paα and Brγ, through which it is found that visual extinctions in excess of 10 magnitudes are relatively common among ULIRGs. The ionized hydrogen regions in many ULIRGs are sufficiently obscured that buried active galactic nuclei would remain hidden at 2 μm at the current level of sensitivity. The vibration-rotation lines of molecular hydrogen appear to be predominantly thermal in origin, with effective temperatures generally around 2200 K. The relative nuclear velocities between double nucleus ULIRGs are investigated, through which it is inferred that the maximum deprojected velocity difference is ~ 200 km s^{-1}. This figure is lower than the velocities predicted by physical models of strong interactions/mergers of large, gas-rich galaxies.

2.2 Introduction

Understanding the nature of the ultimate power source in ultraluminous infrared galaxies (ULIRGs) has been a primary driver for numerous scientific investigations ever since the discovery in the 1980's that ULIRGs represent the most luminous class of galaxies in the local universe. With total power outputs comparable to those of quasars, characterizing the source of power is of fundamental importance in understanding the composition and evolution of normal galaxies. ULIRGs are found to share the common trait that virtually all have recently or are currently experiencing major encounters with other galaxies (Murphy et al., 1996; Clements et al., 1996; Sanders et al., 1988; Carico et al., 1990). Encounters like these may play a significant role in the process of building normal galaxies. With the discovery of faint sources at sub-millimeter wavelengths having characteristic spectral energy distributions like that typically found in ULIRGs (e.g., Arp 220), the importance of understanding these systems and their role in the evolution of normal galaxies has been heightened.

The present survey was designed to look for signs of obscured active galactic nuclei (AGN) in ULIRGs, either by the presence of velocity-broadened Paα emission or by the appearance of the high excitation [Si VI] coronal line. A summary of the findings of this survey are contained in Murphy et al. (1999) (Chapter 3, this thesis). Only two of the 33 sample galaxies show clear indications for AGN activity, with the rest appearing to be dominated by star formation processes. Either the AGN phenomenon is relatively rare among ULIRGs, or the extinction at 2 μm is still too high to permit a proper assessment. Mid-infrared studies (e.g., Genzel et al., 1998; Rigopoulou et al., 1999) favor the former conclusion, though it is found in this study that the extinction at 2 μm may often be greater than four magnitudes, resulting in over one magnitude of extinction at mid-infrared wavelengths.

This chapter presents the individual nuclear spectra for the sample galaxies, for both the primary and secondary nuclei where possible. Two-dimensional spectra are also presented to give a qualitative view of the line emission distributions typically found in ULIRGs. Some discussion of extinction measures, molecular hydrogen exci-

tation mechanisms, and velocity differences among double nucleus systems is included. Additionally, a summary of typical line ratios found in ULIRGs is included for reference.

2.3 The Sample

The sample of 33 ULIRGs in this survey approximately represents a complete, volume-limited sample originating from the 2Jy sample of *IRAS* (Infrared Astronomical Satellite) galaxies defined by Strauss et al. (1990, 1992). The galaxies in the present sample are chosen to meet the following criteria:

1. 60 μm flux density, $F_\nu(60\ \mu\mathrm{m}) > 1.94$ Jy
2. Moderate or high quality IRAS flux measurements at 60 and 100 μm (as defined in the IRAS PSC, Explanatory Supp., 1988)
3. $F_\nu^2(60\ \mu\mathrm{m}) > F_\nu(12\ \mu\mathrm{m}) \times F_\nu(25\ \mu\mathrm{m})$, where $F_\nu(\lambda)$ is the *IRAS* flux density
4. Far-infrared luminosity $L_{FIR} > 5 \times 10^{11} L_\odot$
5. Absolute Galactic latitude, $|b| > 5°$
6. Declination, $\delta > -35°$
7. Redshift, $0.055 < z < 0.108$

The first six conditions are those used to define the northern 2 Jy ULIRG sample in Murphy et al. (1996), such that the current sample is a subset of this work. The seventh condition places both the Paα and Brγ lines in the K band atmospheric window. The far-infrared luminosity is computed from the IRAS flux densities by the following conversion:

$$L_{FIR} \equiv 3.86 \times 10^5 D^2 \left[2.58 F_\nu(60\,\mu\mathrm{m}) + \mathrm{F}_\nu(100\,\mu\mathrm{m})\right] L_\odot,$$

(IRAS PSC, Explanatory Supp., 1988, p. X-13) where D represents the luminosity distance to the source in Mpc.

Due to the redshift constraint, the current sample approximately represents a complete volume-limited sample, because even the galaxies with the minimum 60 μm flux density are luminous enough to meet the sample criteria at all allowed redshifts. At the outer redshift limit of the survey, corresponding to a luminosity distance of 455 Mpc using $H_0 = 75$ km s^{-1} Mpc^{-1} and $q_0 = 0$ (as is assumed throughout), the minimum 60 μm flux density of 1.94 Jy by itself accounts for $4 \times 10^{11} L_\odot$ of the total far-infrared luminosity. To make up the remaining $10^{11} L_\odot$ necessary for sample inclusion, the 100 μm flux density needs only be greater than 1.25 Jy, implying a maximum $F_\nu(60\ \mu\mathrm{m})/F_\nu(100\ \mu\mathrm{m})$ ratio of 1.55. ULIRGs very rarely have 60 μm to 100 μm flux density ratios this high, such that the volume limit imposed by the upper redshift cutoff is more stringent than the flux density cutoff, resulting in a sample that is mostly volume-limited rather than flux-limited. Taking the 64 ULIRGs defined in the northern 2 Jy sample of Murphy et al. (1996), one finds an average $F_\nu(60\ \mu\mathrm{m})/F_\nu(100\ \mu\mathrm{m})$ ratio of 0.90 ± 0.22, with a median value of 0.86 and a maximum of 1.64 (in IRAS 08572+3915), which is the only ratio exceeding the maximum of 1.55 compatible with the volume-limited case. The ULIRG from the northern 2 Jy sample with the second highest ratio is IRAS 05246+0103, with $F_\nu(60\ \mu\mathrm{m})/F_\nu(100\ \mu\mathrm{m}) = 1.31$. Both of these galaxies are contained in the present sample.

Of the 35 ULIRGs in the redshift survey of Strauss et al. satisfying the above conditions, two are not included here for the following reasons. The spectra of IRAS 21396+3623 show this galaxy to be at a redshift of $z = 0.1493$, rather than the previously reported $z = 0.097$. IRAS 19297−0406 was free of any discernible lines, which may be the result of improper pointing, producing the spectrum of a nearby star in the very crowded field. Therefore, the entire sample contains 33 galaxies, and is very nearly complete in the volume-limited sense. A list of the sample galaxies appears in Table 2.1.

Table 2.1. Spectroscopic Survey Sample

Galaxy Name	cz (km s^{-1})	L_{IR} ($10^x L_\odot$)	Separation[a] (arcsec)
IRAS 00262+4251	29205	12.08	S
IRAS 01521+5224	23959	11.95	5.5
IRAS 04232+1436	23640	11.99	S
IRAS 05246+0103[b]	29105	12.05	6.0
IRAS 08030+5243	24946	11.97	S
IRAS 08311−2459[b]	30167	12.40	S
IRAS 08344+5105	28999	11.94	S
IRAS 08572+3915[b,c]	17491	12.08	5.6
IRAS 09061−1248	22014	11.97	5.6
IRAS 09111−1007	16247	11.98	(37)
IRAS 09583+4714	25748	11.98	25.5
IRAS 10035+4852	19449	11.93	9.8
IRAS 10190+1322	22898	11.98	4.0
IRAS 10494+4424	27671	12.15	S
IRAS 11095−0238	31936	12.20	S
IRAS 12112+0305[c]	22009	12.27	2.9
IRAS 14348−1447[c]	24798	12.28	3.3
IRAS 14352−1954	26938	11.95	S
IRAS 14394+5332	31401	12.04	(28)
IRAS 15245+1019	22629	11.96	2.6
IRAS 15250+3609[c]	16515	11.99	S
IRAS 15462−0450	30060	12.16	S
IRAS 16487+5447	31110	12.12	3.1
IRAS 17028+5817	31805	12.11	13.0
IRAS 18470+3233	23520	12.02	(7.0)
IRAS 19458+0944	29983	12.36	S
IRAS 20046−0623	25286	12.02	S
IRAS 20087−0308	31613	12.39	S
IRAS 20414−1651	26061	12.19	S
IRAS 21504−0628	23343	11.94	S
IRAS 22491−1808[c]	23264	12.12	1.6
IRAS 23327+2913	32225	12.03	12.5
IRAS 23365+3604	19305	12.13	S

[a]Nuclear separation is given where applicable. S denotes a single nucleus. Numbers in parentheses denote a double nucleus system for which only the primary nucleus spectrum is presented, generally because the separation exceeds the slit length.

[b]Galaxies with "warm" infrared colors: $F_\nu(20\ \mu\text{m})/F_\nu(60\ \mu\text{m}) > 0.2$.

[c]Members of the Bright Galaxy Sample (BGS) of Soifer et al. (1987).

2.4 Observations & Data Reduction

Observations were conducted using the Palomar longslit infrared spectrograph (Larkin et al., 1996), operating on the 200-inch Hale Telescope and employing a 256×256 HgCdTe (NICMOS 3) array. Observations were made over a time period beginning in 1995 July, and ending in 1997 December. Each object was observed in three grating settings, with each spanning $\sim$ 0.12 μm at a scale of $\sim$ 0.0006 μm pixel^{-1}. Typical slit widths of $\sim$3.75 pixels, or 0$''$.625, resulted in spectra with resolutions of $R \equiv \lambda/\Delta\lambda \approx 1000$, corresponding to $\sim$300 km s^{-1}. The grating settings were chosen to cover the Paα line at 1.8751 μm, the suite of Brδ, H_2 1–0 S(3), and [Si VI] lines centered at 1.954 μm, and the H_2 1–0 S(1) and Brγ lines centered at 2.14 μm. The slit was generally rotated such that spectra of both primary and secondary nuclei were obtained simultaneously when possible, or otherwise to coincide with the major axis of the galaxy, where evident.

Observational data is provided for each source in Table 2.2. Individual exposure times were 300 s, with total integration times generally around 1800 s. In all cases, the galaxy was dithered between two positions on the slit, generally $\sim$ 20$''$ apart, with a smaller scale dither pattern employed about these points to eliminate the effects of static bad pixels. In this way, the sky integrations were obtained simultaneously, with the effective sky position alternating by 20$''$ to either side. Wavelength calibration was provided either by the atmospheric OH airglow spectrum, or by arc lamp spectra for the H_2 1–0 S(1)+Brγ grating settings, where the OH lines become unavailable. Wavelengths reported here are in air units, with the OH wavelength data coming from Oliva & Origlia (1992). Atmospheric transmission variations as a function of wavelength were compensated via observations of the nearly featureless spectra of G V stars at similar airmass, and similar telescope pointing, when possible. The G star observations were performed either immediately prior to or following each galaxy observation. Stellar types and airmasses of the calibrators are listed for each object in Table 2.2. The light from the calibrator star was made to uniformly fill the slit aperture by chopping the telescope secondary mirror in a triangle-wave pattern.

As such, the atmospheric calibrators perform the dual function of operating as the flat field for the spectral observations. Details about the treatment of the spectral calibration appear below. The calibration star observation for IRAS 12112+0305 was compromised beyond repair, so the spectra for this galaxy were divided by an atmospheric template.

Each spectrum is reduced pair-wise in the following manner. Pairs containing spectra at the two opposite slit positions are subtracted, with cosmic rays and static bad pixels interpolated. The data are divided by the G star spectrum and multiplied by a Planck function, described in more detail below. A wavelength reference image is produced using either a median combination of the data frames to produce an OH airglow spectrum, or by using a combination of noble gas arc lamp spectra. The wavelength calibration image is spatially and spectrally rectified onto a rectilinear grid using predetermined maps of the distortion in each of these directions. A cubic function of fixed cubic coefficient and zero quadratic coefficient (determined empirically to fit the distortion well) is fit to the wavelength reference, providing a mapping from pixel coordinates to linear wavelength coordinates. This mapping is added to the predetermined distortion maps, and then applied in a single interpolation to the data frames. Once rectified, the pairs are combined into a single spectrum, using Gaussian centroids for the spatial registration, or known pixel offsets for galaxies having diffuse or faint continua. This process removes any residual sky subtraction signal, as one effectively subtracts the simultaneous sky at the alternate slit position in the process. The noise at each pixel in the two-dimensional spectra is computed along with the spectral data by quadrature combination of read noise and Poisson noise based on signal level for each pixel. Pixel replacement, atmospheric calibrator division, and interpolation in the data frames are also properly treated in the noise frames throughout the process. The same extractions applied to the spectral data are performed on the noise image, producing a one-dimensional noise array along with the extracted spectrum.

The seeing at the time of observation was assessed by taking short guided exposures, typically 10 s in duration, of nearby field stars through the wide-open slit of

the spectrograph, with the spectrograph operating in imaging mode. In this way, the point spread function (PSF) of the telescope plus atmosphere during the spectral observations could be estimated. These PSF exposures were typically taken 3–4 times during an observation, usually at the beginnings and ends of the 30–40 minute intervals spent at each grating setting. The full-width at half-maximum (FWHM) along the slit direction was measured for each PSF image, and the nuclear extractions of the spectra were based on this measurement. In each case, the PSF FWHM was rounded up to an integral number of pixels, and extractions matching these integer widths were performed. The centers of these apertures were not constrained, however, such that fractional pixels were summed in the production of the nuclear spectra. The widths of the extractions, in arcseconds, are listed in Table 2.2.

Table 2.2. Observational Parameters

Galaxy	Grating Setting	Date	Integration (sec)	Slit P.A.	Atmos. Calib.	Obj./Cal. Airmass	Extraction (″)
IRAS 00262+4251	Paα:	3 Jan 1996	1800	0°	G1.5V	1.02/1.05	1.5
	[Si VI]:		1800			1.11/1.04	1.7
	H_2+Brγ:		1800			1.05/1.05	1.5
IRAS 01521+5224	Paα:	2 Jan 1996	1800	26°	G5Vb	1.06/1.09	2.0
	[Si VI]:		1800			1.06/1.08	1.8
	H_2+Brγ:		1800			1.07/1.08	1.7
IRAS 04232+1436	Paα:	26 Nov 1996	1800	5°	G0V	1.07/1.04	0.7
	[Si VI]:		1800			1.07/1.06	0.8
	H_2+Brγ:		1800			1.06/1.06	0.7
IRAS 05246+0103	Paα:	5 Dec 1996	1200	109°	G1V	1.19/1.18	0.8
	[Si VI]:		1800			1.21/1.21	0.8
	H_2+Brγ:		1800			1.18/1.17	0.7
IRAS 08030+5243	Paα:	31 Dec 1995	1800	151°	G5V	1.07/1.07	1.5
	[Si VI]:		1800			1.07/1.06	1.3
	H_2+Brγ:		1800			1.06/1.07	1.3
IRAS 08311−2459	Paα:	8 Apr 1996	1800	0°	G3V	1.91/1.99	1.7
	[Si VI]:		1800			1.92/1.82	1.7
	H_2+Brγ:		1200			1.94/1.93	1.0
IRAS 08344+5105	Paα:	3 Jan 1996	1800	0°	G0V	1.09/1.10	1.7
	[Si VI]:		1800			1.05/1.09	1.5
	H_2+Brγ:		1800			1.07/1.09	1.5
IRAS 08572+3915	Paα:	25 Nov 1996	2400	150°	G0V	1.01/1.01	0.8
	[Si VI]:		1200			1.03/1.02	0.7
	H_2+Brγ:		1800			1.01/1.01	0.7
IRAS 09061−1248	Paα:	28 Nov 1996	1800	21°	G0V	1.49/1.51	1.5
	[Si VI]:		1800			1.47/1.43	2.0
	H_2+Brγ:		1800			1.45/1.46	1.8
IRAS 09111−1007	Paα:	11 Feb 1997	1800	40°	G2V	1.39/1.45	1.7
	[Si VI]:		1200			1.42/1.39	1.5
	H_2+Brγ:		1800			1.39/1.41	1.7
IRAS 09583+4714	Paα:	3 Jan 1996	1800	56?5	G0V	1.03/1.03	1.5
	[Si VI]:		1800	56?5		1.03/1.04	1.2
	H_2+Brγ:	31 Dec 1995	1800	125°		1.04/1.03	0.8
IRAS 10035+4852	Paα:	22 Feb 1997	1200	33°	G0V	1.04/1.05	1.0
	[Si VI]:	23 May 1997	1800		G1V	1.21/1.15	0.8
	H_2+Brγ:		1800		F9V	1.09/1.06	0.7
IRAS 10190+1322	Paα:	22 May 1997	1800	65°	G0V	1.15/1.16	1.0
	[Si VI]:		1800		G1V	1.26/1.23	1.2
	H_2+Brγ:		1800		G0V	1.44/1.42	1.0
IRAS 10494+4424	Paα:	22 Feb 1997	1800	148°	G2V	1.03/1.02	1.0
	[Si VI]:		1200		G0Vs	1.15/1.10	0.8
	H_2+Brγ:		1800			1.09/1.10	0.7
IRAS 11095−0238	Paα:	6 May 1996	1800	38°	G1V	1.24/1.26	1.0
	[Si VI]:		1800			1.29/1.31	1.0
	H_2+Brγ:		1800			1.25/1.29	0.8
IRAS 12112+0305	Paα:	5 May 1996	1800	34°	···	1.09/ ···	1.0
	[Si VI]:		1800			1.05/ ···	0.8
	H_2+Brγ:		1800			1.07/ ···	1.0
IRAS 14348−1447	Paα:	5 May 1996	1800	32°	G1V	1.51/1.47	1.0
	[Si VI]:		1800		G4V	1.72/1.68	1.0
	H_2+Brγ:		1800			1.59/1.62	1.0
IRAS 14352−1954	Paα:	6 May 1996	1800	0°	G3V	1.70/1.73	1.2
	[Si VI]:		1800		G0V	1.71/1.79	0.8
	H_2+Brγ:		1800		G3V	1.68/1.72	0.8
IRAS 14394+5332	Paα:	5 May 1996	1800	56°	G1V	1.34/1.30	0.8
	[Si VI]:	6 May 1996	1800			1.51/1.50	0.8
	H_2+Brγ:		1800			1.36/1.32	0.7

The most significant stellar absorption feature present in the 2 μm window for the atmospheric calibrator stars is the Brγ line at 2.1655 μm. While a template stellar spectrum may be adequate for removal of this line, we instead interpolated over the line in the two-dimensional G star calibration/flat-field spectrum before dividing the galaxy data by the calibrator data. Multiplying the corrected galaxy spectrum by a Planck blackbody function with a temperature matching that of the calibrator rectifies the spectrum to a proper representation in flux density. To remove the effects of the weaker absorption lines in the atmospheric calibrator, the galaxy spectrum was multiplied by a normalized solar spectrum, smoothed and re-binned to the same resolution. For the long wavelength grating setting covering the H_2 1–0 S(1) and Brγ lines, the CO band structure becomes significant when using late-type G stars for the atmospheric calibration. When the atmospheric calibrator was of type G4–G8, a linear combination of G3 V and K0 V template spectra from Kleinmann & Hall (1986) was used instead of the solar spectrum. Again, this template was smoothed and re-binned to match the individual galaxy spectra.

2.5 Results

The chief results from the spectroscopic survey—that AGN appear to be rare among ULIRGs—are reported in Murphy et al. (1999) (Chapter 3). In this chapter we focus attention on the range of observed properties rather than on the collected sample as a whole.

Figure 2.1 presents spectral extractions for the primary nuclei in the 33 sample galaxies, with aperture sizes indicated in Table 2.2. Each plot is fixed in the rest frame, with the observed wavelength scale indicated at bottom. Annotations mark the locations of every common emission line, though in any individual spectrum only the lines with reasonable detections are labeled. The location of the tick marks is based on the observed redshift of the Paα line, as is the rest wavelength scale at top. Each spectrum is composed of three independent spectral datasets. For each of the three spectral ranges, a best linear fit to the line-free continuum is assessed for the purpose

Table 2.2—Continued

Galaxy	Grating Setting	Date	Integration (sec)	Slit P.A.	Atmos. Calib.	Obj./Cal. Airmass	Extraction (″)
IRAS 15245+1019	Paα:	22 May 1997	1800	113°	G8V	1.11/1.12	1.2
	[Si VI]:		1800			1.09/1.11	1.0
	H_2+Brγ:		1800			1.10/1.10	1.0
IRAS 15250+3609	Paα:	21 May 1997	1800	135°	G2V	1.03/1.01	1.0
	[Si VI]:		2400			1.01/1.02	1.0
	H_2+Brγ:		1800			1.00/1.01	0.7
IRAS 15462−0450	Paα:	7 Apr 1996	1800	60°	G2.5V	1.32/1.35	1.0
	[Si VI]:	8 Apr 1996	1800			1.41/1.36	0.8
	H_2+Brγ:	7 Apr 1996	1800			1.39/1.37	1.0
IRAS 16487+5447	Paα:	21 May 1997	1800	71°	G5V	1.08/1.11	0.7
	[Si VI]:		1800			1.11/1.12	0.8
	H_2+Brγ:		1800		G0Va	1.17/1.20	0.7
IRAS 17028+5817	Paα:	22 May 1997	1800	95°	G2V	1.14/1.13	0.8
	[Si VI]:		1800			1.18/1.14	1.0
	H_2+Brγ:		1800		G0Va	1.24/1.26	0.7
IRAS 18470+3233	Paα:	31 Jul 1996	1800	67°	G8V	1.05/1.00	0.8
	[Si VI]:		1800			1.00/1.00	1.0
	H_2+Brγ:		1800			1.01/1.00	1.0
IRAS 19458+0944	Paα:	2 Aug 1996	1800	121°	F5V+G0V	1.09/1.09	0.7
	[Si VI]:		1200			1.09/1.12	0.7
	H_2+Brγ:		1800			1.09/1.09	0.7
IRAS 20046−0623	Paα:	12 Aug 1997	1800	76°	G2V	1.37/1.40	1.0
	[Si VI]:		1200		G1V	1.31/1.27	1.0
	H_2+Brγ:		1200			1.31/1.27	1.0
IRAS 20087−0308	Paα:	11 Aug 1997	1800	90°	G1V	1.36/1.35	1.0
	[Si VI]:		1800		G0V	1.51/1.43	0.8
	H_2+Brγ:	12 Aug 1997	1800		G1V	1.39/1.43	1.3
IRAS 20414−1651	Paα:	1 Aug 1996	1800	64°	G2V	1.56/1.56	1.0
	[Si VI]:		1200		G1V	1.71/1.70	0.8
	H_2+Brγ:		1800		G2V	1.62/1.56	0.8
IRAS 21504−0628	Paα:	3 Aug 1996	1800	150°	G0V	1.30/1.33	0.8
	[Si VI]:		1200		G8V	1.54/1.62	2.0
	H_2+Brγ:		1800		G0V	1.34/1.33	0.7
IRAS 22491−1808	Paα:	2 Aug 1996	1800	108°	G8V	1.62/1.61	1.0
	[Si VI]:		1800			1.63/1.62	1.2
	H_2+Brγ:		1800			1.60/1.61	1.0
IRAS 23327+2913	Paα:	11 Aug 1997	1800	175°	G1.5V	1.00/1.01	1.0
	[Si VI]:		1200			1.03/1.01	0.7
	H_2+Brγ:	10 Jul 1995	1200		G0V	1.00/1.00	0.8
IRAS 23365+3604	Paα:	26 Nov 1996	1800	173°	G1.5V	1.01/1.01	0.8
	[Si VI]:	28 Nov 1996	1800		G2V	1.00/1.01	2.0
	H_2+Brγ:	26 Nov 1996	1800		G1.5V	1.03/1.02	0.8

of determining an overall average slope for the spectrum. The individual spectra are then scaled to lie on a common linear "backbone" defined by the average slope, and combined in a noise-weighted manner across the overlap region around 1.92 μm. The vertical scale is normalized such that the continuum is at one unit of flux density at 2.155 μm, corresponding to the middle of the K_s bandpass.

Figure 2.2 contains spectra of the secondary nuclei in the 14 sample galaxies with a nearby galactic companion. Annotations and scalings are the same as for Figure 2.1, though some of the weaker lines are not marked by default in this set. The tick marks denoting line positions are based on the redshift of the Paα line in the *primary* nucleus, such that velocity displacements between the two nuclei are more easily seen. The numerical flux density scale for each is identical to that for the corresponding spectrum in Figure 2.1, allowing direct comparison of the relative levels for each. No matching of continuum levels was attempted for this set of spectra, as it is assumed that the scalings determined for the primary nuclear spectra apply to these as well. The fact that the secondary nuclear spectra produced in this manner appear to match up reasonably well at the interfaces justifies this simple approach.

The choice of primary versus secondary nucleus is based solely on the continuum level, with the brighter nucleus designated as the primary. The only exception is IRAS 22491−1808, for which the dominant line-emitting nucleus is the weaker continuum source to the east. The western nucleus is 30% brighter, but lacks the strong H_2 emission that is associated with *every* other primary ULIRG nucleus. Comparison of Figures 2.1 and 2.2 indicate that the primary nuclei, besides being the brightest continuum sources, also dominate in terms of line emission. Yet despite the weaker line strengths, the secondary nuclei often show appreciable line emission activity, appearing relatively similar to the primary nuclei. If the observed Paα line strength is proportional to star formation rates—and therefore total luminosity—then even though the dominant luminosity can be associated with one nucleus, the lesser nucleus still contributes a substantial fraction of the total luminosity.

Table 2.3 presents the line measurements from the data shown in Figures 2.1 and 2.2. For each galaxy, the continuum slope and measured Paα FWHM are given, as

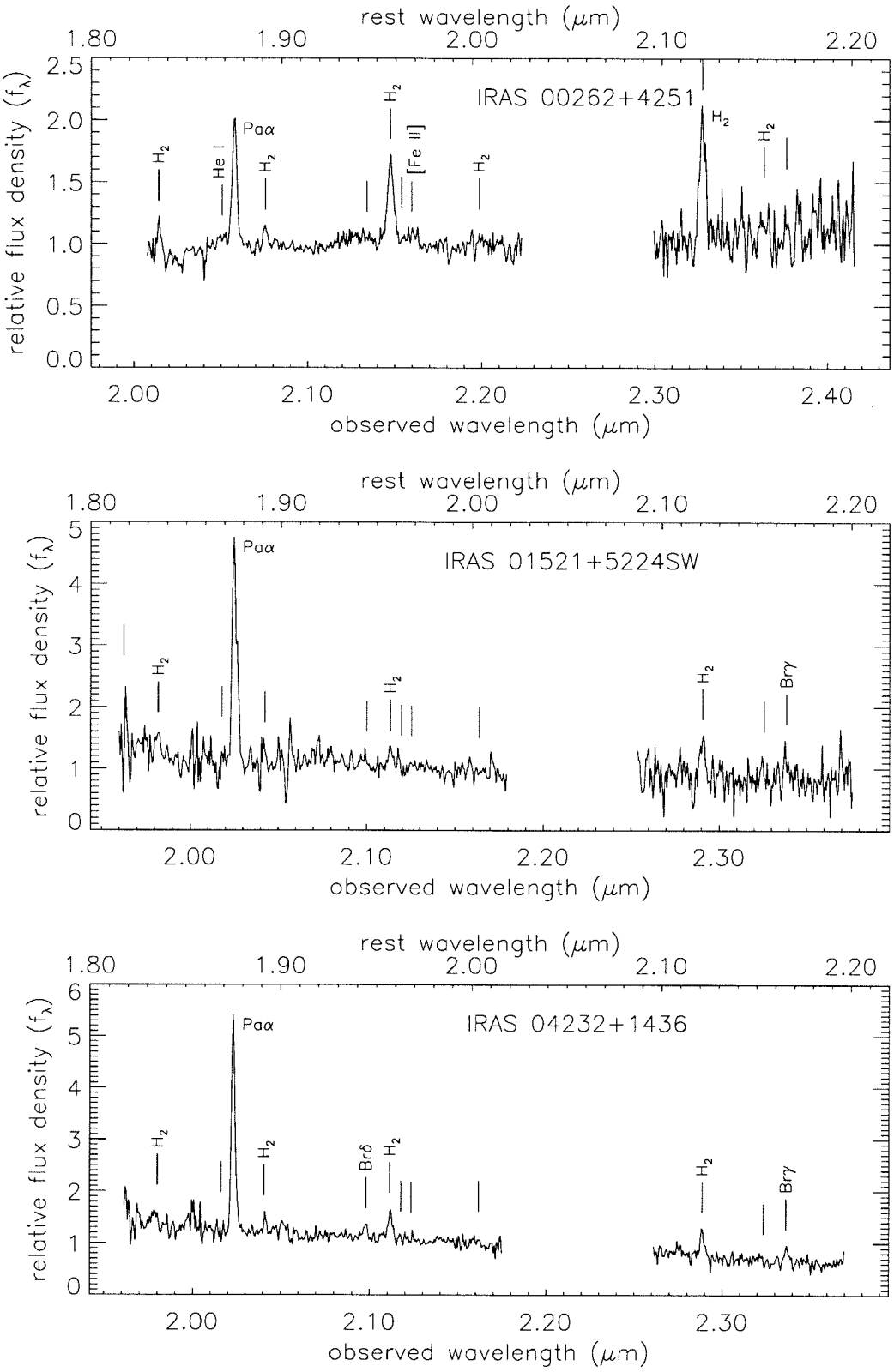

Figure 2.1: Spectral extractions for the 33 primary ULIRG nuclei.

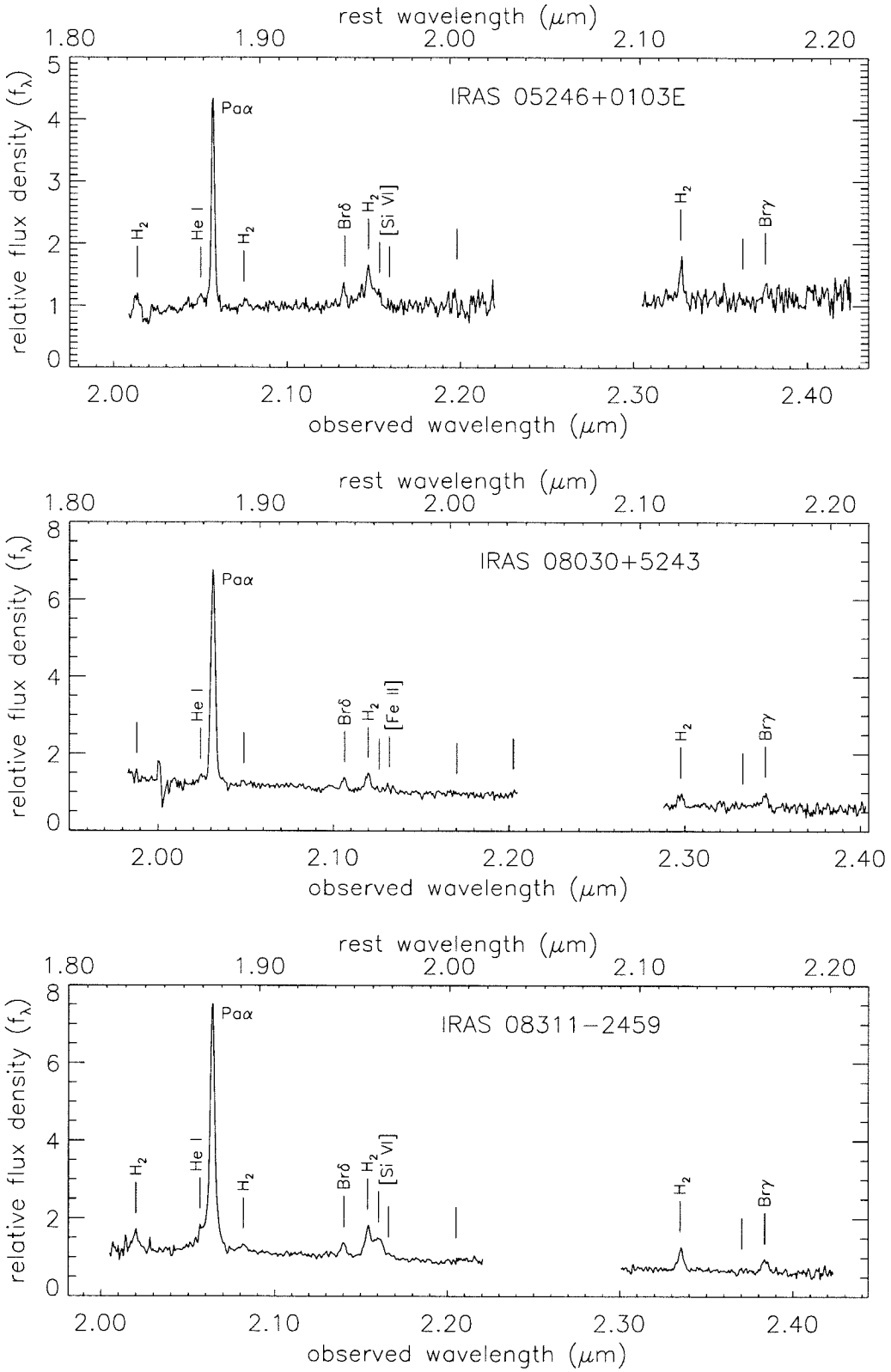

Figure 2.1: continued

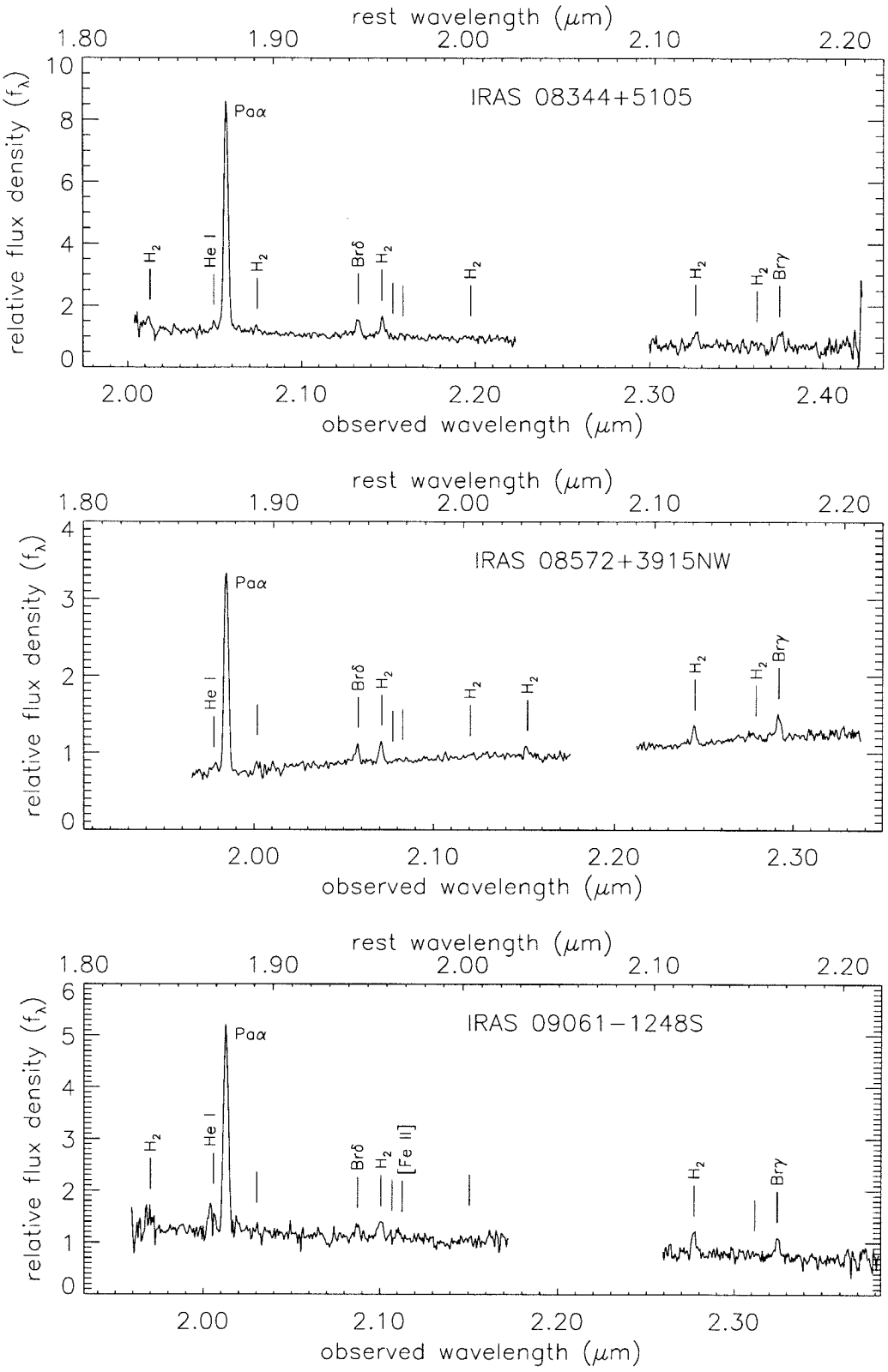

Figure 2.1: continued

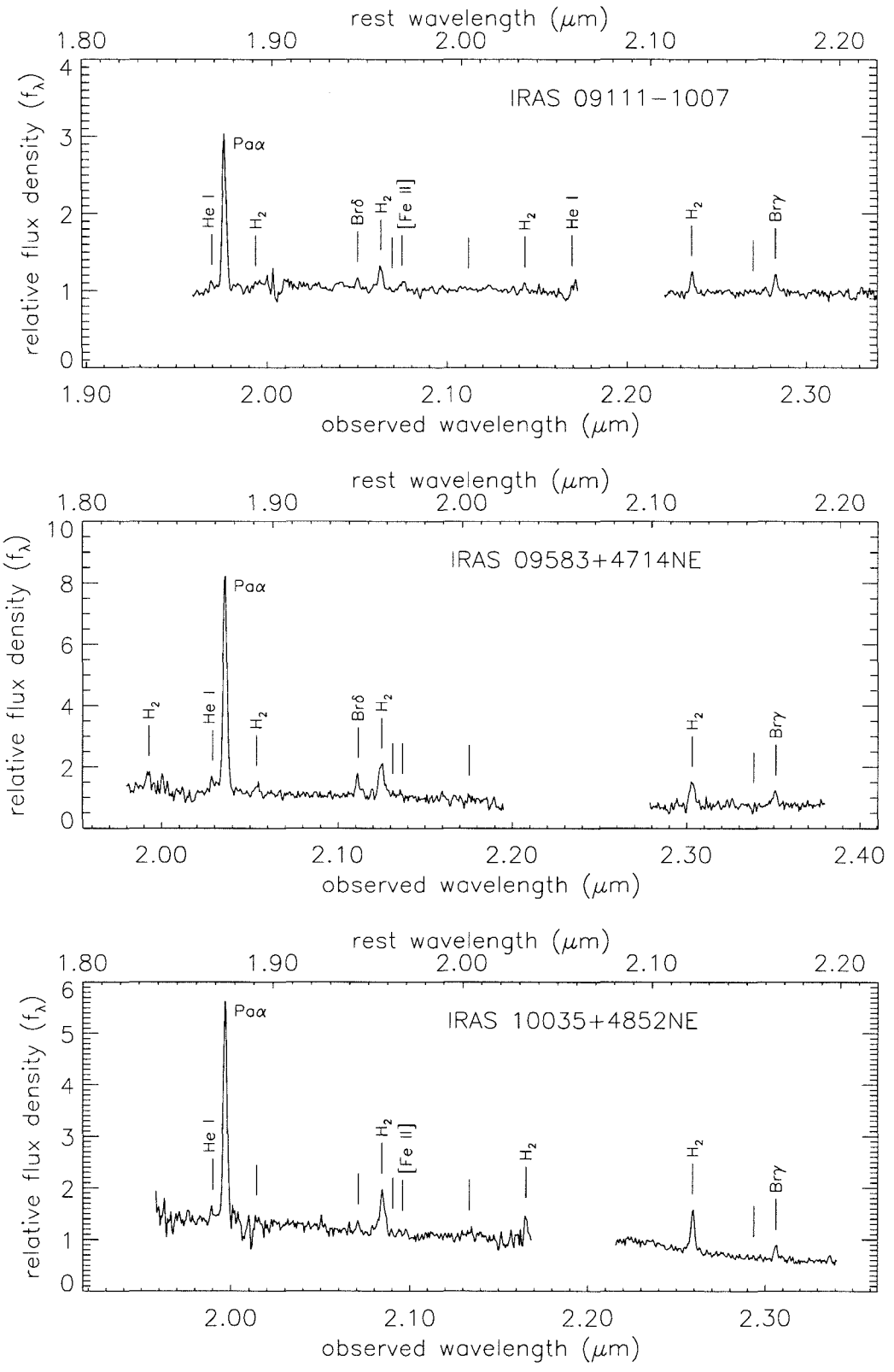

Figure 2.1: continued

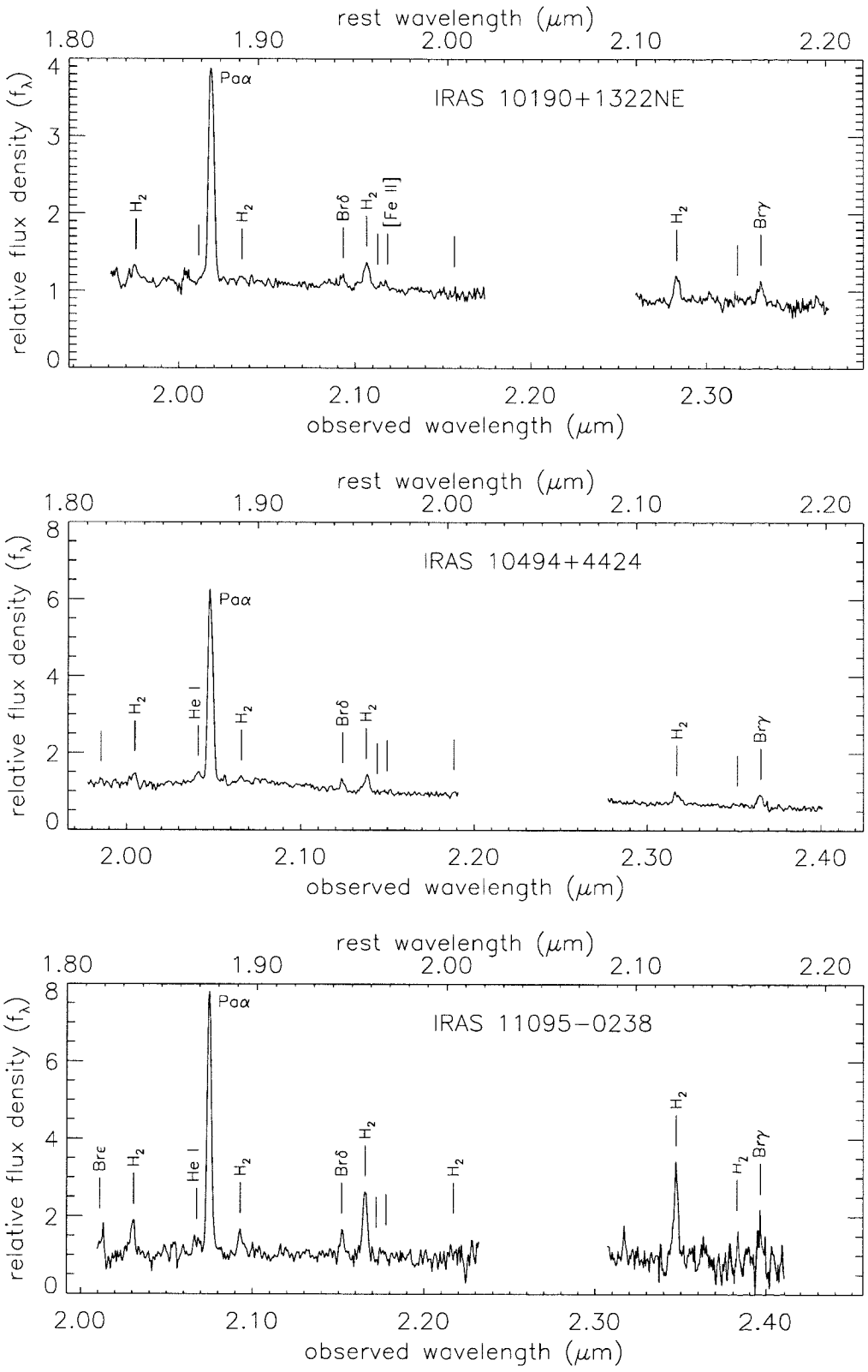

Figure 2.1: continued

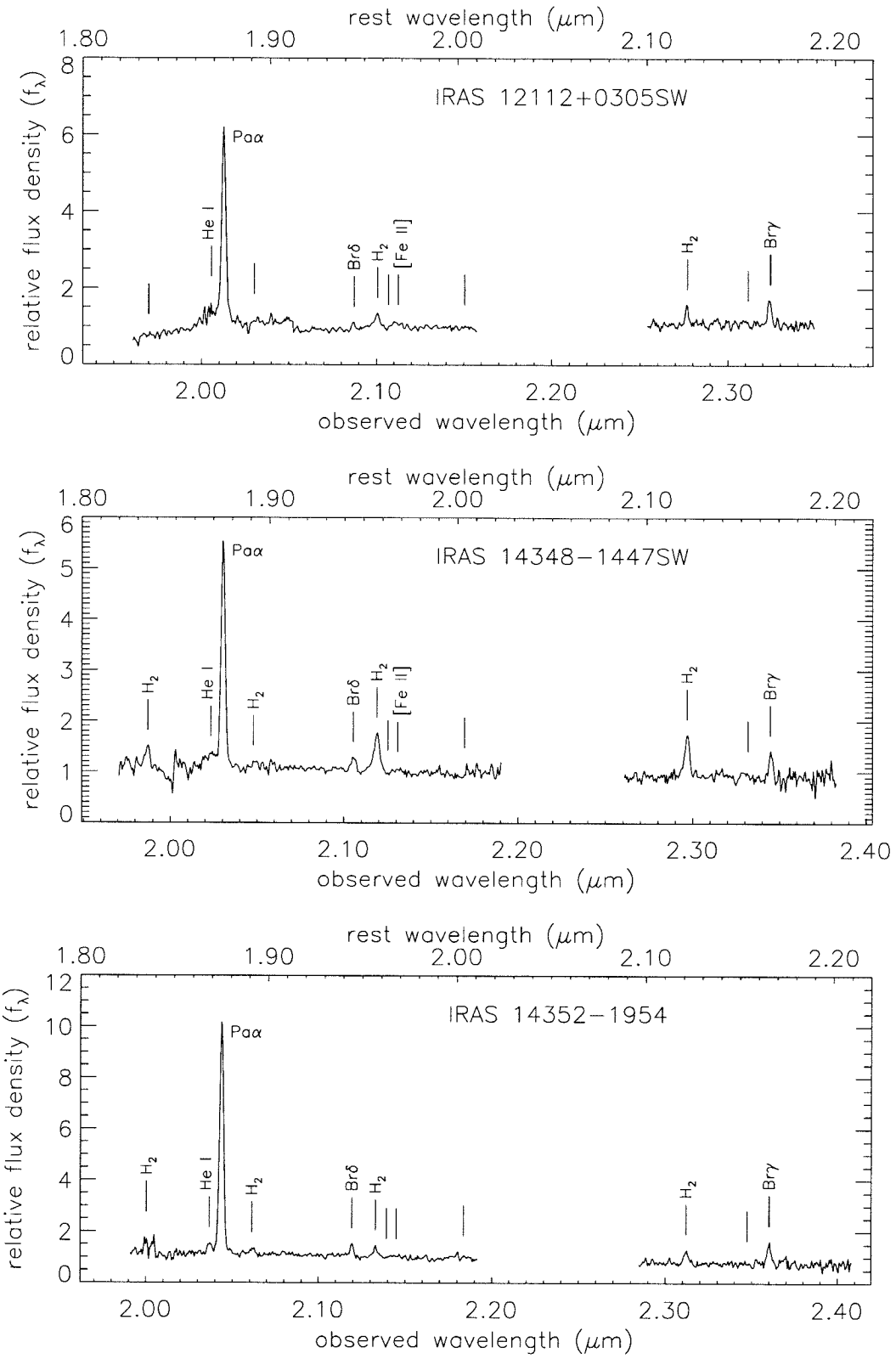

Figure 2.1: continued

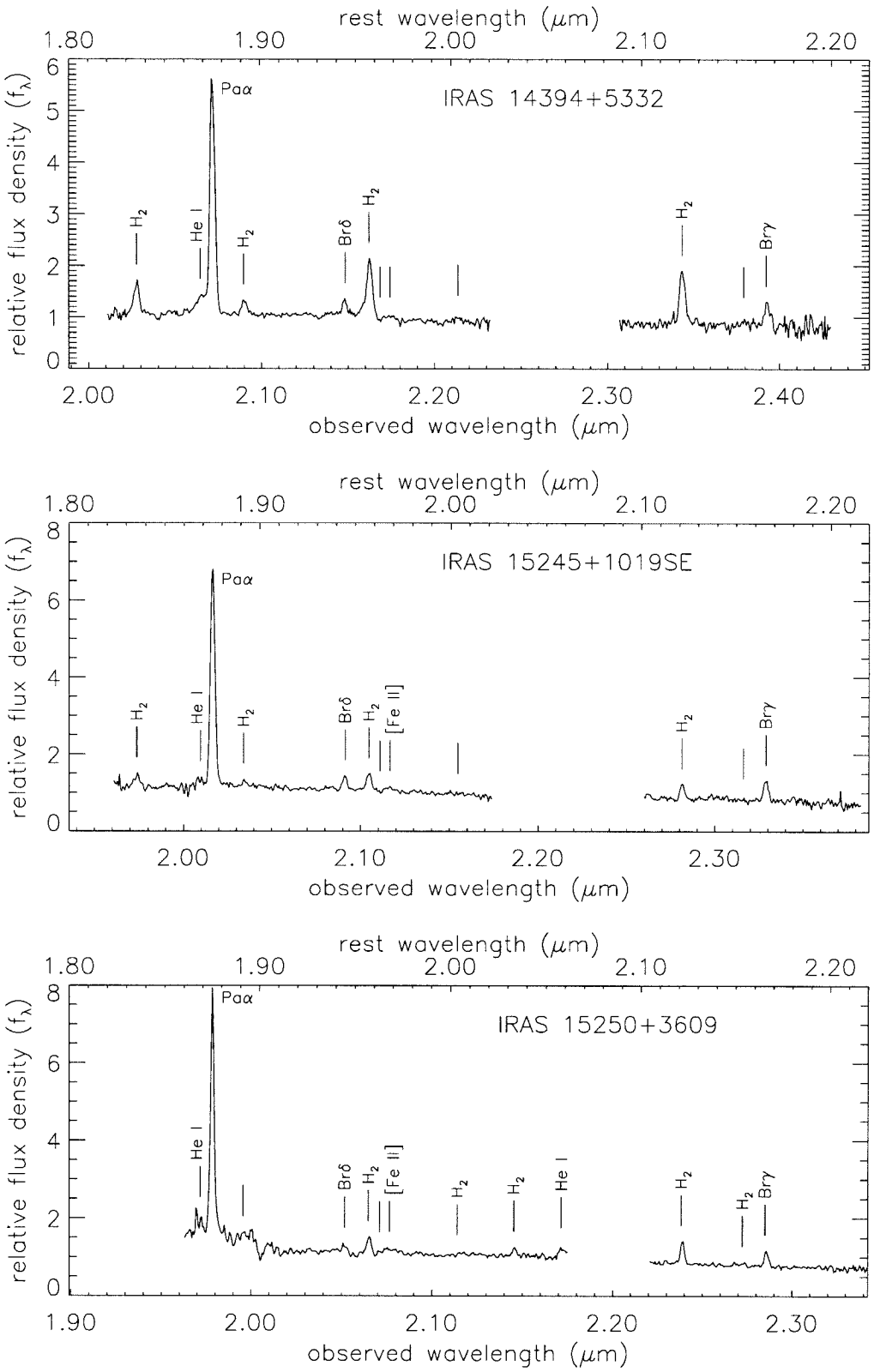

Figure 2.1: continued

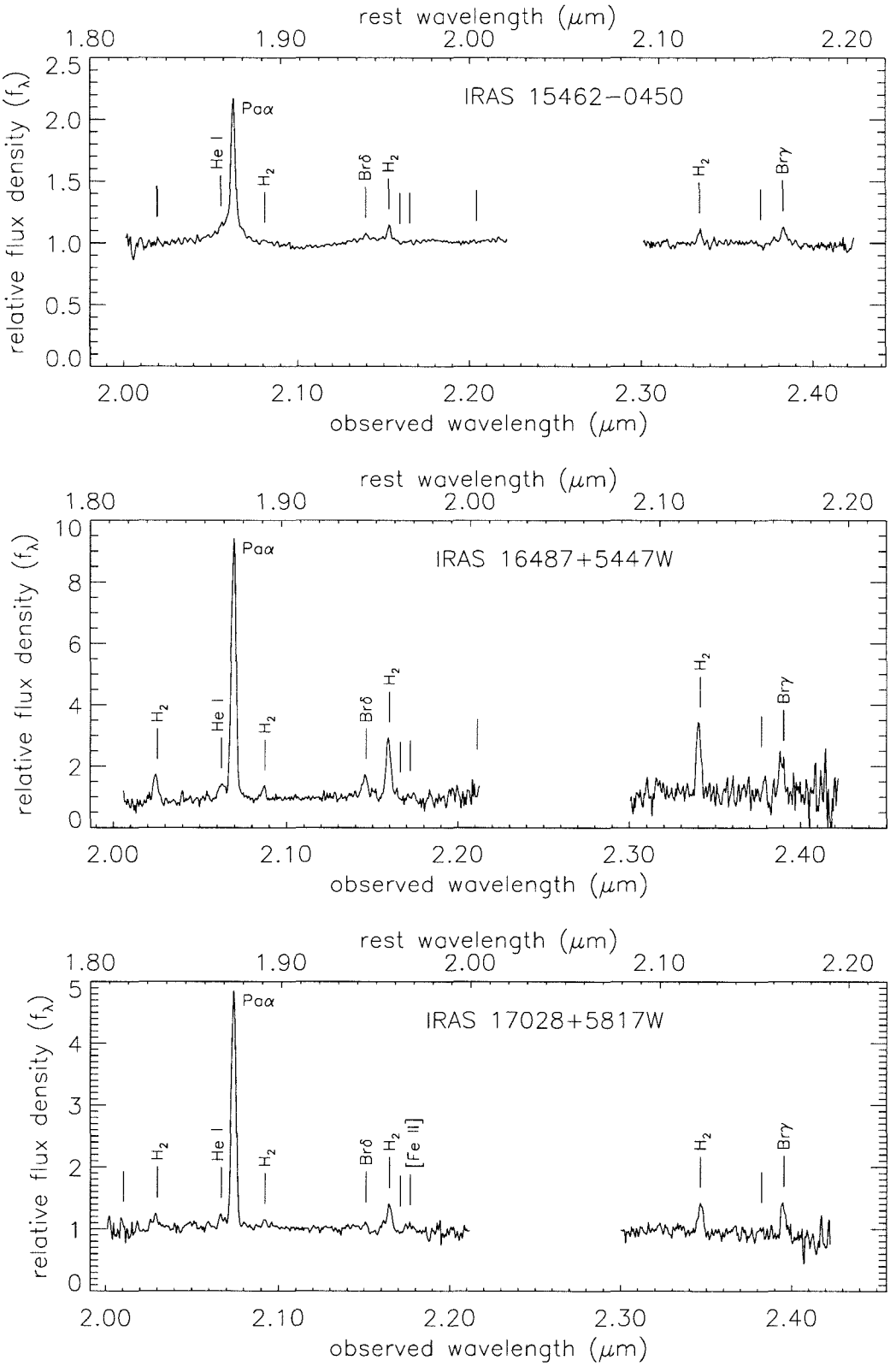

Figure 2.1: continued

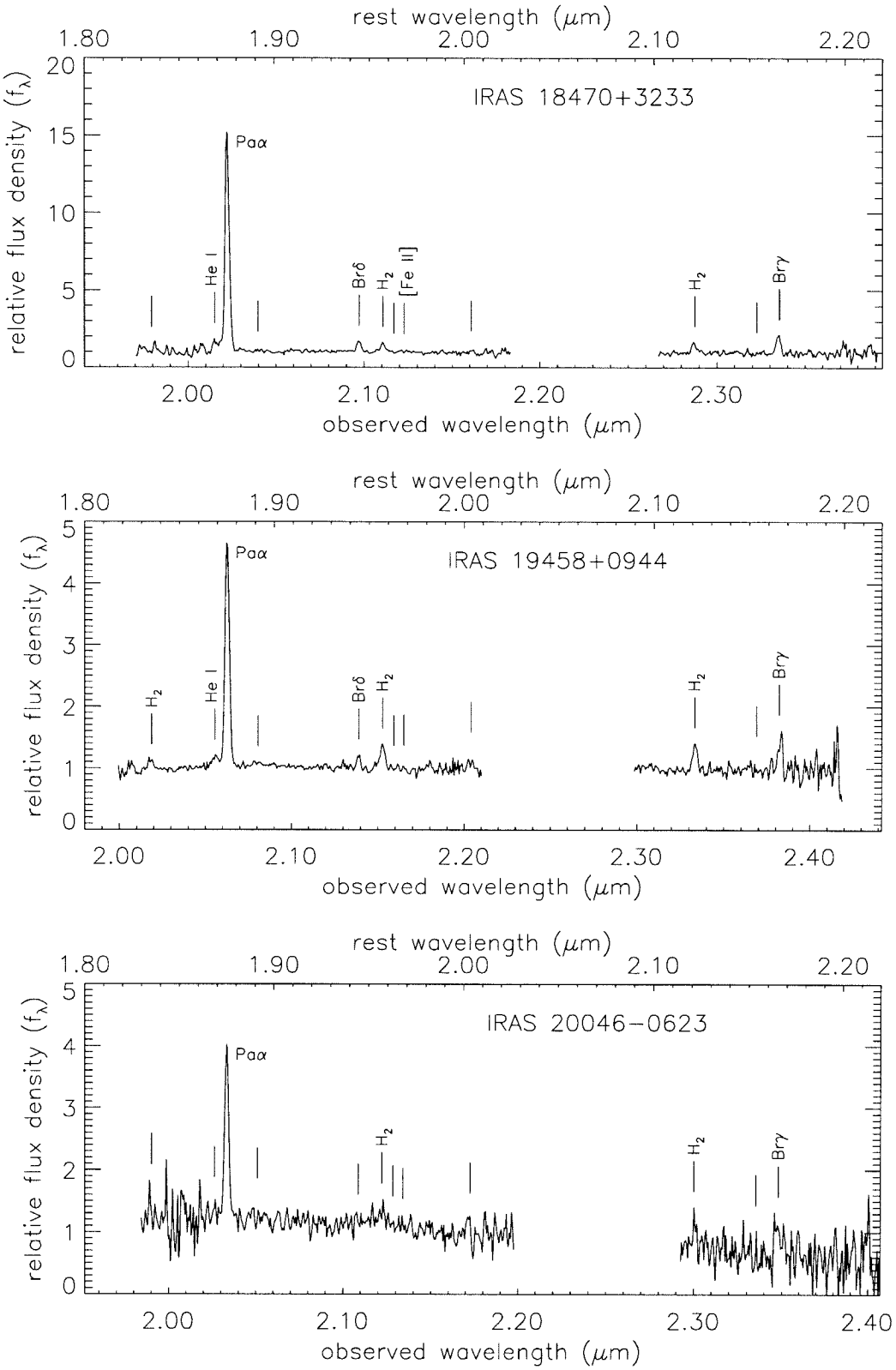

Figure 2.1: continued

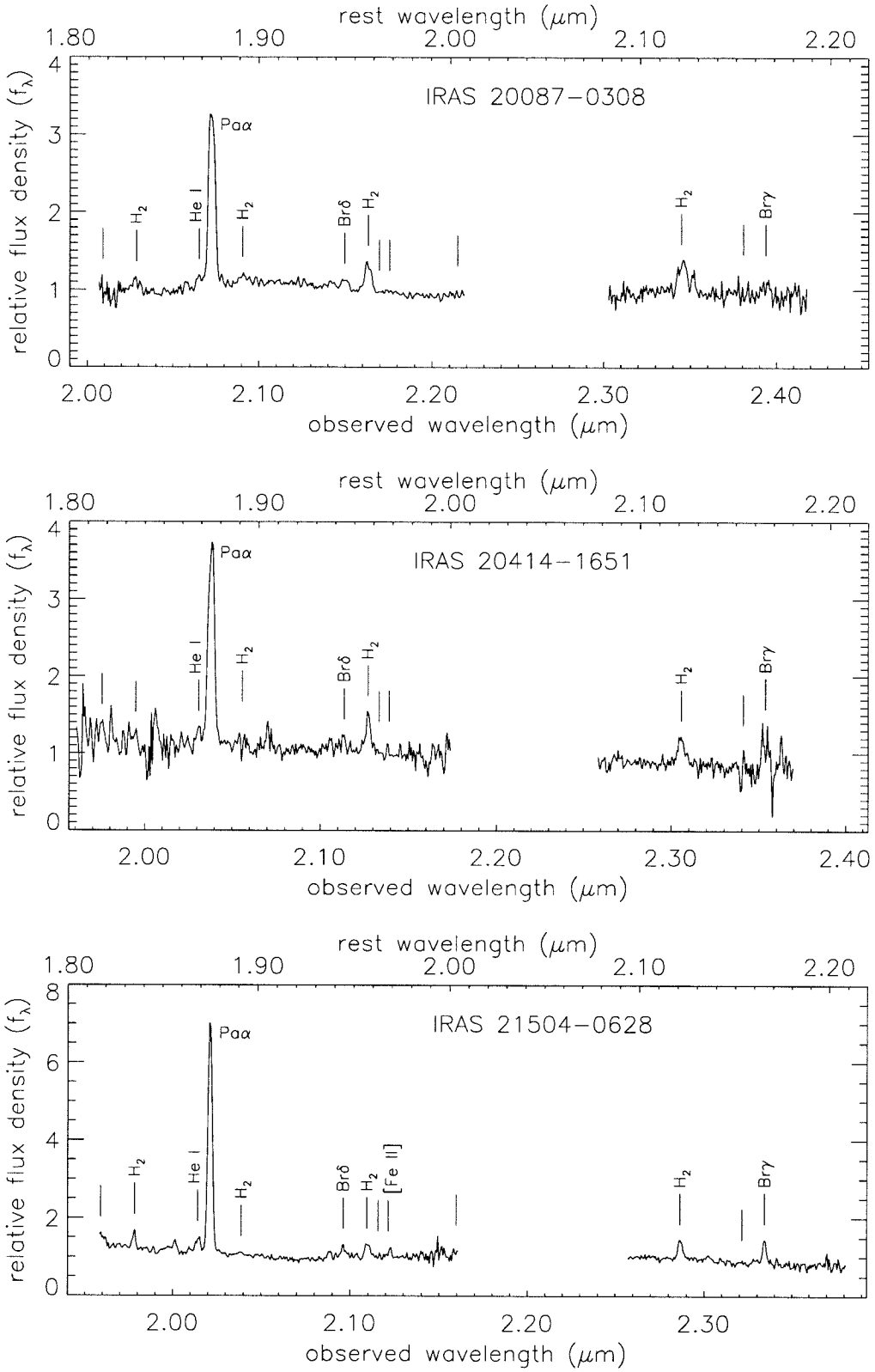

Figure 2.1: continued

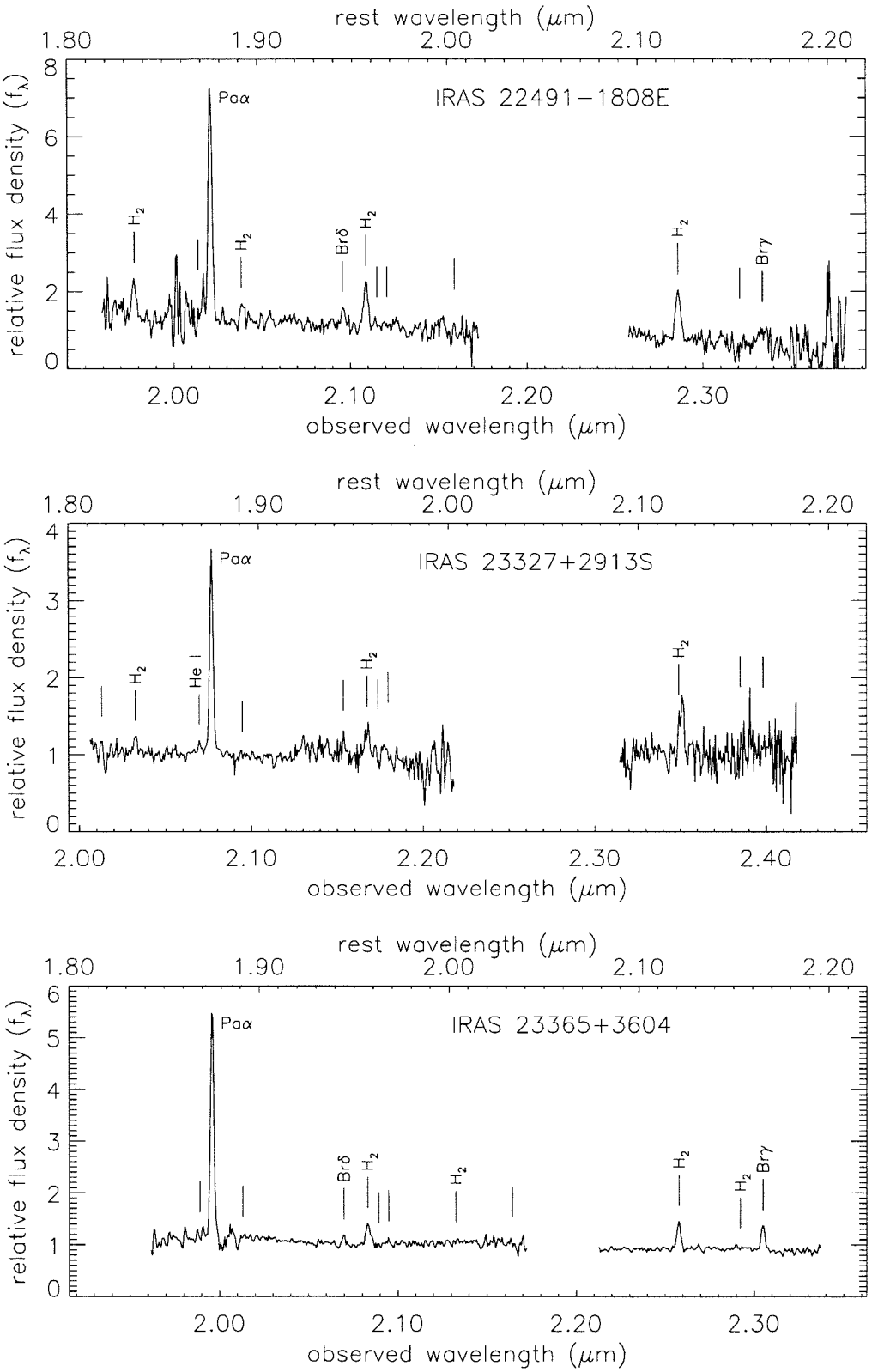

Figure 2.1: continued

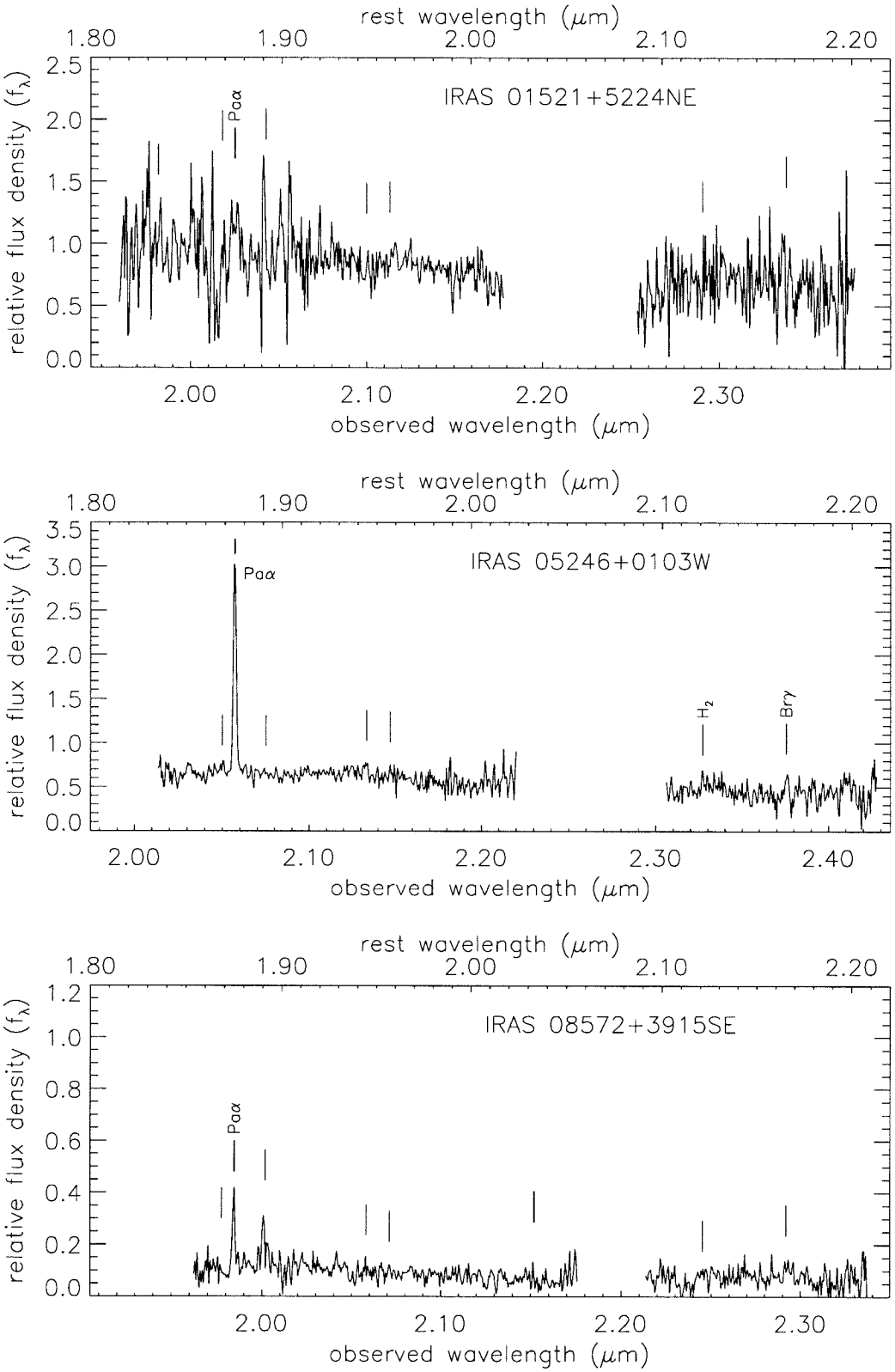

Figure 2.2: Spectral extractions for the 14 ULIRG nuclei.

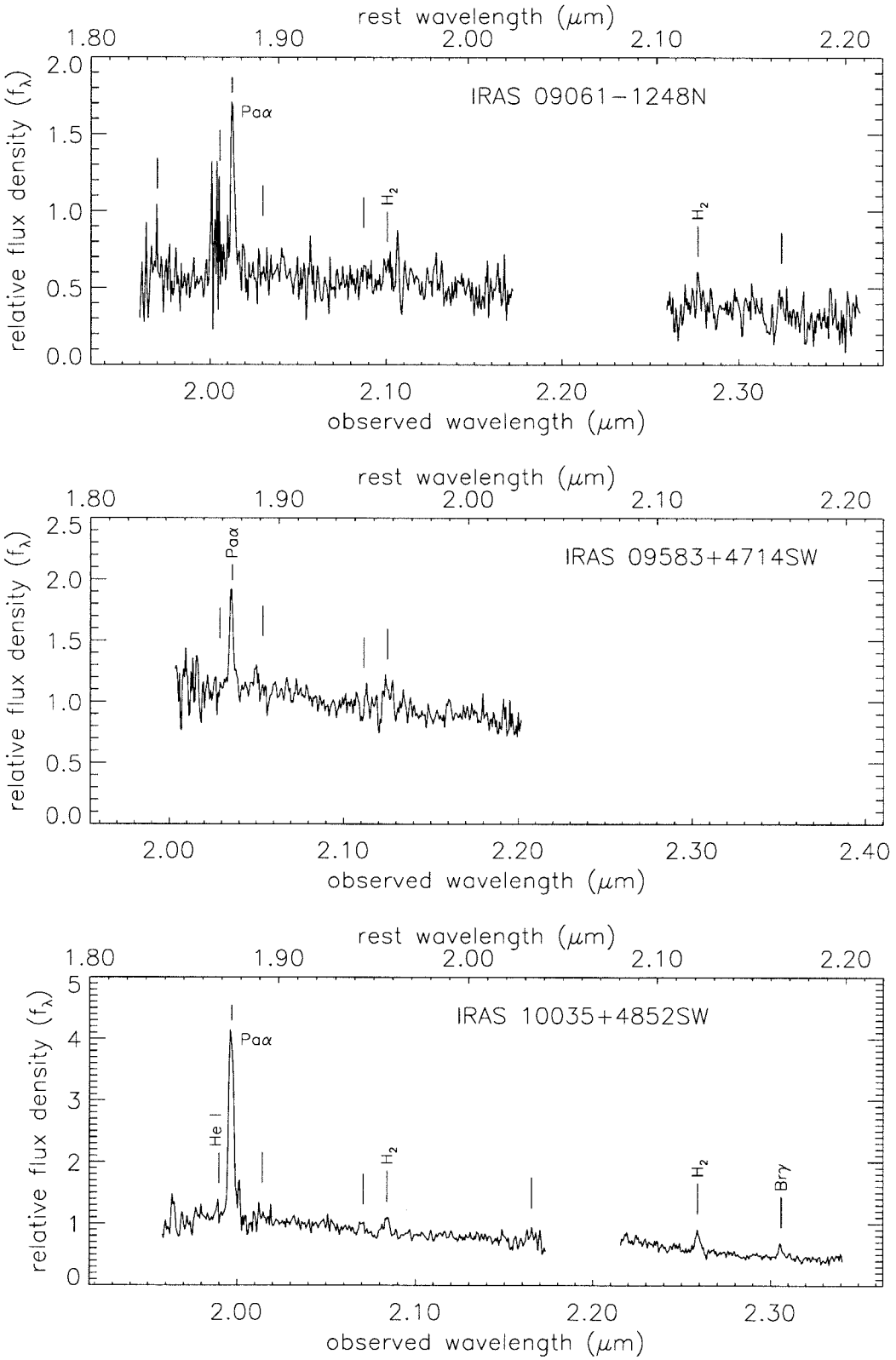

Figure 2.2: continued

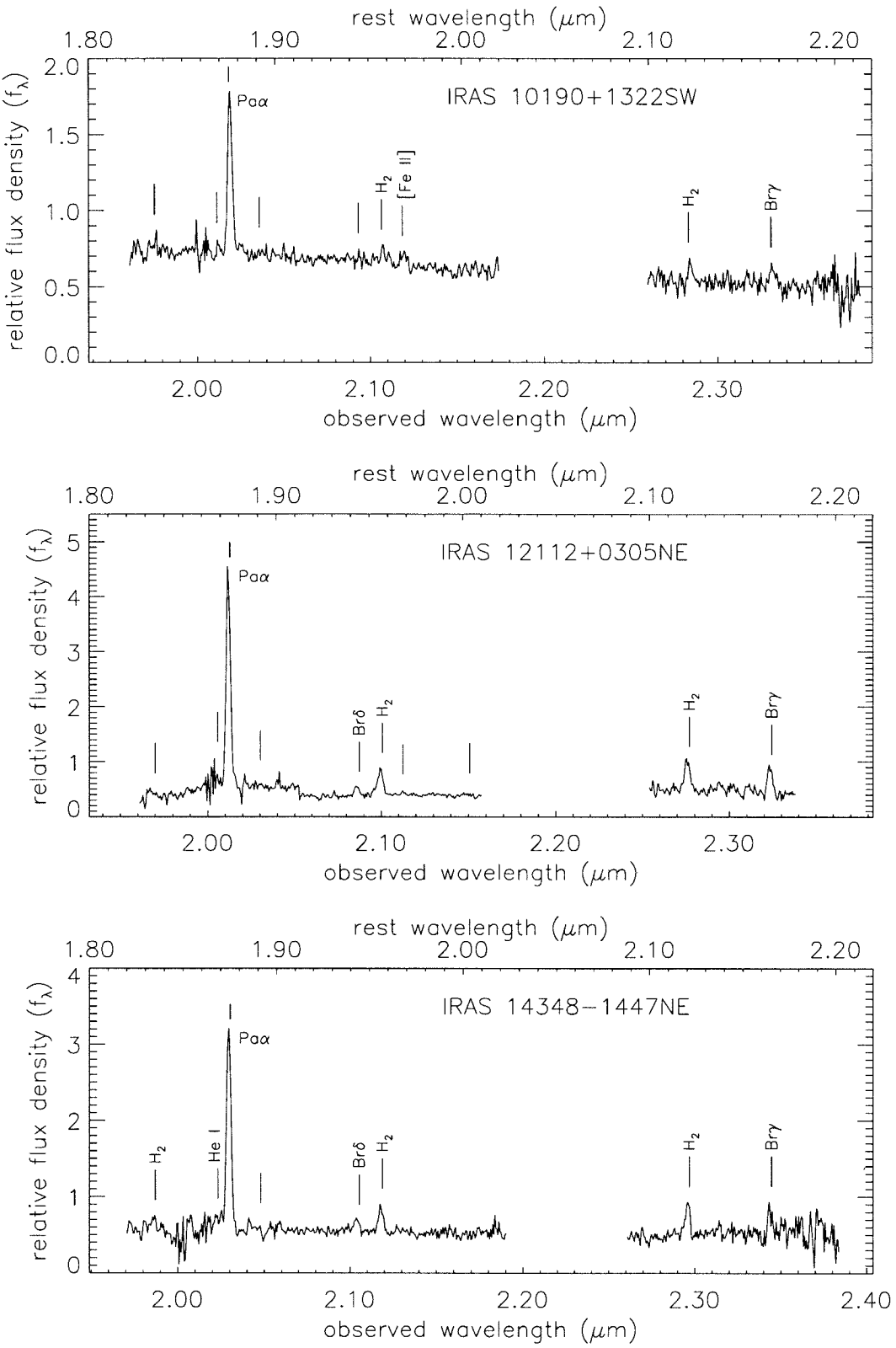

Figure 2.2: continued

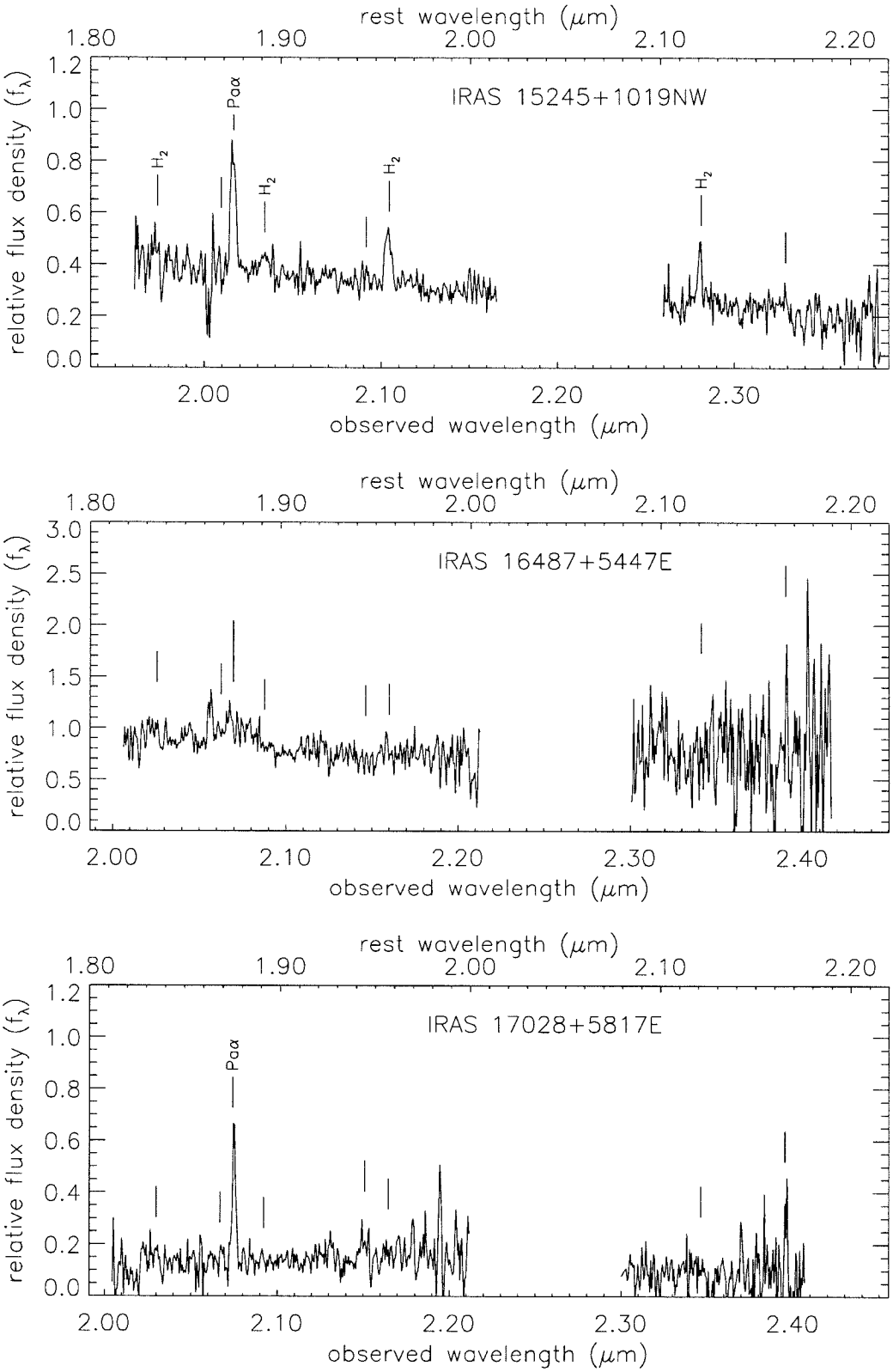

Figure 2.2: continued

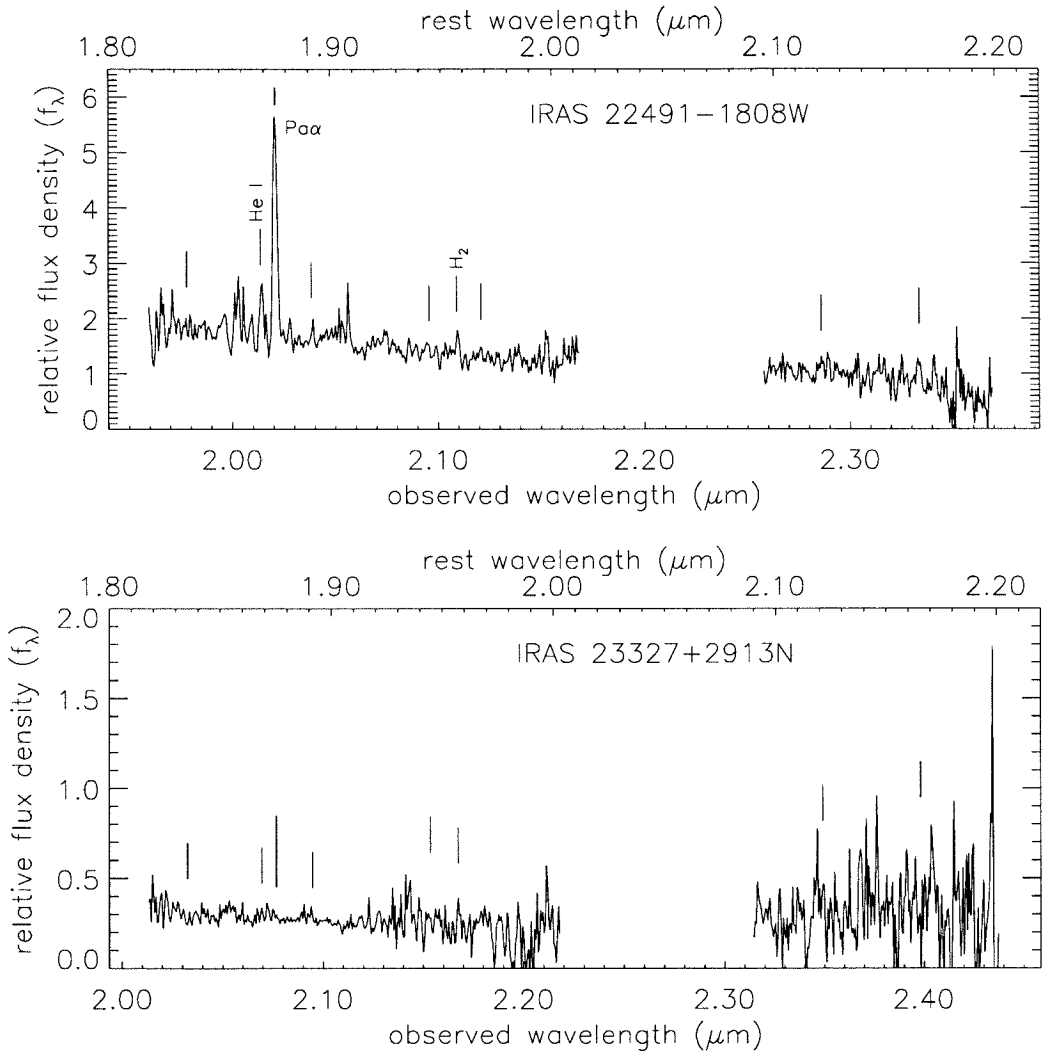

Figure 2.2: continued

well as equivalent width, FWHM, and velocity centroid of each significant line. In this context, weaker lines of hydrogen recombination and molecular hydrogen vibration-rotation are excluded from the table as their properties follow from those of the stronger lines. The continuum slope is reported as the change in flux density per unit micron in wavelength, using the normalization wherein the flux density at 2.155 μm is set to unity—as is the case for the primary nuclear spectra as displayed in Figure 2.1.

The line properties reported in Table 2.3 represent measured values from the spectrum, rather than Gaussian fit parameters. Especially for the weaker lines, the quality of the continuum subtraction is vital to proper line characterization. This is done with a simultaneous multiple Gaussian line fit and quadratic continuum fit. In all but a few cases, this results in a very close fit to the continuum. For those few cases where the continuum fit is questionable, some of the weaker lines are excluded from Table 2.3. All of the fitting procedures make use of the noise estimate computed on a pixel-by-pixel basis, as described earlier. In the end, the noise is scaled slightly (typically by factors of less than 30%) in order to make the final reduced chi-squared value equal to one. The scaled noise is used in estimating errors on the values in Table 2.3. Each of the line parameters is computed based on the following line definition procedure. Each potential line is searched for by summing two resolution elements (7 pixels) of information around the line center, and determining if there is emission above the continuum exceeding 2.5σ. For lines satisfying this condition, cutoffs are established on the red and blue sides of the line center by the following rules:

1. If the spectrum extends below the continuum level, establish a cutoff, including only positive valued points.

2. If there exists a local minimum, followed by at least three higher points, assume that the following points belong to another line and exclude them, keeping only the minimum point.

3. If the next two pixels are between 0–1σ above the continuum, include them and quit.

These procedures obviously cannot practice the same discrimination that a diligent scientist might, but we find that a reasonable job is performed—especially on lines whose boundaries are obvious to the eye. Nonetheless, lines with a final computed equivalent width measuring less than 2.5σ are typically excluded, though those that appear to be real in the one-dimensional spectra are preserved. Conversely, a few lines with reported detections greater than 2.5σ are excluded on the basis of either poor local continuum fit or simply less-than-believable results.

Table 2.3. Measured Line Properties

Galaxy	Continuum Slope[a]	Paα FWHM[b] (km s^{-1})	Rows[c]	He I 1.8689	Paα 1.8751	H_2 S(3) 1.9570	[Si VI] 1.9629	[Fe II] 1.9670	H_2 S(1) 2.1213	Brγ 2.1655
IRAS 00262+4251	0.354	331								
			EW	0.42±0.1	3.52±0.15	2.95±0.14		0.404±0.088	3.88±0.24	
			FWHM	420±240	366±27	480±42		260±160	380±56	
			cz	−67±78	29204±18	−18±29		5±63	−44±27	
IRAS 01521+5224S	−0.90	394								
			EW		12.02±0.44	0.79±0.14			2.44±0.36	1.38±0.49
			FWHM		356±23	170±96			290±120	0±110
			cz		24011±16	−58±46			−101±34	−95±76
IRAS 01521+5224N	−1.00	403								
			EW		1.12±0.6					
			FWHM		190±230					
			cz		23990±170					
IRAS 04232+1436	−1.89	183								
			EW		8.74±0.25	1.34±0.15			1.76±0.16	1.4±0.26
			FWHM		218±18	195±70			203±51	220±100
			cz		23666±15	25±33			−11±26	63±46
IRAS 05246+0103E	0.546	110								
			EW	1.09±0.13	8.89±0.19	3.15±0.26	0.86±0.2		1.53±0.14	0.61±0.24
			FWHM	497±78	190.1±9.6	575±77	310±260		161±40	210±210
			cz	−83±51	29105±22	255±47	−180±55		27±38	70±110
IRAS 05246+0103W	−1.176	54								
			EW	0.46±0.16	7.93±0.31				0.94±0.29	
			FWHM	0±140	72±19				60±100	
			cz	−60±120	29103±23				126±77	
IRAS 08030+5243	−1.95	322								
			EW	0.53±0.13	14.46±0.16	1.3±0.11		0.39±0.1	1.36±0.22	2.32±0.28
			FWHM	340±160	326.2±6.8	331±77		0±91	270±130	380±110
			cz	97±71	24959±12	−29±34		16±87	−47±31	−173±44
IRAS 08311−2459	−1.603	314								
			EW	1.27±0.22	22.69±0.29	3.68±0.15	3.005±0.088	0.488±0.078	2.734±0.092	2.18±0.25
			FWHM	0±100	477±10	501±41	708±52	360±130	351±27	470±170
			cz	52±31	30114±16	129±26	78±20	154±45	104±21	94±34
IRAS 08344+5105	−1.453	287								
			EW	0.67±0.13	20.08±0.26	1.64±0.13			2.16±0.27	2.32±0.36
			FWHM	60±110	300±13	196±40			310±100	310±140
			cz	−45±39	29002±12	60±28			0±30	52±35
IRAS 08572+3915N	1.511	340								
			EW	0.84±0.13	11.192±0.1	0.695±0.062			0.448±0.027	0.762±0.072
			FWHM	440±110	334.8±8	139±45			135±30	271±62
			cz	−51±53	17493±19	−69±37			−78±31	−56±37
IRAS 08572+3915S	−2.004									
			EW		2.92±0.21					
			FWHM		0±19					
			cz		17465±22					
IRAS 09061−1248S	−1.523	371								
			EW	1.16±0.5	10.33±0.25	1.215±0.092		0.56±0.19	1.53±0.13	1.47±0.23
			FWHM	240±280	320±24	421±99		100±240	266±58	260±110
			cz	−260±120	22017±13	−81±26		−250±96	34±23	7±45
IRAS 09061−1248N	−1.670									
			EW		5.52±0.59	0.84±0.29			2.13±0.39	
			FWHM		252±76	0±170			253±95	
			cz		22030±30	−60±140			81±61	

Table 2.3—Continued

Galaxy	Continuum Slope[a]	Paα FWHM[b] (km s^{-1})	Rows[c]	He I 1.8689	Paα 1.8751	H_2 S(3) 1.9570	[Si VI] 1.9629	[Fe II] 1.9670	H_2 S(1) 2.1213	Brγ 2.1655
IRAS 09111−1007	−0.203	223								
			EW	0.42±0.11	5.53±0.1	0.736±0.033		0.295±0.052	0.682±0.035	0.59±0.062
			FWHM	290±210	246±13	189±27		310±91	164±25	168±66
			cz	67±99	16231±12	−12±17		69±51	78±20	54±26
IRAS 09583+4714NE	−1.466	247								
			EW	0.74±0.11	16.75±0.2	3.58±0.22			4.06±0.25	1.85±0.25
			FWHM	0±63	263.6±6.1	411±74			384±59	256±98
			cz	−78±24	25754±12	25±25			13±28	−134±38
IRAS 09583+4714SW	−2.368	186								
			EW		1.97±0.16	0.94±0.19				
			FWHM		246±41	320±180				
			cz		25696±31	138±76				
IRAS 10035+4852NE	−2.220	237								
			EW	0.454±0.049	8.71±0.19	2.46±0.13		0.21±0.11	2.915±0.089	1.08±0.15
			FWHM	0±61	254±12	315±43		0±240	256±18	201±71
			cz	−43±29	19435±17	38±35		10±170	−2±28	46±44
IRAS 10035+4852SW	−2.628	424								
			EW	0.59±0.23	10.33±0.54	1.03±0.13			1.88±0.14	1.36±0.17
			FWHM	50±160	430±31	320±110			292±47	212±67
			cz	−60±130	19443±31	−61±54			26±42	−17±48
IRAS 10190+1322E	−0.848	445								
			EW		9.6±0.13	1.164±0.081		0.154±0.072	1.248±0.096	1.12±0.11
			FWHM		437±16	412±72		0±130	336±65	320±91
			cz		22889±19	12±37		−230±140	7±32	22±34
IRAS 10190+1322W	−1.053	265								
			EW		4.51±0.14	0.41±0.092		0.31±0.11	0.64±0.13	0.72±0.18
			FWHM		271±26	40±110		0±150	63±89	150±120
			cz		23012±21	−70±64		190±170	47±56	−28±68
IRAS 10494+4424	−1.847	430								
			EW	1.04±0.11	14.96±0.12	1.612±0.072			1.89±0.11	1.73±0.16
			FWHM	510±160	404.2±7.1	377±38			427±65	364±75
			cz	−51±34	27675±16	−2±29			−3±29	−51±31
IRAS 11095−0238	−0.558	269								
			EW	1.62±0.3	20.38±0.39	5.65±0.25			8.56±0.61	2.5±1
			FWHM	360±180	286±12	350±49			241±43	0±100
			cz	−38±64	31968±18	−59±26			−73±35	80±130
IRAS 12112+0305SW	0.544	159								
			EW	1.68±0.61	13.97±0.39	1.095±0.086		0.34±0.14	0.957±0.071	1.57±0.15
			FWHM	380±340	303±21	295±63		220±290	0±31	185±53
			cz	80±140	21980±21	−65±42		−280±190	−19±30	−51±33
IRAS 12112+0305NE	0.307	196								
			EW		21.49±0.52	4.62±0.13			4.05±0.2	3.67±0.39
			FWHM		271±19	401±27			366±49	278±78
			cz		21875±20	−110±36			−47±30	−12±36
IRAS 14348−1447SW	−0.454	227								
			EW	1.47±0.15	12.78±0.19	3.15±0.12		0.244±0.083	3.11±0.14	1.35±0.2
			FWHM	550±120	236.8±8.4	450±35		120±210	334±36	127±80
			cz	150±43	24802±22	−65±35		−10±110	−46±30	35±40
IRAS 14348−1447NE	−0.165	283								
			EW	2.06±0.3	15.41±0.35	1.98±0.15			2.5±0.25	1.64±0.5
			FWHM	450±160	272±14	218±63			274±76	0±120
			cz	133±64	24681±23	−31±35			−66±36	20±100

Table 2.3—Continued

Galaxy	Continuum Slope[a]	Paα FWHM[b] (km s^{-1})	Rows[c]	He I 1.8689	Paα 1.8751	H_2 S(3) 1.9570	[Si VI] 1.9629	[Fe II] 1.9670	H_2 S(1) 2.1213	Brγ 2.1655
IRAS 14352−1954	−1.154	192								
			EW	1.102±0.089	23.54±0.23	1.19±0.11			1.88±0.15	2.97±0.26
			FWHM	258±55	205.3±4.9	193±58			243±48	166±46
			cz	19±33	26942±17	9±37			35±34	6±32
IRAS 14394+5332	−0.656	363								
			EW	1.602±0.064	15.75±0.13	5.03±0.097		0.143±0.08	4.9±0.16	2.14±0.27
			FWHM	558±77	381.8±8.7	490±22		160±280	426±33	370±110
			cz	−137±33	31373±21	−5±31		20±170	61±33	127±47
IRAS 15245+1019E	−1.087	283								
			EW	0.277±0.069	15.32±0.14	1.324±0.067		0.341±0.078	1.242±0.088	2.08±0.13
			FWHM	0±75	294.6±7.3	307±46		300±210	247±50	304±51
			cz	25±39	22634±16	−19±30		−41±67	25±27	−15±25
IRAS 15245+1019W	−1.622	426								
			EW		4.36±0.38	2.7±0.19			2.19±0.24	
			FWHM		310±70	406±74			78±54	
			cz		22577±31	−72±42			−100±41	
IRAS 15250+3609	−1.716	57								
			EW	0.43±0.23	9.49±0.16	1.45±0.14		0.55±0.1	1.928±0.059	1.429±0.077
			FWHM	0±180	147.8±9.9	323±88		400±180	223±19	204±34
			cz	−70±200	16535±17	6±35		−190±60	58±32	100±33
IRAS 15462−0450	−0.023	285								
			EW	0.653±0.068	5.232±0.085	0.48±0.029			0.268±0.024	0.516±0.06
			FWHM	480±160	535±15	297±53			102±43	360±110
			cz	−122±43	29917±24	229±40			158±32	237±44
IRAS 16487+5447W	0.683	347								
			EW	1.96±0.18	29.02±0.34	7.13±0.29			5.95±0.39	3.46±0.89
			FWHM	500±140	332.3±9.1	374±36			265±54	230±140
			cz	29±40	31106±23	−52±33			−134±30	−195±78
IRAS 17028+5817W	−0.283	339								
			EW	0.631±0.097	11.89±0.13	1.26±0.078		0.35±0.13	1.53±0.14	2.13±0.25
			FWHM	320±130	315.6±8.7	250±48		140±170	301±74	336±94
			cz	46±46	31805±24	3±33		−60±130	6±39	22±45
IRAS 17028+5817E	−1.429	0								
			EW		9.66±0.76					
			FWHM		97±33					
			cz		31938±32					
IRAS 18470+3233	−0.207	228								
			EW	2.21±0.4	41.07±0.44	2.04±0.16		0.41±0.16	2.46±0.17	3.52±0.25
			FWHM	200±120	258.2±6.9	305±68		200±300	319±49	249±50
			cz	−9±51	23517±21	11±44		−40±120	11±34	−101±30
IRAS 19458+0944	−0.116	269								
			EW	0.668±0.086	11.093±0.075	1.46±0.13			1.236±0.089	1.74±0.29
			FWHM	390±180	272.9±5.1	324±84			237±50	150±110
			cz	−27±58	29982±35	−83±59			3±47	73±53
IRAS 20046−0623	−1.852	244								
			EW		6.3±0.21	1.16±0.2		0.45±0.2	1.63±0.44	3.67±1
			FWHM		247±27	190±100		0±140	0±88	310±170
			cz		25293±14	−16±43		−130±140	6±60	100±80
IRAS 20087−0308	−0.138	595								
			EW	0.465±0.093	10.22±0.14	1.611±0.067			2.11±0.15	0.64±0.24
			FWHM	270±150	574±23	475±49			570±110	280±280
			cz	−92±48	31600±20	−41±33			64±30	36±97

Because the weaker lines do not have a well defined full-width at half-maximum, the FWHM values in Table 2.3 are based on a combination of line flux and peak amplitude. If a Gaussian shape is assumed, the FWHM of the line would be proportional to the line flux divided by the peak amplitude, times the proportionality constant of $\sqrt{\ln(256)/2\pi} = 0.94$. Performed in this manner, it is relatively simple to compute the error of such an estimate. A strict measure of the FWHM is provided in Table 2.3 for the Paα line in each galaxy for comparison to the value estimated by this technique. All of the reported FWHM values have been reduced to intrinsic line widths by subtracting the instrumental resolution in quadrature. Each spectrum uses the measured line widths in the wavelength calibration spectrum as a basis for the decomposition. Values in Table 2.3 for which the measured line width is exceeded by the instrumental width are listed as unresolved lines of zero width. Almost all of the lines in this survey are resolved, typically around 200–300 km s^{-1} in width.

The velocity measurements in Table 2.3 are indicated relative to Paα, though the Paα velocity itself is expressed as a direct quantity in km s^{-1}. These values are simply computed as first-moment measures in the spectral lines, with error estimates computed from the noise estimates in a straightforward way. Added to this error estimate is a wavelength calibration error, assumed to be 10–15 km s^{-1}, and a slit placement error. The latter uncertainty attempts to estimate the wavelength offset induced by a non-uniform slit illumination. When the line source is spatially compact enough to produce a discernible peak somewhere in the slit, the location of this peak within the slit influences the ultimate wavelength associated with this emission. For these purposes, it is assumed that the line source has a real physical size roughly half that of the continuum, which is almost always spatially resolved. Further, it is assumed that the source is centered in the slit with a Gaussian 1σ placement error of one-quarter of a slit width. Only cases of exceptional seeing result in an appreciable error from this source, with a median error estimate of 15 km s^{-1} and a maximum of 38 km s^{-1}. Despite the accounting of uncertainties, the velocities indicate a dispersion outside of the error budgets that is not correlated with line species or grating setting. It may well be that the variable spectral range over which the line is summed is largely

Table 2.3—Continued

Galaxy	Continuum Slope[a]	Paα FWHM[b] (km s^{-1})	Rows[c]	He I 1.8689	Paα 1.8751	H_2 S(3) 1.9570	[Si VI] 1.9629	[Fe II] 1.9670	H_2 S(1) 2.1213	Brγ 2.1655
IRAS 20414−1651	−0.896	515								
			EW	0.82±0.16	10.47±0.21	1.64±0.16			1.71±0.17	2.23±0.63
			FWHM	400±190	488±20	287±82			460±120	170±180
			cz	53±71	26043±25	16±49			35±46	−137±92
IRAS 21504−0628	−1.69	256								
			EW	1.07±0.14	16.82±0.14	0.87±0.14			1.684±0.099	1.74±0.13
			FWHM	230±100	260.8±5.6	250±130			310±43	144±40
			cz	−17±52	23352±26	46±44			43±43	−4±41
IRAS 22491−1808W	−1.806	86								
			EW	0.95±0.38	5.61±0.19	0.43±0.2				
			FWHM	0±130	0±22	0±94				
			cz	76±99	23274±23	−230±200				
IRAS 22491−1808E	−1.968	128								
			EW		13±0.38	3.07±0.23			5.3±0.38	3.32±0.88
			FWHM		127±18	0±52			303±62	450±350
			cz		23277±24	−35±41			−2±33	6±74
IRAS 23327+2913S	0.039	151								
			EW	0.43±0.11	6.85±0.12	0.87±0.26			1.92±0.36	
			FWHM	170±130	193±9	110±120			210±120	
			cz	68±76	32235±18	−1±77			219±51	
IRAS 23365+3604	−0.677	186								
			EW		9.284±0.083	1.291±0.079			1.493±0.057	1.345±0.094
			FWHM		191.1±5	245±45			219±22	216±39
			cz		19309±17	60±24			−36±25	−9±28

[a]Slope expressed as units per micron when the continuum level is normalized to one unit at a wavelength of 2.155 μm.

[b]Strictly formal measure of the full-width at half-maximum of the Paα line, deconvolved by the instrumental resolution.

[c]For each galaxy, the following measures are provided for selected lines: equivalent width (EW) is given in nanometers; FWHM as estimated via line flux and peak amplitude (see text), deconvolved by the instrumental resolution; first moment centroid of the line, expressed as recessional velocity (cz) for Paα, and velocity offsets from Paα for all other lines. The first moment measure looses accuracy for weak lines depending on the spectral range summed, and therefore is of limited use here.

responsible for determining the offset, as the range is biased to contain only positive points, and will extend as far as possible from the line center to include such points. With the large moments generated from distant points, the estimated velocity may wander far from its true center. Thus the values of velocity in Table 2.3, especially for weaker lines, are perhaps of little use. Gaussian fit centers may do a better job of appropriately representing the line velocities.

Figure 2.3 presents the two-dimensional spectra around the Paα line for each of the sample galaxies. In each, the horizontal axis origin is located at the center of the primary nucleus. The apertures corresponding to the extractions displayed in Figures 2.1 and 2.2 are indicated at the top and bottom of each panel. Annotations to the left and right of each panel denote the sense of the slit orientation, the exact position angles for which are listed in Table 2.2. The two-dimensional spectrum for IRAS 09583+4714 has been split into two panels, though the horizontal scale reflects the real separation between the two nuclear components.

2.5.1 Hydrogen Recombination & Extinction

The K band spectra of the galaxies in this sample are dominated by the Paα line, which is the obvious place to look for any signs of broad emission. Only in two of the sample galaxies is any such emission apparent: IRAS 08311−2459 and IRAS 15462−0450. Both of these galaxies are optically classified Seyfert galaxies, so it seems that obscured AGN ULIRGs are either extremely rare, or suffer a few magnitudes of extinction even at near-infrared wavelengths. A few galaxies, such as IRAS 14348−1447 and IRAS 14394+5332, have excess emission on the blue side of the Paα line, but in both cases there appears to be emission from He I contributing significantly to this flux, and no appreciable emission on the red side of the narrow Paα profile. Furthermore, the H_2 lines in IRAS 14394+5332 have an asymmetric blue shape more typical of wind or outflow phenomena than of velocity-broadening due to an AGN. IRAS 20087−0308 has some hint of broad emission at the base, though not significantly elevated out of the noise, and again confused by He I. As seen in Figure 2.3, the moderate 600 km s^{-1}

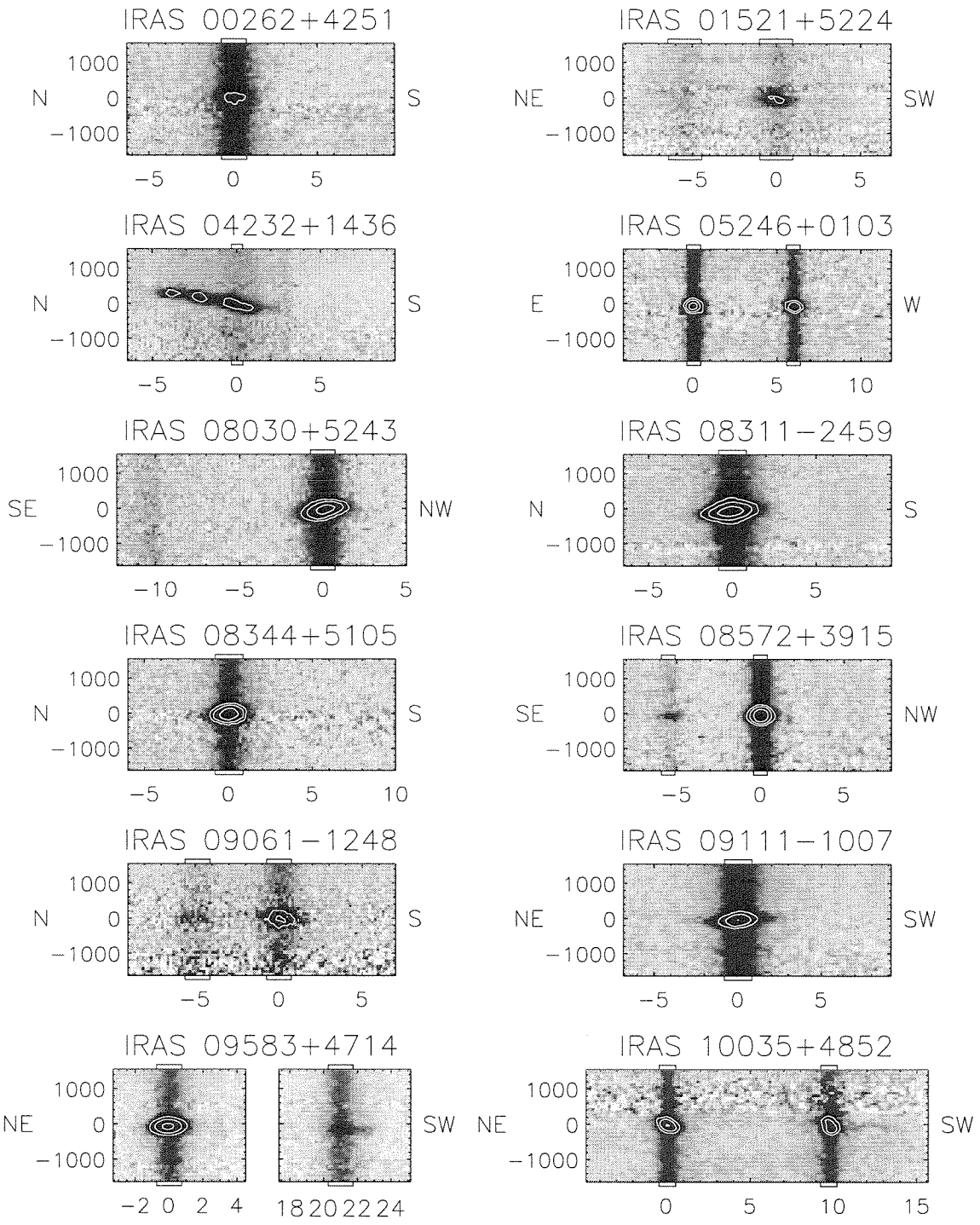

Figure 2.3: Two-dimensional spectra around the Paα line for each galaxy. The horizontal scale is in arcseconds, with the primary nucleus at the origin. The spectral direction spans about 11 resolution elements, or about 3300 km s^{-1}. Extraction apertures are indicated on the top and bottom of each frame.

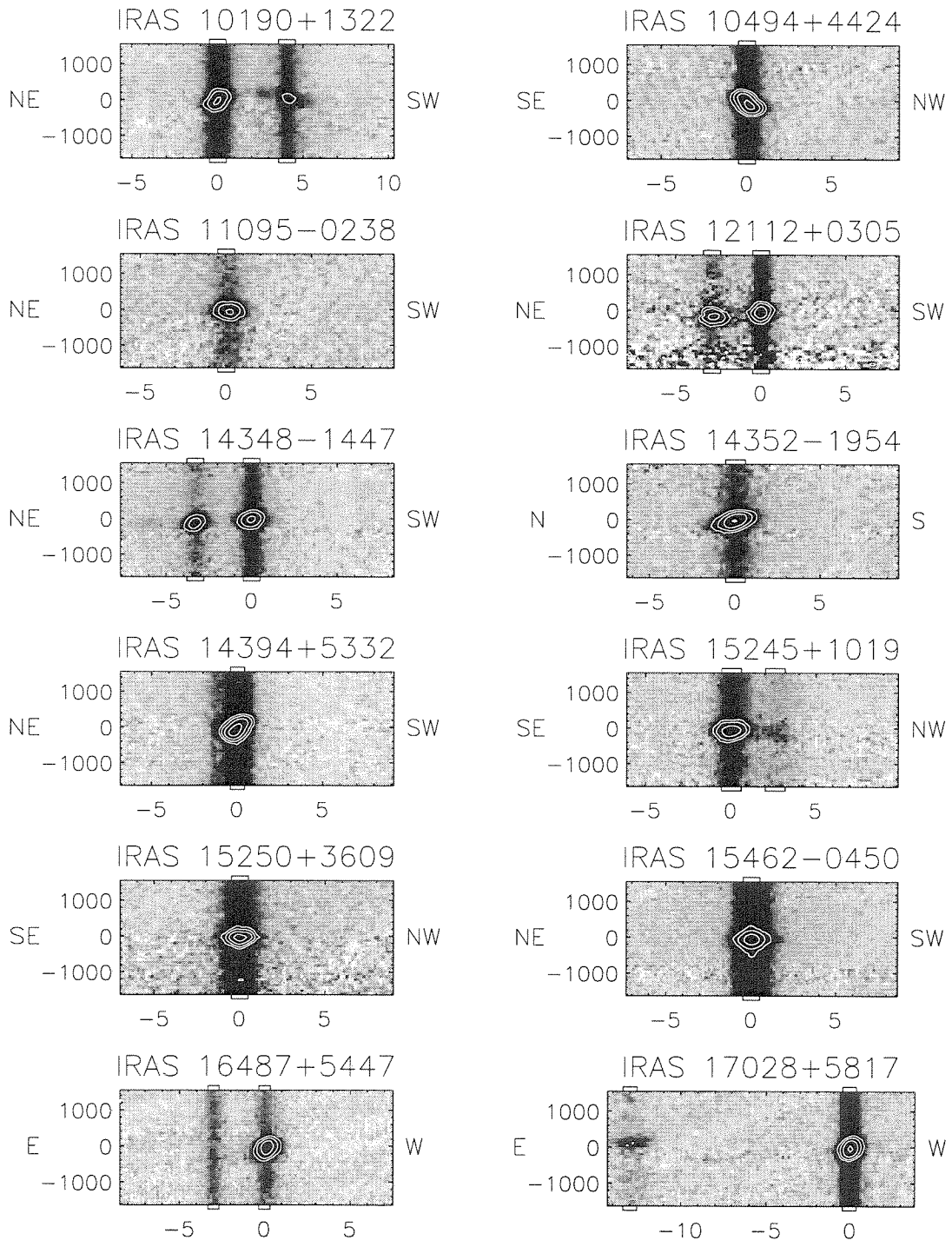

Figure 2.3: continued

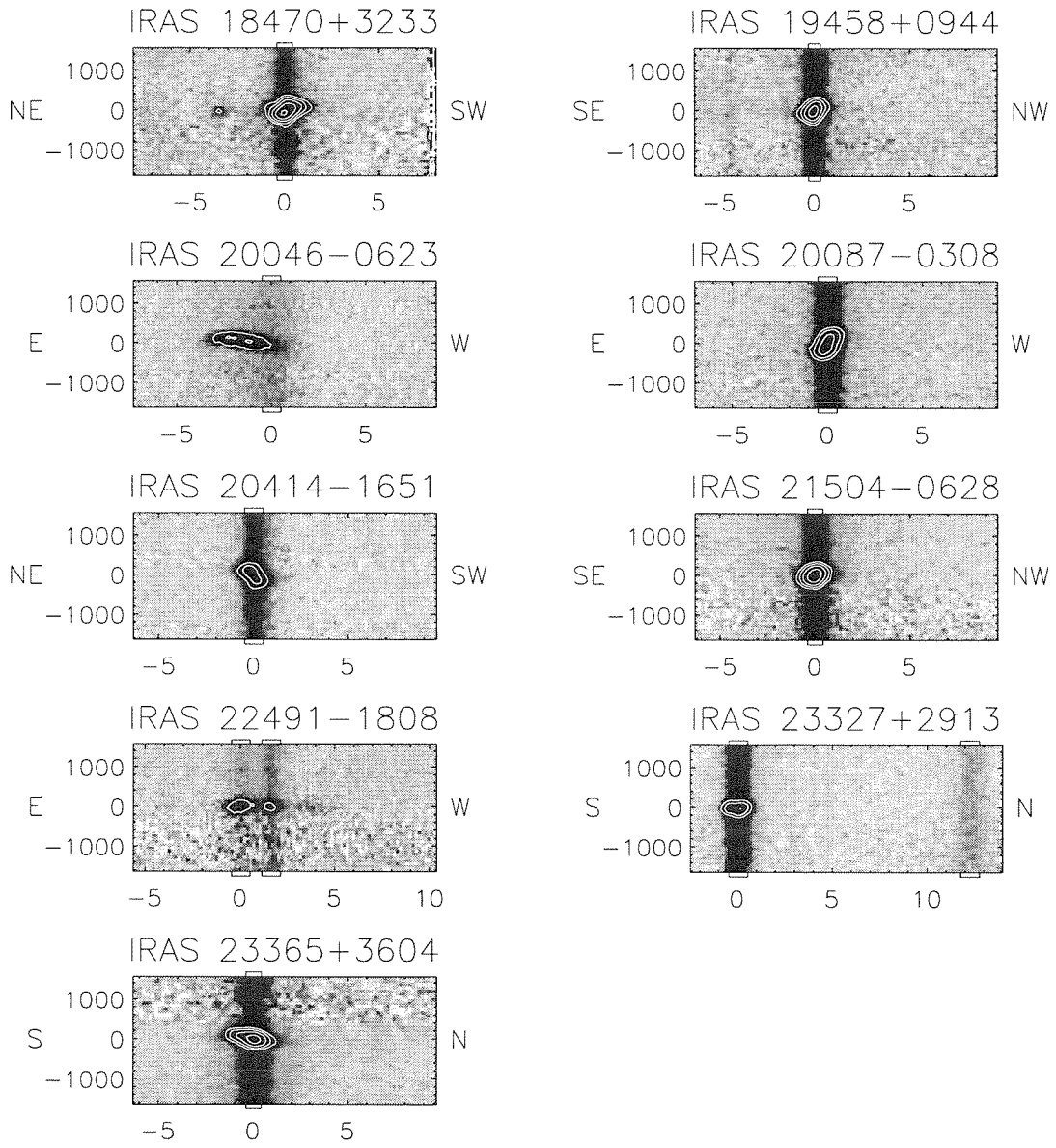

Figure 2.3: continued

width of the narrow portion of the Paα profile in IRAS 20087−0308 can be attributed to a steep rotation gradient on the nucleus. The apparent broad base on the Paα line in the southwestern nucleus of IRAS 12112+0305 unfortunately cannot be trusted, as this is the one galaxy in the sample whose spectra were not calibrated by a G star observation, but rather by a template atmospheric spectrum. The excess blue emission happens to be coincident with the significant CO_2 atmospheric absorption at 2.00–2.02 μm, so that a slight error in estimated column depth results in a large localized continuum offset in the corrected spectrum.

The two-dimensional spectra of Paα in Figure 2.3 demonstrate that the atomic recombination line emission in ULIRGs is almost always dominated by a nuclear component. Many ULIRGs show off-nuclear emission at lower levels, and a couple of sources appear to be dominated by such diffuse emission—namely IRAS 04232+1436 and IRAS 20046−0623. When two nuclei are present, the secondary nucleus generally shows emission in Paα as well. Exceptions to this are IRAS 16487+5447 and IRAS 23327+2913. The extra continuum object seen in the panel with IRAS 08030+5243 is a nearby star.

The sample was chosen to allow coverage of both the Paα and Brγ emission lines so that a comparison between these two could be made in order to assess extinction to the line emitting source. Table 2.4 lists the inferred visual extinction values for the sample galaxies. Though there exists very little leverage in wavelength between Paα and Brγ, some ULIRGs are obscured enough to show definite reddening across this short range. Typical 1σ errors on the extinction estimates are around 5 magnitudes, though the actual errors could be larger if disparate aperture sizes were used in the spectral extractions. Indeed, each of the four ULIRGs with extinctions more negative than 1σ have aperture differences between the Paα and Brγ spectra of at least 50%. Almost half of the ULIRGs have estimated extinctions greater than the 1σ limit, and 11 have at least 2σ extinction estimates—typically corresponding to $A_V > 10$ mag, with many in the range of $A_V \sim 25$ mag. These estimates assume an intrinsic ratio for Paα/Brγ of 12.1 (Osterbrock, 1989, Case B with $n_e = 10^4$ cm^{-3} and $T = 10000$ K), and $A_{Pa\alpha} = 0.145 A_V$ and $A_{Br\gamma} = 0.116 A_V$ (interpolated from the extinction law

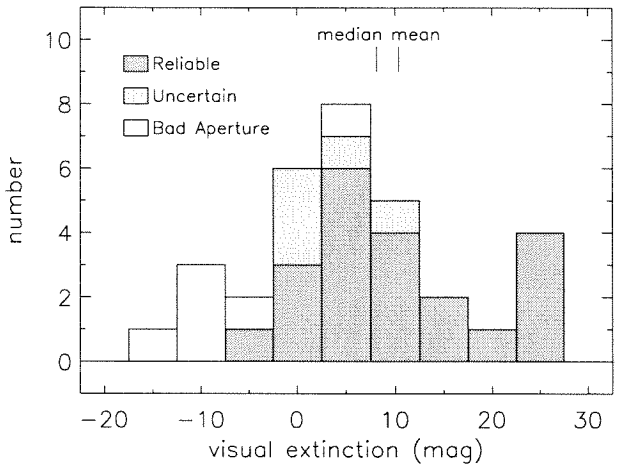

Figure 2.4: Histogram of estimated visual extinctions to the Paα line emission for the 33 primary ULIRG nuclei. Different shadings represent varying levels of reliability, with most of the negative estimates owing to mismatched seeing conditions and therefore significant extraction aperture differences. The mean and median points are marked for the reliable set of measurements. One point, corresponding to $A_V \sim 50$, is beyond the plot boundary.

of Rieke & Lebofsky, 1985).

Figure 2.4 presents the extinction measurements in histogram form. Different shading represents varying levels of confidence in the measurement. Higher extinction estimates are allowed greater variance in classifying their reliability, provided they are significantly different from zero extinction. Counting only those ULIRGs with reliable extinction measures, the median visual extinction of ~ 8 mag implies an extinction at Paα of approximately one magnitude, which is by itself probably not capable of hiding AGN activity. But the measured extinction is only to the line emission we can see, and could therefore represent only the outer shell of the nuclear activity. The very large visual extinctions near 25 mag translate to almost 4 mag of extinction at Paα, which almost certainly would hide an AGN from view with the currently achieved signal-to-noise ratio in the ULIRG spectra.

2.5.2 Molecular Hydrogen Emission

The most abundant species of line emission in the ULIRG spectra arise from the vibration-rotation spectrum of molecular hydrogen. The molecular hydrogen emission shows up strongly in *all* of the primary nuclei of this sample. Three or four lines are

Table 2.4. Derived Properties

Galaxy	Extinction (A_V)	T_{rot} (K)	T_{vib}[a] (K)	H_2 Excitation Mechanism[b]
IRAS 00262+4251	0 ± 66	1300 ± 75	4000 ± 1000	mixture
IRAS 01521+5224	3 ± 14	1400 ± 300	5000	thermal*
IRAS 04232+1436	2.3 ± 7.2	2100 ± 225		thermal
IRAS 05246+0103	1 ± 15	2500 ± 375		thermal
IRAS 08030+5243	0.9 ± 4.6	2100 ± 450		thermal
IRAS 08311−2459	-14.5 ± 4.3[c]	4300 ± 500		thermal
IRAS 08344+5105	-5.0 ± 5.8	1800 ± 200	4500 ± 2000	mixture
IRAS 08572+3915	12.1 ± 3.6	2500 ± 300	5000 ± 1500	mixture
IRAS 09061−1248	3.9 ± 6.1	2200 ± 250	3500	thermal*
IRAS 09111−1007	8.7 ± 4.0	2300 ± 200	2700	thermal*
IRAS 09583+4714	-6.2 ± 5.1[c]	2000 ± 250		thermal
IRAS 10035+4852	-9.9 ± 5.3[c]	2900 ± 300		thermal
IRAS 10190+1322	4.4 ± 3.9	2200 ± 125		thermal
IRAS 10494+4424	-10.8 ± 3.4[c]	2400 ± 250	3500	thermal*
IRAS 11095−0238	9.5 ± 16	1700 ± 150	3800 ± 1300	mixture
IRAS 12112+0305	19.5 ± 3.7	2500 ± 300	5000	thermal*
IRAS 14348−1447	5.7 ± 5.7	2000 ± 125		thermal
IRAS 14352−1954	2.8 ± 3.2	1600 ± 150		thermal
IRAS 14394+5332	12.0 ± 4.8	2200 ± 150	2800	thermal*
IRAS 15245+1019	7.3 ± 2.3	4900 ± 800		thermal
IRAS 15250+3609	4.6 ± 2.1[c]	2000 ± 150	3100 ± 600	mixture
IRAS 15462−0450	8.2 ± 4.4	> 4000		thermal
IRAS 16487+5447	23.3 ± 9.9	1700 ± 150		thermal
IRAS 17028+5817	27.2 ± 4.4	2200 ± 200		thermal
IRAS 18470+3233	0.5 ± 2.7	1600 ± 100		thermal
IRAS 19458+0944	24.3 ± 6.3	2300 ± 100		thermal
IRAS 20046−0623	50 ± 11	1900 ± 300		thermal
IRAS 20087−0308	-10 ± 15	2200 ± 350		thermal
IRAS 20414−1651	26 ± 11	2400 ± 225		thermal
IRAS 21504−0628	3.4 ± 2.8	2600 ± 300		thermal
IRAS 22491−1808	16 ± 11	2100 ± 250		thermal
IRAS 23327+2913	2 ± 73	1600 ± 200		thermal
IRAS 23365+3604	14.5 ± 2.6	1900 ± 150	4200 ± 900	mixture

[a]Given only for definite thermal/fluorescent mixtures (with errors) and for likely mixtures (both 2–1 lines above rotation temperature prediction). The vibration temperature assumes an ortho-to-para ratio of 2:1 in the 2–1 transition states.

[b]Classified as consistent with purely thermal, definite mixture of thermal and fluorescence, or possible mixture of the two (with asterisk).

[c]Apertures for the Paα and Brγ spectral extractions differ by at least 50%.

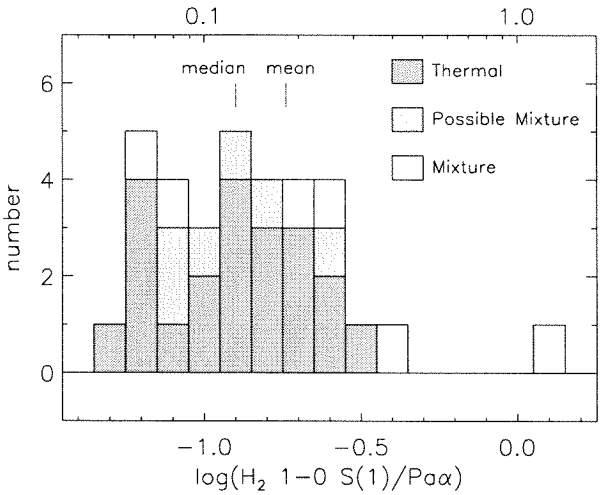

Figure 2.5: Ratio of the H_2 1–0 S(1) line strength to that of Paα for the 33 primary ULIRG nuclei. A linear scale appears at top. Typical 1σ errors are comparable to the bin width, though perhaps a little smaller. The mean is performed on the linear scale, rather than on the logarithmic scale. Shadings indicating excitation mechanisms are included for reference.

typically present in each spectrum, most notably the odd rotation state 1–0 transitions. The H_2 line strengths vary by more than one order-of-magnitude relative to Paα. Figure 2.5 shows the range of observed line ratios, comparing the H_2 1–0 S(1) line to Paα. A typical ULIRG has a H_2 1–0 S(1)/Paα ratio around 0.15, varying from $\sim$ 0.05 to 0.40, with one galaxy (IRAS 00262+4251) boasting H_2 emission even stronger than the Paα line. The bins in Figure 2.5 are shaded to reflect the classification of the H_2 excitation mechanisms, as will be discussed below.

The apparent weakness of the even rotation transitions is an indication that the emission is thermally excited, as the thermal condition produces three times as many odd (ortho) states as even (para) states. This so-called ortho-to-para ratio is more typically in the range of 1.0–1.8 for fluorescent excitation conditions (Black & van Dishoeck, 1987). In addition, the lack of strong emission from the 2–1 vibration transition indicates a thermal origin.

The specific mechanism responsible for the H_2 emission can be investigated via population diagrams. By accounting for various degeneracies, transition probabilities, and photon energy, one may compute the relative populations of the upper states of each transition based on the observed line flux. In pure thermal equilibrium, the

population levels will follow an exponential profile with respect to upper state energy. More formally, the intensity of a given transition is described by

$$I(v_1, v_2, J_1, J_2) \propto g_s(J_1) A(v_1, v_2, J_1, J_2)(2J_1 + 1) h\nu_{12} e^{-\frac{E}{kT}},$$

where the upper and lower states are denoted by the 1 and 2 subscripts, v represents vibration state, J the rotation state, $g_s(J_1)$ the ortho/para degeneracy, $A(v_1, v_2, J_1, J_2)$ the transition probability, ν_{12} the emitted photon frequency, E the upper state energy, and T the equilibrium temperature. Therefore, a logarithmic plot of the line intensities divided by the terms multiplying the exponential above produces a linear relation against the upper energy scale with a slope proportional to the inverse of the temperature.

When the molecular hydrogen is not in thermal equilibrium—such as may be the case in fluorescent excitation by ultraviolet photons—a diagram such as that described above will not show all points lying along a common line, but rather disconnected linear segments, with common vibration states each defining a line connecting the different rotation states. The characteristic temperature of this line is referred to as the rotation temperature, T_{rot}. Ideally, each vibration state has the same characteristic rotation temperature, and these segments can be connected with another line characterized by a vibration temperature, T_{vib}. The thermal case simply has $T_{rot} = T_{vib} = T$. Typically, pure fluorescent conditions are characterized by $T_{rot} = 800$—1400 K, and $T_{vib} = 5000$–6000 K (Black & van Dishoeck, 1987; Takayanagi, Sakimoto, & Onda, 1987). Excitation conditions associated with thermal processes are typically found to have $T_{rot} = 1600$–2400 K, with a slight difference between rotation and vibration temperatures characterized by $T_{rot} \approx 0.8 T_{vib}$ (Tanaka et al., 1989; Hasegawa et al., 1987; Beckwith et al., 1983).

Population diagrams were constructed for each of the primary nucleus extractions in the sample, and each characterized in terms of rotation temperature, vibration temperature (where appropriate) and classified in terms of thermal or mixed thermal/fluorescent excitation. Examples of these diagrams are shown in Figure 2.6. The

even rotation state transitions are plotted as two points representing ortho-to-para ratios of 3:1 and 1:1. The 3:1 points, represented by boxes in Figure 2.6, are almost always preferred over the 1:1 points appearing below them. The great majority of ULIRGs in this sample have no detections in the 2–1 transition lines, but with error bars consistent with purely thermal excitation. A few ULIRGs appear to support definite mixtures of thermal and fluorescent excitation, with the population diagrams showing the 2–1 data points well above the rotation temperature line passing through the 1–0 points. A number of other ULIRGs have somewhat elevated 2–1 measures, with both the S(2) and S(4) lines above the 1–0 rotation temperature line, but with error bars that are still consistent with pure thermal emission. These characterizations of excitation mechanisms are summarized in Table 2.4. For the mixed cases, a vibration temperature estimate is given, assuming that the high energy states exist with a lower ortho-to-para ratio, likely around 2:1. This has been observed in other mixed excitation cases (e.g., Tanaka et al., 1989), and is explained by the fact that the enhanced 2–1 transition emission arises from molecules that are primarily excited by fluorescent processes, and thus reflect an ortho-to-para ratio closer to that expected for pure fluorescence.

One point that should be mentioned in the context of the line population diagrams is the possible blend of a 2.0024 μm [Fe II] line with the H_2 2–1 S(4) line at 2.0035 μm. The expected flux ratio between the [Fe II] line at 1.9670 μm and that at 2.0024 μm is 2–3:1. With the 1.9670 μm line appearing to be present in a number of ULIRGs, it is to be expected that the H_2 2–1 S(4) line will suffer some contamination by the [Fe II] line. Indeed, the population diagrams often show an anomalously high 2–1 S(4) line flux, with an incompatibly low 2–1 S(2) flux. There is a good correlation between such cases and galaxies for which the 1.9670 μm [Fe II] line is believed to be present.

Figure 2.7 illustrates the distribution of H_2 rotation temperatures, indicating a strong clustering around 2200 K. It is interesting to note that two of the three ULIRGs with estimated rotation temperatures in excess of 4000 K are classified as having AGN. It is possible in these cases that a significant fraction of the H_2 emission arises from molecular gas excited by X-ray radiation from the central source. Draine &

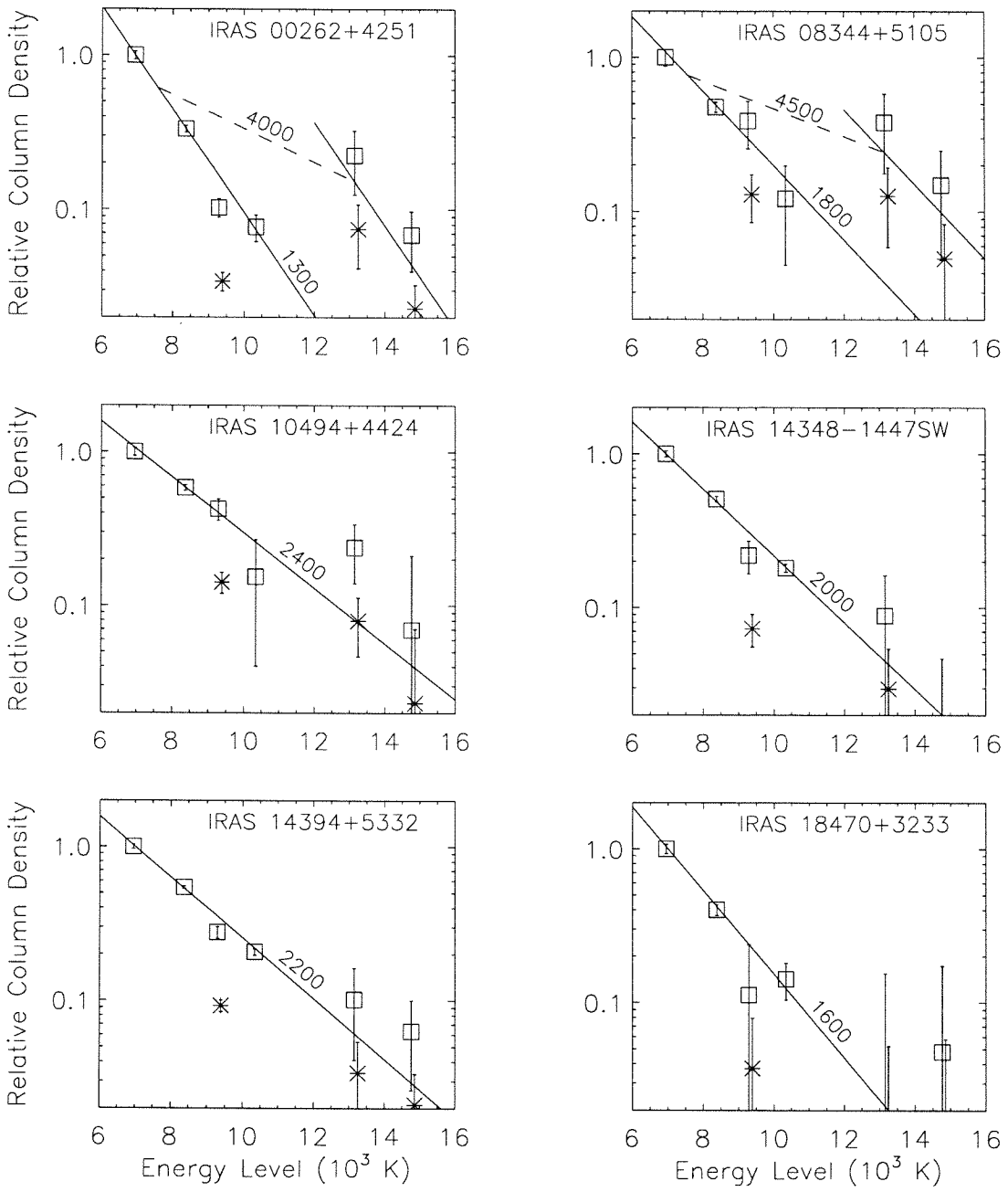

Figure 2.6: Molecular hydrogen population diagrams for six of the ULIRGs, showing the range of properties seen in the H_2 excitation. The top two show examples of mixed thermal and fluorescent excitation, while the bottom four are consistent with a single temperature characterization. IRAS 10494+4244 and IRAS 1439+5332 may have some slight component of fluorescent excitation, judging by the elevated 2–1 lines. For even (para) rotation states, two points are plotted, corresponding to ortho-to-para ratios of 3:1 and 1:1, with boxes corresponding to the 3:1 case, and asterisks for 1:1. The population diagram for IRAS 18470+3233 is fairly typical of most of the ULIRGs in this sample in terms of excitation information and signal-to-noise ratio. Line fits are accompanied by temperatures corresponding to the slopes.

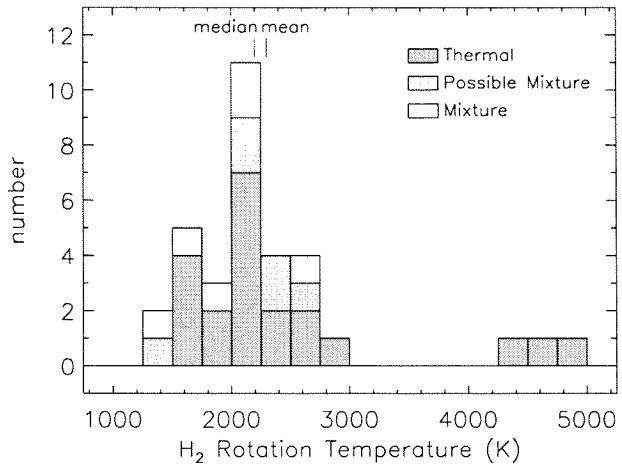

Figure 2.7: Rotation temperatures determined for the 33 primary ULIRG nuclei. The majority are consistent with thermal emission, for which the rotation temperature represents the ambient equilibrium temperature. A few are definitely mixtures of thermal and fluorescent processes, with vibration temperatures in the range of 3100–5000 K.

Woods (1990) found this mechanism to be the most viable source of H_2 excitation in NGC 6240, with the X-rays in this instance most probably arising from frequent supernovae or from merger-induced shock activity.

Referring to Figure 2.5, there does not appear to be an overwhelming trend between H_2 line strength and excitation mechanism, except for a possible slight tendency for mixtures to be seen among the brighter lines. This could simply be a consequence of higher signal-to-noise levels for the weak 2–1 lines in those galaxies with bright H_2 lines. More mixture states may be revealed with greater sensitivity, most likely in those cases identified here as possible mixtures.

Because ULIRGs tend to show relatively uniform H_2 emission properties—namely those corresponding to thermal emission at 1500–2500 K—it may be useful for other researchers to have a table of expected H_2 line strengths in the K band for a range of typical temperatures. Table 2.5 provides such a reference, with line intensities normalized to the H_2 1–0 S(1) line. These estimates assume an ortho-to-para ratio of 3:1, and $T_{rot} = 0.8T_{vib}$, as is found empirically (Tanaka et al., 1989; Hasegawa et al., 1987). In order to regain the pure thermal regime characterized by a single temperature, the 2–1 entries in Table 2.5 should be multiplied by $\exp(-1107/T)$, and the 3–1 transition multiplied by $\exp(-2144/T)$, lowering these values considerably.

Table 2.5. Expected H_2 Line Ratios

Transition	λ_{air} (μm)	T_{rot} = 1500 K	T_{rot} = 2000 K	T_{rot} = 2500 K	T_{rot} = 4000 K
1–0 S(0)	2.22268	0.228	0.211	0.201	0.187
1–0 S(1)	2.12125	1.000	1.000	1.000	1.000
1–0 S(2)	2.03320	0.336	0.374	0.398	0.438
1–0 S(3)	1.95702	0.805	1.019	1.174	1.450
1–0 S(4)	1.8914	0.177	0.261	0.329	0.468
1–0 S(5)	1.8353	0.295	0.519	0.728	1.211
2–1 S(0)	2.3550	0.015	0.030	0.045	0.083
2–1 S(1)	2.2471	0.068	0.143	0.225	0.441
2–1 S(2)	2.1536	0.023	0.053	0.089	0.191
2–1 S(3)	2.0729	0.055	0.145	0.259	0.622
2–1 S(4)	2.0035	0.012	0.037	0.072	0.197
2–1 S(5)	1.9443	0.020	0.072	0.156	0.496
2–1 S(6)	1.8942	0.003	0.014	0.033	0.124
2–1 S(7)	1.8523	0.004	0.020	0.054	0.246
3–2 S(3)	2.2008	0.003	0.016	0.045	0.202

Note. — This table assumes that $T_{rot} = 0.8T_{vib}$. To recover a strictly thermal regime ($T_{rot} = T_{vib} = T$), multiply the 2–1 transistions by $\exp(-1107/T)$ and the 3–2 transition by $\exp(-2144/T)$.

2.5.3 Other Emission Line Strengths

The He I emission line just blueward of Paα is a combination of two lines at 1.86860 and 1.86969 μm, both of the same $1s4f$–$1s3d$ transition, but the former a triplet state and the latter a singlet. As such, the shorter wavelength line is three times stronger than the longer wavelength line, with a centroid wavelength of 1.8689 μm. The splitting between lines is less than half a resolution element for the present spectra, so that the line combination is treated as one.

The He I line is detected in the majority (27/33) of the primary nuclear spectra, and in a number of the secondary spectra. The noise-weighted mean of detected He I/Paα is 0.058, with a relatively small dispersion of $\sim$ 0.03 about this value. The median He I/Paα ratio is 0.063 among detected lines, and 0.056 including non-detections as zero-valued points. The full range of detected ratios goes from 0.02 (IRAS 15245+3609) to about 0.11 (IRAS 14348−1447; IRAS 14394+5332). Lower resolution near-infrared spectra could easily mistake this line for a blue wing on the Paα line.

The [Fe II] line at 1.9670 μm appears in several spectra, most notably the primary nuclei of IRAS 00262+4251, IRAS 09111−1007, IRAS 15245+1019, and IRAS 15250+3609, and the secondary nucleus of IRAS 10190+1322. These stronger [Fe II] emitters have [Fe II]/Paα ratios up to 0.05, though IRAS 00262+4251, with its weak Paα, has a ratio around 0.12. There are many possible line detections near the noise limit that have typical [Fe II]/Paα ratios around 0.01–0.02. Lines weaker than 1% of Paα are generally too weak to be detected with confidence. The [Fe II] line reported for IRAS 08311−2459 is possibly confused with the wing of [Si VI]. A more thorough analysis of this line complex at slightly higher resolution does not find conclusive evidence for the [Fe II] line in this galaxy (Murphy et al., 2000a, Chapter 6, this thesis).

As mentioned above, a second [Fe II] line at 2.0024 μm is expected to be 2–3 times weaker than the 1.9670 μm line, possibly mixed with the H_2 2–1 S(4) line. This line may be visible in the IRAS 09111−1007 spectrum, though marked as H_2.

The [Si VI] line was a primary driver for the present spectroscopic survey. With a 167 eV excitation potential, this line indicates a high probability of the presence of a resident active nucleus. While possible to produce Si^{5+} atoms via powerful shocks, Marconi et al. (1994) find that photoionization is the more likely excitation mechanism among a sample of nearby Seyfert galaxies. As stars are incapable of producing significant quantities of photons at this high energy, the natural photoionization source is an active nucleus with its power-law spectrum extending into the far-ultraviolet wavelength range.

Only one galaxy in the sample of 33 ULIRGs exhibits prominent [Si VI] emission. IRAS 08311−2459 has a very strong [Si VI] line, comparable to the adjacent H_2 1–0 S(3) line in strength, and appearing broader than the other lines in the spectrum. More discussion of the [Si VI] line in this galaxy can be found in Chapters 3 and 6.

The only other galaxy in the present sample with a possible [Si VI] detection is IRAS 05246+0103. The spectrum from this galaxy shows emission at the expected position of [Si VI], with a signal-to-noise ratio of ∼5. The adjacent H_2 line appears broad on the short-wavelength side as well, calling to question the nature of the emission on the long-wavelength side of this line. No emission appears at this position in the secondary nucleus spectrum of Figure 2.2, ruling out a problem with atmospheric calibration or related issues. The H_2 1–0 S(1) line appears unresolved in the primary nucleus, deepening the mystery. While IRAS 05246+0103 has no evidence of broad line emission, it does have a peculiar radio spectrum. Crawford et al. (1996) find this galaxy to be a gigahertz-peaked-spectrum (GPS) radio source, with a 6 cm flux density much higher than that measured at 20 cm. This condition is not found in many ULIRGs, with the Parks (PKS) galaxy IRAS 13451+1232 being the only other 2 Jy ULIRG identified as a GPS source. This galaxy may also have [Si VI] emission, as reported by Veilleux, Sanders, & Kim (1997), though the blend with the H_2 line at their resolution makes it difficult to estimate the relative contribution of [Si VI]. The rest of the H_2 lines in IRAS 13451+1232, as presented in Veilleux, Sanders, & Kim, indicate a H_2 rotation temperature around 2500 K, in which case the [Si VI] line would account for ∼30% of the total combined line flux. IRAS 13451+1232 does show impressive

broadening of the Paα line, clearly standing out as an AGN-dominated source. While IRAS 05246+0103 has a similar radio spectrum to IRAS 13451+1232, it is almost three orders of magnitude less luminous at 20 cm, according to Crawford et al. Perhaps there is a low-luminosity active nucleus component to IRAS 05246+0103, with the total infrared luminosity dominated by star formation.

2.5.4 Relative Nuclear Velocities

The double nucleus ULIRGs often exhibit strong Paα emission on both nuclei, which can be used to study orbital dynamics of the galactic pair. Table 2.6 lists the relative radial velocities for the 12 ULIRGs with measured Paα velocities on both nuclei. The reported errors are considerably smaller than would be obtained by simply subtracting the velocities presented in Table 2.3, reflecting the fact that the relative velocities are not effected by systematics associated with wavelength calibration or slit illumination.

Surprisingly, the velocity differences are very small, with the largest difference at 120 km s^{-1}. Certainly projection effects greatly diminish the observed relative velocities, as the most probable observing configuration involves viewing the system from the "equator" of the axis defined by the relative velocity vector. If all ULIRGs have the same relative nuclear velocity, random orientations would produce a distribution of observed velocities described by a cosine curve, with the peak at zero observed relative velocity. Binning the data from Table 2.6 into 50 km s^{-1} bins, the best fit to a cosine function has a maximum velocity of about 190 km s^{-1}, shown in Figure 2.8. Using 40 km s^{-1} bins results in a 165 km s^{-1} maximum relative velocity.

The lack of high relative velocities among ULIRGs contrasts with the predictions obtained either from simple Newtonian calculations or from more sophisticated N-body models of galaxy interactions which include gas dynamics and dynamical friction. Below we discuss these two approaches, with attention to how these models might be modified to match the observations.

First, we will treat the galaxies as point masses approaching each other from far away. These calculations assume conservative dynamics—i.e., that all loss of potential

Table 2.6. Relative Nuclear Radial Velocities

Galaxy	Relative Velocity (km s^{-1})	Projected Separation (kpc)
IRAS 01521+5224	-50 ± 25[a]	7.6
IRAS 05246+0103	-1 ± 12	9.8
IRAS 08572+3915	-26 ± 11	5.8
IRAS 09061−1248	12 ± 28	7.2
IRAS 09583+4714	-53 ± 30	37.5
IRAS 10035+4852	8 ± 28	11.2
IRAS 10190+1322	114 ± 11	5.3
IRAS 12112+0305	-98 ± 13	3.7
IRAS 14348−1447	-112 ± 10	4.7
IRAS 15245+1019	-54 ± 27	3.4
IRAS 17028+5817	120 ± 22	23.0
IRAS 22491−1808	-3 ± 10	2.2

[a]From Chapter 7. The current dataset yields -22 ± 169.

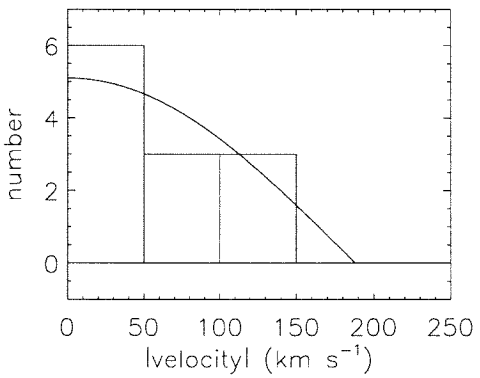

Figure 2.8: Histogram of the absolute values of projected relative nuclear velocities. If all ULIRGs had the same relative velocity, projection effects would result in our observing a cosine distribution. The best fit cosine to the data has a 190 km s^{-1} velocity amplitude.

energy is converted into kinetic energy of the galaxies. In reality some fraction of the energy is lost to dynamical friction, which is why the galaxies do eventually merge. The foregoing discussion will not explicitly treat the frictional component, but will concentrate on the more basic elements of merger dynamics that offer a much greater latitude in ultimate relative velocities. The reader should bear in mind that velocities will be reduced somewhat by dynamical friction processes. In the point mass scenario, the galaxies would reach a relative velocity $\Delta v = 2\sqrt{GM/r}$ in excess of 1300 km s^{-1} at a separation distance of 10 kpc, assuming total system masses of $10^{12} M_{\odot}$. Even ten times less mass per galaxy results in over 400 km s^{-1} of relative motion at 10 kpc. Changing the initial separation from infinity to 100 kpc or 50 kpc reduces these speeds by 5% and 10%, respectively.

The high velocities computed above are obviously not consistent with the observations, but perhaps understandably given that galaxies are not well represented by point masses at close range. Galaxy masses are dominated by very large dark halos that act to soften the potential gradients—i.e., accelerations—experienced during a close encounter.

Dark halos are thought to exist based on the anomalously flat rotation curves of galaxies to very large radii. Such phenomena suggest the enclosed spherical mass is proportional to radius, such that the rotation velocity, $v_c = \sqrt{GM_{encl}/r}$, is constant. Rotation curves of large samples of galaxies via optical emission lines (e.g., Dale et al., 1999) indicate that this scaling persists at least out to 10–15 kpc. Observations in H I find a continuation of the flat rotation curves at radii 2–3 times the optical radii, often to 20–30 kpc (e.g., Casertano & van Albada, 1990; Fich & Tremaine, 1991). Assuming a spherical halo distribution, the total halo mass following the $M_{encl} \propto r$ scaling is given by

$$M_{\rm halo} = 10^{11} \left(\frac{v_c}{208\,{\rm km\,s^{-1}}}\right)^2 \left(\frac{r_{\rm cutoff}}{10\,{\rm kpc}}\right) M_{\odot},$$

where v_c is the circular velocity, and $r_{\rm cutoff}$ is the outer dimension of the halo distribution. Under this prescription, two galaxies falling from infinity are moving with a

relative velocity of $\sqrt{2}v_c$ by the time the halos touch, or when the galaxies are $2r_{\rm cutoff}$ apart. The galaxies will clearly accelerate even more as the separation decreases to $\sim$ 10 kpc, even though the acceleration is somewhat moderated by the effect of overlapping halo masses. This already presents a problem in that the observed relative velocities are less than or similar to the typical rotation velocities observed in ULIRGs.

The simulations by Mihos & Hernquist (1996) provide a means of evaluating encounter velocities against models employing realistic halo potentials and dynamical friction. Output from these models is shown in Figure 2.9. We will focus our attention here on the "Low Mass Halo" model, as this more highly concentrated mass model more suitably represents the disk rotation velocities seen among ULIRGs. This model defines a halo that yields a total galaxy mass of 4×10^{11} $M_\odot$ when scaled to the Milky Way's rotation velocity. The halo has a relatively small physical extent, containing most of its mass within 25 kpc, and with an effective cutoff radius at 40 kpc. The simulations start with identical galaxies approaching from infinity (parabolic orbits), resulting in time-averaged velocities of $\sim$ 350 km s^{-1} when the nuclei are between 4–25 kpc apart. This average sums over first, second, and third encounters. The peak velocities are in the neighborhood of 500 km s^{-1}, as seen in Figure 2.9. Starting the galaxies from rest at a 100 kpc separation rather than infinity reduces the peak velocities by only $\sim$ 15%.

Many ULIRGs are found at times well after the first major encounter, judging by the fact that their tidal features, formed at the epoch of the first significant encounter, are often vastly more extended than the nuclei are separated. However, some ULIRGs are believed to be experiencing their first major encounter (Murphy et al., 2000b, Chapter 7, this thesis). Looking at the first-encounter and late-encounter model predictions separately, the simulation discussed above predicts first-encounter velocities averaging 475 km s^{-1}, after which the galaxies separate by 50 kpc, followed by a final merger sequence with an average velocity around 275 km s^{-1}, ranging from 0–500 km s^{-1} during this time.

Models with larger-scale halos maintaining the same internal rotation structure demand higher total masses, resulting in increased net velocity differences between

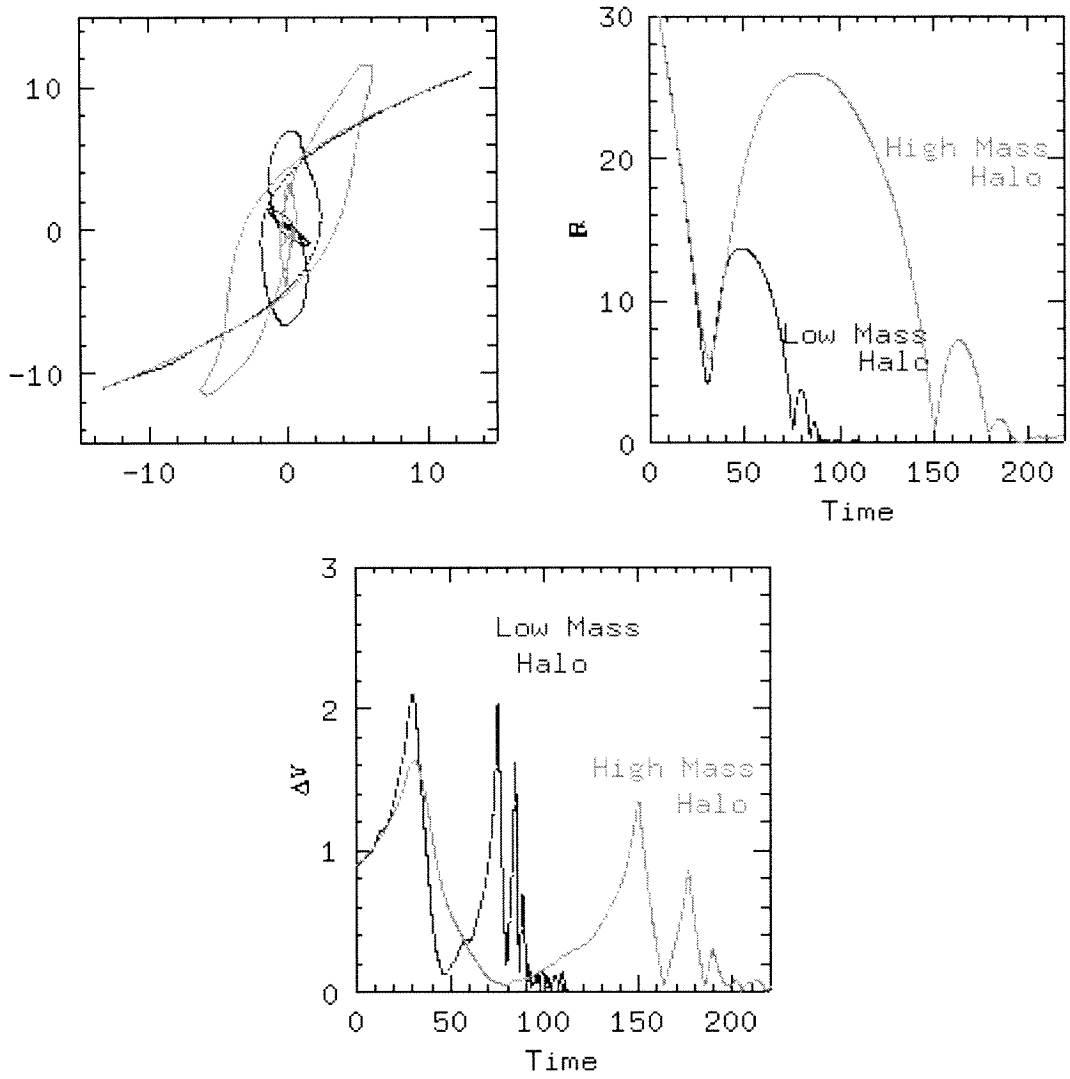

Figure 2.9: Simulations of galaxy interactions, courtesy of J. C. Mihos. At upper left is the orbital track, at upper right is nuclear separation as a function of time, and at bottom is the relative velocity as a function of time. Units of distance, time, and velocity are 3.5 kpc, 1.3×10^7 yr, and 250 km s^{-1}, respectively. Both "Low Mass Halo" (black) and "High Mass Halo" (gray) models correspond to the same total mass of $4 \times 10^{11} M_\odot$, with the low mass model corresponding to a more compact mass distribution, yielding a Milky-Way-like disk rotation velocity. The high mass model is simply more diffuse, with a lower effective disk rotation velocity. The low mass model probably better represents ULIRG mass concentrations.

the merging galaxies. On the other hand, if ULIRGs lacked any halo material past 10 kpc, corresponding to total masses around 10^{11} $M_{\odot}$, the galaxies would behave much more like point masses, and dynamical friction would be less important. In this scenario, the 10 kpc velocities would be approximately 400 km s^{-1}.

In summary, it is very difficult to reproduce the small observed relative velocities among ULIRGs with simple physical models—with or without large halos. ULIRGs are massive, gas-rich galaxies with rotation velocities and near-infrared absolute magnitudes characteristic of galaxies at least as massive as the Milky Way. The highest observed relative velocity in this sample is a mere 120 km s^{-1}, though the observed distribution is consistent with a typical deprojected velocity difference of 200 km s^{-1}. Some ULIRGs have been observed with velocity differences very near this value (e.g., IRAS 20046−0623; IRAS 19252−7245: Murphy et al., 2000b; Mihos & Bothun, 1998), but none are seen near the 400 km s^{-1} mark as expected from a variety of physical predictions.

One possibility deserves mention, which is that during the late-merger state, eccentric orbits may conspire with the delay in coordinating fuel for a nuclear starburst in such a way as to select ULIRGs at the apocenters of their orbits, when velocities are low. Referring to Figure 2.9, during the final merger process (well after the initial encounter), the nuclear orbits are very eccentric, owing to the removal of angular momentum, largely by tidal debris. The very high velocity peaks near 500 km s^{-1} are associated with the close passages. If the ultraluminous activity is episodic in nature, with relatively short duration bursts occurring in reaction to transitory tidal disruptions, then the ULIRGs we see may represent stages shortly after these close encounters. A finite time is required to organize gas motions in response to the close encounter, with the ultraluminous activity turning on only after a significant gas concentration has been established. It is not difficult to imagine in this scenario that the gas—moving more slowly than the galaxy, but with less distance to travel—will reach the nucleus at approximately the same time that the galaxies reach apocenter. Keeping in mind that we are discussing the events occurring after the second close encounter, the orbital timescale is $\sim 10^8$ yr, such that apocenter is reached a few$\times 10^7$

yr after close approach. This timescale is in rough agreement with expectations of the dynamical timescale within a few kpc of the nucleus—the region from which the fuel for the nuclear event is gathered. The idea of repetitive starbursts in the final stages of merging was first explored by Noguchi (1991), though in the context of cloud-cloud collisions in this case. The scheme proposed here of episodic bursting would bias ULIRGs to larger separations and thus lower velocities, quite possibly consistent with the observed distribution. The problem with first encounter ULIRGs remains, since the average first encounter velocity is around 475 km s^{-1}. Unfortunately, the current sample is not large enough to probe possible differences in the velocity distributions of early and late ULIRG encounters.

2.6 Summary

Near-infrared spectra in the 2 μm window have been obtained for a sample of 33 ULIRGs resulting in a nearly complete, volume-limited set of observations. Lines of atomic hydrogen and helium recombination, molecular hydrogen vibration-rotation, [Fe II], and [Si VI] are seen in the spectra. Initiated as a search for optically hidden active galactic nuclei, only two such galaxies are found, both of which are characterized as Seyfert galaxies based on visible-light spectra. It is found via comparison of the Paα and Brγ lines that significant extinction of several magnitudes persists into the near-infrared bands, such that buried active nuclei cannot be ruled out in many objects.

Strong molecular hydrogen emission is seen in all of the primary nuclear spectra. The molecular hydrogen spectrum indicates that most H_2 emission in ULIRGs stems from thermal excitation rather than fluorescent processes. Some ULIRGs appear to have a small fraction of their molecular hydrogen emission owing to fluorescent processes, but none approach pure fluorescent conditions.

The relative radial velocities found in this sample of ULIRGs does not exceed $\sim$ 120 km s^{-1}, with an inferred maximum deprojected velocity differential of around 200 km s^{-1}. This relatively low velocity differential is difficult to produce from interactions between galaxies with masses comparable to that of the Milky Way using simple

physical assumptions.

We thank Michael Strauss for his role in defining the sample of ULIRGs, and for participating in the early stages of the Caltech effort in studying ULIRGs. We also thank Chris Mihos, Gerry Neugebauer, Nick Scoville, and Sterl Phinney for helpful discussions. James Graham provided information on [Fe II] transition strengths and wavelengths. Many persons accompanied us on the observing runs to Palomar, most notably Rob Knop and James Larkin, both of whom provided expert tutelage on the use of the spectrograph, and on methods of data reduction. We thank the night assistants at Palomar, Juan Carasco, Rick Burruss, Skip Staples, and Karl Dunscombe. for their assistance in the observations. This research has made use of the NASA/IPAC Extragalactic Database (NED), which is operated by the Jet Propulsion Laboratory, Caltech under contract with NASA. T.W.M. is supported by the NASA Graduate Student Researchers Program, and the Lewis Kingsley Foundation. This research is supported by a grant from the National Science Foundation.

Bibliography

Beckwith, S., Evans, N. J., Gatley, I., Gull, G., & Russel, R. W. 1983, *Astrophysical Journal*, 264, 152

Black, J. H., & van Dishoeck, E. F. 1987, *Astrophysical Journal*, 322, 412

Carico, D. P., Graham, J. R., Matthews, K., Wilson, T. D., Soifer, B. T., Neugebauer, G., & Sanders, D. B. 1990, *Astrophysical Journal*, 349, L39

Casertano, S. & van Albada, T. S. 1990, in *Baryonic Dark Matter*, ed. D. Lynden-Bell & G. Gilmore (Dordrecht: Kluwer) p. 298

Clements, D. L., Sutherland, W. J., McMahon, R. G., & Saunders, W. 1996, *Monthly Notices of the Royal Astron. Soc.*, 279, 477

Crawford, T., Marr, J., Partridge, B., & Strauss, M. A. 1996, *Astrophysical Journal*, 460, 225

Dale, D. A., Giovanelli, R., Haynes, M. P., Hardy, E., & Campusano, L. E. 1999, *Astronomical Journal*, 118, 1468

Draine, B. T., & Woods, D. T. 1990, *Astrophysical Journal*, 363, 464

Fich, M., & Tremaine, S. 1991, *Annual Review of Astron. & Astrophys.*, 29, 409

Genzel, R., et al. 1998, *Astrophysical Journal*, 498, 579

Hasegawa, T., Gatley, I., Garden, R. P., Brand, P. W. J. L., Ohishi, M., Hayashi, M., & Kaifu, N. 1987, *Astrophysical Journal*, 318, L77

IRAS Point Source Catalog, Explanatory Supplement, eds. Beichman, C. A., Neugebauer, G., Habing, H. J., Clegg, P. E., & Chester, T. J. 1988 (U.S. GPO, Washington, D. C.)

Kleinmann, S. G., & Hall, D. N. B. 1986, *Astrophysical Journal Supp. Series*, 62, 501

Larkin, J. E., Knop, R. A., Lin, S. Matthews, K., & Soifer, B. T. 1996, *Publ. of the Astron. Soc. of the Pacific*, 108, 211

Marconi, A., Moorwood, A. F. M., Salvati, M., & Oliva, E. 1994, *Astronomy & Astrophysics*, 291, 18

Mihos, J. C., & Hernquist, L. 1996, *Astrophysical Journal*, 464, 641

Mihos, J. C., & Bothun, G. D. 1998, *Astrophysical Journal*, 500, 619

Murphy, T. W., Armus, L., Matthews, K., Soifer, B. T., Mazzarella, J. M., Shupe, D. L., Strauss, M. A., & Neugebauer, G. 1996, *Astronomical Journal*, 111, 1025

Murphy, T. W., Soifer, B. T., Matthews, K., Kiger, J. R., & Armus, L. 1999, *Astrophysical Journal*, 525, L85, Chapter 3, this thesis

Murphy, T. W., Soifer, B. T., Matthews, K., Armus, L. 2000a, *Astronomical Journal*, submitted, Chapter 6, this thesis

Murphy, T. W., Soifer, B. T., Matthews, K., & Armus, L. 2000b, in preparation, Chapter 7, this thesis

Noguchi, M. 1991, *Monthly Notices of the Royal Astron. Soc.*, 251, 360

Oliva, E., & Origlia, L. 1992, *Astronomy & Astrophysics*, 254, 466

Osterbrock, D. E. 1989, *Astrophysics of Gaseous Nebulae and Active Galactic Nuclei* (Mill Valley: University Science Books)

Rieke, G. H., & Lebofsky, M. J. 1985, *Astrophysical Journal*, 288, 618

Rigopoulou, D., Spoon, H. W. W., Genzel, G., Lutz, D., Moorwood, A. F. M., & Tran, Q. D. 1999, *Astronomical Journal*, 118, 2625

Sanders, D. B., Soifer, B. T., Elias, J. H., Madore, B. F., Matthews, K., Neugebauer, G., & Scoville, N. Z. 1988, *Astrophysical Journal*, 325, 74

Soifer, B. T., Sanders, D. B., Madore, B. F., Neugebauer, G., Danielson, G. E., Elias, J. H., Lonsdale, C. J., & Rice, W. L. 1987, *Astrophysical Journal*, 320, 238

Strauss, M. A., Davis, M., Yahil, A., & Huchra, J. P. 1990, *Astrophysical Journal*, 361, 49

Strauss, M. A., Huchra, J. P., Davis, M., Yahil, A., Fisher, K. B., & Tonry, J. 1992, *Astrophysical Journal Supp. Series*, 83, 29

Takayanagi, K., Sakimoto, K., & Onda, K. 1987, *Astrophysical Journal*, 318, L81

Tanaka, M., Hasegawa, T., Hayashi, S. S., Brand, P. W. J. L., & Gatley, I. 1989, *Astrophysical Journal*, 336, 207

Veilleux, S., Sanders, D. B., & Kim, D.-C. 1997, *Astrophysical Journal*, 484, 92

Chapter 3 Near-Infrared Spectra of ULIRGs: Summary

3.1 Chapter Overview

Near-infrared spectra with resolution $\lambda/\Delta\lambda \approx 1100$ in the rest wavelength range 1.8–2.2 μm have been obtained for a complete sample of 33 ultraluminous infrared galaxies. Of the 33 objects observed, 2 show evidence of a central AGN through either a broad Paschen α line or emission in the 1.963 μm fine structure of [Si VI]. In the median spectrum of the remaining 31 objects, the lines present are recombination lines of Hydrogen, neutral Helium, vibration-rotation lines of H_2, and [Fe II]. There is no indication of AGN activity in the median spectrum, either through broad atomic recombination lines or high ionization lines. No trends in luminosity are apparent when subsets of the 31 non-AGN ULIRGs are binned by luminosity and median combined. When secondary nuclei exist in ULIRGs, they typically have spectra very much like those seen in the primary nuclei.

3.2 Introduction

From the initial realization that ultraluminous infrared galaxies (hereafter ULIRGs) represent a significant class of the highest luminosity objects in the local universe (Soifer et al., 1987; Sanders et al., 1988), a central question has been what powers this luminosity. Various studies have attempted to address this question by probing the centers of these highly dust enshrouded systems at wavelengths where the opacity of dust is vastly reduced from that found at visible wavelengths, ranging from X-ray (Rieke, 1988; Nakagawa et al., 1999) to near-infrared (Carico et al., 1990; Veilleux et al., 1999) to mid-infrared (Genzel et al., 1998; Soifer et al., 2000), as well as to

radio wavelengths (Smith, Lonsdale, & Lonsdale, 1998). These studies have generally found that direct detection of AGN (Active Galactic Nucleus) properties in the nuclei of these systems is rare.

In this chapter we summarize the results of a near-infrared spectroscopic survey of 33 bright, nearby ULIRGs undertaken for the purpose of identifying sources where the effects of dust might be hiding the presence of an AGN in the visible spectra of ULIRGs. This is a natural explanation of the paucity of such spectra, given that the ULIRGs are known to have nuclear regions that are extremely rich in gas and dust (Sanders et al., 1988). The reduced extinction in the near-infrared as compared to the visible (i.e., $A_{Pa\alpha} \sim 0.1 A_V$, Rieke & Lebofsky, 1985) enables extremely sensitive searches for characteristics of AGN hidden by large columns of dust. This survey concentrates on searching for a high velocity component to the strong Paα line, as well as the presence of the very high excitation [Si VI] line. The detailed results of this study are presented elsewhere (Murphy et al., 2000, Chapter 2, this thesis).

3.3 The Sample

The complete sample of 33 ULIRGs for this spectroscopic study is a subset of the sample of Strauss et al. (1990, 1992), which is a complete sample of galaxies selected to have S_ν >1.94 Jy at 60 μm and an infrared luminosity of $\gtrsim 10^{12} L_\odot$. The selection criteria for the present sample additionally require a declination $\delta > -35°$, and a redshift in the range of $0.055 < z < 0.108$. This last constraint allows observations of both Paα and Brγ in the 2 μm atmospheric window. The list of sample galaxies can be read directly out of Murphy et al. (1996) with the above redshift constraint imposed. Two of the 35 galaxies from this sublist have been removed from the present sample: IRAS 21396+3623 is actually at a redshift of $z = 0.1493$, and IRAS 19297−0406, at galactic latitude $b \sim -11°$, does not appear to be properly identified as a ULIRG.

3.4 Observations & Data Reduction

Observations were obtained with the Palomar Longslit Infrared Spectrograph (Larkin et al., 1996) on observing runs over the period 1996 January to 1997 December. In all cases the object was observed in at least 2 grating settings, and for about 90% of the objects 3 grating settings were employed. Each grating setting covers ~ 0.12 μm with a scale of 0.0006 μm pixel^{-1}. The slit width of 4 pixels, or 0.″67, corresponds to a spectral resolution of $R \equiv \lambda/\Delta\lambda \approx 1100$, corresponding to $\sim$280 km s^{-1}. The grating settings were chosen to cover the Paα line at 1.8751 μm, the suite of Brδ, H_2 1–0 S(3) and [Si VI] lines centered at 1.954 μm, and if a third setting was used, the H_2 1–0 S(1) and Brγ lines centered at 2.14 μm. The slit was generally rotated to coincide with the major axis of the ULIRG, where evident, or such that spectra of a secondary nucleus was simultaneously obtained when possible.

Typically, integration times were 1800 s at each grating setting, with the object alternately displaced along the slit such that sky integrations were obtained simultaneously. Wavelength calibration was provided by a combination of OH airglow lines and arc lamp spectra. Atmospheric transmission is compensated by observing the nearly featureless spectra of G V stars, and the spectrum divided by a Planck curve of appropriate temperature. The Brγ absorption feature in the G star is removed by interpolation. Other minor absorption features present in the G star calibration spectrum are removed using a template spectrum from Kleinmann & Hall (1986). Spectral extractions, centered on the primary nucleus of each ULIRG, were chosen to match the seeing at the time of observation, typically 0.″8–1.″2. Extractions on the secondary nuclei, when applicable, were performed in the same manner. A more detailed description of the observations and data reduction procedures can be found in Murphy et al. (2000) (Chapter 2), in which the individual spectra are also presented.

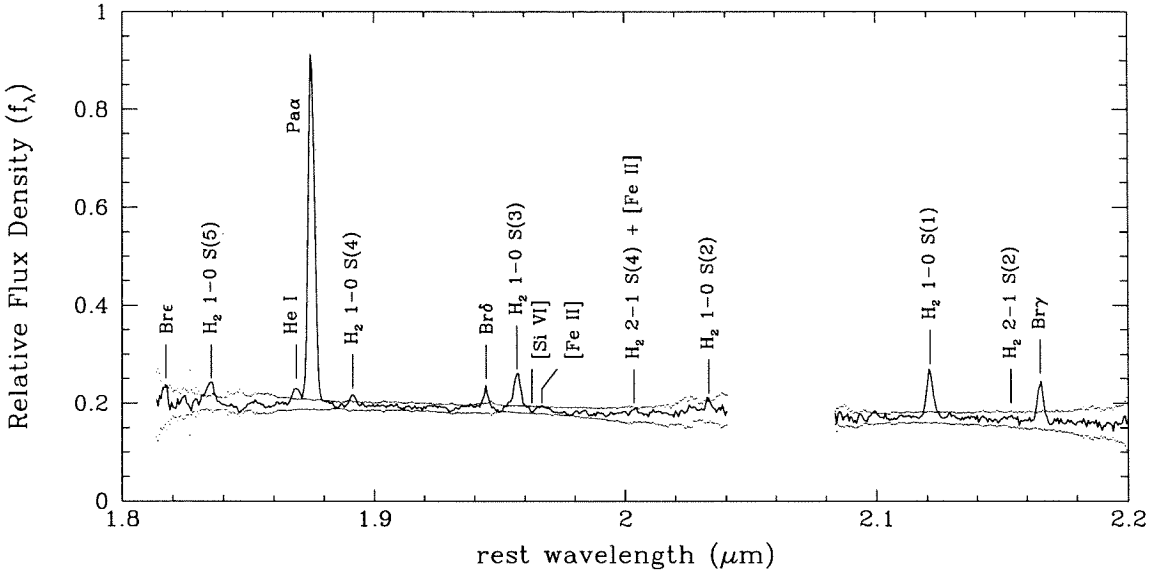

Figure 3.1: Median ULIRG spectrum, composed of 31 ULIRGs showing no evidence for AGN activity in their individual spectra. Paα dominates the K band spectrum, with strong contributions from molecular hydrogen and from other atomic recombination lines. There is no evidence for broad Paα emission or for the [Si VI] line in the combined spectrum. A 3σ envelope about the continuum level is provided for reference. The median spectrum is not displayed for wavelength regions in which fewer than five ULIRG spectra are available for combination.

3.5 Results

The most striking property of the collection of ULIRG spectra is that, with a few notable exceptions, there exists remarkable similarity among the vast majority (31 of 33) of spectra of galaxies in the sample. This similarity prompted us to combine all the similar spectra into a single, representative composite ULIRG spectrum. It is our belief that this composite spectrum provides an accurate representation of the typical ULIRG spectrum.

Figure 3.1 shows the median of spectra from 31 of the ULIRGs normalized to their continuum level, and shifted in wavelength corresponding to the redshift of Paα. The objects selected to be included in the combination were chosen to show no obvious evidence for broad lines or high excitation lines based on inspection of the individual spectra. Combining the spectra facilitates identification of any faint features that might be commonly present but with low signal to noise ratio in individual spectra.

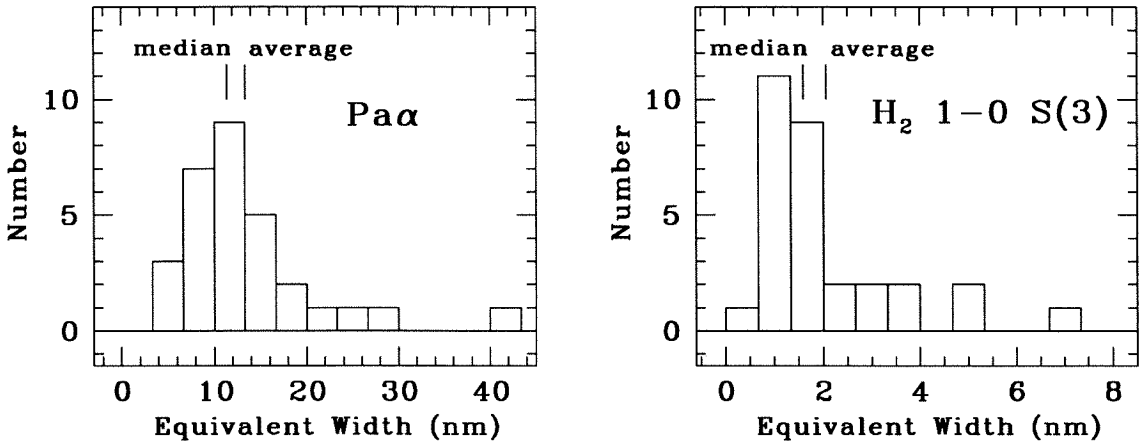

Figure 3.2: Distribution of equivalent widths for the Paα and H_2 1–0 S(3) lines, representing the ULIRGs that comprise the median spectrum in Figure 3.1. The median and average equivalent width values are marked in each of the histograms.

An average spectrum was also generated, the features of which are indistinguishable from those in the median spectrum. Specific properties and identifications of the lines in the median spectrum are discussed in Section 3.5.1.

Figure 3.2 demonstrates the range of line strengths seen in the ULIRG sample in the form of equivalent widths of the Paα and H_2 1–0 S(3) lines. Most of the ULIRGs lie within roughly one bin-width of the median value, as displayed in Figure 3.2, though there are a number of outliers with significantly higher equivalent widths than the median value. We do not find any correlation between the Paα and H_2 equivalent widths.

A median spectrum of 13 secondary ULIRG nuclei has also been constructed for the purpose of comparing the properties of primary and secondary nuclei. While two of the secondary nuclei exhibit featureless spectra, the median spectrum shows that secondary nuclei tend to be spectroscopically similar to the primary ULIRG nuclei. In general, all of the spectral features visible in the primary nuclei (i.e., Figure 3.1), with the exception of the He I line, are visible in the median spectrum composed of secondary ULIRG nuclei, though with lower equivalent widths.

3.5.1 Median Spectrum Line Properties

3.5.1.1 Atomic Recombination Lines

As can be seen in Figure 3.1, Paα emission dominates the near-infrared spectrum of the typical ULIRG. Other recombination lines of hydrogen, specifically Brγ, Brδ, and Brϵ are also readily seen in the median spectrum. The extinction to the line emitting region can be crudely estimated from the ratio of the Paα and Brγ lines. The reddening derived in this way from the median spectrum is $A_V = 5$–10 mag. There is some evidence that the extinction is higher in the secondary ULIRG nuclei.

The weak line at 1.869 μm is identified with a pair of He I recombination lines at 1.8686 μm and 1.8697 μm, with a centroid at 1.8689 μm. We have found that this line is comparable in strength to the He I line at 2.058 μm. Because of the small separation between the Paα line and the He I line, at lower spectral resolution this line might be confused with a blue wing of the Paα line.

3.5.1.2 Molecular Hydrogen Lines

Vibration-rotation lines of H_2 are also prominent in the median spectrum. The H_2 1–0 lines S(1), S(3), S(4), and S(5) are clearly present in the median spectrum and the S(2) line is evident at low significance. There is marginal evidence for the H_2 2–1 S(2) and S(4) lines in the median spectrum, but these are at very low significance. The observed H_2 spectrum is consistent with purely thermal excitation at a temperature of $T = T_{vib} = T_{rot} \sim 2500$ K. At this temperature, contributions to the spectrum from H_2 6–4 O(5) and 7–5 O(3) at 1.8665 and 1.8721 μm, potential contributors to the blue wing of Paα (e.g., Veilleux et al., 1999), are of negligible significance. The appearance of line emission at the position of the 2–1 S(4) line is inconsistent with the apparent weakness of the 2–1 S(2) line, suggesting the presence of [Fe II] at 2.0024 μm. This possibility is further discussed below.

At a spectral resolution of 280 km s^{-1}, the H I lines appear to be spectrally unresolved in the median spectrum of Figure 3.1. The H_2 lines, on the other hand, appear to have a broader spectral profile, especially evident near the bases of these

lines. Random velocity offsets between the H I and H_2 line emission would indeed tend to broaden the H_2 lines when using Paα as the redshift reference for the combination. However, when the H_2 lines themselves are used as the redshift reference, the H_2 profiles are seemingly uneffected, with no apparent broadening of the Paα profile.

3.5.1.3 Iron Lines

A faint line appears in the median spectrum at 1.967 μm, close to the wavelength of [Si VI] at 1.963 μm. We do not identify this line with the [Si VI] line for two reasons. First, in one object we directly detect the [Si VI] line correctly centered at 1.963 μm (see below). In addition, there is a matching line from [Fe II] at 1.967 μm. Such a feature is consistent with the known strength of [Fe II] lines in starburst galaxies of lower luminosity. This identification would imply that the [Fe II] 1.644 μm and 1.258 μm lines should be present at much greater strength in these spectra. While such observations are limited there is evidence, e.g., Veilleux et al. (1997) that such strong Fe lines are common in ULIRGs. The presence of the 1.967 μm [Fe II] line also supports the existence of the suspected [Fe II] line at 2.0024 μm, coincident with the H_2 2–1 S(4) line. The 2.0024 μm [Fe II] line is expected to be two to three times weaker than the line at 1.967 μm, which is consistent with the observed low-level line at 2.003 μm being a blend of [Fe II] and H_2 lines.

3.5.2 ULIRGs with AGN Properties

In Figure 3.3, we show spectra of the two objects in the sample where evidence of AGN associated spectral features is clearly present in the individual object spectra. While the spectra of these two galaxies have characteristics not found in the median spectrum, these spectra are still quite similar in appearance to the median spectrum of Figure 3.1.

The near-infrared spectrum of IRAS 08311−2459 ($z = 0.1006$), presented in Figure 3.3, shows a strong, and slightly broad [Si VI] line along with the H I recombination lines and H_2 lines. The strength of the [Si VI] line is quite unusual for ULIRGs in

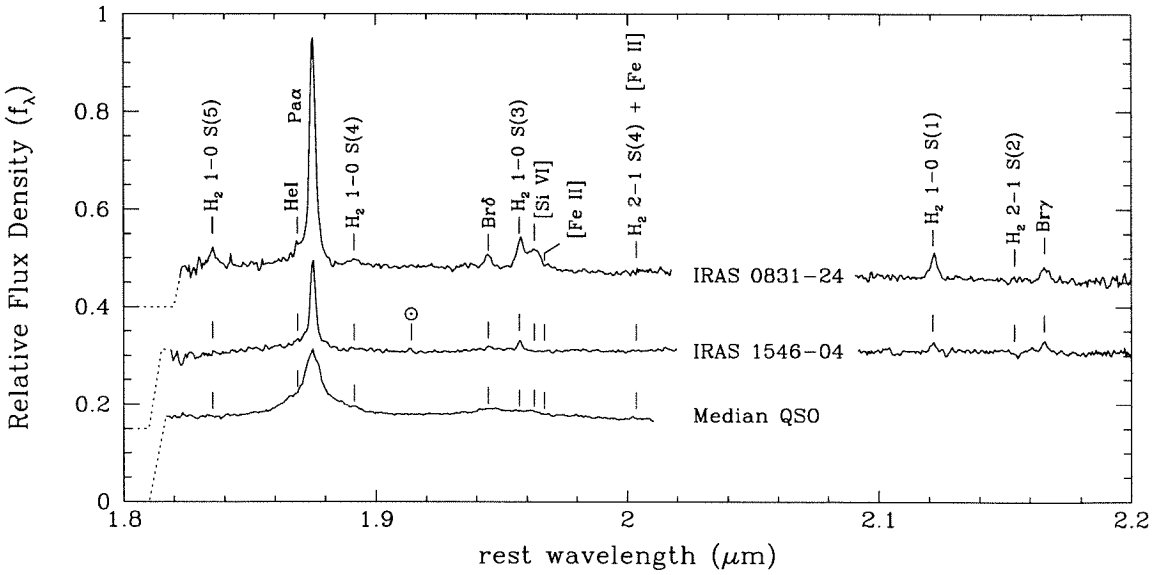

Figure 3.3: Individual spectra of the two ULIRGs in the sample showing some signs of AGN activity. IRAS 08311−2459 has a strong [Si VI] detection plus a low-level broad blue wing on the Paα line. IRAS 15462−0450 shows a broad base on the Paα line, though no evidence for [Si VI] emission. The median quasar spectrum is provided as a reference, showing both the broad Paα and [Si VI] emission features. The line at λ1.914 μm in the spectrum of IRAS 15462−0450 is a residual from Mg absorption in the G star atmospheric calibrator. The zero flux density "floors" for the three spectra lie at the values 0.4, 0.15, and 0.0 on the vertical axis, ordering the spectra from top to bottom.

general, being roughly equal in strength to the H_2 1–0 S(3) line. The presence of the [Si VI] line directly demonstrates the existence of high energy photons since the ionization potential of Si^{5+} is 167 eV. IRAS 08311−2459 also shows the suggestion of a broad Paα base with an asymmetric blue wing that is not consistent with being a He I recombination line. This appears to be a high velocity component of the H I line.

The near-infrared spectrum of IRAS 15462−0450 ($z = 0.1003$), presented in Figure 3.3, shows a broad component of Paα in addition to the strong narrow component of this line, as well as evidence for the He I line. There is no evidence for the [Si VI] line in the spectrum, though the H_2 1–0 S(3) line is clearly present.

For comparison, a median quasar spectrum is included in Figure 3.3. This spectrum is composed from ten quasars ranging in redshift from $z = 0.089$–0.182, observed with the same instrument and in the same manner as that described above for the ULIRGs. The median quasar spectrum is dominated by broad Paα emission, though a velocity-broadened blend of Brδ, H_2 1–0 S(3), and [Si VI] can also be discerned. The [Si VI] line appears to be comparable in strength to the H_2 1–0 S(3) line, as is also the case for IRAS 08311−2459.

3.6 Discussion

The most direct result from this work is that the great majority of ULIRGs (31 of 33) show no indication of AGN activity when viewed at 2 μm with relatively high spectral resolution and sensitivity. Of the 33 objects observed, 90% have luminosities $L_{ir} < 2 \times 10^{12} L_{\odot}$ and of these nearly all (29/30) lack spectroscopic evidence for broad line regions or high energy photons. In the 3 objects with $L_{ir} \geq 2 \times 10^{12} L_{\odot}$, one shows spectroscopic evidence of AGN activity. While lacking the numbers to make a statistically significant argument, this fraction is consistent with findings in previous near-infrared spectroscopic surveys, even though our resolution and sensitivity is higher than the previous studies (Veilleux et al., 1997, 1999).

Where evidence for AGN activity is present, it is readily detectable in the individual spectrum, and spectroscopic evidence for the AGN activity is also present

in the visible light spectrum of the object. IRAS 15462−0450 is classified as a Seyfert 1 system based on its visible spectrum, while our unpublished observations of IRAS 08311−2459 show that it has a Seyfert 2 visible spectrum. Lutz, Veilleux, & Genzel (1999) also report that ULIRGs showing infrared signatures of the AGN phenomenon are usually classified as active galaxies based on their visible light spectra. The converse statement—that all ULIRGs showing no evidence for AGN activity in their near-infrared spectra are optically classified as non-active galaxies—seems also to be supported. Of the 16 non-AGN ULIRGs in the present sample with available optical spectroscopic identifications, only one (IRAS 14394+5332) is characterized as a Seyfert galaxy based on a marginally high [O III]/Hβ ratio (Kim, Veilleux, & Sanders, 1998). While this galaxy does exhibit a blue wing on the H I and H_2 lines, there is no corresponding emission redward of the unresolved narrow line component. We therefore do not associate this velocity structure with a massive compact central source, but rather with organized gas motion, such as might be found in outflow phenomena.

The median spectrum of the ULIRGs that do not show evidence for AGN activity presents an important new result, i.e., there are not faint broad or high excitation lines present in the spectra that are not detected in the individual spectra. The relative H I and H_2 line strengths in the AGN and median spectra are quite comparable, while the limits on the strength of a broad component of Paα or [Si VI] 1.963 μm are at least an order of magnitude less in the median spectrum than in the individual sources with AGNs clearly evident. Furthermore, no luminosity-dependent spectroscopic trends are seen in the 31 non-AGN ULIRGs when the spectra are divided into subsets and median-combined in separate luminosity bins. In particular, there is no more evidence for low-level broad Paα in the higher luminosity ULIRGs than there is in the lower luminosity sets or in the collection as a whole. These findings can be explained in several ways. Most obviously it could be that there are simply not AGN associated with the ULIRGs where such features are not obvious. This would imply that for $L_{ir} < 2 \times 10^{12} L_{\odot}$, only a very small fraction of ULIRGs are powered by AGNs. Presumably the power source in these cases is star formation in extremely compact star forming regions. Alternatively, if all these sources harbor an AGN it could be

that the fraction of sources with visible spectroscopic evidence for AGN activity is a measure of geometric effects, i.e., there are highly attenuating dust tori with $A_{Pa\alpha}$ >2.5 mag covering > 90% of the sky from the central source. Other more carefully contrived configurations of dust are also possible. While we cannot conclusively argue one way or another, the highly sensitive survey we have conducted for dust enshrouded AGN, combined with other such surveys at other wavelengths, is providing mounting evidence that star formation is powering the vast majority of ULIRGs with $L_{ir} < 2 \times 10^{12} L_{\odot}$.

We thank Michael Strauss for his role in defining the sample of ULIRGs, and for participating in the early stages of the Caltech effort in studying ULIRGs. We also thank Gerry Neugebauer for helpful discussions. Many persons accompanied us on the observing runs to Palomar, most notably Rob Knop and James Larkin, both of whom provided expert tutelage on the use of the spectrograph, and on methods of data reduction. We thank the night assistants at Palomar, Juan Carasco, Rick Burruss, Skip Staples, and Karl Dunscombe for their assistance in the observations. T.W.M. is supported by the NASA Graduate Student Researchers Program, and the Lewis Kingsley Foundation. This research is supported by a grant from the National Science Foundation.

Bibliography

Carico, D. P., Graham, J. R., Matthews, K., Wilson, T. D., Soifer, B. T., Neugebauer, G., & Sanders, D. B. 1990, *Astrophysical Journal*, 349, L39

Genzel, R., et al. 1998, *Astrophysical Journal*, 498, 579

Kim, D.-C., Veilleux, S., & Sanders, D. B. 1998, *Astrophysical Journal*, 508, 627

Kleinmann, S. G., & Hall, D. N. B. 1986, *Astrophysical Journal Supp. Series*, 62, 501

Larkin, J. E., Knop, R. A., Lin, S. Matthews, K., & Soifer, B. T. 1996, *Publ. of the Astron. Soc. of the Pacific*, 108, 211

Lutz, D., Veilleux, S. & Genzel, R. 1999, *Astrophysical Journal*, 517, L13

Murphy, T. W., Armus, L., Matthews, K., Soifer, B. T., Mazzarella, J. M., Shupe, D. L., Strauss, M. A., & Neugebauer, G. 1996, *Astronomical Journal*, 111, 1025

Murphy, T. W., Soifer, B. T., Matthews, K. et al. 2000, in preparation, Chapter 2, this thesis

Nakagawa, T. et al. 1999, Kyoto IAU Symposium 186, abstract S186-103T

Rieke, G. H., & Lebofsky, M. J. 1985, *Astrophysical Journal*, 288, 618

Rieke, G. H. 1988, *Astrophysical Journal*, 331, L5

Sanders, D. B., Soifer, B. T., Elias, J. H., Madore, B. F., Matthews, K., Neugebauer, G., & Scoville, N. Z. 1988, *Astrophysical Journal*, 325, 74

Smith H. E., Lonsdale C. J., & Lonsdale, C. J. 1998, *Astrophysical Journal*, 492, 137

Soifer, B. T., Neugebauer, G., Matthews, K., Egami, E., et al. 2000, *Astronomical Journal*, 119, 509

Soifer, B. T., Sanders, D. B., Madore, B. F., Neugebauer, G., Danielson, G. E., Elias, J. H., Lonsdale, C. J., & Rice, W. L. 1987, *Astrophysical Journal*, 320, 238

Strauss, M. A., Davis, M., Yahil, A., & Huchra, J. P. 1990, *Astrophysical Journal*, 361, 49

Strauss, M. A., Huchra, J. P., Davis, M., Yahil, A., Fisher, K. B., & Tonry, J. 1992, *Astrophysical Journal Supp. Series*, 83, 29

Veilleux, S., Sanders, D. B., & Kim, D. -C. 1997, *Astrophysical Journal*, 484, 92

Veilleux, S., Sanders, D. B., & Kim, D. -C. 1999, *Astrophysical Journal*, 522, 139

Chapter 4 Motivation for Integral Field Spectroscopy

4.1 Introduction

This chapter presents the scientific motivations behind the construction of the Palomar Integral Field Spectrograph (PIFS), and provides a logical transition from the longslit work on ULIRGs to the integral field work that follows. In addition, the concept of integral field spectroscopy is introduced, and various potential uses beyond the scope of ultraluminous infrared galaxies are briefly presented.

4.2 Integral Field Spectroscopy

Integral field spectrographs, which obtain spectra simultaneously for all spatial resolution elements in an area on the sky, are only now being introduced for astronomical spectroscopy. Astronomers are eager to embrace this new approach to spectroscopy, which was made very clear during the Imaging the Universe in Three Dimensions conference in March of 1999. Though very few actual instruments of this type exist to date, the 3D spectrograph of the Max Planck Institute (Weitzel, 1994; Weitzel et al., 1996) in Garching has shown the power of such an instrument when used at near-infrared wavelengths (Genzel et al., 1995, 1996; Kroker et al., 1996; Tecza et al., 2000).

Integral field spectrographs differ from traditional longslit spectrographs in a single, fundamental way. Rather than admitting light through a slit, integral field spectrographs rearrange the light falling onto a two-dimensional focal plane into a pattern *resembling* a long slit. The artificially constructed—and sometimes virtual—slit is passed to a spectrograph of traditional design. Longslit spectrographs convolve any

spatial structure existing across the narrow dimension of the slit with spectral information. Slits are typically chosen to be narrower than any expected spatial structure (e.g., seeing limit or diffraction limit) in order to avoid the ambiguity introduced by this convolution. As such, longslit spectra represent a single dimension of spatial information. Integral field spectrographs, by rearranging the two-dimensional focal plane into a one-dimensional geometry preserve the full two-dimensional spatial nature of the source, while providing spectral information from each position in the field.

The resulting product of an integral field observation is a "datacube," with two spatial and one spectral dimension. Datacubes can be obtained by other, more traditional techniques, such as stepping a longslit across an object, or tuning a Fabry Perot imager across a range of wavelengths. Integral field spectroscopy, besides the obvious efficiency gains, offers a critical advantage over these sequential techniques—simultaneity. Variations in seeing, photometric conditions, airmass, etc., plus imprecision in telescope pointing or etalon tuning limit the sequential techniques in very fundamental ways. In fact, variable conditions can make it impossible to stitch together a set of sequential observations in a meaningful way. By gathering all the spatial and spectral information at the same time, very subtle features in the data may be investigated. In addition, one becomes sensitive to the discovery of unexpected phenomena. Examples of the more unique capabilities of integral field spectrographs include:

- Discerning small spatial offsets between continuum and line emission
- Discerning small spatial offsets between emission lines of different species or radial velocities
- Measuring subtle differences in the spatial extents of different emission line species
- Determination of rotation with arbitrary position angle
- Serendipitous identification of line emission in the field

4.3 Scientific Motivation

The two-dimensional spectra of ultraluminous infrared galaxies (ULIRGs) presented in Chapter 2 contain a wealth of complex information that is not exploited in the longslit survey. Given the spatial complexity prevalent among ULIRGs, it may be hopeless to embark on such a task with only one spatial dimension. Even measurements of total line flux are impossible given the inadequacy of a single slit to capture the non-trivial two-dimensional spatial structure. ULIRGs do not always exhibit well-behaved velocity fields in the single-slit spectra, and those that do often reveal unexpected deviations from this picture when viewed in more dimensions.

4.3.1 ULIRGs

Ultraluminous infrared galaxies represent the largest population of objects in the local universe with luminosities $L_{bol} > 10^{12} L_{\odot}$. As a result of the disruptive galactic encounter, the gas within these galaxies is perturbed from normal circular motions, and often collects in the centers of host galaxies. It is this concentration of gas that provides the fuel source for the powerful processes taking place behind the veil of dust. Once active, the power source often has a profound effect on the local interstellar medium of the remnant galaxy. Ionization fronts, jets, and large scale, fast outflows called superwinds are all seen in these objects.

Investigating the dynamics of the complex environment of a central starburst/AGN interacting with an exceedingly high concentration of gas and dust, such as exists in ULIRGs, is an ideal task for a high spatial resolution near-infrared spectrograph such as the PIFS. Longslit spectra of ULIRGs (Chapter 2) taken with the Palomar Longslit Infrared Spectrograph (PLIS) (Larkin et al., 1996) offer tantalizing glimpses of the complex spatial structures that exist in the emission nebulae of these objects. These data make it clear how much better a physical picture we would obtain with spectral information over the full two-dimensional extent of these galaxies.

Possible scenarios of gas kinematics that may be understood via integral field spectra include the following important classes of motion. Gaseous infall is at the heart

of the ULIRG phenomenon, from the standpoint that very high concentrations of gas and dust are seen in the nuclear regions of ULIRGs, providing the copious fuel needed to power these luminous sources. As alluded to earlier, outflow phenomena have been observed in ULIRGs as well, possibly stemming from explosive energy releases of supernovae in regions of intense star formation activity. Rotation is a ubiquitous property of all disk galaxies, and any residual rotation signature in the parent galactic nuclei could potentially help solve issues of orientation and merger geometry. Finally, one must be prepared to see seemingly random gas motions attributable to the complex interactions of two overlapping galaxies. Certainly some of the longslit spectral data have peculiar properties that are not immediately identifiable as one of the organized motions described above. Adding an extra dimension of information may in some cases complicate the picture, but our hope is that the additional information will enable a better understanding of the processes responsible for the gas kinematics of ULIRGs.

4.3.2 Example Longslit Data

Chapter 2 presented two-dimensional spectral data around the Paα line for the 33 ULIRGs of the survey (Figure 2.3). Most of these spectra are dominated by nuclear emission, with the exception of IRAS 04232+1436 and IRAS 20046−0623. Even so, many of the ULIRGs have diffuse, extended line emission. Often this emission appears carry a rotation signature, but some cases are not easily classified in this way.

Figure 4.1 presents three additional spectra not seen in Chapter 2. This figure presents K_s images with slit positions indicated, together with the two-dimensional spectra corresponding to those slit locations. Spectra for two different slit positions are presented for IRAS 01521+5224. This galaxy, whose spectrum appeared in Chapter 2 at yet a third position angle, is also featured in Chapter 7, in which the full merger geometry is deduced. It is obvious from the K_s band image of IRAS 01521+5224 that complexity reigns in this galaxy, with two primary nuclei visible and many low surface brightness clumps and streamers extending in many directions. The two spectra, each

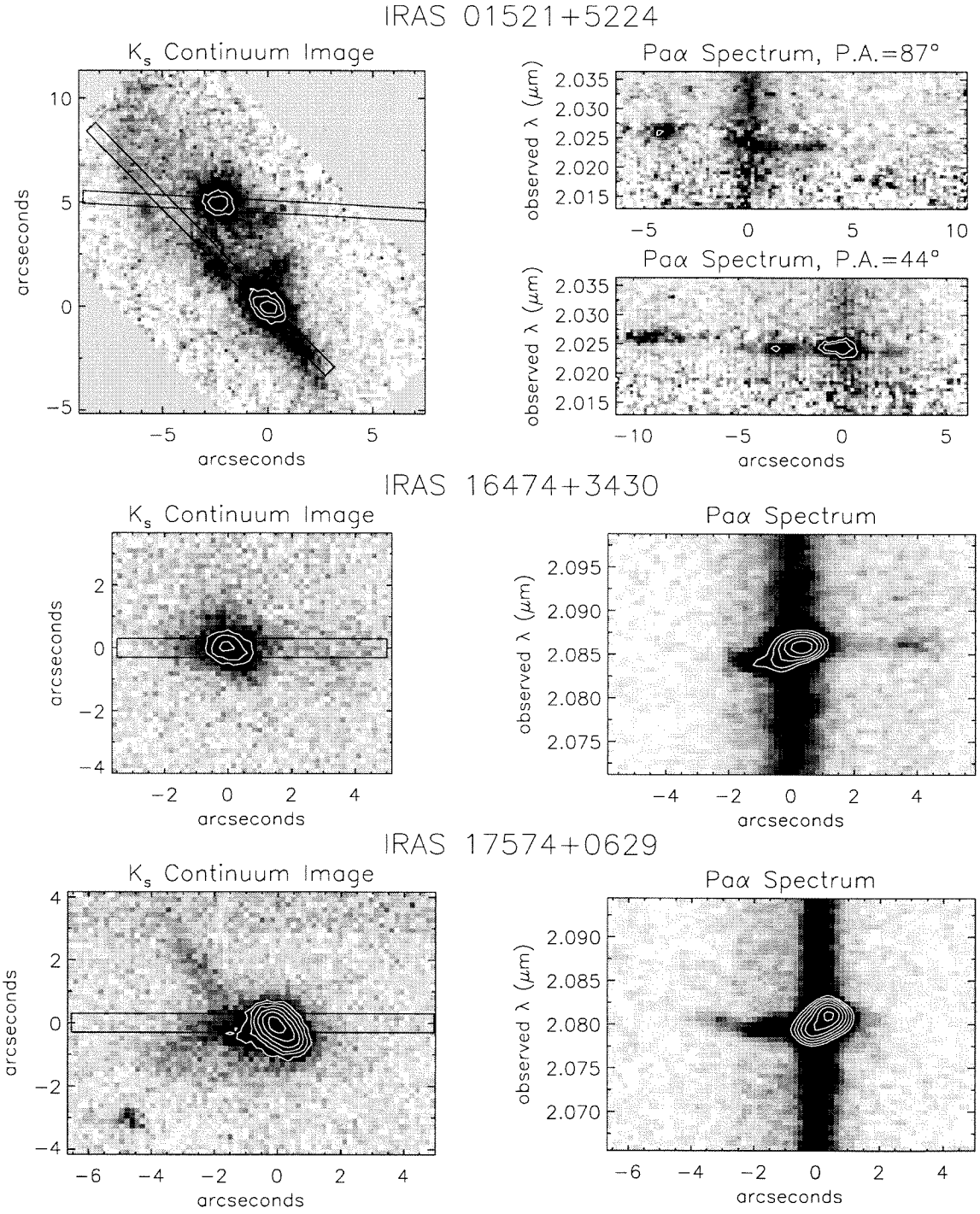

Figure 4.1: Images and longslit spectra for three ULIRGs, indicating the spatial complexity, the differing distribution of continuum and line emission, and the presence of velocity information. Details of the individual galaxies are discussed in the text. The top image is oriented with north up and east to the left, while the others are rotated for horizontal slit placement.

passing through one of the nuclei, show a similarly clumpy line emission distribution, with velocity information clearly visible as well. Understanding the nature and state of this system based on the longslit data is at best a serious challenge. The view that the integral field technique offers is a radical improvement, as will be seen in Chapter 7.

IRAS 16474+3430 is less complex than the previous example, but still harbors surprises in the spectral domain. The K_s image of this galaxy is not of high quality, with better imaging to be found in Murphy et al. (1996). The slit orientation is at a position angle of 160°, with north towards the right and east just left of the upward direction. In the spectrum, one sees Paα extended to the left of the continuum as well as far to the right. The peak emission is offset to the right of the continuum center. The velocity structure has the appearance of rotation, with extended emission to either side tying into the curve, possibly representing the outer circular velocity of the parent disk. With the offset line emission and the large extent of the line emitting nebula, this galaxy would be a good candidate for study with an integral field device.

IRAS 17574+0629 is morphologically typical of ULIRGs, with a single, distorted nucleus surrounded by diffuse, arcing structures resembling tidal tails. The K_s image in Figure 4.1 has the slit at a position angle of 51°, with north to upper left and east to lower left. The spectrum shows a substantial amount of off-nuclear emission, with a peculiar kink in the velocity gradient about 2.″5 to the left of the continuum center. The dominant nuclear emission, as with the previous example, is offset from the continuum. This emission has a velocity gradient in the opposite sense of the gradient seen at far left in the diffuse emission. The peculiar Paα emission to the left is associated with a region that does not particularly stand out in continuum light, making one wonder what the rest of the diffuse continuum region looks like in line emission. Integral field data for this galaxy is presented in Chapter 7.

These examples are meant to illustrate the potential utility of an integral field device in understanding ULIRG gas kinematics, especially in light of the incomplete picture offered by the longslit data. Tantalizing spectra like those presented here, together with examples from Chapter 2, are what drove the effort to develop the PIFS instrument. It was not immediately clear at the outset what we might find, but it was

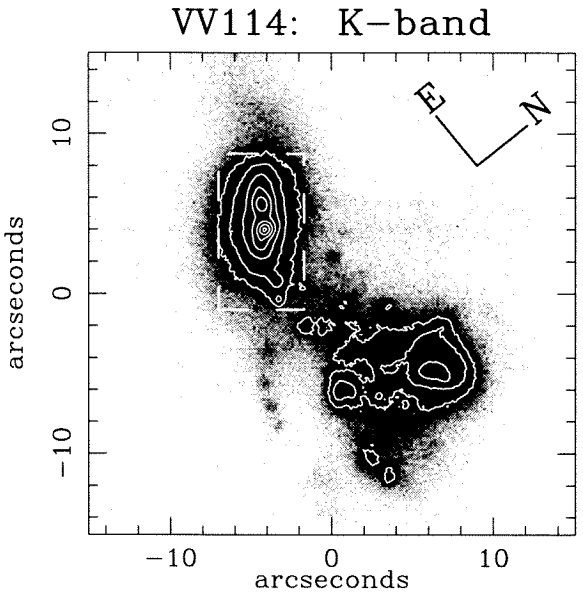

Figure 4.2: K band image of VV 114. The dashed box represents the size of the PIFS field of view.

clear that more spatial information would be necessary to have any reasonable chance for success at understanding the gas motions in these very complex systems.

4.3.3 Other Scientific Applications

Luminous infrared galaxies (LIRGs), like their ultraluminous cousins, are often found in interacting systems which generate complex dynamical environments much like those found in ULIRGs. While the main scientific objective of the PIFS instrument is understanding the processes associated with the most luminous galaxies in the universe, the instrument is equally well suited to the detailed study of the very similar LIRGs. With 20–30 times the local space density of ULIRGs, LIRGs are often found at much closer distances, allowing higher spatial resolution and access to weaker emission lines. These dusty systems can be studied in recombination lines of hydrogen (Paα, Brγ), as well as lines of H_2 (1–0 S(1), 1–0 S(3), etc.), and [Fe II] $\lambda 1.644 \mu$m. Using these lines, one may attempt to characterize the distribution, rate, and age of star formation, relating this activity to the local dynamics of the galaxies.

An example of a system where the PIFS will be able to provide a detailed picture of the complex environment of an interacting high luminosity starburst galaxy is

VV 114. A 2μm continuum image of this interacting galaxy system obtained at the Keck Observatory is shown in Figure 4.2. The image shows many isolated clumps of emission thought to be recently formed stellar aggregates. This galaxy represents a testbed for the process of star formation in violently interacting galaxies. The nuclear separation in VV 114 is still large enough for us to explore the starburst and the merger separately. Longslit spectra of VV 114 at a resolution of $R \approx 1000$ taken with the PLIS at a few position angles show strong lines such as Brγ, H_2, and [Fe II] emission extended over the face of the system, with clear velocity gradients along the slit. High spatial resolution studies of this galaxy can usefully probe the spatial extent of the starburst on a sub-kiloparsec scale. With a small number of pointings, a fully sampled spatial and velocity distribution of the strong infrared emission lines in VV 114 can be obtained to determine how the starburst is developing over this interacting galaxy system.

Other applications of integral field spectroscopy that are compatible with the design parameters of the PIFS are studies of the circumnuclear regions of Seyfert galaxies, the examination of spatial and kinematical structure in high redshift radio galaxies, and applications involving spectrophotometry, wherein it is important to capture all of the light from a source, while maintaining adequate spectral resolution.

Bibliography

Genzel, R., Weitzel, L., Tacconi-Garman, L. E., Bleitz, M., Krabbe, A., & Lutz, D. 1995, *Astrophysical Journal*, 444, 129

Genzel, R., Thatte, N., Krabbe, A., Kroker, H., & Tacconi-Garman, L. E. 1996, *Astrophysical Journal*, 472, 153

Kroker, H., Genzel, R., Krabbe, A., Tacconi-Garman, L. E., Tezca, M., Thatte, N., & Beckwith, S. V. W. 1996, *Astrophysical Journal*, 463, L55

Larkin, J. E., Knop, R. A., Lin, S., Matthews, K., & Soifer, B. T. 1996, *Publ. of the Astron. Soc. of the Pacific*, 108, 211

Murphy, T. W., Armus, L., Matthews, K., Soifer, B. T., Mazzarella, J. M., Shupe, D. L., Strauss, M. A., & Neugebauer, G. 1996, *Astronomical Journal*, 111, 1025

Tecza, M., Genzel, R., Tacconi, L. J., Anders, S., Tacconi-Garman, L. E., & Thatte, N. 2000, *Astrophysical Journal*, sumitted (astro-ph/0001424)

Weitzel, L., PhD thesis, Ludwig-Maximilian-Universitat, Munich

Weitzel, L., Krabbe, A., Kroker, H., Thatte, N., Tacconi-Garman, L. E., Cameron, M., & Genzel, R. 1996, *Astronomy & Astrophysics Supplements*, 119, 531

Chapter 5 The Palomar Integral Field Spectrograph

5.1 Chapter Overview

We present the design, construction, and performance of a near-infrared integral field spectrograph now in operation at the Palomar Observatory 200-inch Telescope. The spectrograph acts as a front-end to one of two existing infrared cameras, covering the 1–2.5 μm and 1–5 μm wavelength ranges. An all-aluminum image slicer splits the $5.4'' \times 9.6''$ field of view into eight slits, feeding two independent spectrographs within the same dewar. Spectra are simultaneously obtained for all points within the field, with seeing-limited spatial resolution. Two resolution modes of $R \approx 1300$ and $R \approx 600$ are available, as well as a broad-band imaging mode for photometry and target acquisition. The spectrograph was first operated on the 200-inch Telescope in 1998 September. Performance has been as predicted, with a total system throughput of $\sim$22% from the top of the atmosphere to electron counts. Sensitivity is estimated to allow detection of a $K = 18$ mag (0.04 mJy) continuum point source at the 5σ level in one hour of integration at the high resolution setting. Example data from the spectrograph are presented here.

5.2 Introduction

The introduction of large-format infrared arrays in the early 1990s made possible the development of imaging systems with moderate fields of view and spectrographs with good spectral coverage at moderate resolutions. The large arrays also permit the implementation of integral field spectroscopy, wherein spectral information is simultaneously gathered for all points in a two-dimensional field, and recorded on the

two-dimensional array. A single integration thus results in a datacube, with two spatial axes and one spectral axis. This technique was first exploited in the near-infrared by Weitzel et al. (1996), with an instrument called 3D.

The advantages of integral field spectroscopy in generating three-dimensional datacubes go beyond the efficiency aspect of gathering multiple adjacent longslit spectra simultaneously (see Weitzel et al., 1996). The simultaneity itself results in observations that are insensitive to problems associated with variable atmospheric conditions, such as seeing and photometry. Unlike sequentially generated datacubes obtained by either stepping a longslit across the object, or tuning a Fabry-Perot imager to a sequence of wavelength settings, the integral field technique is not effected by lack of precision in telescope pointing or etalon tuning. The simultaneous coverage of continuum and line emission in two dimensions allows subtle offsets and morphological differences to be elucidated. An additional advantage over longslit spectroscopy is that all the flux from the observed object is represented on the array, rather than some portion being lost at the slit. Integral field spectroscopy is particularly useful for observations of morphologically complex objects, especially those with structure in the velocity domain as well.

The Palomar Integral Field Spectrograph was designed primarily for the study of ultraluminous infrared galaxies, though it is also well suited for observations of high-redshift radio galaxies, circumnuclear environments of Seyferts, and quasar host environments.

5.3 Instrument Design

The Palomar Integral Field Spectrograph (PIFS) operates at the tip-tilt corrected $f/70$ focus of the Palomar 200-inch Telescope. It is designed to present an $f/70$ output focal plane to one of two existing infrared imaging cameras. The primary design camera employs a 256×256 HgCdTe (NICMOS 3) array, which operates from 1–2.5 μm. Also available is a 256×256 InSb array camera, permitting operations out to 5 μm. The approach of having separate dewars for spectrograph and camera, while

introducing extra optical elements—and more significantly, a warm window interface—was taken to facilitate a rapid and inexpensive instrument project. The technique has been successfully implemented in the Palomar Longslit Infrared Spectrograph (PLIS) (Larkin et al., 1996), upon which the PIFS design is based. For simplicity, the PIFS design was tailored to fit within the PLIS dewar envelope. This constraint guided the overall size and appearance of the spectrograph, though ultimately the PIFS was housed in its own dewar.

5.3.1 The Image Slicer

A cryogenic image slicer is used to rearrange the two-dimensional focal plane into effectively a long slit. This effective long slit is actually made of smaller sub-slits, which are sliced out of the focal plane. By mapping the two-dimensional focal plane into a pseudo-one-dimensional arrangement, one can disperse light in the cross-slit direction to effectively obtain a spectrum at each position in the two-dimensional field without convolving spatial and spectral information. Figure 5.1 illustrates this concept.

The use of existing cameras to record the spectral image imposes a predetermined pixel scale of 0.167 arcsecond pixel^{-1} for the HgCdTe array camera, which is the assumed camera in all that follows. The total unvignetted field of view of the camera is just under 40″ across. With a slit width of 0.″67 (4 pixels), the total area of a longslit spanning the array is about 25 arcsec^2. In order to double the total field of view, the image slicer is designed to produce two effective longslit outputs, as depicted in Figure 5.1. In doing this, only half the array is available for spectral dispersion of each slit, sacrificing spectral coverage per slit in favor of increased field of view. While a slit width of 0.″33 (2 pixels) would have produced a critically sampled spectral output, the effective field area would be half that attainable with a 4-pixel wide slit. For the PIFS science drivers, field of view is more important than spectral coverage. The final design of the image slicer therefore has a total field of view of $\sim$50 arcsec^2, slicing this field with 0.″67 wide slits, corresponding to a 4 pixel width on the HgCdTe

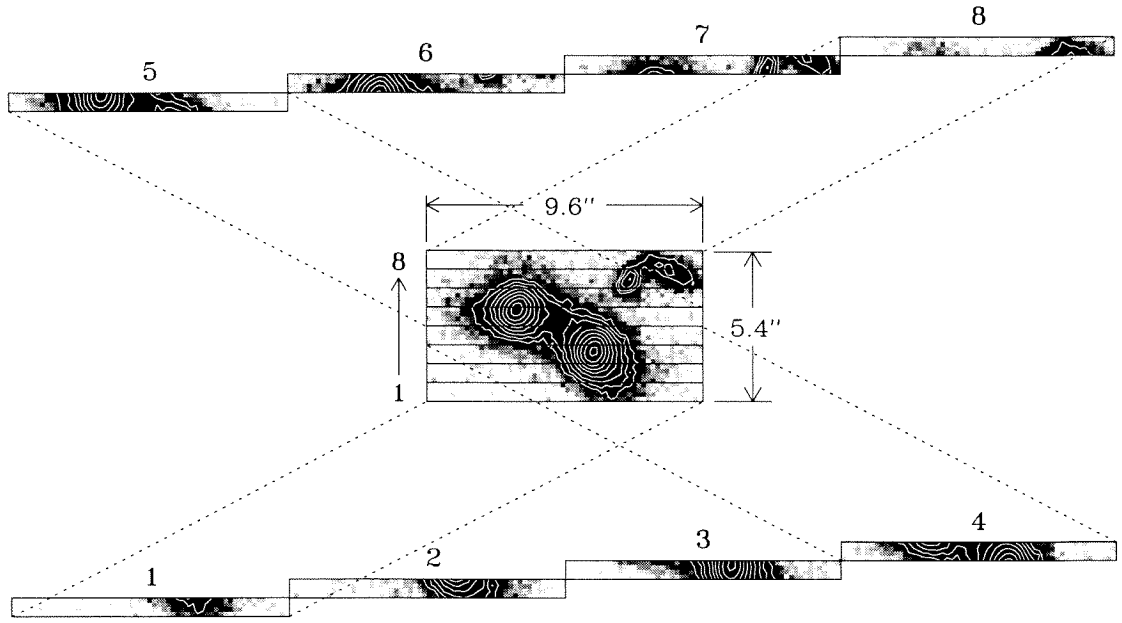

Figure 5.1: Schematic representation of the image slicing concept. The rectangular field is sliced into eight strips, or sub-slits, which are rearranged in an end-to-end configuration such that light from each slit may be dispersed without overlapping. The PIFS image slicer produces two effective long slits, for reasons described in the text.

array camera.

A rectangular field pattern is chosen to provide observational flexibility, and to simplify the image slicer design by reducing the number of sub-slits needed. The $5\farcs4 \times 9\farcs6$ field of view can be rotated to any position angle on the sky by rotating the Cassegrain instrument mount about the telescope optical axis.

The image slicer is constructed entirely out of aluminum alloy #6061-T651. The optical elements have diamond fly-cut reflective surfaces coated with protected silver. The first set of image slicer optics are eight planar facets each measuring 1.17 mm$\times$17.8 mm in size. These facets sit at the $f/70$ focal plane, directing the incident light into eight different directions. Sitting roughly 100 mm away from the focal plane are a second set of planar facets, these being 2.92 mm$\times$17.2 mm in size. Upon reaching these mirrors, the eight slits have separated into two groups of end-to-end patterns, as depicted in Figure 5.1. Each of the second set of mirrors intercepts the light from one of the flat mirrors in the focal plane and sends it toward the spectrograph as if originating from a common pupil at the distance of the telescope secondary mirror.

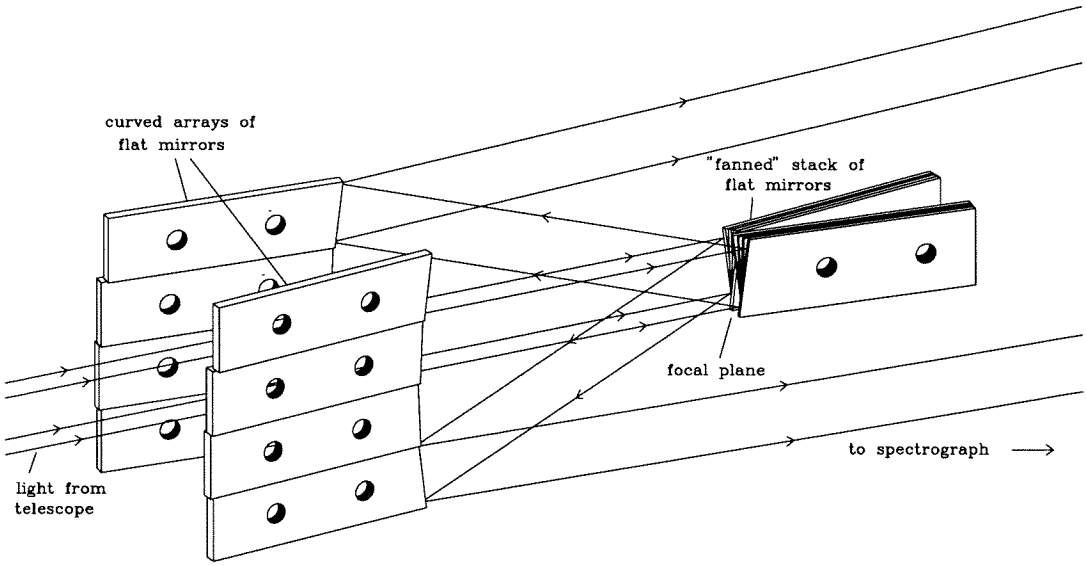

Figure 5.2: Arrangement of image slicer optical elements. The optical elements are aluminum plates, diamond fly-cut on the ends to form optically flat reflective surfaces. The stack of thin mirrors at the focal plane redirects the field onto eight collector mirrors, at left, which send the light towards the spectrograph in the end-to-end pattern depicted in Figure 5.1. The four rays shown illustrate the optical paths for the two outermost slits in the focal plane.

Figure 5.2 depicts the physical arrangement of the end-polished optical elements in the image slicer, and shows the optical paths through the system.

Producing an image slicer with eight separate optical paths yet preserving the $f/70$ pupil to a few percent of the pupil diameter requires angular alignment of each mirror to $\sim$0.1 milliradian. This alignment must be maintained in the cryogenic environment. The technique for fabricating the image slicer optics is such that random alignment errors were minimized. The image slicer optics are then mounted onto a monolithic aluminum fixture, which helps to control random alignment error and provides a homogeneous material environment such that thermal contraction is the same for both fixture and optics.

Each slicer optical element is a thin plate roughly 17 mm$\times$60 mm in size, with a flat optical surface on one end. Each plate has a common set of two pinholes establishing the final position and alignment of the optic on the mounting fixture. One of these holes is centered on each plate near the front—or reflecting—end of the optic. The second pinhole is at the back end, in one corner of each plate. A third pinhole at the

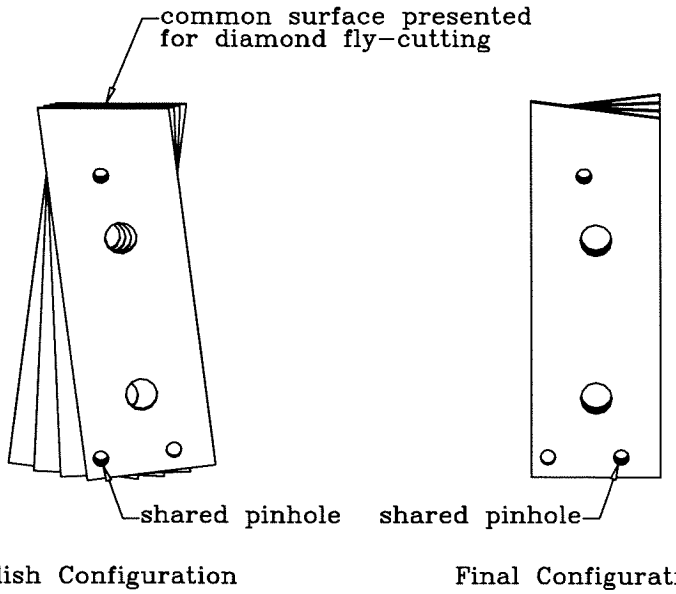

Figure 5.3: The image slicer optics were diamond fly-cut simultaneously in the stack configuration illustrated at left. The final configuration, with a variety of reflector orientations, is shown at right. Precision pinholes used in the fly-cut and final configurations completely determine the relative angles of the reflective surfaces. See text for details.

back end of the plate, in combination with the front, or pivot, pinhole establishes an alternate configuration such that the line between these two pinholes is perpendicular to the optical surface. When all the plates are stacked together with a pair of pins running through this alternate set of pinholes, a single, coplanar surface is presented. A flat surface is diamond fly-cut on the end of this stack to simultaneously produce all of the optical surfaces. The final configuration, established by the pivot pinhole and the common corner pinhole, will then fan the reflecting surfaces out in a variety of angles. The relative angle between surfaces is solely determined by the angle between the three pinholes in any given plate. Thus controlling alignment to $\sim$0.1 milliradian with pinholes separated by $\sim$50 mm requires a pinhole positional accuracy of 5 μm, which is within the reach of an accurate milling machine. Figure 5.3 illustrates the principle involved.

The figure accuracy of the thin focal plane optical elements is measured to be flat to $\sim$200nm, peak-to-valley, while the thicker, more robust second set of elements has a peak-to-valley figure accuracy of $\sim$60nm.

The actual slit pattern produced by the image slicer is not the regular stair-stepped

pattern illustrated in Figure 5.1. Because the image slicer optics are tilted about two axes, which is necessary to separate the two long slits, the image slicer focal plane elements are capable of casting shadows on adjacent elements. The actual order of the slits is rearranged to move the focal plane shadows out to the corners of the field rather than have them near the field center. This is accomplished by selecting the high-angle slices, corresponding to the ends of the long slit, to represent the outer slits in the integral field, thus using the low angle slices for the central part of the field. As a result, the actual longslit pattern, rather than being ordered 1-2-3-4 as shown in Figure 5.1, is ordered 1-4-3-2. This pattern is evident in the raw spectra, seen in Figure 5.5. Note that the arrangement of optical elements in Figures 5.2 and 5.3 would produce the regular stair-stepped pattern of Figure 5.1, and therefore do not represent the actual arrangement of the PIFS image slicer optical elements.

5.3.2 The Spectrograph

The PIFS optical layout is shown in Figure 5.4. Because the image slicer delivers two effective longslits, and because the spectra from each of these must not overlap, two identical spectrographs are housed within the same dewar, one for each of these effective slits. Tunable narrow band interference filters offer another potential solution for separating the two spectra. However, the large range of angles passing through the filter location in the infrared cameras used here result in a lack of uniform spectral coverage across the array. Therefore, the separation of spectra is accomplished by physically separating optical paths.

Referring to Figure 5.4, the $f/70$ beam from the telescope reflects off the tertiary fold mirror and into the cryogenic environment through an anti-reflection coated sapphire window. Another fold mirror directs the beam to a focus at the image slicer. The action of the image slicer is described in Section 5.3.1. Following one of the two effective slits from the image slicer, the beam goes to one of the two identical spectrographs. A 940 mm focal length spherical collimator places an image of the 13 mm pupil on the grating surface. A mirror can be rotated in front of the grating to produce

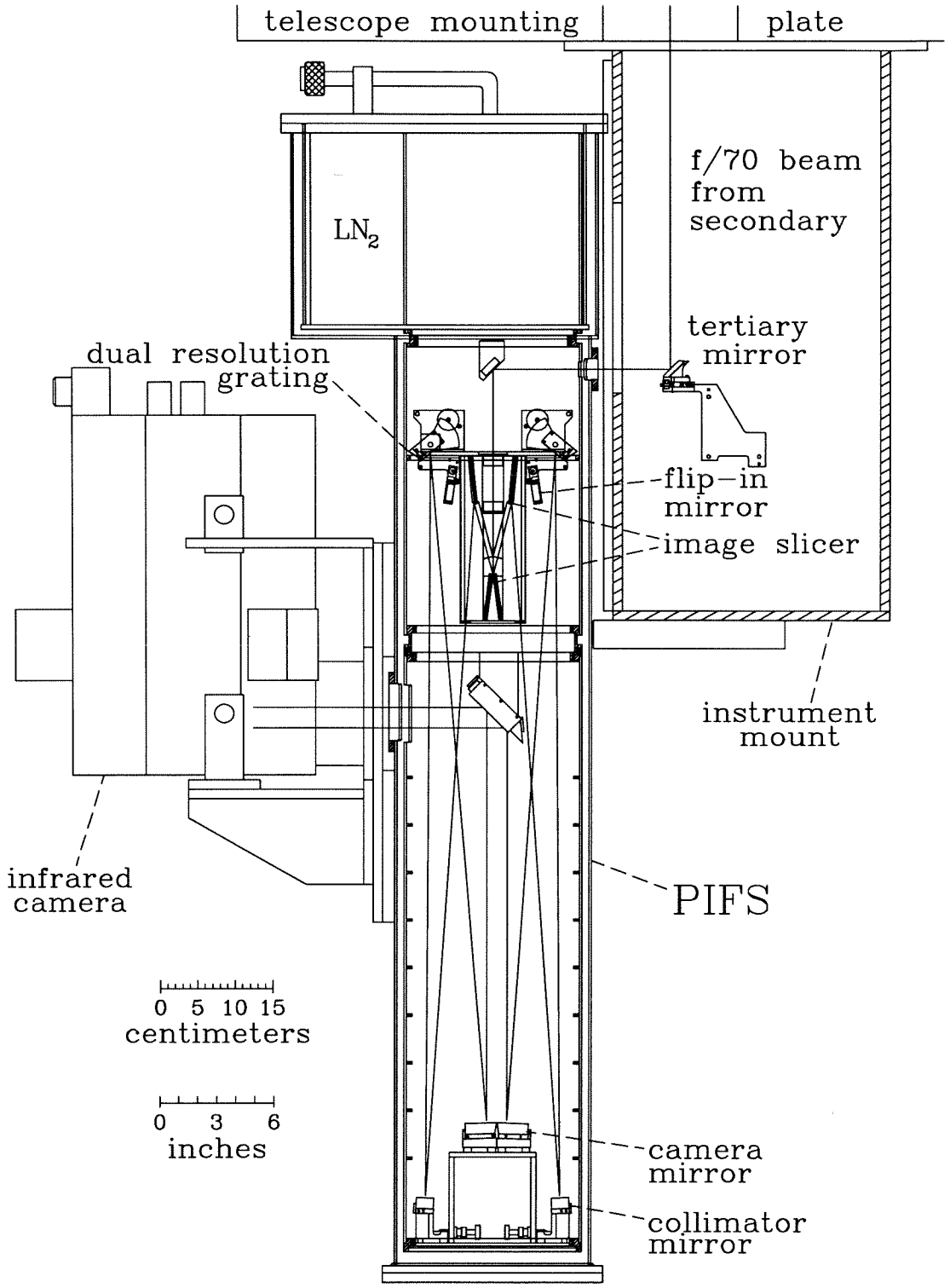

Figure 5.4: The PIFS dewar and optical path. The infrared camera is a separate dewar attached to the PIFS dewar at left.

an image of the slit rather than a spectrum. Because this is a separate mechanism, the grating position is not disturbed during this operation, allowing one to switch between imaging mode and spectral mode without effecting grating reproducibility. For each spectrograph there are two aluminum-coated epoxy replicas affixed to a single aluminum substrate. One of the grating surfaces has a blaze angle of 36.°8 and 300 grooves per mm, providing a spectral resolution of $R \equiv \lambda/\Delta\lambda \approx 1300$. The grating may be rotated via stepper motors in steps of 0.2 milliradians for wavelength selection. Rotating the grating block through $\sim 50°$ moves the second replicated grating surface into the beam, with a blaze angle of 17.°5 and 150 grooves per mm for $R \approx 600$ spectra. From the grating, the beam travels to another spherical mirror, identical in focal length to the collimator mirror. An $f/70$ converging beam is produced, and merging with the beam from the twin spectrograph, is deflected off a fold mirror, exiting through the CaF_2 dewar window en route to the infrared camera. All mirrors except those in the image slicer are overcoated gold on fused silica substrate. Raytracing of the integrated system produces a spot size of <0.05 arcsecond at the camera focal plane.

Order sorting is accomplished via filters within the infrared camera. A 5% circular variable filter (CVF) performs this function for the wavelength range of 1.5–2.5 μm, and broadband filters are used for wavelengths outside of this range. Each spectrum spans ~25 resolution elements on the array, corresponding to ~5000 km s^{-1} in high resolution mode, and ~12000 km s^{-1} in low resolution mode. The spectral coverage in low resolution mode is sufficient for simultaneous acquisition of line pairs such as H_2 1–0 S(1) + Brγ, [Fe II] + Paβ, and even [O III] + Hβ in high redshift sources.

Spectral calibration is provided in part by the OH airglow emission where available. Emission lines from neon, argon, krypton, and xenon arc lamps are used to supplement or substitute for the OH lines. Any combination of lamps may be turned on at once, the light from which strikes a retractable sandblasted surface roughly at the position of the tertiary mirror.

The gratings and the flip-in mirrors used for imaging are rotated by stepper motors external to the dewar. Motor driven shafting is fed through a series of o-rings and

spacers, bracketed by ball bearings. Following each feed-through is a flexible coupling, a fiberglass shaft, a shaft coupling, a wafer spring coupling, a fixed bearing, and a bi-directional clutch. The flip-in mirrors are direct-drive, while the gratings move through a double gear reduction with a total reduction of about 1:78. Torsion springs force the flip-in mirrors against their mechanical stops, and coiled constant-force springs attached to the gratings load the grating gear trains. Grating reproducibility has been measured at better than 0.2 pixels, or $\sim$0.05 milliradians.

The spectrograph, including the image slicer, is cooled by liquid nitrogen to a temperature below $\sim$ 80 K in an effort to minimize dilution of the astronomical signal by thermal emission from the optical surfaces and surrounding supports. This is particularly beneficial for preventing stray light from mixing into the many beams of the image slicer, which is virtually impossible to baffle. The liquid nitrogen is held in a cylinder at the top of the instrument, as seen in Figure 5.4. The dewar has a capacity of 22 liters, with a hold time of approximately three days.

The PIFS optical path is heavily baffled, with eight baffle fins between the entrance window and the image slicer focal plane, and eleven baffle planes located between the optics at the top end of the dewar and the optics at the bottom. Considering the multiple passes, a single photon traverses 48 baffle plates while inside the PIFS dewar. Most internal surfaces of the PIFS dewar are coated with Aeroglaze WZ306 flat black polyurethane coating. In addition to these stray light controls, the mechanical couplings to the outside stepper motors, which are partially isolated by a fiberglass shaft connection, are surrounded by cold baffle material, such that no direct light path exists from the warm outside environment to the optical train without first intercepting a cold surface. An additional baffle box surrounds the grating assembly, further reducing stray light from the vicinity of the grating. The infrared camera contains similar baffling systems, in addition to a cold Lyot stop to filter out unwanted light at the pupil.

The imaging camera is situated in a gimbal with two translational degrees of freedom and two rotational degrees of freedom allowing for proper positioning of the focal plane and alignment of the PIFS pupil to the camera's cold stop. Alignment

of the PIFS dewar to the telescope pupil is accomplished via an adjustable tertiary mirror, which sits on a sliding stage within the warm instrument mount.

Internal spectrograph alignments are all accomplished via motions of the spherical mirrors at the base of the dewar. The alignment can only be performed when the dewar is warm and the vacuum vessel open to the atmosphere. The all aluminum construction nullifies differential contraction such that alignment is maintained in the cold state. Because the alignment involves spherical mirrors, translational motions are equivalent to rotations. Each mirror has two-dimensional fine-adjust motion capability for the purpose of alignment. Co-alignment of the twin spectrographs is critical, since each independent spectrograph pupil must fall on the same cold stop in the camera.

The measured efficiency of the PIFS-camera system in high resolution spectral mode is ~22% from the top of the atmosphere to detected photons, assuming an 80% combined transmission of the the atmosphere and telescope. The PIFS dewar itself has a throughput of ~58% with the grating on blaze. The dominant loss in the system is due to the grating. The image slicer throughput, including pupil losses, is 90–95%. An additional source of loss for the entire system is a pair of CaF_2 windows separating the camera dewar from the PIFS dewar. The combined transmission of this pair of windows is about 85%. Estimates of sensitivity indicate the ability to detect a $K = 18$ mag continuum point source (0.04 mJy) at 5σ in one hour of on-source integration under good seeing conditions.

The entire optical assembly is cantilevered off the bottom plate of the nitrogen tank. A perforated tube internal to the nitrogen canister acts as an extension of the optical tube, adding structural rigidity to the assembly by connecting the top and bottom plates of the nitrogen canister together. Flexure of the assembly, as measured via lamp line spectral positions at the camera focal plane, is never more than one-half pixel for any motion of the telescope above an elevation of 25°.

5.4 Observation Techniques

Observing with the PIFS is a straightforward process, typically involving alternating object and sky integrations. If the observed object is only a few arcseconds in extent, as is often the case for high-redshift radio galaxies, for instance, the object can be dithered around within the PIFS field such that all integration time is spent on the object. The disadvantage to acquiring separate sky frames is that the OH airglow lines are time variable on the scale of minutes. However, the spatially uniform, spectrally discreet nature of these lines makes removal of residual flux feasible in software.

The imaging mode, with the flip-in mirror placed in front of the grating, produces a sliced image of the field of view. Though not difficult to mentally reconstruct, quick-look software enables immediate reassembly of the field into its original rectangular form. The imaging mode is used to acquire and center observing targets within the field. Unlike longslit spectroscopy, integral field spectroscopy does not require precise positioning within a slit, thereby simplifying the process of target acquisition. The imaging mode is also useful for photometric calibration with broad-band photometric standards, though the spectral modes may also be used for photometric calibration.

Any image slicing spectrograph having little anamorphic magnification and a pixel scale that does not greatly oversample the seeing has an inherent sampling asymmetry in the following way. If the slits correspond to one pixel in width, thereby symmetrically sampling spatial data in both the cross-slit and along-slit directions, the spectral output is undersampled, with unresolved spectral sources spanning only one pixel in the spectral direction. For critically sampled spectral data, the slit must be two pixels in width, which imposes a cruder spatial sampling in the cross-slit direction as compared to the along-slit direction. For the PIFS, with 4-pixel wide slits (see Section 5.3.1 for details), the problem is even more exaggerated. The spatial sampling of a single PIFS exposure is sufficient to resolve $0\farcs33$ structures in the along-slit direction, but sampling in the cross-slit direction limits resolution to a crude $1\farcs33$. To compensate for this asymmetry, an appropriate dither pattern can, in stable seeing conditions, allow one to recover the full spatial resolutions in both dimensions. In

practice, this has worked quite well, as can be seen in the example data shown in Section 5.6.

Atmospheric opacity as a function of wavelength is measured just prior to or just after the object observation by observing a featureless stellar spectrum at similar airmass and direction in the sky. Main-sequence G-stars with $V < 6.5$ mag are used for this purpose. Within the near-infrared bands, these stars very nearly approximate blackbodies with only minor absorption features at Paβ and Brγ, which are easily interpolated over.

Flat fielding is accomplished simultaneously with spectral calibration observations of the G-star, by uniformly illuminating the PIFS field with the light of the star. In practice this is done by chopping the $f/70$ secondary mirror in a triangle-wave pattern, in a direction coinciding with the PIFS slit direction. By guiding on the endpoint of the chopped star with a moving autoguider head, the star is steadily dragged across all the slits, with a double-pass taking roughly 180 seconds. Thus the object-sky pair is obtained in ~400 seconds. Telescope shake, seeing variability, etc., can unevenly distribute light among the slits, so a second spectrum is taken, this time with the star chopped across the slits, rather than along them. A brief exposure provides a relative flux reference, as it is known that each slit receives the same amount of light. In addition, this exposure establishes a spatial reference with which to tie the spectral observations together. This complicated technique is done to properly cancel the effects of fringing due to a sapphire coating on the NICMOS 3 array. The coating acts as a Fabry-Perot, producing a non-uniform family of fringes on the spectrally dispersed frames. It is found that dome flats produce a somewhat different fringe pattern, rendering them ineffective at canceling fringes in the observed spectra.

5.5 Data Reduction Overview

Reduction of the PIFS data is conceptually no harder than reducing any longslit infrared spectral data, as the PIFS output is recorded on the array as eight independent longslit spectra. The sky-subtracted spectra are divided by the normalized

main-sequence G-star spectrum, acting both as an atmospheric reference and as the flat-field by the technique described in Section 5.4. Each spectrum is corrected for spatial curvature and spectral curvature, using calibration lamps and OH airglow lines (Oliva & Origlia, 1992) to rectify the spectral domain onto a uniform wavelength grid. The eight spectra are tied together spatially with help of the G-star chopped across all eight slits, as mentioned in Section 5.4. The spectra are then multiplied by a black-body with the temperature of the G-star used for atmospheric calibration. Each of the eight two-dimensional longslit spectra are then inserted into their proper positions within a datacube. The datacube is more finely gridded in the cross-slit dimension than the number of slits by a factor of four. In this way, the full spatial resolution can be reconstructed provided stable seeing conditions prevail and the dither pattern mentioned in Section 5.4 is followed. Photometric variability from one integration to the next is easily compensated with scaling of the individual spectra to produce a self-consistent spatial profile. The power of integral field spectroscopy in simultaneously acquiring full two-dimensional spatial information is also used to advantage in the data reduction process.

Once the datacube is assembled, pure continuum and pure line images are easily extracted, as are one-dimensional spectra at any point or region within the field. But care must be taken in the interpretation of spectra or in the construction of velocity-resolved line images. The presence of spatial gradients across the various slits induce apparent wavelength offsets with respect to the spatially uniform calibration sources, such as lamp lines and OH lines. Therefore, false velocity shifts will be perceived if extracting wavelength bins with respect to the calibration sources. Knowing the local spatial profile of the line emission source, and how this profile is partitioned by the slits is sufficient to reconstruct the apparent velocity shifts. An improved map of line emission gas at a particular velocity can then be constructed, and used, if necessary to iterate until a self-consistent solution is obtained.

5.6 First Results

The PIFS was first operated on the Palomar 200-inch Telescope in the Fall of 1998. After three observing runs, the instrument has proven itself to be both reliable and scientifically powerful. Example data highlighting the capabilities of the instrument are presented below.

5.6.1 NGC 6240

The luminous infrared galaxy, NGC 6240 is a well known example of a major galactic merger. The galaxy shows two continuum peaks, or nuclei, separated by $\sim 1\farcs5$ at 3.6cm (Colbert, Wilson, & Bland-Hawthorn, 1994). Millimeter-wave studies in CO have indicated the accumulation of cold molecular gas in the region between nuclei (Bryant & Scoville, 1999; Tacconi et al., 1999), in agreement with simulations (e.g., Barnes & Hernquist, 1991) showing the collisional gas leading the stars in coalescing to the central potential. Fabry-Perot imaging of NGC 6240 in the near-infrared by Van der Werf et al. (1993) in three velocity channels showed widespread emission from the 1–0 S(1) vibration-rotation transition of molecular hydrogen. New data with the PIFS, obtained on 1999 March 27 present a similar picture to the work by Van der Werf et al.

Four five-minute on-source integrations of NGC 6240, with an equal number of sky integrations, produced a datacube around the H_2 1–0 S(1) line at $\lambda_{rest} = 2.12$ μm. A single raw frame, accompanied by the same frame following sky subtraction is shown in Figure 5.5, illustrating the arrangement of the eight independent spectra on the array. The unsubtracted OH line emission from the atmosphere is clearly shown. Obvious in the single sky-subtracted frame is extended H_2 emission, differing dramatically in morphology from the continuum source. Also evident is the broad nature of the H_2 line profile, especially contrasted with the 230 km s^{-1} resolution element seen in the OH airglow lines of the raw frame. Figure 5.6 displays a reconstructed pure continuum image along with total H_2 emission and three velocity bins of the same line feature. The broad nature of the line emission manifests itself in the velocity-resolved line

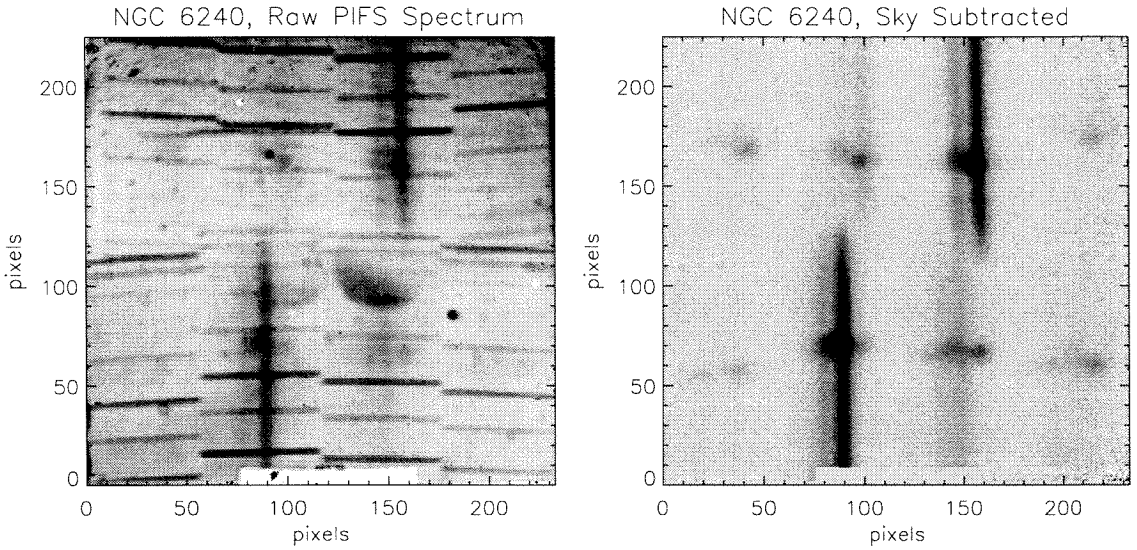

Figure 5.5: PIFS spectra of the H_2 1–0 S(1) line in NGC 6240, representing 5 minutes of on-source integration time in the high resolution mode. The raw frame is displayed at left, and the sky-subtracted frame at right. Wavelength increases outward from the center of the array. The OH airglow lines show the pattern of the slit, which differs from the schematic slit pattern of Figure 5.1 for reasons discussed in the text. The continuum is clearly visible, marking the central two slits in the rectangular field. The molecular hydrogen emission is immediately seen to show more extent than the continuum, by the fact that line emission appears in all eight slits.

images in that the three images are more similar than different. However, differences do exist, perhaps most notably the shift of the peak H_2 emission from one nucleus to the other as one moves from red to blue.

5.6.2 4C 39.37

The $z = 3.22$ FRII radio galaxy, 4C 39.37, was imaged with the PIFS on 1999 March 25. The extent of the object is small enough such that the object can be dithered around within the PIFS field. In this way, 16 five-minute spectral integrations at 2.1 μm were taken to capture the [O III] doublet. The resulting spectrum shows definite, nonlinear spatial extension of the line emission, with a large range of velocities seen in the two-dimensional spectra. Figure 5.7 shows the spatial distribution of the total 0.5007 μm line emission, as well as three velocity bins of the same data. The radio axis of the galaxy is oriented horizontally in the figure, which corresponds to the major

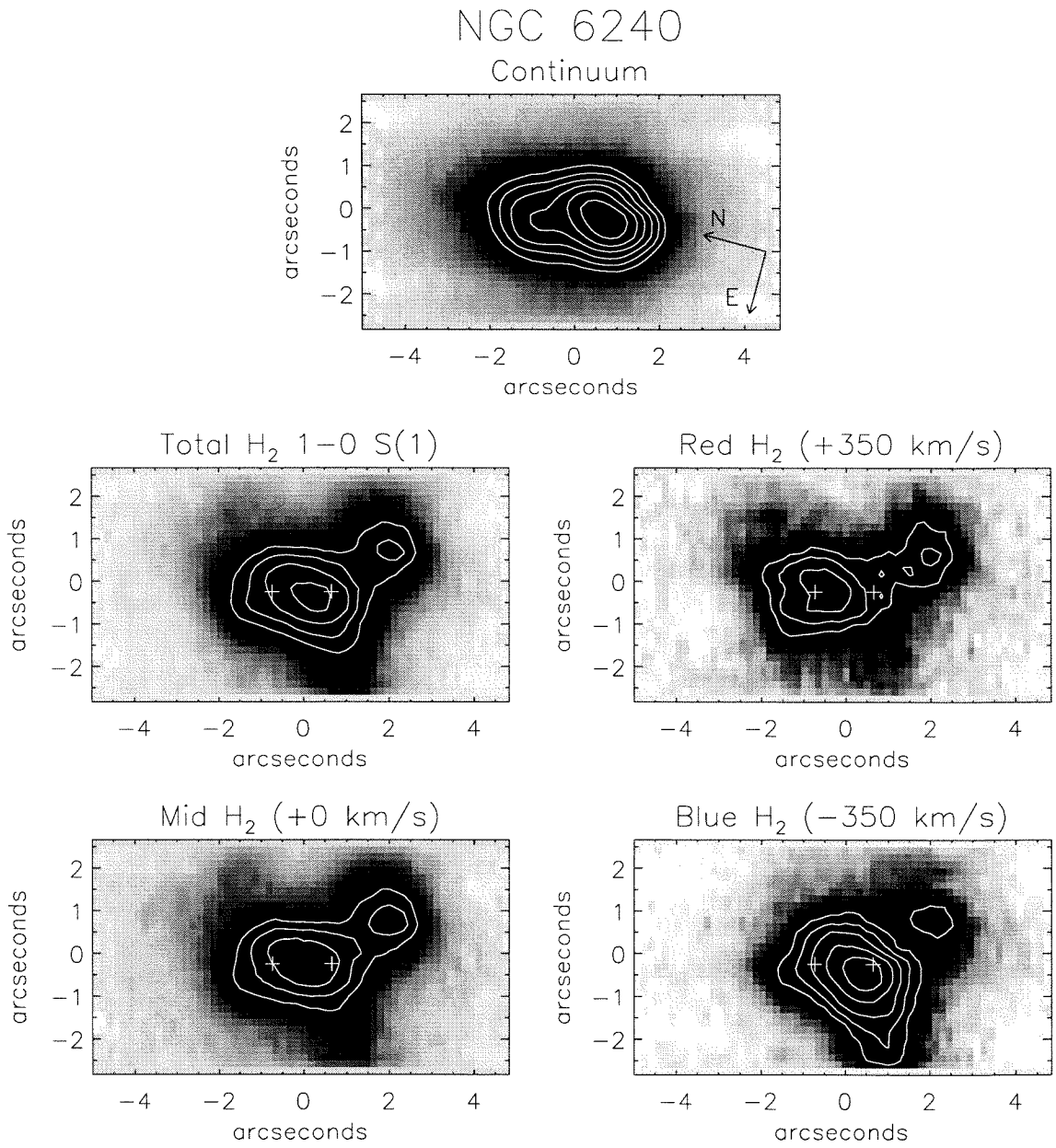

Figure 5.6: Reconstructed images of NGC 6240 from 20 minutes of on-source integration. At top is the pure continuum image, collapsed from the datacube. The two continuum peaks are indicated in subsequent images by crosses. The lower four panels present continuum-subtracted line images of the H_2 1–0 S(1) line, the first showing the total H_2 flux, and the following three panels representing three different velocity bins of the emission line. The velocity bins are 350 km s^{-1} wide, separated by the same amount. The spectral resolution element of the PIFS is 230 km s^{-1}.

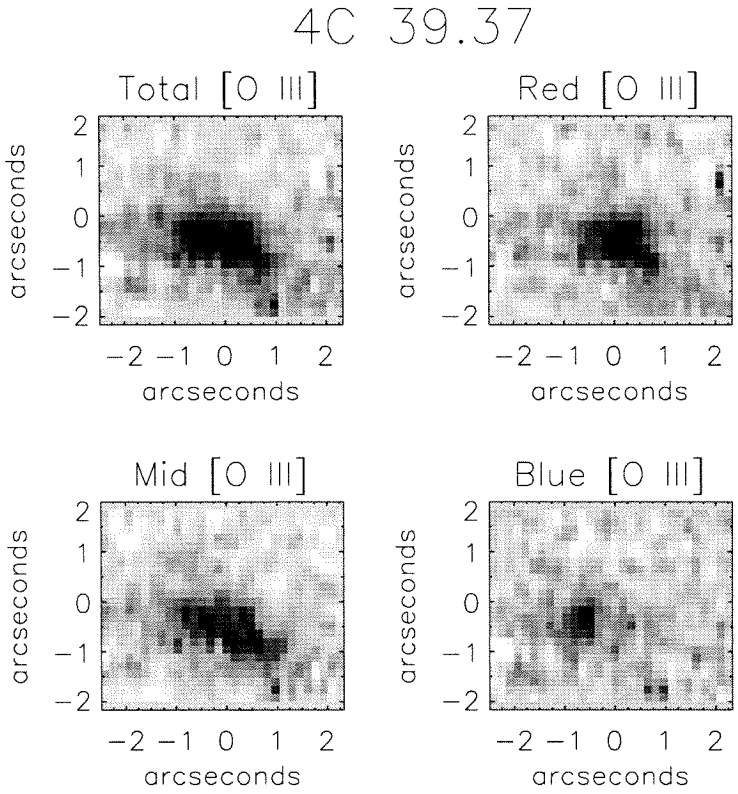

Figure 5.7: PIFS images of [O III] emission in the z=3.22 radio galaxy, 4C 39.37. The data here represent 80 minutes of integration time, with the object dithered within the PIFS field for object-sky pairs. The total line emission, at upper left, shows clear spatial extent, primarily in the horizontal direction, corresponding to the radio axis. Velocity-resolved line images, presented in bins of 350 km s^{-1}, show that the morphology changes as a function of velocity.

axis of the line emitting nebula. A clear morphological dependence on velocity is seen, possibly indicative of gas flowing out along the radio axis.

5.7 Summary

We have described the design, construction, and performance of a new cryogenic integral-field spectrograph for near-infrared observations at the 200-inch Hale Telescope. The properties of the spectrograph are summarized here:

1. Operation from 1–2.5 μm or 1–5 μm with one of two existing 256×256 infrared array cameras.

2. Total field of view of $5\farcs4 \times 9\farcs6$, sliced into eight slits, each $0\farcs67 \times 9\farcs6$in size, with seeing-limited spatial resolution across the entire field of view.

3. Two resolution modes, offering resolutions of $R \approx 1300$ and $R \approx 600$. Spectral coverage is $\sim$5000 km s^{-1} and $\sim$12000 km s^{-1} for these two modes, respectively.

4. Slit imaging mode for photometric calibration and target acquisition.

The design and construction of the Palomar Integral Field Spectrograph represents part of the thesis work of T. W. Murphy. We thank James Larkin, Robert Knop, and Sean Lin for their roles in developing the longslit spectrograph, which acted as a launching point in the design of the PIFS. Conversations with Gerry Neugebauer helped guide the instrument development. Special thanks to Armando de las Casas, who did a significant portion of the machining work, and to Rick Paniagua, who advised TWM on countless innovative machining techniques, and also made his tool box available. Thanks also goes to Mike Gerfen, Ramon Devera, Richard Borup, Nathaniel White, Terry Scott, Phillip Wood, and Larry Kuntz for their machining contributions to the project. Thanks to Doug Warden for providing odds and ends, and for wiring the motors. Eiichi Egami is thanked for occasionally lending a hand, and for his help with photo-documentation. Diamond fly-cutting of the image slicer optics was performed by Manasota Optics. The PIFS dewar was built by Precision Cryogenics. Don Loomis figured the fused silica optics. Infrared Optical Products provided the CaF_2 windows, and the gratings were replicated by Richardson Grating Lab. Thanks to telescope night assistants, Rick Burruss, Karl Dunscombe, and Jean Mueller for their skillful manipulation of the telescope. We are also grateful for the efforts of Mike Doyle, Dave Tenant, Steven Kunsman, John Henning, and the rest of the Palomar staff, whose efforts promoted problem free integration of the PIFS into the existing infrastructure. Lee Armus accompanied some of the observations presented here. Funding for the PIFS was provided by the National Science Foundation, and by grants from the W. M. Hurt Foundation and Caltech. TWM is supported by the NASA Graduate Student Researcher Program.

Bibliography

Barnes, J. E., & Hernquist, L. 1991, *Astrophysical Journal*, 370, L65

Bryant, P. M., & Scoville, N. Z. 1999, *Astronomical Journal*, 117, 2632

Colbert, E. J. M., Wilson, A. S., & Bland-Hawthorn, J. 1994, *Astrophysical Journal*, 436, 89

Knop, R. A. 1997, Ph.D. Thesis, California Institute of Technology

Larkin, J. E., Knop, R. A., Lin, S., Matthews, K., and Soifer, B. T. 1996, *Publ. of the Astron. Soc. of the Pacific*, 108, 211

Larkin, J. E. 1996, Ph.D. Thesis, California Institute of Technology

Oliva, E., & Origlia, L. 1992, *Astronomy & Astrophysics*, 254, 466

Tacconi, L. J., Genzel, R., Tecza, M., Gallimore, J. F., Downes, D., and Scoville, N. Z. 1999, *Astrophysical Journal*, 524, 732

Van der Werf, P. P., et al. 1993, *Astrophysical Journal*, 405, 522

Weitzel, L., Krabbe, A., Kroker, H., Thatte, N., Tacconi-Garman, L. E., Cameron, M., and Genzel, R. 1996 *Astronomy & Astrophysics Supplements*, 119, 531

Chapter 6 The Active Nucleus in IRAS 08311−2459

6.1 Chapter Overview

Near-infrared spectroscopy using the new Palomar Integral Field Spectrograph indicates the presence of an AGN (active galactic nucleus) in the ultraluminous infrared galaxy IRAS 08311−2459. The broad wings of the Paschen-α hydrogen recombination line are seen to be spatially unresolved, and with no positional offset between red and blue high velocity emission. The [Si VI] coronal line, with a 167 eV excitation potential, is also spatially unresolved with a velocity width comparable to that of the broad Paα emission. The low velocity component of the Paα emission is seen to be rotating, and is extended over $\sim$ 2 kpc. Molecular hydrogen is also extended, and elongated along the maximum velocity gradient, sharing the same rotation profile as the narrow Paα emission. The simple picture in agreement with the observations is that of an AGN surrounded by a rotating disk of star formation. These observations lend strength to the usage of [Si VI] as a diagnostic of AGN activity in ultraluminous infrared galaxies, and also highlight the utility of integral field spectroscopy in elucidating subtle morphological differences in line emitting regions.

6.2 Introduction

Ultraluminous infrared galaxies (ULIRGs) are among the most luminous sources in the universe, with infrared luminosities of $L_{ir} \gtrsim 10^{12} L_{\odot}$. The bulk of the energy emitted from these sources emerges in the far-infrared, suggesting that the light we see is thermally processed by warm dust in the galaxies. As such, the optically thick dust prohibits direct viewing of the mechanism responsible for the extreme power

generation. Quasars (or more generally QSOs—quasi stellar objects) and massive starbursts are perhaps the only phenomena capable of producing the high luminosities observed in these systems. Recent spectroscopic programs at infrared wavelengths have shown that the great majority of ULIRGs with $L_{ir} < 2 \times 10^{12} L_{\odot}$ are powered predominantly by starbursts rather than by AGN (Genzel et al., 1998; Rigopoulou et al., 1999; Murphy et al., 1999; Veilleux, Sanders, & Kim, 1997, 1999). At luminosities higher than this, the AGN fraction rises to between one-third and one-half.

IRAS 08311−2459 is a ULIRG at $cz = 30150$ km s^{-1} (1 arcsec = 1.7 kpc) with $L_{ir} = 2.5 \times 10^{12} L_{\odot}$, and is classified as a "warm" ULIRG by the definition of Sanders et al. (1988). This galaxy is selected from the 2Jy ULIRG sample of Strauss et al. (1990, 1992), and is a single-nucleus galaxy surrounded by tidal debris (Murphy et al., 1996). The near-infrared spectrum of IRAS 08311−2459 (Murphy et al., 1999, Chapter 3, this thesis) shows emission line features suggestive of AGN activity, though a scenario involving strong shocks and high velocity outflows could also explain these spectral features. Calculated quantities involving luminosities and physical scales assume a cosmology with $H_0 = 75$ km s^{-1} Mpc^{-1} and $q_0 = 0$ throughout this chapter.

Near-infrared integral field spectroscopy, which effectively provides simultaneous velocity-resolved imaging capabilities of multiple emission lines, allows subtle morphological differences between various line emitting regions to be elucidated. In this chapter we present integral field observations of the Paα, H_2 1–0 S(3), and 167eV excitation [Si VI] emission lines in IRAS 08311−2459, which together form a consistent picture of a galaxy containing a central AGN surrounded by a starburst disk.

6.3 Observations & Data Reduction

Observations were made using the Palomar Integral Field Spectrograph (PIFS) situated at the $f/70$ focus of the 200-inch Hale Telescope. This instrument produces simultaneous spectra for eight slits in a contiguous two-dimensional field of view. A description the PIFS instrument, along with general observing and data reduction procedures can be found in Murphy, Matthews, & Soifer (1999) (Chapter 5, this the-

sis). IRAS 08311−2459 was observed on the night of 25 March 1999. The $R \approx 1300$ resolution mode ($\Delta v \approx 225$ km s^{-1}) was used to obtain two spectra centered on the redshifted Paα, and H_2 1–0 S(3)+[Si VI] lines, respectively. Separate sky exposures were alternated with the on-source integrations, with integration times of 300 s. A positional dither pattern was employed for the sequence of integrations enabling recovery of seeing-limited spatial resolution in the cross-slit direction. The pixel scale for these observations is 0.167 arcsec pixel^{-1}. An offset field star was used for auto guiding, with image motion compensated by driving the active secondary mirror. Guided observations of a nearby star, with 10 s exposures, accompanied the spectral observations for the purpose of evaluating the point spread function (PSF). Wavelength calibration is provided through a combination of OH airglow lines (Oliva & Origlia, 1992) and arc lamp spectra taken at the time of observation. All wavelengths are referred in air units. Atmospheric opacity and spectral flat-fielding are compensated simultaneously using the light from HR 3862, a 4.9 mag G0 V star, spread uniformly across the field of view. At the time of observation, the G star was at an airmass of ~ 1.95, well matched to the airmass of the science observations.

For these observations, the $5\farcs4 \times 9\farcs6$ field of view was oriented with the long axis at a position angle of 90°. The Paα line was observed with 1800 s of on-source integration time at an average airmass of 2.00. The H_2+[Si VI] lines were observed for 2100 s of on-source time at an average airmass of 1.96. The seeing for the Paα dataset, as determined via imaging of the PSF star, was measured at $1\farcs00$ midway through the observation, and $1\farcs15$ at the end. The telescope was then focused, resulting in a PSF full-width at half-maximum (FWHM) of $1\farcs05$. Observations of the H_2+[Si VI] line immediately followed, with the PSF measuring $0\farcs85$ midway through, and $0\farcs95$ at the end of the observation. The measures of seeing should not be taken entirely at face value, as variability over the time scales of the spectral observations limits the accuracy of the very short PSF exposures at estimating the average seeing conditons. All observations presented here were made in clear photometric conditions. Photometric calibration was performed via K_s imaging of the galaxy and of the faint standard star 9143 from Persson et al. (1998), using a flip-in mirror in front of the grating, thereby

establishing the continuum flux density at 2.155 μm. The continuum slopes observed in the Paα and H_2+[Si VI] spectra were used to estimate the continuum level for the Paα spectrum.

Data reduction consists of first performing the sky subtraction, interpolating static bad pixels and cosmic ray artifacts, division by the G star spectrum, and multiplication by a blackbody spectrum matched to the G star's temperature of 5930 K. The H_2+[Si VI] spectrum was multiplied by a template G3 V spectrum from Kleinmann & Hall (1986), smoothed and resampled to the PIFS resolution, in order to remove the Brγ stellar absorption line introduced in the division by the HR 3862 spectrum. No calibrator absorption lines of any significance effect the Paα spectrum. Spatial and spectral distortions are corrected using previously generated distortion maps appropriate for the particular grating setting. Co-registration of the eight slits in the spatial dimension is based upon observation of the G star with its light extended perpendicular to the slit pattern by chopping the telescope secondary mirror in a triangle-wave pattern. The two-dimensional spectra from the eight slits are placed into the three-dimensional datacube according to the positional dither pattern, with a common wavelength axis established by the calibration lines. Residual OH airglow lines are removed by subtracting a scaled version of the raw sky spectrum, with typical scalings of $\sim$2% in absolute value, sometimes as large as 5%. Photometric variability among individual integrations is compensated by small scaling adjustments such that the object flux is consistent from one integration to the next. A more complete description of the data reduction procedures may be found in Murphy, Matthews, & Soifer (1999) (Chapter 5, this thesis).

In the data presented here, the pure continuum images are constructed directly from the integral field datacube, and constructed from spectral regions free of line emission as well as OH airglow emission. For each spatial pixel, a linear fit is made to the line-free portion of the continuum spectrum. The line images are formed by subtracting this continuum fit from the datacube, then summing over a small range in the spectral dimension. In this way, the line images simulate continuum-free narrow band images at arbitrary wavelengths—or velocities—within the datacube. The co-

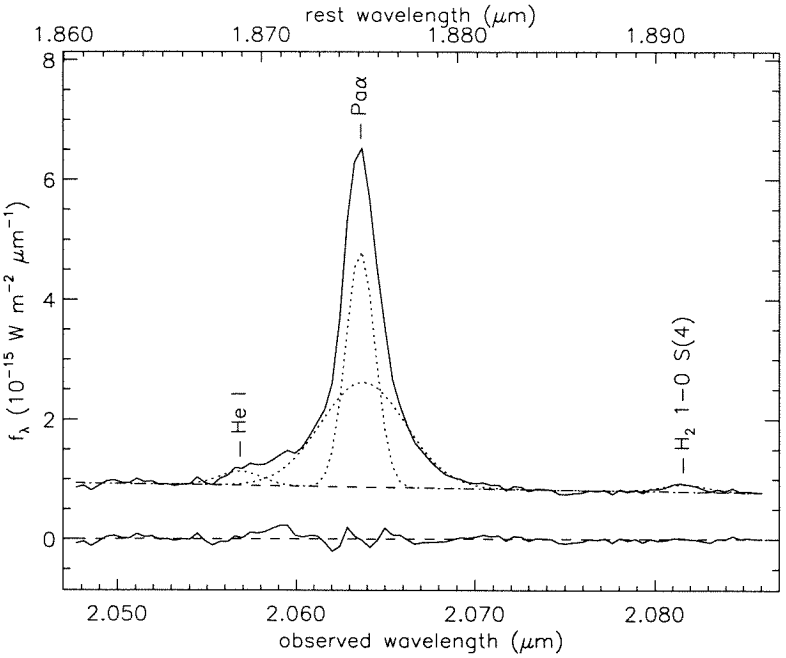

Figure 6.1: Nuclear spectrum of the Paα line extracted from a 0.″83×0.″83 aperture in the datacube. Positions of the He I and H_2 1–0 S(4) lines are marked at the systemic velocity determined from Paα. In addition to the spectral data, the continuum fit and Gaussian fit components are shown, as is the residual to the functional fits. The broad component of the Paα emission is clearly seen, and is rather symmetric after accounting for the He I line. The absolute flux density scale corresponds to light within the aperture only. Only 18% of the total continuum flux from a $5'' \times 5''$ box centered on the galaxy falls within this aperture. Aperture corrections for the line emission can be found in Table 6.1 of Appendix 6.A.

registration of the continuum and line images is implicit, as the images are derived from the same dataset.

6.4 Results

6.4.1 Paα Emission Line

Figure 6.1 shows the appearance of the Paα spectrum (λ_{rest} = 1.87510 μm), taken from a 0.″83×0.″83 square aperture centered on the continuum peak of the galaxy. The resolved velocity profile of the line shows broad wings around a moderately narrow peak. The wings appear asymmetric, with more emission blue-ward of the line center. Part of this asymmetry likely comes from the He I line at a rest wavelength of 1.8689

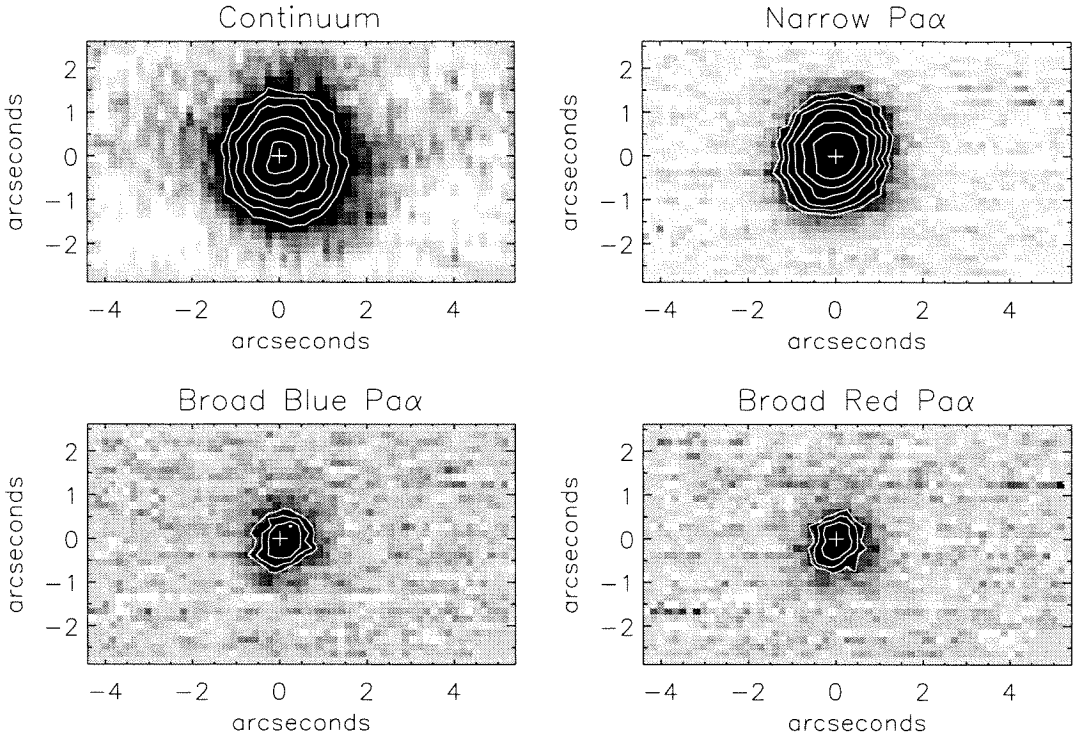

Figure 6.2: Morphologies of the continuum and of the Paα emission in three velocity bins, centered at $v = 0$ and $v = \pm 425$ km s^{-1}, each 250 km s^{-1} wide. All show rather round, symmetric morphologies, though the broad emission is significantly more compact than either the narrow Paα or continuum emission. The FWHM of the broad line emission measures $\sim$1.″1, compared to 1.″55 and 1.″75 for the narrow Paα and continuum emission, respectively. North is up, and east is to the left in all images. Contours are placed at $\sqrt{2}$ multiplicative intervals.

μm, with an estimated contribution of $\sim$ 5% of the Paα flux, as is characteristic in ULIRGs (Murphy et al., 2000, Chapter 2, this thesis). Subtracting the expected He I contribution with the same velocity profile as Paα results in a Paα profile consistent with being symmetric. A multiple Gaussian line fit, whose components are displayed in Figure 6.1, fits a well-centered 800 km s^{-1} broad component plus a narrow, 160 km s^{-1} wide component to the Paα line, with comparable total fluxes. See Appendix 6.A and Table 6.1 for details on the line fits. Throughout this chapter we refer to this 800 km s^{-1} emission feature as the "broad" component, though it does not represent a canonical broad line region. We simply use this term to indicate velocities larger than would be expected in ordinary galaxy kinematics, such as rotation.

The continuum morphology is presented in Figure 6.2, along with images of three

different spectral ranges within the Paα line profile. Referring to the line peak at 2.06366 μm as the zero velocity reference, the three continuum-subtracted narrow band images correspond to central velocities of -425, 0, and $+425$ km s^{-1}, each 250 km s^{-1} wide. The narrow line image is more compact than the continuum, with characteristic FWHM values of 1.″55 and 1.″75, respectively. The line emission is also slightly elongated compared to the round continuum, with an ellipticity (major-to-minor axis ratio) of $\sim$ 1.1. The two images of the line wings are significantly more compact than either the continuum or narrow line Paα images, and are in fact consistent with the estimated 1.″1 seeing limit at the time of observation. No significant difference in shape, size, or center can be distinguished between the red and blue line wing images, though they each exhibit an ellipticity of $\sim$ 1.12. The observed ellipticity could be the result of a slightly defocused, astigmatic telescope. Such a distortion would not noticeably distort the much larger continuum shape, and likewise would not fully account for the similar elongation of the narrow Paα image.

With confidence in the generic morphological character of the line emission, we may turn to a more detailed representation of the line extents by plotting the line emission FWHM as a function of wavelength. Figure 6.3 shows the measured spatial FWHM in both the x and y dimensions of the array, corresponding to the east–west and north–south directions. Each data point represents a single spectral pixel, which spans roughly one quarter of a spectral resolution element. The horizontal dotted lines delimit the range of atmospheric seeing measured in conjunction with the spectral observations, with a dashed line indicating the mean of these two values. The extended nature of the narrow line emission stands out in clear contrast to the seeing-limited extent of the line wings. The increase in width at the left edge of the plot coincides with the red side of the He I emission line. Due to the low signal-to-noise ratio in the region of the He I line, it was not possible to extend the plot data to shorter wavelengths. The continuum FWHM, measured beyond the line wings, is represented by the dashed line at top, and the continuum-subtracted line profile is plotted for convenient reference at bottom.

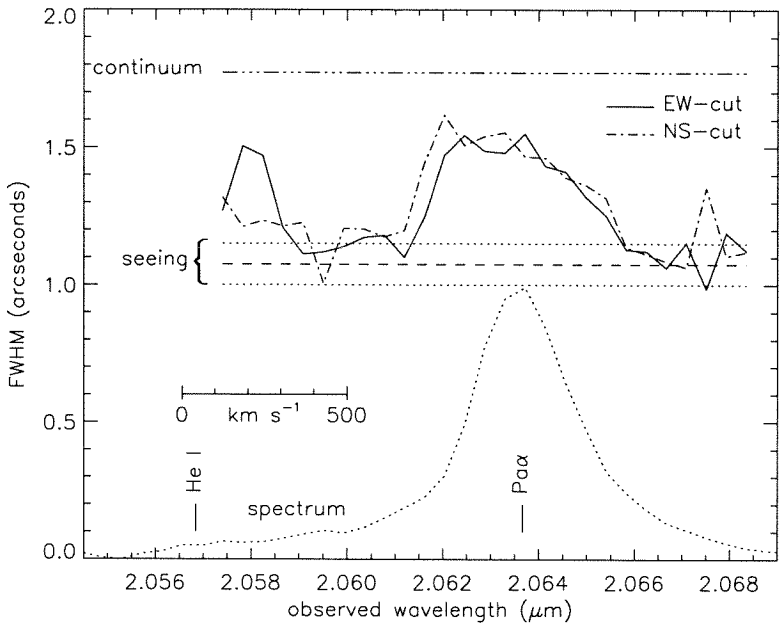

Figure 6.3: Spatial line extent as a function of wavelength for the Paα line, showing the spatially resolved nature of the narrow line emission in contrast to the spatially unresolved high velocity regions. Two plots are shown, representing measures in the orthogonal array directions. The size of the continuum source is shown at the top of the plot. The estimated range in seeing is indicated, as measured from PSF images intermixed with the spectral data. The profile at bottom shows the continuum subtracted spectrum of the Paα line from Figure 6.1 for immediate comparison to the spatial extents. The increase in spatial width at the left edge of the plot is attributable to the He I line. Line centers are marked for the systemic velocity, and a velocity scale is provided for convenient reference.

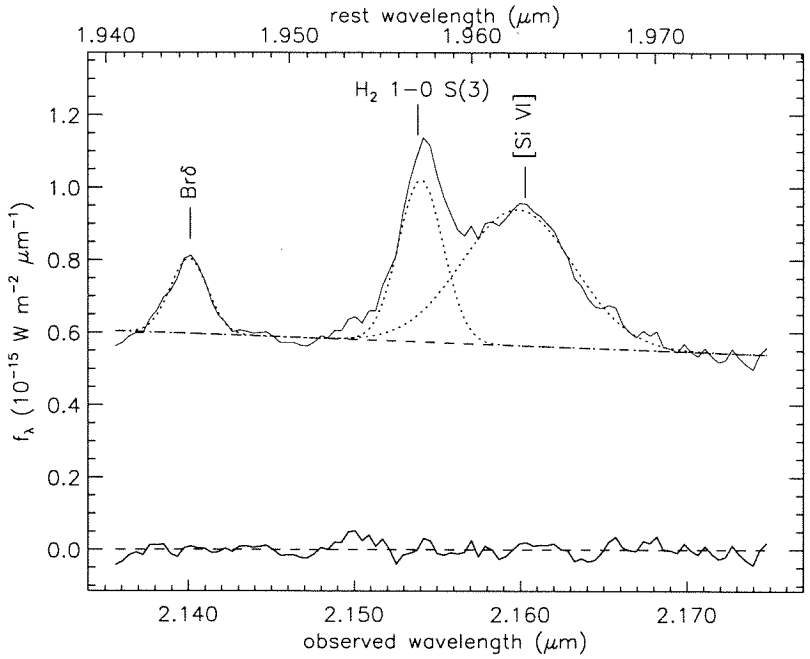

Figure 6.4: Nuclear spectrum of the H_2 1–0 S(3) + [Si VI] line region, extracted from a $0''.67 \times 0''.67$ aperture in the datacube. The Brδ line is also seen. In addition to the spectral data, the continuum fit and Gaussian fit components are shown, as is the residual to the functional fit. The [Si VI] line is clearly broader than the other lines in the spectrum, and comparable in strength to the H_2 line. Line centers are marked at the systemic velocity. The absolute flux density scale corresponds to light within the aperture only. Only 13.5% of the total continuum flux from a $5'' \times 5''$ box centered on the galaxy falls within this aperture. Aperture corrections for the various emission lines can be found in Table 6.1 of the Appendix.

6.4.2 H_2 1–0 S(3) & [Si VI] Emission Lines

The integral field spectrum of IRAS 08311−2459 at 2.15 μm contains the Brδ, H_2 1–0 S(3), and [Si VI] emission lines at rest wavelengths of 1.94456 μm, 1.95702 μm, and 1.96287 μm, respectively. Figure 6.4 shows the one-dimensional spectrum, extracted from a $0''.67 \times 0''.67$ square aperture centered on the continuum peak. The Brδ line is largely ignored here, as the Paα line is a far more effective probe of hydrogen recombination, and the combination of Brδ's weakness plus its spectral proximity to Paα limits its usefulness as a measure of extinction. The $1''.35$ spatial extent of the Brδ line is perfectly consistent with the Paα extent, accounting for the seeing difference between the observations. The [Fe II] line at 1.9670 μm, seen in some ULIRGs (Murphy et al., 2000, Chapter 2, this thesis), does not appear in the spectrum, though the Brγ feature from the atmospheric calibrator coincides with this same wavelength, making

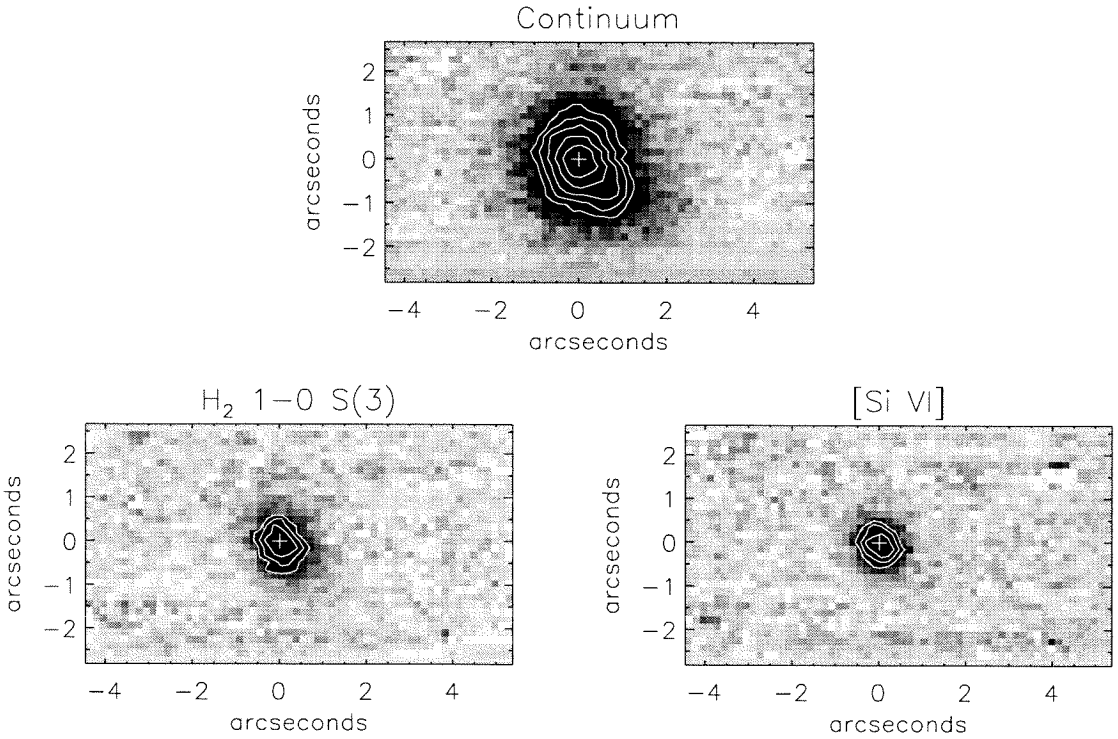

Figure 6.5: Continuum and line morphologies for the H_2 and [Si VI] lines. The line images are each 400 km s^{-1} wide, centered on the line peaks. The [Si VI] emission is completely unresolved, as well as symmetric. The H_2 line is slightly resolved, and extended along a 30° position angle, roughly consistent with the disk direction inferred from the rotation. The continuum shape differs slightly from that seen in Figure 6.2, in that a small extension appears to the SW. The seeing conditions were better for this image, and the compact symmetry of the [Si VI] line suggests that this extension is real. Orientation and contours are as described for Figure 6.2.

the presence of [Fe II] uncertain.

All lines in the H_2+[Si VI] spectrum are spectrally resolved, with the H_2 line resembling the atomic hydrogen lines in terms of observed line width. Though the H_2 line is blended with the [Si VI] line, it is known to be symmetric by comparing with the H_2 1–0 S(1) line profile (Murphy et al., 1999, Chapter 3, this thesis). The [Si VI] line is significantly broader than its neighboring lines, with a FWHM of $\sim$ 1000 km s^{-1}. See Appendix 6.A and Table 6.1 for more information on the functional fits to these lines.

Figure 6.5 shows the continuum and narrow band line images of IRAS 08311−2459 in H_2 1–0 S(3) and [Si VI] emission. The continuum morphology appears different

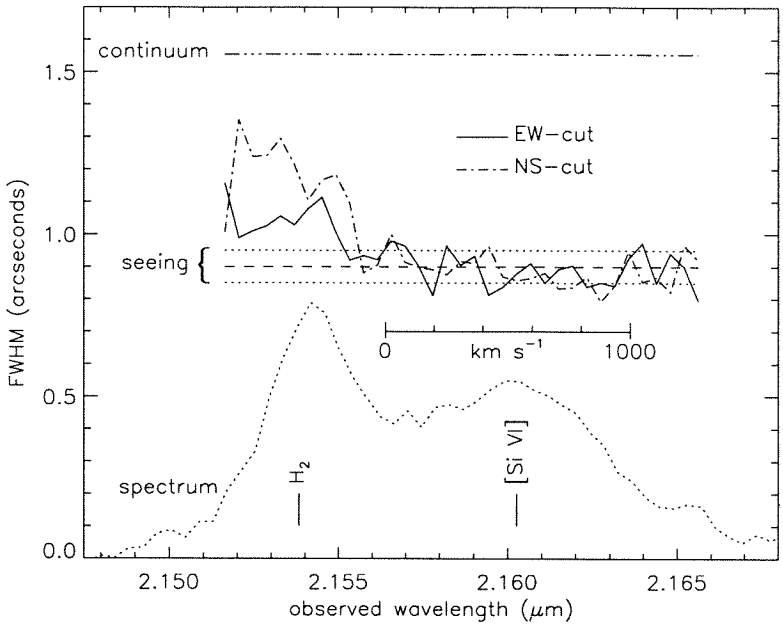

Figure 6.6: Spatial line extent as a function of wavelength for the H_2 1–0 S(3) and [Si VI] lines, showing the spatially unresolved nature of the [Si VI] emission in contrast to the spatially resolved H_2 emission. See the caption for Figure 6.3 for a description of plot features. The spectrum at bottom is a continuum subtracted version of that seen in Figure 6.4.

in Figures 6.2 and 6.5, mainly due to 20% better seeing and telescope focus in the latter (see Section 6.3). In Figure 6.5 the continuum appears to have a weak extension to the SW. The line images are clearly more compact than the continuum, and the near perfect symmetry of the [Si VI] emission suggests that the structure seen in the continuum is real, and simply not resolved in Figure 6.2. Indeed the central contours of the continuum image in Figure 6.5 appear much more symmetric than the outer contours. The line images are created in the same manner as those in Figure 6.2, with the spectral range encompassing points within ± 200 km s^{-1} of the line center. The [Si VI] emission line is slightly more compact than the neighboring H_2 line. An elliptical Gaussian fit to each of these line images yields FWHM sizes (average of major and minor axes) of $1\farcs1$ for H_2 and $0\farcs9$ for [Si VI], with ellipticities (major-to-minor axis ratios) of 1.30 and 1.03, respectively. The H_2 elongation appears to be real, with a position angle on the sky of $\sim 30°$—similar to the disk orientation implied by the rotation axis, discussed in Section 6.4.3.

A more detailed look at the difference in spatial distribution between H_2 and

[Si VI] can be seen in Figure 6.6, which, like Figure 6.3, plots the spatial FWHM of the line distribution in the east–west and north–south directions as a function of wavelength. Referring to the line profile at the bottom of Figure 6.6, it is clear that throughout the wavelength range corresponding to the broad [Si VI] emission, both the x and y widths are consistent with the seeing limit, indicating that the entire [Si VI] emission line is spatially unresolved. The similarity in widths in the two orthogonal directions further demonstrates the symmetry of the PSF during the observation. On the short wavelength side of the [Si VI] emission, the spatial profile broadens, marking the location of the H_2 line. Here, the north–south extent is larger than the east–west extent, owing to the elongated nature of the emission at a 30° position angle.

6.4.3 Rotation of H_2 & Narrow Paα

Taking advantage of the coexistence of two-dimensional spatial plus spectral information, we can construct velocity fields of the line emitting gas. At each spatial pixel, the wavelength of the peak line emission is computed, and converted to a velocity. Figure 6.7 displays the velocity fields obtained in this manner for IRAS 08311−2459 in both the Paα and H_2 1–0 S(3) lines. Both lines exhibit a velocity structure indicative of pure rotation. The color scale is the same for both maps, through which it is seen that the rotation is not only aligned along the same axis for the two lines, but with roughly the same amplitude. The rotation axis is at a position angle of $\sim 110°$, implying a projected disk major axis of $\sim 20°$, consistent with the observed elongation observed for H_2. Figure 6.7 also shows the rotation curves obtained for both lines, in a 0.″67 wide aperture through the galaxy center at a 20° position angle. Though the molecular hydrogen data has much more scatter than does the Paα curve, it is clear that the two constituents—the narrow Paα and the H_2 emission—share the same physical rotation.

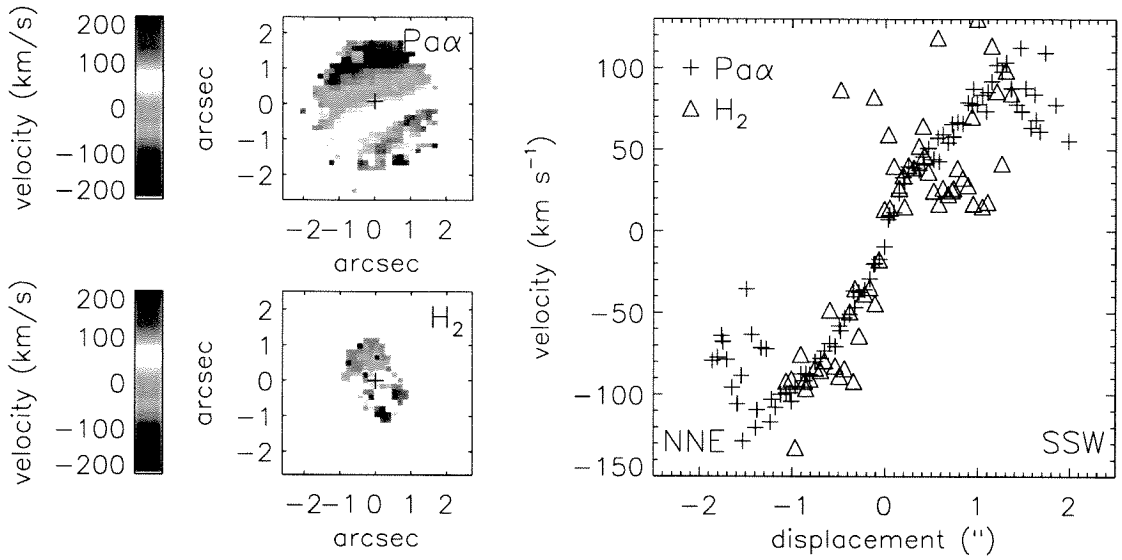

Figure 6.7: Velocity fields of both the Paα and H_2 lines. To the left are color images representing the velocity of the peak emission, with red indicating redshift, etc. A clear rotational signature is seen in both. To the right is a position-velocity plot for both species along a 0.″67 "slit" at a position angle of 20°, corresponding to the angle of maximum velocity gradient. The Paα points (plus symbols) trace out a very clean rotation pattern, and the noisier H_2 points (triangles) follow the same profile.

6.5 Discussion

Combining visible light spectroscopic surveys of ULIRGs (e.g., Kim, Veilleux, & Sanders, 1998; Veilleux, Kim, & Sanders, 1999) with infrared observations (Veilleux, Sanders, & Kim, 1997, 1999), it is found that 20–25% of ULIRGs can be characterized as containing AGN. The visible studies generally utilize the [O III]/Hβ line ratio as the primary diagnostic, while infrared observations of AGN are based on the presence of broad atomic recombination lines, and occasionally of [Si VI]. ULIRGs are known to sometimes harbor galactic-scale superwinds (Heckman, Armus, & Miley, 1990), which could potentially contribute to the observed broad line wings and to [Si VI] emission through powerful shock excitation. The present integral field data for IRAS 08311−2459 argue for a simple picture of a compact AGN surrounded by a more diffuse starburst—at least some of which is occurring in a rotating disk around the nucleus. While massive outflows and expanding shells are present in some ULIRGs, they may not be ubiquitous. The PIFS data on IRAS 08311−2459 highlights the

important role that integral field spectroscopy can play in untangling the dynamics and excitation of the circumnuclear gas in ULIRGs.

Without considering the contribution of the He I line to the Paα line profile, one might conclude that the apparently blue-asymmetric profile of Paα indicates the presence of outflow phenomena, as is often the case for asymmetric line profiles (e.g., Heckman, Armus, & Miley, 1990; Wang et al., 1997). Knowledge of the He I line on the blue side of Paα, with expectations on typical ULIRG line strengths (Murphy et al., 2000, Chapter 2, this thesis) allow us to understand the Paα profile as the combination of a symmetric Paα line mixed with a similarly shaped He I line. The Gaussian line fits give the He I line 4% of the Paα flux—consistent with expectations from the ULIRG population (Chapter 2). Perhaps the strongest evidence that the He I line is contributing to the total line profile comes from the observation of increased spatial extent coincident with the red side of the He I line, shown in Figure 6.3.

The symmetry of the Paα line profile resulting from proper accounting of the He I flux, together with the fact that both sides of the profile's broad wings are spatially unresolved (< 500 pc) in the full two-dimensional sense, argue that the broad emission does not arise from an outflow, or wind, phenomenon. Additionally, the red and blue wing components show no relative displacement greater than the $0\farcs05$ level, or ~ 100 pc, further supporting this conclusion. We believe the broad emission arises from the near vicinity of an obscured AGN, and that this component is not associated with the rotating, narrow emission discussed at the end of this section.

The presence of [Si VI] in the spectrum of IRAS 08311−2459 is a clear indicator of high energy processes at work in the galaxy. [Si VI] is not commonly seen in ULIRGs, even those exhibiting broad Paα emission (Murphy et al., 1999, Chapter 3, this thesis). Veilleux, Sanders, & Kim (1997, 1999) see evidence for [Si VI] in a few ULIRGs, though blending with the comparably strong H_2 1–0 S(3) line prohibits accurate estimates of flux contributions. The [Si VI] emission in IRAS 08311−2459 measures $6 \times 10^7 L_\odot$ in luminosity, uncorrected for extinction. This is among the most luminous [Si VI] emission line yet observed, although relative to the bolometric luminosity only slightly more luminous than that found in nearby Seyfert galaxies

(Marconi et al., 1996). The [Si VI]-to-bolometric luminosity ratio for quasars is the same as that seen in IRAS 08311−2459, based on the template QSO spectrum in Murphy et al.

Main sequence stars are incapable of producing significant flux at 167 eV—the requirement for creating Si^{5+}. Only ionizing radiation from an AGN or fast shocks can account for the [Si VI] emission (Contini & Viegas, 1992). It is difficult to differentiate between these excitation processes observationally, though a diagnostic utilizing the [Fe VII] $\lambda 0.6087$ μm line was explored by Marconi et al. (1996), in which all instances of [Si VI] detections in Seyfert galaxies are attributed to photoionization.

The integral field data contribute a clue to the nature of the [Si VI] excitation. The molecular hydrogen emission—often associated with collisional excitation—has a significantly different morphological character than the [Si VI] emission. Namely, the H_2 line originates from a region roughly one kpc larger than that of [Si VI]. The underlying morphology of violent shocks in major mergers is not clearly understood. However, if the [Si VI] were shock excited—perhaps tracing out a physical boundary along a shock front—and the H_2 emission was associated with the same shock phenomenon, then a large fraction of the molecular hydrogen emission would likely originate from the near vicinity of the shock front (Draine & McKee, 1993), thereby sharing similar spatial structure with the [Si VI] emission. This arrangement is not seen in the integral field data, which casts doubt on the existence of a powerful shock as the primary source of [Si VI] excitation.

Further differentiating the H_2 distribution from that of [Si VI] is the fact that the H_2 emission is extended along the direction of maximum velocity gradient—the inferred disk axis. A simple quadrature decomposition of the H_2 $1\farcs0 \times 1\farcs3$ FWHM ellipse with a $0\farcs9$ seeing disk yields an intrinsic aspect ratio of greater than 2:1, with a long axis extent of about 1.6 kpc. The rotation curve derived from the H_2 emission is in complete agreement with that seen for Paα (Figure 6.7), suggesting that the narrow Paα and H_2 emission arise from the same rotating disk. Similar observations of elongated molecular gas concentrations coincident with disk orientation and rotation are also seen in CO data of luminous infrared galaxies (Bryant & Scoville, 1999).

A picture emerges wherein both the H I and H_2 narrow line emission arises from a rotating, star forming disk. Alternatives for production of the narrow line emission include X-ray photoionization of the disk from the central source, or photoionization of the gas from "precursor" radiation emanating from a powerful shock front. Both of these alternatives suffer from the same difficulty of requiring the ionizing radiation to penetrate almost 1 kpc through the disk in order to produce the large scale emission observed. If indeed star formation is occurring on a scale of $\sim$ 1.5 kpc—as the H_2 emission indicates—then IRAS 08311−2459 boasts star formation on a significantly larger scale than the 100–300 pc typically seen among ULIRGs in mid-infrared studies (Soifer et al., 2000).

If the narrow, rotating component of the Paα line is produced by young stars in a disk, the implied star formation rate (SFR) is $\sim$ 75 $M_\odot$ yr^{-1}, assuming an intrinsic Hα/Paα line flux ratio of 8.6 (Osterbrock, 1989, Case B with $n_e = 10^4$ cm^{-3} and $T = 10000$ K) and a conversion between Hα luminosity and SFR following Kennicutt (1983). Of course, this conversion takes into account neither the extinction at Paα, nor the contribution of the central AGN to the narrow Paα line flux—both of which may be significant in this system, yet would effect our SFR estimate in opposite senses.

If the entire far-infrared luminosity in IRAS 08311−2459 were attributable to star formation, then one may compute the expected total star formation rate by two methods. The first, from Scoville & Young (1983), puts a lower bound on the bolometric luminosity by assuming that the luminosity is dominated by stars converting protons to He via the CNO cycle, and that the rate of mass reduction is the rate at which stars are forming. This approach yields an expected SFR of $\sim$ 200 $M_\odot$ yr^{-1}. The other method, from Hunter et al. (1986), integrates the total stellar luminosity output to produce an estimated SFR of 650 $M_\odot$ yr^{-1}, assuming all of the stellar luminosity is reprocessed into infrared emission ($\beta = 1$ in their model). Therefore, it is likely that either there is a large amount of star formation that remains obscured at 2 μm, or that the hidden AGN is a substantial contributor to the infrared luminosity in this system. Given the presence of the unresolved, relatively strong [Si VI] emission we favor the latter interpretation, though with an estimated SFR of 75 $M_\odot$ yr^{-1}, star formation

could clearly contribute a significant portion of the total luminosity.

6.6 Conclusions

Integral field spectroscopy of the suspected AGN-powered ULIRG, IRAS 08311−2459, provides important constraints on the nature of the line emitting regions in this galaxy. The evidence presented can be reasonably explained by the presence of a bona-fide quasar embedded within a disk of star formation in the post-merger system. Both components contribute significantly to the total energy production in the galaxy. The salient points derived from these data are:

1. The low velocity emission of Paα, along with H_2, has been identified with a rotating disk of material with a diameter of $\sim$ 1.5 kpc. It is likely that widespread star formation is responsible for the observed narrow line emission from this region.

2. Broad emission is seen in both Paα and [Si VI], with a projected FWHM$\approx$ 1000 km s^{-1}. The broad emission is spatially unresolved ($<$ 500 pc) in both species. Both lines are spectrally symmetric, and there is no observed spatial offset between the red and blue wings of the broad Paα emission. Outflow phenomena are therefore unlikely to account for the high velocity emission, with an AGN being the preferred source of the [Si VI] and broad Paα emission.

We thank Michael Strauss for his role in the early stages of the Caltech effort in studying ULIRGs. The wavelength reference for the [Fe II] line was provided by James Graham. We also thank the night assistant at Palomar, Rick Burruss, for assistance in the observations. T.W.M. is supported by the NASA Graduate Student Researchers Program, and the Lewis Kingsley Foundation. This research is supported by a grant from the National Science Foundation.

Appendix 6.A Functional Line Fits

Functional line and continuum fits have been applied to the extracted nuclear spectra of IRAS 08311−2459, and displayed in Figures 6.1 and 6.4. In each case, the continuum is fit with a linear function, and all lines except for Paα are fit with a single Gaussian profile. Attempting to fit Paα with a single Gaussian resulted in an obviously inadequate fit, but the resulting parameters are useful in fitting weaker atomic lines. The signal-to-noise ratio in the weaker lines does not justify the use of multiple component fits, yet their underlying profiles are expected to closely resemble Paα. The single-fit Paα has a central velocity of 30147 km s^{-1} and a FWHM of 415 km s^{-1}; accounting for an instrumental resolution of 230 km s^{-1}, this translates to an intrinsic line width of 345 km s^{-1}. These numbers become the constraints used, where necessary, for the low ionization atomic lines.

The Paα spectrum contains three observable emission features, fit with four Gaussian profiles—two for Paα itself. It was found to be necessary to fix the He I line center and width according to the single-Gaussian Paα values as discussed above, leaving only the flux as a free parameter. The two components in the Paα line fit were unconstrained, and tended to repeatably settle to the same parameters despite factors of two modifications to the initial estimated values. The H_2 1–0 S(4) line was constrained to share the 380 km s^{-1} line width found for the H_2 1–0 S(3) line, as discussed below. The plot of fit residuals at the bottom of Figure 6.1 shows that the two-Gaussian fit for Paα does a passable job, but excess emission on the blue side well above the noise level demonstrates the approximate nature of the fitting business. For this reason, the separate components in the Paα fit are not to be taken as individual, distinct physical components, but rather as a tool for gaining a qualitative feel for the nature and symmetry of the broad emission. Table 6.1 lists the line properties and their fit parameters.

The H_2+[Si VI] spectrum contains three lines, each fit with a single Gaussian profile. The fit was performed placing no constraints on the three parameters of each line fit. Figure 6.4 shows the result of the combined fit, and Table 6.1 gives the

Table 6.1. Fit Parameters & Line Fluxes

Line	$cz - 30150$ (km s^{-1})	FWHM[a] (km s^{-1})	Equiv. Width (nm)	Aperture[b] Correction	Total Flux[c] ($\times 10^{-18}$ W m^{-2})
He I	0[d]	339[d]	0.78	0.21[e]	3.6
Paα narrow	−9	156	9.3	0.19[f]	45.9
broad	16	779	12.0	0.30[f]	34.1
H_2 1–0 S(4)	7	376[d]	0.48	0.26[e]	1.7
Brδ	−14	297	0.97	0.15[f]	3.5
H_2 1–0 S(3)	28	384	2.6	0.21[f]	7.4
[Si VI]	−66	1066	5.6	0.30[f]	10.8

[a]Deconvolved via simple quadrature by the instrument resolution of 230 km s^{-1} in the Paα spectrum, and 220 km s^{-1} in the H_2 + [Si VI] spectrum.

[b]Ratio of flux within extraction aperture (i.e., spectra presented in Figures 6.1 and 6.4) to total line flux encompassing detected extent of line emission. For strong lines with spectrally distinct spatial characteristics (as determined from Figures 6.3 and 6.6), this ratio is measured directly from the datacube.

[c]Aperture-corrected flux scaled from line fit, within 5 arcsec aperture; 15% estimated error.

[d]Held fixed in line fit.

[e]Calculated based on line FWHM and aperture size assuming symmetric Gaussian spatial profile.

[f]Measured directly from datacube.

properties of the individual line fits.

Bibliography

Bryant, P. M. & Scoville, N. Z. 1999, *Astronomical Journal*, 117, 2632

Contini, M. & Viegas, S. M. 1992, *Astrophysical Journal*, 401, 481

Draine, B. T., & McKee, C. F. 1993, *Annual Review of Astron. & Astrophys.*, 31 373

Genzel, R., Lutz, D., Sturm, E., Egami, E. et al. 1998, *Astrophysical Journal*, 498, 579

Heckman, T. M., Armus, L., & Miley, G. K. 1990, *Astrophysical Journal Supp. Series*, 74, 833

Hunter, D. A., Gillett, F. C., Gallagher, J. S., Rice, W. L., & Low, F. J. 1986, *Astrophysical Journal*, 303, 171

Kennicutt, R. C. 1983, *Astrophysical Journal*, 272, 54

Kim, D.-C., Veilleux, S., & Sanders, D. B. 1998, *Astrophysical Journal*, 508, 627

Kleinmann, S. G., & Hall, D. N. B. 1986, *Astrophysical Journal Supp. Series*, 62, 501

Lutz, D., Veilleux, S. & Genzel, R. 1999, *Astrophysical Journal*, 517, L13

Marconi, A., van der Werf, P. P., Moorwood, A. F. M., & Oliva, E. 1996, *Astronomy & Astrophysics*, 315, 335

Murphy, T. W., Armus, L., Matthews, K., Soifer, B. T., Mazzarella, J. M., Shupe, D. L., Strauss, M. A., & Neugebauer, G. 1996, *Astronomical Journal*, 111, 1025

Murphy, T. W., Soifer, B. T., Matthews, K., Kiger, J. R., & Armus, L. 1999, *Astrophysical Journal*, 525, L85, Chapter 3, this thesis

Murphy, T. W., Matthews, K., & Soifer, B. T. 1999, *Publ. of the Astron. Soc. of the Pacific*, 111, 1176, Chapter 5, this thesis

Murphy, T. W., Soifer, B. T., Matthews, K., Armus, L., & Kiger, J. R. 2000, in preparation, Chapter 2, this thesis

Oliva, E., & Origlia, L. 1992, *Astronomy & Astrophysics*, 254, 466

Osterbrock, D. E. 1989, *Astrophysics of Gaseous Nebulae and Active Galactic Nuclei* (Mill Valley: University Science Books)

Persson, S. E., Murphy, D. C., Krzemenski, W., Roth, M., & Rieke, M. J. 1998, *Astronomical Journal*, 116, 2475

Rigopoulou, D., Spoon, H. W. W., Genzel, G., Lutz, D., Moorwood, A. F. M., & Tran, Q. D. 1999, *Astronomical Journal*, 118, 2625

Sanders, D. B., Soifer, B. T., Elias, J. H., Neugebauer, G., Matthews, K. 1998, *Astrophysical Journal*, 328, L35

Scoville, N. Z., & Young, J. S. 1983, *Astrophysical Journal*, 265, 148

Soifer, B. T., Neugebauer, G., Matthews, K., Egami, E., et al. 2000, *Astronomical Journal*, 119, 509

Strauss, M. A., Davis, M., Yahil, A., & Huchra, J. P. 1990, *Astrophysical Journal*, 361, 49

Strauss, M. A., Huchra, J. P., Davis, M., Yahil, A., Fisher, K. B., & Tonry, J. 1992, *Astrophysical Journal Supp. Series*, 83, 29

Veilleux, S., Sanders, D. B., & Kim, D. -C. 1997, *Astrophysical Journal*, 484, 92

Veilleux, S., Kim, D. -C., & Sanders, D. B. 1999, *Astrophysical Journal*, 522, 113

Veilleux, S., Sanders, D. B., & Kim, D. -C. 1999, *Astrophysical Journal*, 522, 139

Wang, J., Heckman, T. M., Weaver, K. A., & Armus, L. 1997, *Astrophysical Journal*, 474, 659

Chapter 7 Age-Dating Ultraluminous Infrared Galaxies Along the Merger Sequence

7.1 Chapter Overview

Near-infrared spectroscopy using the new Palomar Integral Field Spectrograph is presented for the Paα line in four ultraluminous infrared galaxies. The resulting integral field datacubes reveal line emission possessing a wide range of complex spatial morphologies, often quite different from the appearance of the continuum. The velocity fields are equally diverse in nature, often failing to resemble typical modes of galactic motion. In most cases, we are able to establish the geometry of the merger, and thus the current time along the merger sequence at which we are viewing the system. The resulting range in estimated ages, some of which are very young encounters ($\sim 5 \times 10^7$ yr), is not predicted by merger models, which can produce high rates of star formation either 1–2 $\times$ 10^8 years after the first encounter or very late ($\sim$ 10^9 yr) in the merger process. Even in the very young mergers, despite a sample selection based on extended line emission, the ultraluminous activity appears to be centrally concentrated on the nucleus of one of the progenitor galaxies. The extinction to these concentrations is high, usually at least 1 magnitude at the wavelength of Paα.

The presence of a population of very young ultraluminous mergers, together with the majority of ultraluminous infrared galaxies existing in the final stages of merger activity, indicates that the ultraluminous galaxy phase is at least bimodal in time. An evolutionary scenario is proposed for ultraluminous infrared galaxies, wherein the far-infrared luminosity may undergo multiple ultraluminous bursts during the course of the encounter. A substantial fraction of the merger lifetime may be spent in a phase

identified with the less powerful luminous infrared galaxy class.

In addition to this unifying theme, we see a variety of interesting phenomena in the individual mergers including possible formation of tidal dwarf galaxies; star formation rates exceeding 5 $M_\odot$ yr^{-1} in young tidal tails; a post-encounter disk which obeys the Tully-Fisher relation; a large scale emission line nebula possibly associated with a massive outflow; and an apparently single merging system possessing two distinct kinematical axes belying the presence of a second, obscured galaxy.

7.2 Introduction

Ultraluminous infrared galaxies (ULIRGs) are among the most luminous sources in the universe, with infrared luminosities of $L_{ir} \gtrsim 10^{12} L_\odot$. Imaging surveys of ULIRGs find that the vast majority are morphologically distorted, with spatial structures indicative of galactic mergers (Sanders et al., 1988; Murphy et al., 1996; Clements et al., 1996). ULIRGs are found to exist in various states of merging, from well separated galaxies to single nucleus systems that appear to have completed their nuclear coalescence. From millimeter wavelength studies of molecular gas in ULIRGs, it is found that the constituent galaxies are typically large, gas-rich spirals (Sanders, Scoville, & Soifer, 1991; Downes, Solomon, & Radford, 1993; Solomon et al., 1997). In general terms, the merging process destabilizes the orbits of gas within the galaxies, leading to accumulation of gas in the central potential of the individual galaxies or merger remnant. The resulting high concentrations of molecular gas stimulate the production of stars, or in some cases fuel a massive central black hole. In addition, cloud-cloud collisions may occur within the disrupted disk, or as the galaxies begin to overlap, leading to widespread star formation. Veiled by the vast quantities of dust mixed with the molecular gas, these energetic processes are seen via dust-reprocessed light at far-infrared wavelengths, and are held to be responsible for the extreme luminosity of these systems (see Sanders & Mirabel, 1996, for a review).

A new integral field spectrograph (Murphy, Matthews, & Soifer, 1999) working at near-infrared wavelengths on the Palomar 200-inch Telescope has provided a new

way in which to look at the properties of the interstellar medium in these galaxies. Combining imaging capabilities with longslit spectroscopy, the integral field data permit simultaneous acquisition of spatial and velocity information of emission line gas over a two-dimensional region on the sky. For complex sources such as ULIRGs, the advantage over more traditional longslit or narrow-band techniques is substantial.

This chapter presents the spatial and kinematic structures of the Paα line emission nebulae in four ULIRGs of various morphological types. Most of the line emission traced out in these galaxies is spectrally unresolved at the resolutions involved. Therefore, this chapter concentrates simply on the morphologies and peak velocities of the line emission structures. The four galaxies are taken from the 2 Jy sample of Strauss et al. (1990, 1992), and are selected for their peculiar spatial and velocity structures in line emission as seen in two-dimensional near-infrared spectra taken from Murphy et al. (2000) (Chapters 2 and 4). Table 7.1 lists the properties of the four ULIRGs in the present sample. All cosmology-dependent calculations in this chapter assume $H_0 = 75$ km s^{-1} Mpc^{-1} and $q_0 = 0$.

The selection of the sample ULIRGs based on their complexity biases our sample in several fundamental ways. First, the morphology biases the sample galaxies to early merger states in which the constituent galaxies have been disrupted, yet have not coalesced into a post-merger remnant. Also, the selection of galaxies with complex morphologies, and whose two-dimensional spectra show large spatial extent and non-trivial velocity structures yields a sample that presents the greatest challenge to understand. Despite the latter effect, the integral field spectroscopy has allowed some insight into the nature of these highly disturbed systems. One additional consequence of the selection based partly on morphological complexity seems to be a greater likelihood of chance superpositions, and alignment with the orbital plane. This appears to play a role in at least two of the four galaxies in the sample.

The lack of uniformity in the galaxy selection is also apparent in the textual presentation. The amount and nature of discussion on each galaxy varies according to the special circumstances of each case. Following the descriptions of individual galaxies, a general discussion section explores some of the overall conclusions from this diverse

body of observations.

7.3 Observations & Data Reduction

7.3.1 Integral Field Data

Observations were made using the Palomar Integral Field Spectrograph (PIFS) situated at the $f/70$ Cassegrain focus of the 200-inch Hale Telescope. A description of this instrument along with general observing procedures can be found in Murphy, Matthews, & Soifer (1999). The $5\farcs4 \times 9\farcs6$ field of view was rotated to optimally cover the extent of the galaxies as seen in broadband infrared light, with two contiguous field positions required to cover the larger structure of IRAS 01521+5224. All observations were made in clear conditions. See Table 7.2 for a summary of the observations. The $R \approx 1300$ resolution mode was used to obtain spectra centered on the redshifted Paα line in each galaxy. Separate sky exposures were alternated with the on-source integrations, with individual integration times of 300 s. A positional dither pattern was employed for the sequence of integrations enabling recovery of seeing-limited spatial resolution in the cross-slit direction. Observations of nearby stars for the purpose of evaluating the point spread function (PSF) accompanied the spectral observations. Wavelength calibration is provided through a combination of OH airglow lines and arc lamp spectra taken at the time of observation. Atmospheric opacity and spectral flat-fielding are compensated simultaneously using the light from a G dwarf star, spread uniformly across the field of view.

Data reduction consists of first performing the sky subtraction, interpolating static bad pixels and cosmic ray artifacts, division by the G star spectrum, and multiplication by a blackbody matched to the G star's temperature. Spatial and spectral distortions are then corrected using previously generated distortion maps appropriate for the particular grating setting. Co-registration of the slits in the spatial dimension is based upon observation of the G star with its light extended perpendicular to the slit pattern by chopping the telescope secondary mirror in a triangle-wave pattern. The two-

Table 7.1. ULIRG Sample

Galaxy	Morphological[a] Classification	cz[b] (km s^{-1})	L_{ir} [c] $10^x L_\odot$	physical scale[c] (kpc arcsec^{-1})
IRAS 01521+5224	double	23931	11.95	1.38
IRAS 10190+1322	double	22867	11.98	1.33
IRAS 17574+0629	single ?	32701	12.10	1.82
IRAS 20046−0623	single ?	25219	12.02	1.45

[a]Based on K_s band morphology

[b]Measured from this dataset at the position of the continuum peak coinciding with the strongest Paα emission

[c]Assumes $H_0 = 75$ km s^{-1}, and $q_0 = 0$

Table 7.2. Integral Field Observations

Galaxy	Date	Integration Time	Seeing	P.A.	$\lambda_{\mathrm{Pa}\alpha}$ (μm)
IRAS 01521+5224S	15 November 1999	3600 s	0.″8	87°	2.0248
IRAS 01521+5224N	15 November 1999	2400 s	0.″8	87°	2.0248
IRAS 10190+1322	24 March 1999	2400 s	0.″8	65°	2.0189
IRAS 17574+0629	24 July 1999	2400 s	0.″9	51°	2.0806
IRAS 20046−0623	25 July 1999	1200 s	0.″75	90°	2.0337

dimensional spectra from the eight slits are placed into the three-dimensional datacube according to the positional dither pattern, with a common wavelength axis established by the calibration lines. Residual OH airglow lines are removed by subtracting a scaled version of the raw sky spectrum, with typical scalings of $\sim$2% in absolute value, sometimes as large as 10%. Photometric variability among individual integrations is compensated by small scaling adjustments such that the object flux is consistent from one integration to the next. A more detailed description of these general procedures may be found in Murphy, Matthews, & Soifer (1999).

In the data presented here, the pure continuum images are constructed directly from the integral field datacube, avoiding spectral regions associated with OH airglow emission or poor atmospheric transmission. For each spatial pixel, a linear fit is made to the line-free portion of the continuum spectrum. The line images are formed by subtracting this continuum fit from the datacube, then summing in the spectral dimension over a range encompassing the line emission. Because they are extracted from the same datacube, the co-registration of the continuum and line images is implicit.

The velocity fields are constructed in the following manner. At each spatial pixel, the wavelength of the peak emission is computed, and converted to a velocity. Because spatial gradients of flux across the individual slits can mimic shifts in velocity, the morphology of the line emission at the line peak is used to assess these gradients and correct the peak velocity values. These corrections are typically no larger than 30–40 km s^{-1}. A "maximum Paα" image is also presented for each ULIRG in order to show weaker emission with greater sensitivity. This image, also continuum subtracted, represents a single spectral resolution element centered for each spatial pixel on the wavelength of maximum line emission intensity. In other words, this image extracts spectral information only around the peak line intensity, following the velocity indicated in the velocity field.

Photometric calibration was performed using the photometric system of Persson et al. (1998). Images of the standard stars were taken in the spectrograph's imaging mode through a K_s filter, and the total flux was compared to images of the science object taken in the same manner. The photometry is corrected for atmospheric opacity,

and for Galactic extinction based on dust measurements by Schlegel, Finkbeiner, & Davis (1998), and using the extinction law of Rieke & Lebofsky (1985). For each of the galaxies in this sample, near-infrared spectra were available (e.g., Murphy et al., 2000, Chapter 2, this thesis) from which to judge the continuum shape, so that the continuum flux density at Paα could be related to the continuum flux density in the center of the K_s bandpass. The photometric calibration was supplemented by similar procedures using the K_s imaging discussed below.

7.3.2 Supplementary Imaging

Continuum and narrow-band Hα+[N II] images accompany the integral field data, where available, in order to provide a better sense of the overall structure of the continuum and line emission light. Most of the near-infrared images were taken through the wide-open 10 arcsecond slit of the Palomar Longslit Infrared Spectrograph (Larkin et al., 1996), operating on the 200-inch Telescope, and using a 256 $\times$ 256 HgCdTe array with a pixel scale of 0.″167 pixel^{-1}. The near-infrared image of IRAS 20046−0623 was obtained using a 58 $\times$ 62 InSb array camera also operating on the 200-inch Telescope with a pixel scale of 0.″313 pixel^{-1}. Table 7.3 presents the parameters of these observations, all of which used K_s filters.

Visible light imaging is also presented for the four galaxies in this chapter, with r band and Hα+[N II] images obtained at the Palomar 60-inch Telescope. For IRAS 17574+0629 and IRAS 20046−0623, r band images are presented in Murphy et

Table 7.3. Infrared Imaging Observations

Galaxy	Date	K_s Exposures $\times$ Integration Time	Seeing
IRAS 01521+5224	25 November 1996	4 $\times$ 20 s	0.″8
IRAS 10190+1322	22 May 1997	4 $\times$ 10 s	0.″75
IRAS 17574+0629	3 August 1996	6 $\times$ 30 s	0.″7
IRAS 20046−0623	3 August 1993	8 $\times$ 20 s	0.″9

al. (1996), and duplicated here. The data reduction procedures for the r band images in this chapter are described in Murphy et al. The Hα+[N II] images were taken with narrow band filters $\sim$10 nm wide, using the r band images as the continuum reference. Data reduction for the narrow band images is similar to that for the r band images, followed by scaling, shifting, rotating, and subtracting the r band continuum images such that nearby stars were nulled on average. The r filter bandpass does contain the Hα light, but generally at $< 10\%$ of the total flux. Photometric calibration was accomplished by use of the spectrophotometric standards from Oke & Gunn (1983), correcting for atmospheric opacity, and for Galactic extinction by the same methods described at the end of Section 7.3.1. Table 7.4 presents a summary of the visible light observations. No Hα data exist for IRAS 10190+1322, and the r band image for this galaxy is unguided and taken through clouds.

7.4 Individual Objects

7.4.1 IRAS 01521+5224

7.4.1.1 Morphology of Continuum & Line Emission

IRAS 01521+5224 is a morphologically complex galaxy consisting of two primary galaxies and many clumps of distributed tidal debris. The two nuclei are separated by 5.″5 (7.6 kpc projected separation) at a position angle of 25°. Figure 7.1 shows

Table 7.4. Visible Observations

Galaxy	Date	r Exposures × Integration Time	Hα Exposures × Integration Time	Seeing
IRAS 01521+5224	21 January 1996	2 × 600 s	2 × 900 s	1.″5
IRAS 10190+1322	9 December 1996	1 × 300 s	...	2.″3
IRAS 17574+0629	3 June 1994	1 × 600 s	1 × 900 s	1.″2
IRAS 20046−0623	7 November 1993	2 × 600 s	3 × 900 s	1.″5

both a K_s band image and an r band image of the galaxy, along with an image in Hα+[N II]. The nature of the lower surface brightness features is not immediately clear from these images. These features could be tidal tails, small companion galaxies, or fragments of the primary galaxies not entirely resembling the typical pair of tidal tail features. The r band image demonstrates that the morphological features are contained within a relatively small region. In other words, there is no obvious tidal tail component extending away from the main concentration of light. Comparing to simulations of galaxy mergers (e.g., Mihos & Hernquist, 1996; Barnes & Hernquist, 1996), one surmises that this morphologically complex system is seen shortly after a close encounter, most likely its first. Note the absence of a distinct southern nucleus in the r band image, in contrast to the appearance of the well defined nucleus in the K_s image. The Hα+[N II] image, which has a dramatically different morphology from the continuum emission, is discussed in relation to the Paα images in Section 7.4.1.2.

Figure 7.2 presents the PIFS data of IRAS 01521+5224, showing images of the pure continuum, total Paα line emission, maximum Paα distribution, and the velocity field of the Paα emission peak. The large extent of this galaxy required observations in two adjacent and contiguous fields, the positions of which are indicated in Figure 7.1. The Paα emission distribution is markedly different from that of the continuum light. The Paα peak is coincident with the southern galaxy continuum peak, though it is not symmetrically distributed about the continuum peak position. The northern galaxy nucleus has very little Paα emission associated with it, identifying the southern nucleus as the primary source of star formation, and thus of the far-infrared emission.

The off-nucleus Paα emission is extended over an impressive 15 kpc, mostly arranged in clumps along a ring-like structure—much like that seen in the Hα image. More so than in the continuum images, the line images seem to trace out arcing, one-dimensional features appearing very much like tidal tails. Combined with the velocity information provided in the integral field datacube, the morphology of these features enables an understanding of the current merger geometry of the system, as will be discussed in Section 7.4.1.3.

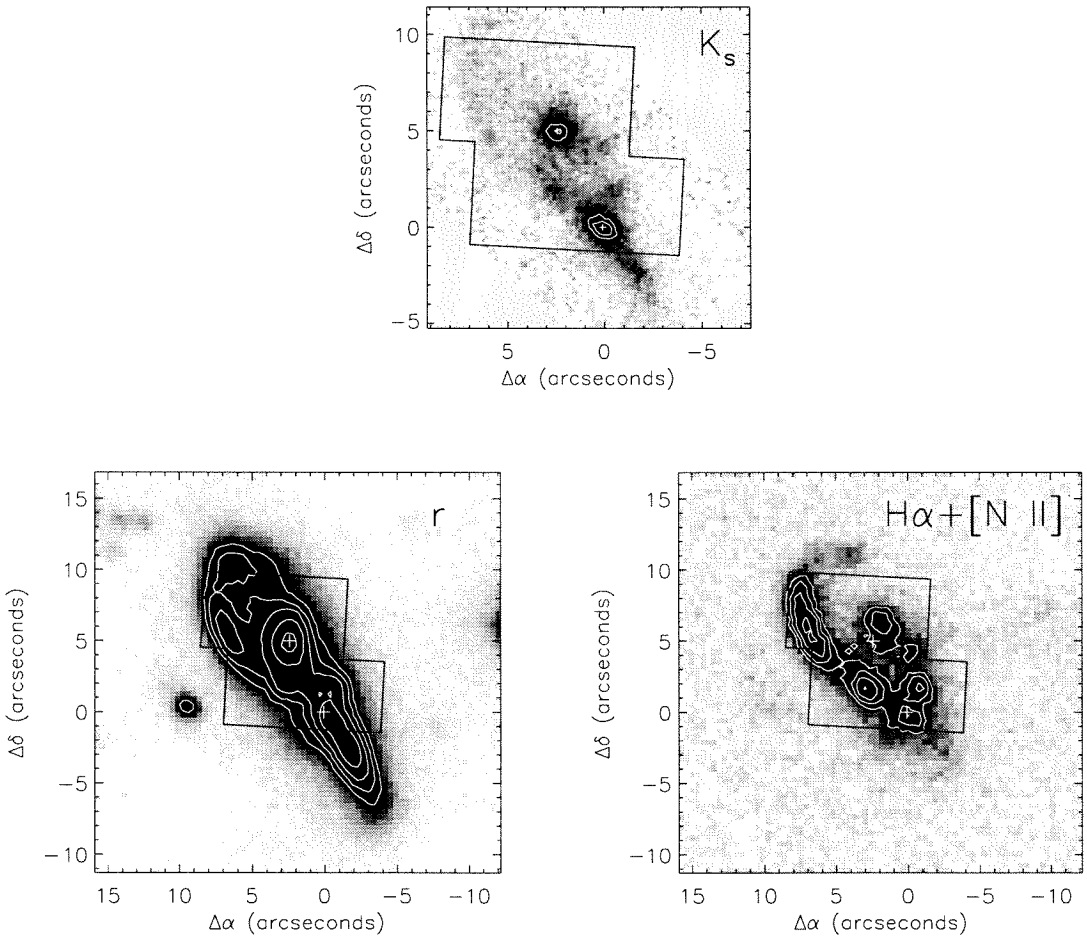

Figure 7.1: Continuum images of IRAS 01521+5224 in K_s (top) and r (lower-left) bands. These images portray a dramatically disturbed ULIRG, with four r band peaks visible, two of which are the obvious nuclei in the infrared image. Note the lack of any major features extending beyond the main grouping. A narrow band image in Hα+[N II] is presented at right, showing many emission peaks arranged along a ring-like structure. The irregular box outline shows the region observed with the integral field spectrograph. North is up, and east is to the left.

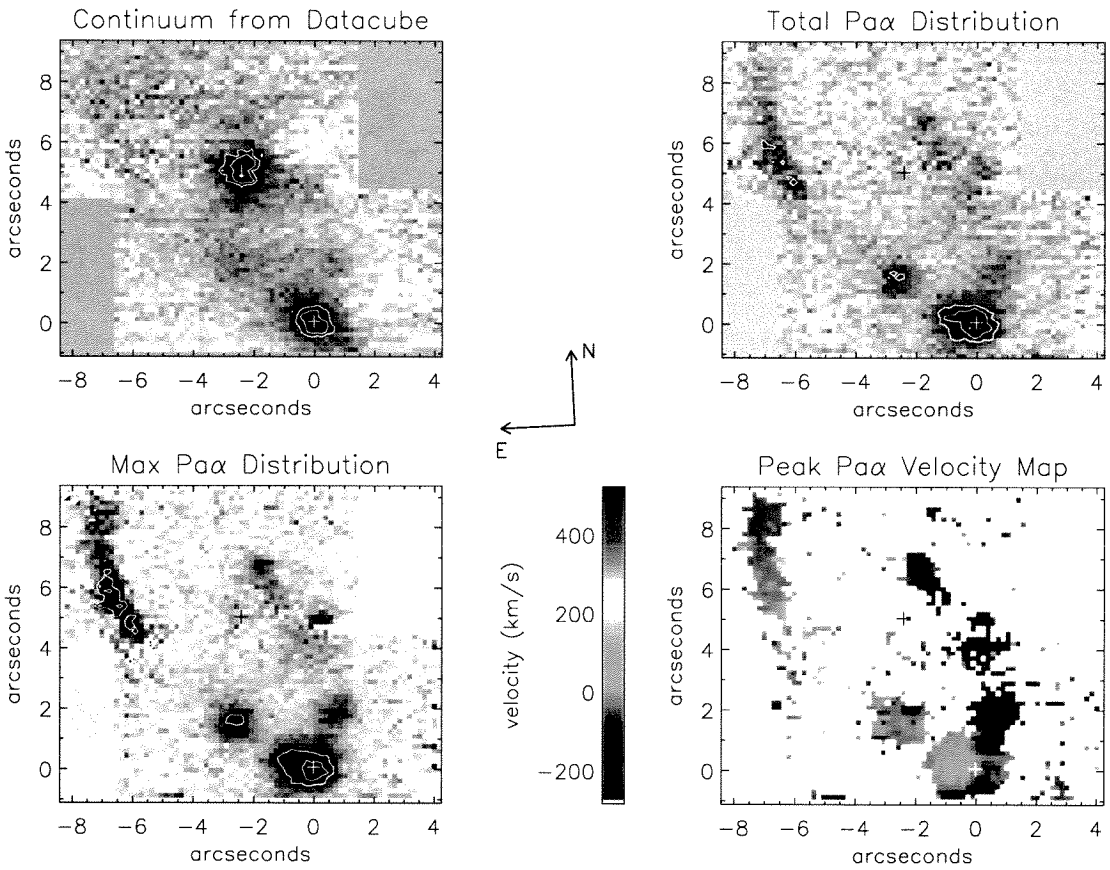

Figure 7.2: PIFS data on the central region of IRAS 01521+5224. At top left is the line-free continuum image reconstructed from the datacube. At top right is the total Paα emission, continuum subtracted, summed from -325 to $+480$ km s^{-1} relative to the systemic velocity. A higher contrast Paα image, following the peak emission as described in the text, is shown at lower left. Finally, the velocity field is represented at lower right as a color diagram, with red representing redshifted gas, and blue representing blueshifted gas. The velocity scale is indicated to the left of the plot. In all images, the continuum peak locations are indicated by crosses. Field orientation is indicated by the arrows, with "left" corresponding to a position angle of 87°.

7.4.1.2 Extinction & Star Formation

Using the Hα image together with the Paα image, one may compute line ratios to derive measures of the extinction to the various regions in the galaxy. The total Paα flux within the PIFS field is $\gtrsim 2.1 \times 10^{-17}$ W m^{-2}, compared to 1.3×10^{-16} W m^{-2} for Hα+[N II] in a similar aperture. Assuming an intrinsic Hα/Paα line ratio of 8.6 (Osterbrock, 1989, Case B, $n_e = 10^4$ cm^{-3}, $T = 10000$ K), a lower limit can be placed on the average extinction to the source of $A_V > 0.5$ mag. The extinction at Paα is interpolated from the extinction law of Rieke & Lebofsky (1985), with $A_{P\alpha\alpha} = 0.145 A_V$. This and all other extinction measures in this chapter assumes no contribution from [N II], which is often half the strength of Hα in star forming regions. Including a flux contribution at this level adds another half-magnitude to the estimated visual extinction. As such, all extinction values are stated as lower limits. The southern nucleus itself garners 30% of the total Paα flux, though a quick inspection of Figure 7.1 shows that the Hα flux from this nucleus contributes a much smaller fraction of the total Hα line emission. The extinction to the southern nucleus line emission measures $A_V \gtrsim 2.5$ mag.

The hydrogen recombination flux can be used to calculate the star formation rate (SFR) in the galaxy, following the prescription for converting Hα flux to the global SFR outlined in Kennicutt (1983). The Paα line is used rather than the Hα line, as it suffers much less from extinction. An extinction-corrected Hα flux, used in calculating the SFR, is inferred from the Paα flux using an intrinsic line ratio of 8.6, as introduced above. The Paα flux is uncorrected for extinction, such that the SFR estimate performed in this manner represents a lower limit. For the entire ensemble of Paα emission recorded in the PIFS field, the SFR is computed to be $\gtrsim 20\ M_\odot$ yr^{-1}. As suggested above, the southern nucleus is responsible for about 30% of this total, with the rest split between the isolated clumps seen in Figure 7.2.

A surprisingly large amount of star formation appears to be occurring in isolated clumps distributed along the tidal tails. Tidal tails generally do contain gas, as they are composed of material rather indiscriminately pulled from a contiguous region of

the parent galaxy, within which stars and gas are mixed into similar distributions. Star formation is known to occur in tidal tails (Chromey et al., 1998), and tails are, in fact, seen to contain many young, blue stars (Tyson et al., 1998; Reshetnikov, 1998). The star formation rate estimated for the bright Paα clump in the NE tail is $\sim 6\ M_{\odot}\ \mathrm{yr}^{-1}$, which is unusually high for such environments (Hibbard & van Gorkom, 1996; Duc & Mirabel, 1998; Duc et al., 2000). Typical star formation rates in tidal clumps and tidal dwarf galaxies are estimated at 0.05–0.2 $M_{\odot}\ \mathrm{yr}^{-1}$. The highest previously observed star formation rates in tidal tails also occurs in ULIRGs, with about 0.5 $M_{\odot}\ \mathrm{yr}^{-1}$ (Mihos & Bothun, 1998). The unusually high rate of star formation may be the result of gas compression induced by crossing orbits in the forming tail. The work by Toomre & Toomre (1972) points out that shortly after tidal tails develop, the tidal material on the inside of the tail overtakes the outer material. The crossing orbits that result very likely compress the gas within the tail, leading to heightened star formation. This scenario, which is relevant only for very young tails, is consistent with the estimated age of the IRAS 01521+5224 encounter, as discussed in Section 7.4.1.4.

7.4.1.3 Merger Geometry

The Paα distribution, to a greater extent than the continuum morphology, is suggestive of tidal tails, insofar as the emission is stretched out into arc-like structures. However, the tidal tail interpretation becomes confused by the appearance of two line-emitting structures emerging from the north side of the southern nucleus, with no obvious relationship between the northern nucleus and tail structures. Moreover, a third extension is seen to the southwest of the southern nucleus in the continuum images of Figure 7.1. While a single galaxy can develop two tidal extensions, this generally involves an $m = 2$ structure, with diametrically opposing features termed "tail" and "bridge" (cf. Toomre & Toomre, 1972). If the visible structures are indeed associated with tidal tails originating from the southern galaxy, then one possible explanation which must be considered is that the southern nucleus represents a post-merger remnant from two previously distinct galaxies. Such multiple encounters are not rare among ULIRGs, as seen in a large sample of Hubble Space Telescope images

by Borne et al. (2000). For the reasons described below, it is more likely that the two visible galaxies are the principal progenitors, and that the southern nucleus is not a post-merger galaxy. The strongest support for this argument owes to the very young appearance of the tidal debris field. In the geometrical scenario that is developed below, the eastern tail does indeed come from the southern nucleus, while the western tail is associated with the northern galaxy, and aligned with the southern nucleus by chance superposition.

The integral field data contain velocity information for the line emission, as represented in Figure 7.2, which can be used to assist our understanding of the merger geometry. Figure 7.3 shows a plot of velocity as a function of position around the loop of Paα emission. The loop was synthesized from five linear segments, with breakpoints and position angles indicated on the plot. The left edge of the plot begins in the NE, with a counter-clockwise progression through the southern nucleus, then back to the north. The southern nucleus occupies the plot origin, and exhibits the maximum velocity gradient. Overall, there exists a ~ 550 km s^{-1} velocity difference between the most redshifted and most blueshifted gas. Note in particular the NE tidal clump, with an average velocity of 300 km s^{-1} relative to the southern nucleus. Section 7.4.1.4 discusses the nature of this clump.

While no significant Paα flux appears at the position of the northern nucleus in Figure 7.2, some nuclear emission is visible in the two-dimensional spectra. Figure 7.4 shows four two-dimensional spectra around the northern nucleus extracted from the datacube at four position angles. Not only is the nuclear emission visible, but a weak velocity gradient can be seen, perhaps most clearly along the 90° and 45° position angles, indicating a redshift to the ENE. The central velocity of the line emission on the northern nucleus is blueshifted from the southern peak by 50 km s^{-1}, with a rotational velocity amplitude of < 100 km s^{-1}.

The following sequence of arguments builds a stepwise reconstruction of the likely full phase state of the merging system. This framework must be prefaced with the caveat that direct observation of only three dimensions of information prohibits a unique definition of the full geometry, so that various symmetries and comparisons

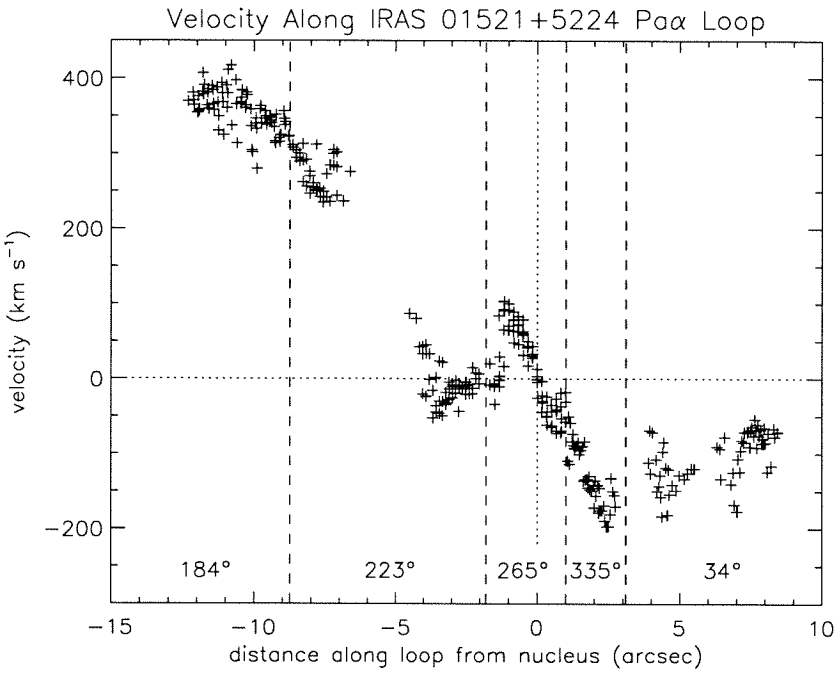

Figure 7.3: Segmented position-velocity plot along the loop of Paα emission in IRAS 01521+5224, starting in the northeast, and winding around in a counter-clockwise sense, through the southern continuum peak, then back to the north. The loop was broken into five straight-line segments, with breakpoints and position angles represented on the plot, delineated by dashed lines. The displacement is plotted as accumulated linear distance along the segments. The southern nucleus is at a position of zero on the horizontal axis, displaying a rotation curve with an amplitude of about 150 km s^{-1}. Note the fast moving clump at upper left (NE clump), with a velocity gradient projecting directly away from the southern nucleus center. This clump was broken into two linear slit segments owing to its spatially curved nature.

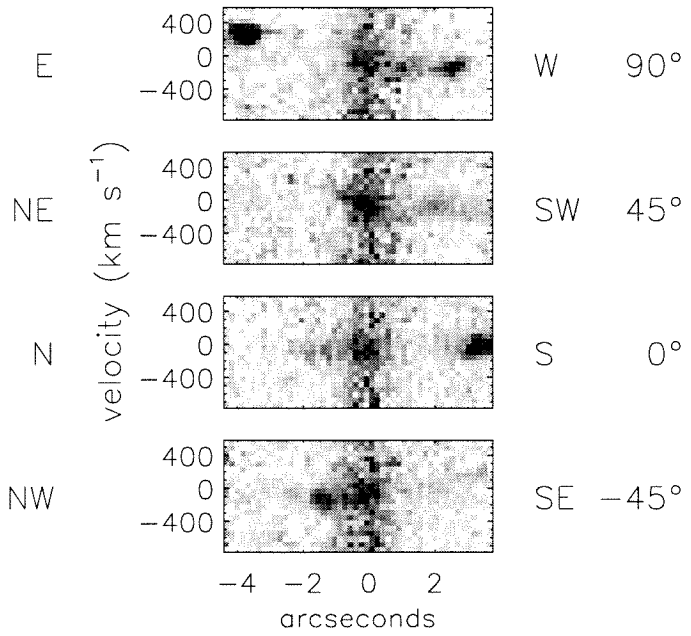

Figure 7.4: Four two-dimensional spectra of the northern nucleus extracted from the IRAS 01521+5224 datacube corresponding to four slits at position angles of 90°, 45°, 0°, and −45° show that there is Paα emission associated with this nucleus. The vertical scale is in km s^{-1} relative to the southern nucleus velocity. The continuum from the nucleus can be seen in the center of each spectrum, with line emission appearing at about −50 km s^{-1}. A slight rotation is inferred from the apparent tilts of the line emission, with the maximum gradient probably at a position angle between 45° and 90°.

to models are necessary to make progress. But the proposed geometry is in excellent agreement with the observables, so we believe this logical chain to be justified by its apparent success.

The first statement posits that the IRAS 01521+5224 merger is very young, and is being viewed shortly after closest approach (pericenter). This is believed to be the case based on the tight confinement of optical flux in the r band image of Figure 7.1. We see tidal tails in this system, but they do not extend very far. Comparison to models (Mihos & Hernquist, 1996; Barnes & Hernquist, 1996) leads to an estimated age of 5–10 $\times 10^7$ yr. This time scale typically puts the merging galaxies at a distance of about twice the pericentric separation, perhaps 10–20 kpc.

The southern nucleus is likely embedded in a nearly edge-on disk. This is supported by four observations. First, the K_s continuum image in Figure 7.1 shows an extension on either side of the nucleus at a position angle of roughly 45°, most prominently visible to the southwest. Second, the edge-on geometry is consistent with the extinction apparent both from the lack of an identifiable nucleus in the visible light image, and from the measured extinction of $A_V \approx 3$ to the line emitting region. The third observation concerns the orientation of the rotation signature in the southern nucleus. The velocity field around the southern nucleus appears at first to have an east-west gradient in Figure 7.2, though a 45° rotation plane is not inconsistent with the observed field. In fact, close inspection of the velocity field shows blue emission along the southern edge of the nucleus. Figure 7.5 shows a position-velocity plot from a 0.″5 "slit" through the nucleus at a position angle of 45°. The velocity field appears to have a clean rotation signature, with an amplitude slightly greater than the corresponding curve in Figure 7.3, which is taken along a position angle of 85°. The fourth piece of evidence comes from an understanding of tidal tail kinematics. As discussed in Appendix 7.A, the maximum velocity available to the tail material is roughly determined by the sum of the disk circular velocity and the orbital velocity. With typical values for both these components of around 200 km s^{-1}, it is most likely that the 250–400 km s^{-1} line emission to the NE is seen in almost pure recession, with little motion in the plane of the sky. As the tail forms in a plane close to the galaxy's

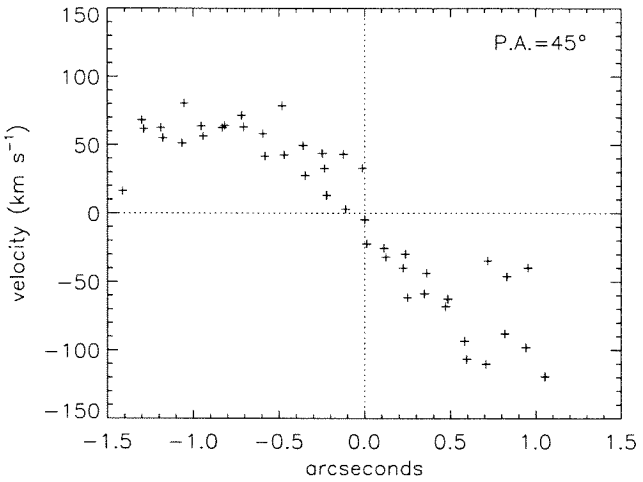

Figure 7.5: Position-velocity plot of the southern nucleus in IRAS 91521+5224 along a slit position angle of 45°. The gas motion along this axis looks like simple rotation, in support of the notion that the southern galaxy's disk axis lies along this direction.

spin plane, the purely recessional motion of the tail argues that our vantage point lies close to the galaxy spin plane. Each of these four pieces of evidence support the claim that we are viewing the southern galaxy at an inclination to our line of sight very near 90°.

The inclination of the southern galaxy is slightly *less* than 90°, as evidenced by the curvature of the tail. Some galaxies are observed with tidal tails that are perfectly straight along their entire lengths (cf. Mrk 273, Sanders et al., 1988), indicating that our line of sight lies close to the spin plane. Tidal tails always possess intrinsic curvature, simply as a result of material being strewn from a rotating disk. The sense of curvature in the IRAS 01521+5224 eastern tail indicates that the normal to the spin plane points to the southeast, with a small component of the normal vector pointing *towards* us.

The very slight velocity difference of 50 km s^{-1} between the two nuclei can be used to restrict our viewing angle relative to the orbital plane and galaxy trajectories. Operating on the assumption that these galaxies are very shortly past closest approach, the actual velocity difference of the nuclei is probably several hundred km s^{-1}. To observe a 50 km s^{-1} difference indicates that our viewing angle is likely confined to the small shaded region depicted in Figure 7.6. This two-dimensional region is

in reality a three-dimensional volume of revolution about the relative velocity vector of the galaxies. Half of this region can be excluded because of the observed tail properties from the southern nucleus. In the schematic diagram of Figure 7.6, the allowed region lies to the upper right, placing the northern galaxy in the foreground. This viewpoint results in the southern galaxy's tidal tail receding from the observer. Though the diagram depicts the southern galaxy's tail as lying in the orbital plane, there could in principle be some misalignment of the spin/tail plane to the orbital plane, which is addressed below. One may question the general orientation of the tidal tails as depicted in Figure 7.6. Half of the possible orientations can be eliminated by the knowledge that soon after pericenter, tidal tails are found on the side of the galaxy opposite the perturbing galaxy. the direction the tail extends from the parent galaxy depends on the direction of disk rotation. The sense of rotation assumed in the diagram is prograde for two reasons. First, retrograde galaxies are not efficient at making tails (Toomre & Toomre, 1972; Mihos & Hernquist, 1996), and second, the observed velocity field is in agreement with the prograde assumption. The prograde geometry carries the additional advantage that it is more adept at transporting gas to the central regions of the galaxy in order to fuel an early nuclear starburst. Prograde and retrograde encounter geometries are defined and discussed in Appendix 7.A.

The final argument establishing orbital geometry and viewing angle is that we are probably witnessing the merger from a viewpoint that is very close to the orbital plane. This claim is difficult to prove conclusively, but the arguments that follow present reasons why this scenario is attractive.

First, the current projected nuclear separation is about 8 kpc. Under the previous assumptions about time since pericenter, the galaxies are now probably separated by about twice the pericenter distance. If we were viewing the system from a vantage point close to the orbital plane normal, then this would imply a pericentric separation of a mere 4 kpc, describing a nearly head-on impact. With initially random galaxy motions, the probability distribution of pericentric distance is proportional to the square of that distance. Thus larger separations are far more likely. On the other hand, an encounter strong enough to result in ultraluminous activity must be at least

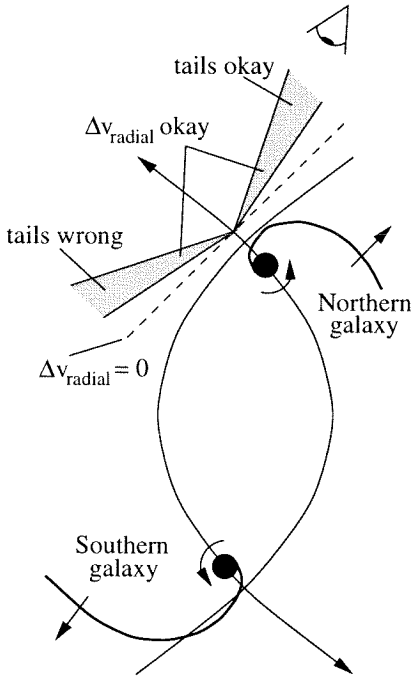

Figure 7.6: Schematic diagram of the likely orbital plane geometry of the IRAS 01521+5224 merger, indicating probable locations of our vantage point. The dashed line represents a plane from which the galaxies would currently show no relative radial velocity. The shaded grey region, when revolved about the current velocity vector, represents the region of space from which the northern galaxy is slightly blueshifted relative to the southern galaxy. Only from the upper right portion of this region do the tidal tails have the correct observed velocities.

close enough that the the disks pass close to the perturbing mass. Merger models capable of producing ultraluminous star forming activity (Mihos & Hernquist, 1996) typically choose a pericentric distance of around 10 kpc. For our purposes, we will assume that we are currently experiencing a projection factor of at least 1.5, such that the pericentric distance was at least 6 kpc. Looking at the diagram in Figure 7.6, we see that the only available viewing angle that allows significant projection, and subject to the constraints imposed by the shaded region, is close to the orbital plane.

A second attractive consequence of the claim that our vantage point lies close to the orbital plane concerns the projected position of the northern galaxy relative to the southern galaxy/tail system. We have established that our view on the southern galaxy is very near the spin plane. If the orbital plane and southern galaxy spin plane were much misaligned, the northern galaxy would now be seen at a position on the sky much further from the southern galaxy's tail.

A third argument is the observation that a purely prograde interaction for the southern galaxy would be maximally effective at providing a rapid supply of gas for a central starburst, and also most efficient at spinning off a strong tidal tail. Both phenomena appear to be occurring in IRAS 01521+5224. If our view from within the southern galaxy's spin plane also corresponds to the orbital plane, then the galaxy is indeed maximally prograde.

A schematic representation of our view on IRAS 01521+5224 is depicted in Figure 7.7. This diagram has an orientation following that in Figure 7.1, and clearly shows the constituent galaxies and their tail orientations.

Finally, appealing to the visual aids provided by merger simulations, the third panel in Figure 7.8 shows quite well the envisioned geometry of the IRAS 01521+5224 system. This view looks down on the orbital plane, but it is not difficult to imagine that a view of this same system from the upper right and just above the plane of the paper could mimic the view of the Paα emission seen in Figure 7.2, at least for the southern (background) galaxy. The northern galaxy, as discussed below, is not well represented in this model view. We should point out that this realized similarity came only *after* arriving at the above geometrical construct based purely on the observational data.

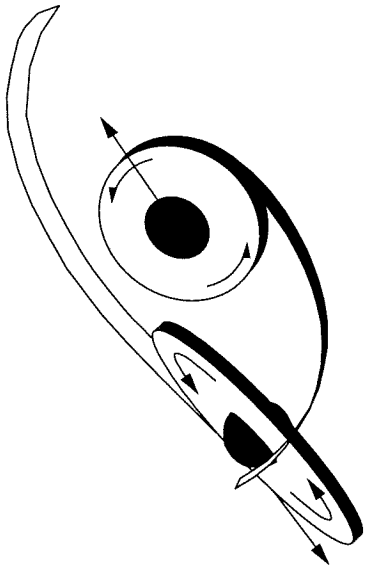

Figure 7.7: A schematic model of the IRAS 01521+5224 system, as seen from our viewpoint. The northern (upper) galaxy, nearly face-on, is in the foreground of the southern galaxy, which is seen nearly edge-on. The eastern tail spins off of the southern galaxy, and is seen in almost pure recession. The western tail, extending from the northern galaxy, is almost in the plane of the sky, explaining the very small observed velocity gradient along this tail. Bulges are placed in the diagram to approximate the appearance of the K_s image in Figure 7.1.

The existence of such a similar view in a model greatly reaffirms our belief that we understand the current state of the merger geometry in IRAS 01521+5224.

The assumed geometry posits that the southern galaxy is almost maximally prograde, yet at first glance, one may assume this galaxy to be retrograde based on the simple observation that the southern galaxy is redshifted with respect to the northern galaxy, and that the red side of the southern galaxy's rotation field is roughly to the north. Taken at face value, this orientation describes a retrograde geometry. The important lesson is that projection effects can easily hide the true nature of the orbital geometry. Referring to Figure 7.6, viewing this system from a direction only 30–45° clockwise from the shaded region to upper right would reverse the sense of relative velocities, resulting the identification of the southern galaxy with a prograde geometry via this simple-minded scheme. Clearly, more information about the three-dimensional system geometry is required before understanding the prograde/retrograde nature of an encounter.

We have not yet addressed the orientation of the northern galaxy relative to the

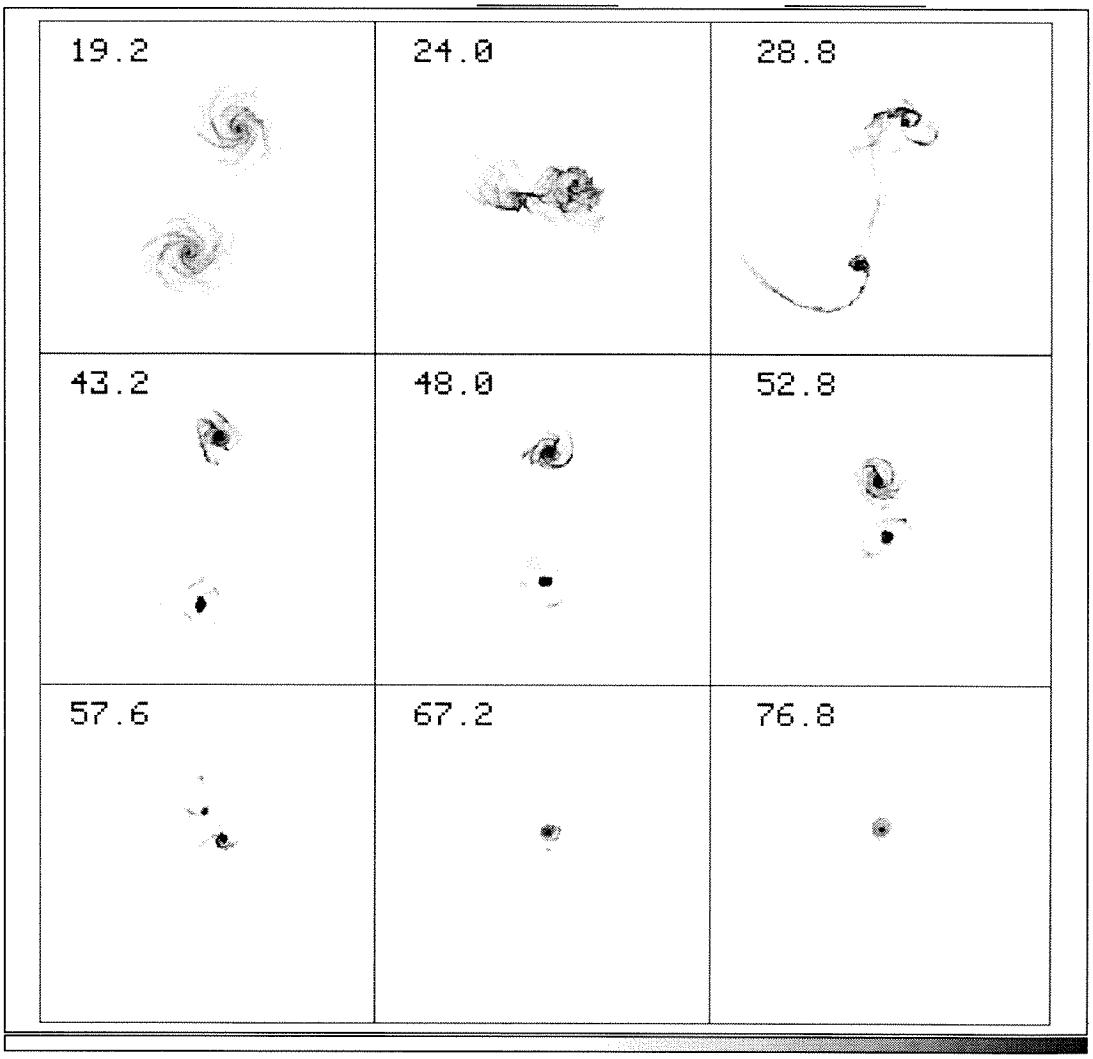

Figure 7.8: This figure, courtesy of J. C. Mihos, presents the estimated star formation morphology during a merger between purely prograde and retrograde galaxies. The prograde galaxy starts out at upper right, and occupies the lower position in panels 3–6. The time stamps are in units of 1.3×10^7 yr, and the box is 70 kpc on a side. These images, representing gas density, have much finer features than does the stellar material, though the two components form roughly the same global structures. The galaxies in this simulation have no central bulge component. The third panel looks very much like IRAS 01521+5224, and the sixth panel closely mimics the view of IRAS 10190+1322.

orbital plane. The purely retrograde geometry assumed by the upper galaxy in the third panel of Figure 7.8 does not seem to reproduce a model morphology consistent with the observed morphology of the northern galaxy in IRAS 01521+5224. Lacking significant Paα emission, this galaxy presents a greater challenge to our understanding. The western tail, which is uniformly blueshifted, probably comes off the northern galaxy much like the schematic representation in Figure 7.6. The blueshifted velocity and general morphology are in support of this picture. The southern end of the tail is superimposed on the southern nucleus, though the close match in velocities at this interface makes it impossible to distinguish two components in the spectra, so that the amount of contamination of the southern nucleus line flux is unknown, though probably not significant. One may object to this chance superposition in both position and velocity space, but two points should be considered. Most importantly, there also exists an excellent velocity match between the tail material and the northern nucleus velocity field, as indicated in Figure 7.4. In particular, note the smooth transition into the northern nucleus rotation curve exhibited by the clumps of gas to the the W and NW of the nucleus. The second point to bear in mind is that we are likely looking very close to the orbital plane, in which case chance superpositions are far more likely.

Having identified the western tail with the northern nucleus, a very important question arises. If the northern nucleus has thrown off a tail, then it probably is more prograde than retrograde. If this is true, then why is the northern nucleus not emitting a Paα flux comparable to the southern nucleus? There are few possible explanations for this. The first is that, based on the near absence of any velocity gradient along the western tail (cf. Figure 7.3), combined with the rather weak rotational signature of the northern nucleus, we are probably seeing this system nearly face on. Together with the assumption that we view this system from near the orbital plane, this galaxy would then be highly inclined, with a weakly prograde orientation based on the observed velocity gradients. The system appears to be enough prograde to have formed a significant tail, so the question remains as to why this galaxy is not as effective as its neighbor at transporting gas to the center where it can fuel a massive starburst.

It could be that the northern galaxy simply does not contain much gaseous mate-

rial. Alternatively, either the northern galaxy, being less prograde than the southern galaxy, requires more time to establish nuclear gas concentrations, or the northern galaxy contains a massive bulge which stabilizes the disk against the bar modes that act to drive gas toward the center (Mihos & Hernquist, 1996). The latter explanation lacks appeal based on the fact that the southern nucleus appears to contain a bulge, as seen in the K_s band image of Figure 7.1. Yet this galaxy has successfully managed to concentrate massive quantities of gas within the nuclear regions in a very short amount of time, judging by the compact Paα morphology and assumed ultraluminous star formation activity taking place within this nucleus.

7.4.1.4 Age of Merger & Dwarf Galaxy Formation

The elongated Paα feature in the northeastern corner of the field is appreciably redshifted relative to the southern nucleus. This clump (hereafter the NE clump) appears to lie in the tidal tail originating from the southern galaxy. The clump's velocity gradient, seen in Figure 7.3, points directly at the plot origin, corresponding to the position-velocity of the southern nucleus. Such an arrangement in position-velocity space would be expected in a very simplified model of tidal tail production, wherein a mass of material is extracted from a single location in the source at an instant in time. In such a scenario, the faster moving mass moves farther away in the same amount of time. In reality, tidal tails are not formed instantly, and the constituent mass is pulled out of a zone in the galaxy, rather than a single point. Yet overall the simulations of tidal tail formation by Toomre & Toomre (1972) are in agreement with this generic velocity profile.

At a projected distance of 10–15 kpc and a line-of-sight velocity of ~ 300 km s^{-1}, the luminous knot in the northeastern tidal tail may not be bound to the system. The deprojected distance between the southern nucleus and the middle of the NE clump is around 15 kpc, based on the geometrical projections discussed in Section 7.4.1.3. This distance is traveled in 5×10^7 yr at the measured recessional speed of 300 km s^{-1}, which is roughly consistent with the timescale for the formation of such structures in the galactic merger models (e.g., Mihos & Hernquist, 1996; Barnes & Hernquist,

1996). In fact, the third panel in Figure 7.8, which so closely resembles the geometry of IRAS 01521+5224, is 6×10^7 years after the previous panel, depicting the merger configuration around the time when the tidal features first formed.

The luminous knot of stars and line emission to the northeast could represent a dwarf galaxy in the making. If the clump is not tidally stable, this single feature could give rise to multiple dwarf galaxies. The notion that dwarf galaxies can be spawned in tidal tails was originally proposed by Zwicky (1956). Schweizer (1978) found observational evidence for this conjecture at the tip of the southern tidal tail in the Antennae (NGC 4038/9). More recent observations (Mirabel, Dottori, & Lutz, 1992; Hibbard & van Gorkom, 1996; Duc & Mirabel, 1998) have found additional evidence for the tidal clump-dwarf galaxy connection. Simulations verify the plausibility of self-gravitating conglomerates with masses similar to dwarf galaxies forming out of tidal tail material (Barnes & Hernquist, 1992; Elmegreen, Kaufman, & Thomasson, 1993). The NE clump, with its high velocity and high rate of star formation, may evolve into a detached, blue galaxy with dwarf galaxy properties.

For the dynamical investigations to follow, it is useful to have an estimate of the masses of the galaxies involved in the IRAS 01521+5224 merger. The total K_s magnitude of the system is about 12.7 mag, with roughly equal $K_s = 13.5$ mag contributions from each of the galaxies. This translates to an absolute magnitude of $M_{K_s} = -24.0$ mag for each of the individual galaxies. Using the Tully-Fisher relation to estimate the absolute magnitude of our Galaxy leads to a value of $M_H = -23.0 \pm 0.2$ mag (Binney & Merrifield, 1998), or $M_K = -23.3$ mag, using typical $H - K$ colors for late-type spirals (Yoshii & Takahara, 1988). Because the K_s band light traces the old stellar population, the factor of two flux ratio at K_s between each of the merging galaxies and the Milky Way is good indicator that the galaxies comprising IRAS 01521+5224 are each about twice the mass of the Milky Way.

Does the NE clump have enough kinetic energy to escape the bounds of the parent galaxy? The escape velocity at the edge of the Milky Way disk is $\sim$ 300 km s^{-1} (Trimble, 1999; Kulessa & Lynden-Bell, 1992). If the parent galaxy to the south is twice as massive as the Milky Way, and escape velocity scales as $\sqrt{M}$, then the NE

clump is close to critical escape velocity, especially at its northern end. Even if bound, the acquired angular momentum relative to the merger center of mass may be sufficient to place it into a very long-lived orbit.

The next natural question regards the self gravitation of the clump. Can this mass of material survive on its own without breaking into smaller clumps, given that the radial velocity from one end of the clump to the other spans 150 km s^{-1}? With $\sim$ 10% of the total system mass, as deduced simply from the K_s band flux ratio, one can compute the expected escape velocity within the clump. With the above mass assumptions, the expected escape velocity would be no less than 250 km s^{-1} for the tidal clump, based on a Milky Way escape velocity of 450 km s^{-1} in the solar neighborhood (Trimble, 1999), and a $\sqrt{M}$ scaling of escape velocity. This scaling implicitly assumes similar mass compositions of both parent and tidal clump, which is to say that the tidal clump has a significant fraction of its mass in the form of dark matter.

Simulations by Barnes & Hernquist (1992), however, show that mass concentrations in tidal tails do not capture much material from the dark matter halos of the parent galaxies, and that their mass-to-light ratios are near unity. Under the assumption that the parent galaxies have a total mass-to-light ratio of around twenty, the stars alone in the NE tidal clump amount to $\sim$ 2% of the Milky Way mass, again assuming that the two progenitor galaxies have total masses roughly twice that of the Milky Way, or $2 \times 10^{12} M_{\odot}$ each (Kulessa & Lynden-Bell, 1992). The clump therefore has about $4 \times 10^{10} M_{\odot}$ of stellar mass, plus some contribution from gas. With no dark matter of its own, the clump still has an escape velocity of $>$ 250 km s^{-1} at 2.5 kpc. This estimate is based on purely Keplerian dynamics, which is appropriate in the absence of a dark halo. Therefore, the clump itself is probably self-gravitating, and could potentially survive as a separate galaxy.

Questions remain about the tidal stability of the departing mass, as the gravitational influence from the nearby galactic nucleus will most likely act to disrupt the cohesion of the clump—regardless of its ability to self gravitate in the absence of such disturbances. This is especially evident in the sense that the northern end of the

NE clump may be moving faster than the escape velocity, while the southern end, at $\sim$ 250 km s^{-1}, almost certainly is not. Even if this structure is eventually separated into smaller groupings of mass, such groupings would have masses closer to those estimated for dwarf galaxies (Hunter & Gallagher, 1985; Thuan et al., 1999). A similar nascent dwarf galaxy has been observed at the tip of one of the tidal tails in the Antennae galaxy (Mirabel, Dottori, & Lutz, 1992), with a computed dynamical mass of $8 \times 10^9 M_\odot$.

7.4.2 IRAS 10190+1322

7.4.2.1 Morphology of Continuum & Line Emission

IRAS 10190+1322 is a double-nucleus ULIRG with a projected nuclear separation of 4.″0 (5.3 kpc) along a position angle of 65°. Figure 7.9 shows the appearance of continuum emission for the merging system. The r band image is of poor quality, and is included only to highlight the differing continuum flux ratio between nuclei in the visible and infrared bands. In the K_s image, the eastern galaxy appears more concentrated than the western galaxy, which shows diffuse emission surrounding the nucleus. While the nuclear components have a 1.6:1 flux ratio in 1.″5 box apertures, the eastern nucleus being brighter, the total continuum fluxes in larger apertures of the companion galaxies approach the same value. Each galaxy measures $K_s \approx 13.05$ mag in $4'' \times 5''$ and $5'' \times 5''$ apertures for the east and west galaxies, respectively. The r band ratio, by contrast, is 0.7:1 in similar apertures.

Figure 7.10 shows the appearance of the Paα emission across this system. The Paα emission is distributed similarly to the continuum emission, with a compact eastern source and a diffuse nebula surrounding the central peak of the western source. The ratio of Paα fluxes in small apertures around the nuclear concentrations is 3.2:1, while the total Paα flux for the two galaxies is roughly the same. Put another way, the line emission is much more diffuse in the western galaxy than in the eastern galaxy. The off-nucleus line emission in the western galaxy is fairly uniform across its large extent, except for a knot of emission between the two nuclei. It is worth noting that

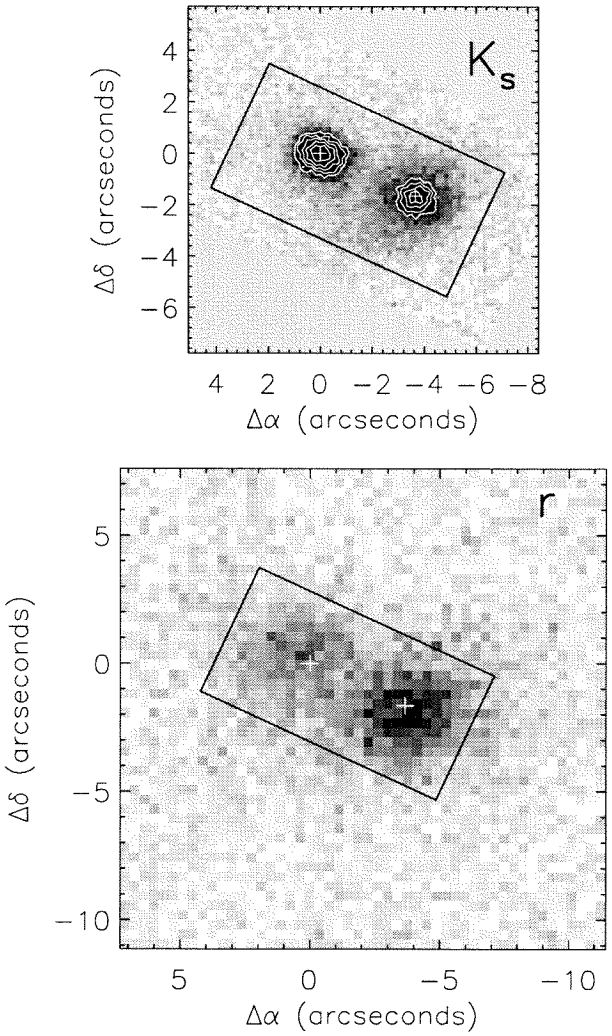

Figure 7.9: Continuum images of IRAS 10190+1322 in the K_s and r bands. The r band image was obtained in adverse conditions, preventing a meaningful investigation of large scale tidal debris. Note the reversal of which nucleus dominates between the visible and infrared images. The PIFS field is represented as a rectangular outline in both images. North is up, and east is to the left.

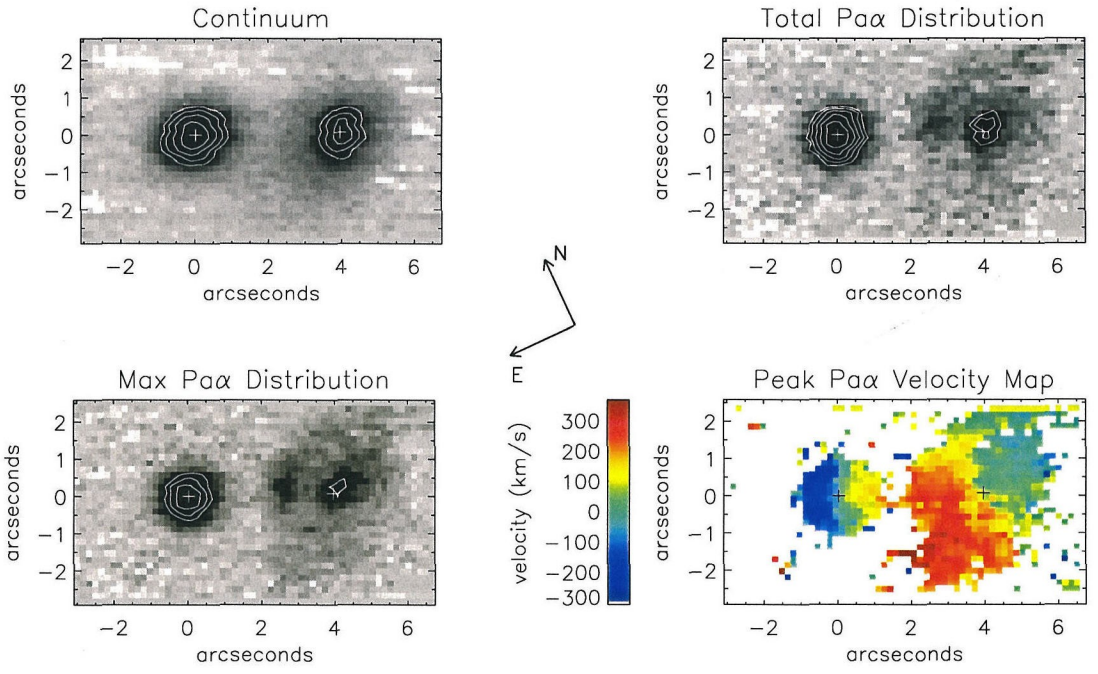

Figure 7.10: Integral field data for IRAS 10190+1322. Description of the four images follows from the Figure 7.2 caption. Crosses coincide with the positions of the continuum peaks. The field orientation is as indicated by the arrows, with "left" corresponding to a position angle of 65°.

a longslit spectrum of this pair of galaxies would have missed the bulk of the line flux in the western galaxy, leading one to potentially misjudge the relative importance of star formation in these two galaxies.

7.4.2.2 Star Formation & Extinction

Converting the total Paα flux in the PIFS field of 2.9×10^{-17} W m^{-2} into a star formation rate, as described in Section 7.4.1.2, yields a total system SFR of 27 $M_{\odot}$ yr^{-1}, split rather evenly between eastern and western galaxies. Most of the star formation is likely buried in the eastern nucleus, as judging by the 6 cm radio continuum from Crawford et al. (1996). The radio map has a 4″ resolution, coinciding with the separation of the two nuclei. The radio contours, peaking on the eastern nucleus, are stretched out toward the direction of the western nucleus. It is obvious that the eastern nucleus dominates the radio emission.

Under the assumption that the radio emission traces star formation, and that Paα

does the same, though subject to greater extinction, one may determine the amount of star forming activity hidden from view at 2 μm in the eastern nucleus. Gaussian smoothing the Paα emission map to a resolution of 4″, and altering the flux ratio of the eastern and western contributions, one finds that the radio map is consistent with a 2.5:1 flux ratio between the two components. Another way to put this is that the eastern galaxy's Paα emission on average suffers one magnitude more extinction than does the Paα emission in the western galaxy. Though no extinction estimate is available from Hα measurements, the foregoing estimate would result in a visual extinction around 7 mag. An actual measurement based on Hα flux would almost certainly be less than this since the dust is probably mixed with the line emission source, so that the Paα light is incapable of probing to the center of the obscuration.

Using the extinction estimated via the 6 cm map to adjust the above star formation rate estimate, the total SFR is closer to 50 $M_\odot$ yr^{-1}, with much of this obscured by heavy dust extinction in the eastern nucleus. This is still probably a lower limit to the star formation in the two galaxies, as extinction common to both galaxies is not taken into account. A rough estimate of the unaccounted star formation may be established by the expectation from Scoville & Young (1983) that the star formation rate will be greater than $\sim$75 $M_\odot$ yr^{-1} for a galaxy with a bolometric luminosity of $10^{12} L_\odot$.

7.4.2.3 Merger Geometry & Age

The velocity map of Figure 7.10 reveals an orderly kinematical pattern, characteristic of rotation of each of the two galaxies. The knot of Paα between the two nuclei does not stand out in the velocity map, showing that it is simply a local hot-spot in the disk of the western galaxy, and not a separate kinematical component. Rotation curves for each of these two galaxies are presented in Figure 7.11. The eastern galaxy has a total velocity amplitude of around 350 km s^{-1}, and the more extended western galaxy shows a 340 km s^{-1} velocity amplitude. The centers of these galaxies are moving at a relative velocity of $\sim$ 110 km s^{-1}, with the eastern galaxy blueshifted relative to the western galaxy. This configuration in velocity space suggests that the eastern galaxy is in a prograde configuration, while the western galaxy is retrograde (see Appendix 7.A

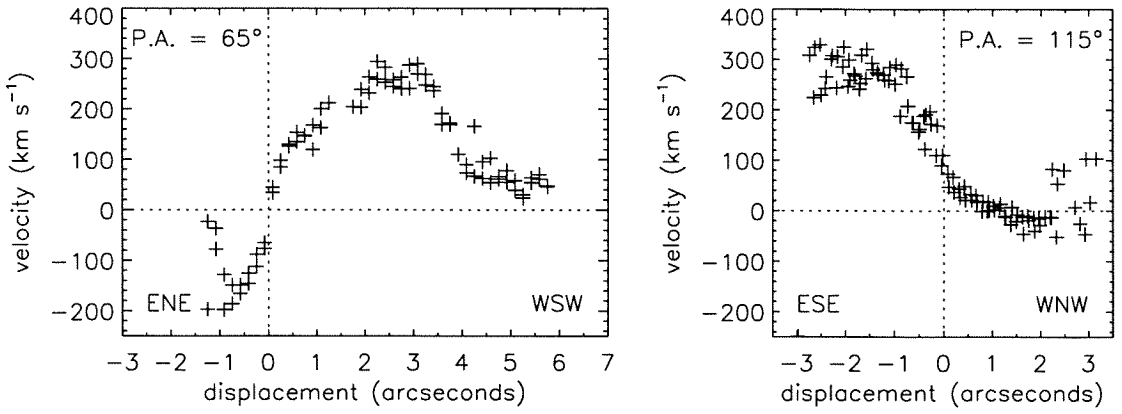

Figure 7.11: Position-velocity plots of IRAS 10190+1322, with the left hand figure representing a cut through both nuclei simultaneously, at the field's long-axis position angle of 65°. The curve on the right is along a position angle rotated 50° relative to the first, showing the full velocity extent of the western galaxy. Both plots share the same vertical scale, and the zero point is placed at the velocity of the eastern continuum peak.

for definitions of these terms). As illustrated in Section 7.4.1.3, one needs to exercise caution when determining the orbital orientation of interacting galaxies, as projection effects can misrepresent the true three-dimensional geometry of the encounter.

The extent of the Paα emission in the western galaxy is an impressive seven kpc across. The morphology is suggestive of a thin disk inclined at about 40°–50°, in which case the deprojected maximum velocity difference along the major axis implies a circular velocity full amplitude of 450–530 km s^{-1}. This value is consistent with the expectation from the H band Tully-Fisher relation based on the broadband absolute magnitude of the western galaxy (K_s =13.0 mag $\rightarrow$ $M_{K_s} = -24.6$ mag $\rightarrow$ $\Delta v \approx 530$ km s^{-1}, assuming $H - K \approx 0.8$ for ULIRGs, as in Carico et al. (1990)).

If indeed the eastern nucleus is prograde and the western galaxy is retrograde, the fact that the eastern galaxy is more compact in Paα than is the western galaxy, and additionally is the site of the most intense star formation, is in excellent agreement with expectations based on encounter geometry. A galaxy in a prograde configuration experiences a near resonance with the orbital motion of the companion, leading to exaggerated tidal disturbances. These disturbances often manifest themselves in the form of bar modes in the galactic disks, which serve to torque and funnel gas from the disk to the central regions of the galaxy (Mihos & Hernquist, 1996), creating a

compact central gas concentration. Retrograde encounters, on the other hand, are far less disruptive (see Toomre & Toomre, 1972), such that the disk is not significantly disturbed owing to an averaging out of tidal forces from the companion. Therefore, retrograde disks do not experience appreciable nuclear gas concentrations following the initial encounter. The match to the observational data for IRAS 10190+1322 is reassuring, and helps strengthen our identification of the eastern galaxy as prograde and the western galaxy as retrograde.

Despite the fact that the majority of the infrared luminosity can be associated with the eastern, prograde galaxy, the western galaxy nonetheless is hosting substantial star formation activity. With an estimated SFR of at least 13 $M_{\odot}$ yr^{-1}, the western galaxy appears to have had its global star formation enhanced by the merger activity. Though lacking a major nuclear starburst, the western galaxy may be experiencing slight disk perturbations that lead to cloud-cloud collisions throughout the disk, resulting in the observed widespread distribution of star formation in this galaxy.

Unlike many ULIRGs, IRAS 10190+1322 exhibits a rather organized kinematical state—that of simple rotation of the two components. Though it would seem that galaxies having endured a close encounter would not be able to maintain a rotation profile in agreement with the Tully-Fisher relation—as observed in the western galaxy—it is found that even rather disturbed disks do not lie far from this relationship (Mihos & Bothun, 1997; Barton, Geller, & Kenyon, 2000).

Comparison of the Paα distribution in IRAS 10190+1322 with the the sixth panel in Figure 7.8 reveals a fantastic morphological similarity. Simply viewing this scene from the upper right at an inclination of about 45° very nicely reproduces the observed scene, both in terms of morphology and velocity. The prograde-retrograde pair in the sixth panel of Figure 7.8 has already undergone one close encounter, and is very rapidly approaching the final merger.

It is worth pointing out that while the galaxies comprising IRAS 10190+1322 have been labeled prograde and retrograde—based on their velocity configuration and striking similarity to the prograde/retrograde model—these galaxies may not be precisely so. In particular, if these galaxies were perfectly prograde/retrograde, then

the orientation of their rotation axes would appear parallel from any vantage point. This is not exactly so with the galaxies in IRAS 10190+1322. In order to display the observed velocity field orientation, the eastern galaxy's spin axis could lie anywhere in the plane defined by the observed velocity axis and our vantage point. The eastern galaxy could in fact be inclined by as much as 90° to the orbital plane, and still present the observed velocity structure and rotation amplitude.

The inferred intermediate age of the IRAS 10190+1322 system—by comparison to the model represented in Figure 7.8—raises a few important issues. First, given the organized velocity fields and symmetric inner isophotes, what large scale morphological signatures might there be to indicate the age of a merger? Does IRAS 10190+1322 display such features, and is it unique among ULIRGs? How does one tell whether a double-galaxy merger is being seen early or late in the merging process? The second major issue is: why now? Why wait until just *before* the final merger to become ultraluminous?

A simple statement regarding the young versus old mergers is that tidal deformations in young mergers ought to be small and of high surface brightness. By the time the galaxies are approaching the final merger, tidal debris is expected to be strewn over relatively large scales, and thus lower in surface brightness. IRAS 10190+1322 does not, in fact, appear to have any significant tidal structure, though deep visible light imaging is not available for this system. The model that produced the remarkable resemblance to IRAS 10190+1322 in Figure 7.8 shows a diffuse stellar debris field around the retrograde galaxy (Mihos & Hernquist, 1996), with a few visible arcs, and a very diffuse tidal tail extending away from the prograde galaxy. Inspection of the digitized Second Palomar Sky Survey red plates does show some hint of tidal arcs around the western galaxy, but at a level only slightly above the noise.

The question regarding why IRAS 10190+1322 has waited until this late time in the merger sequence to initiate ultraluminous activity is difficult to answer. For reasons discussed at length in Section 7.5, the ultraluminous phase must be short relative to the merger timescale, assuming that star formation is responsible for the power generation. Because the disks have yet to experience their second disruptive passage,

it is assumed that the observed ultraluminous phenomenon is in response to the earlier encounter, perhaps 5×10^8 yr ago. Encounter geometry may play a significant role in determining the time of the onset of ultraluminous activity, though many other factors specific to the constituent galaxies including galaxy structure, initial gas distribution, etc. may also be very important. If, as suggested above, the eastern galaxy is not purely prograde, then the weaker tidal perturbation may require more time to develop significant accumulations of gas in the nuclear regions.

7.4.3 IRAS 20046−0623

7.4.3.1 Morphology of Continuum & Line Emission

The morphologically peculiar IRAS 20046−0623, displayed in Figure 7.12, has a continuum shape at first appearing like a warped disk, with one prominent tidal tail extending to the north at the eastern end of the continuum bar. The relative prominence of the tidal tail in the r band image as compared to the K_s image indicates that the tail probably contains a substantial population of young stars relative to the disk. The Hα image is seen to share a somewhat similar appearance to the r band continuum, though the peak line emission is located on the eastern end of the continuum bar. The tidal tail shows emission in Hα, though displaced about 0.″6 to the west of the continuum ridge.

The integral field data for IRAS 20046−0623 are presented in Figure 7.13. Here, the Paα emission and continuum emission are largely exclusive of each other, namely in that the peak of the Paα emission coincides with the outer edge of the continuum bar, and the peak of the continuum emission is located at the edge of the strong Paα structure. Faintly visible is a patch of Paα emission to the NE, coinciding with the Hα emission in the tidal tail.

7.4.3.2 Extinction & Star Formation

The total Paα flux in a $5'' \times 2.''5$ box, oriented east-west and capturing the majority of the Paα emission, measures 3.5×10^{-17} W m^{-2}. Comparing this to the Hα+[N II]

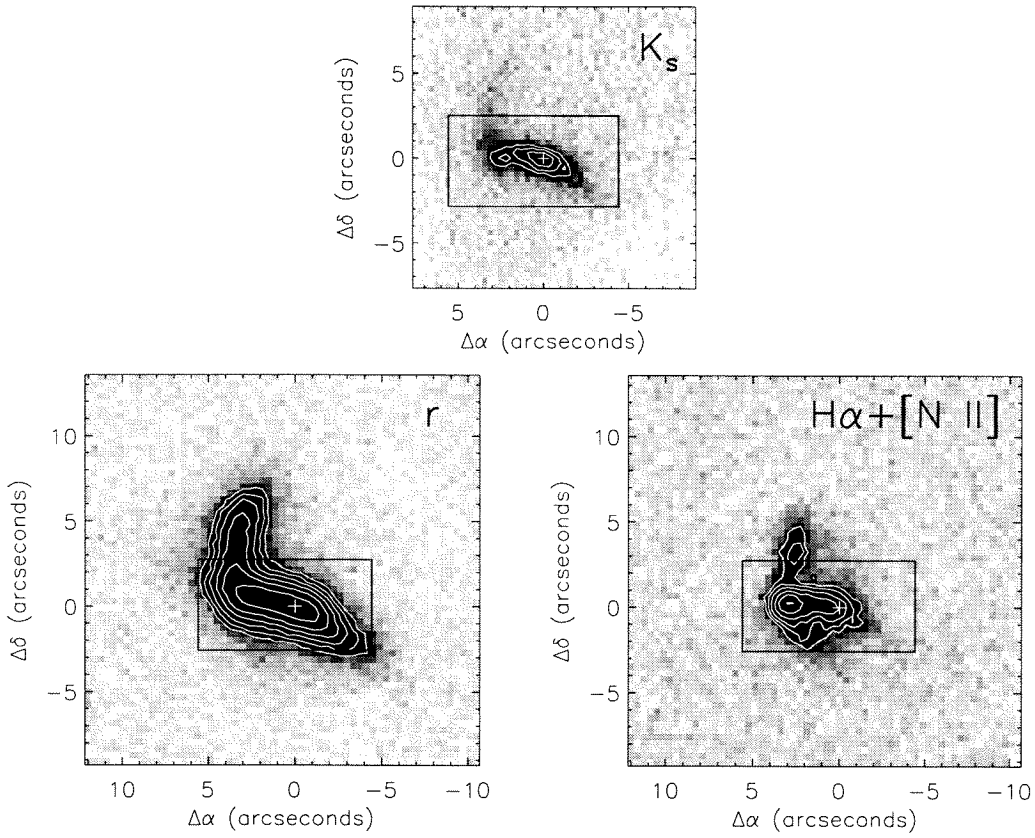

Figure 7.12: Continuum and Hα+[N II] imaging of IRAS 20046−0623. The tidal tail extending to the north is much more prominent in the r band image than in the K_s image, suggesting that it is comprised of young stars. The Hα emission peaks at the eastern end of the continuum bar, and line emission is also seen following the tidal tail. The cross indicates the position of the near-infrared peak, and the rectangular box represents the PIFS field. North is up, and east is to the left.

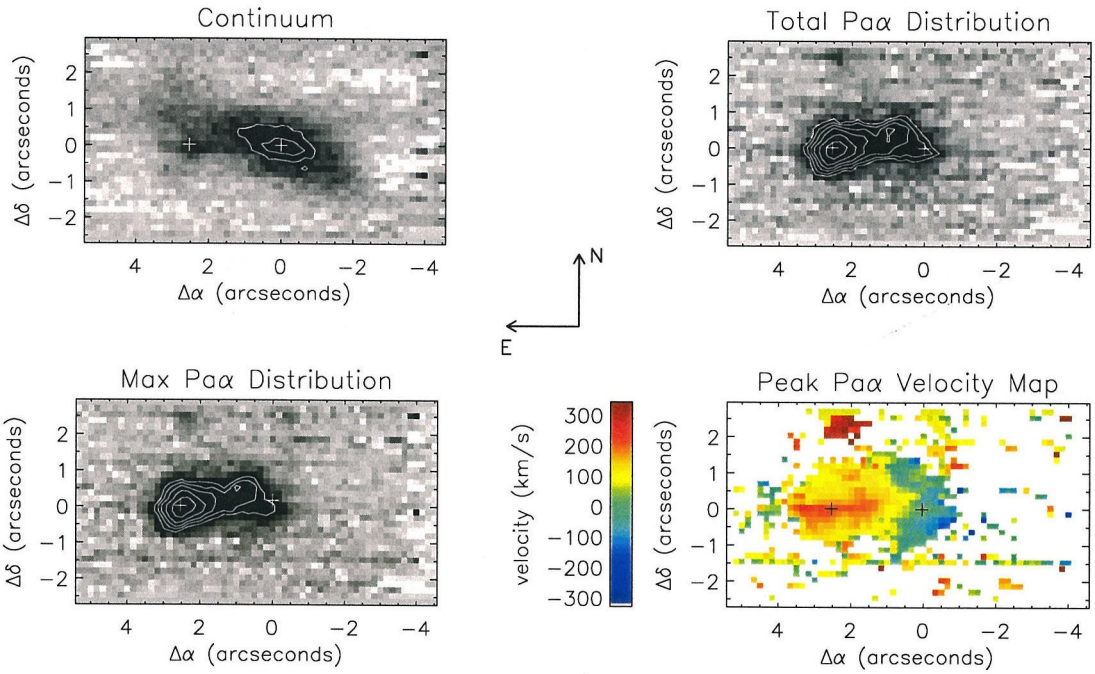

Figure 7.13: Integral field data for IRAS 20046−0623. Description of the four images follows from the Figure 7.2 caption. Crosses represent the positions of the continuum and Paα peaks. North is up, and east is to the left.

flux in a similar aperture yields a comparable flux of 3.6×10^{-17} W m^{-2}. This implies a lower limit on the average extinction to the line emitting gas of $A_V > 3.5$ mag, using the same assumptions detailed in Section 7.4.1.2. A 1.″5×1.″5 aperture centered on the peak emission yields Paα and Hα+[N II] fluxes of 1.75×10^{-17} W m^{-2} and 7.9×10^{-18} W m^{-2}, respectively, implying an extinction of $A_V > 4.6$ mag to this line emission.

The global star formation rate calculated from the Paα flux, following the method presented in Section 7.4.1.2, is about 40 $M_\odot$ yr^{-1} for IRAS 20046−0623, uncorrected for extinction. Using the average visual extinction of 3.8 mag, and taking $A_{Pa\alpha} = 0.145 A_V$ (interpolated from the extinction law in Rieke & Lebofsky, 1985), this value becomes ~ 65 $M_\odot$ yr^{-1}, which approaches the expected SFR for ultraluminous galaxies.

The tidal tail extending to the north also shows appreciable line emission, as seen by the Hα+[N II] light in Figure 7.12. Computing a SFR directly from this light yields 1.4 $M_\odot$ yr^{-1}, uncorrected for reddening. Assuming a moderate extinction of $A_V = 1$ mag boosts this to a few $M_\odot$ yr^{-1}. While not as high as the SFR in the

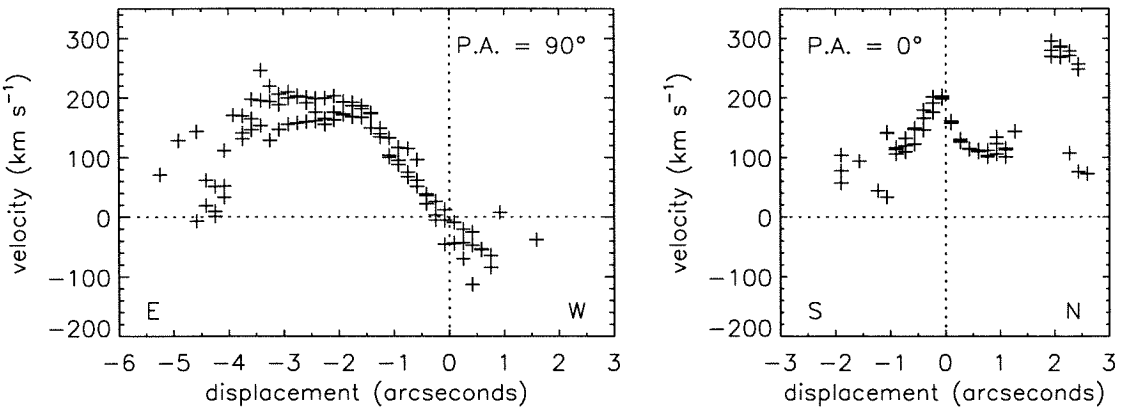

Figure 7.14: Position-velocity plots through two two different axes of IRAS 20046−0623. The plot on the left represents a 0.″5 slit at a position angle of 90° through the continuum peak. The right hand plot is along the orthogonal direction through the Paα peak. Notice the central hump at the position of the Paα peak, and the tidal tail emission redshifted by $\sim$ 300 km s^{-1} relative to the continuum peak's central velocity.

tail of IRAS 01521+5224, this is still higher than previously observed in tidal tails (Hibbard & van Gorkom, 1996; Mihos & Bothun, 1998). Again, this high rate of star formation could be associated with the crossing orbits in very young tails (cf. Toomre & Toomre, 1972), which is consistent with the estimated very early age of this merger, as discussed below.

7.4.3.3 Merger Geometry & Age

IRAS 20046−0623 presents complex velocity field, as seen in Figure 7.13. Here there are two primary axes of importance, which align with the major and minor axes of the continuum morphology. On the western side of the galaxy there exists a velocity gradient with isokinetic contours running roughly parallel to the minor axis. This part of the velocity field looks like rotation of the disk. The eastern side, where the Paα is the strongest, has an orthogonal axis of symmetry—along the major axis. Moreover, the velocity distribution in this region is quadratic rather than linear in nature, with a maximum velocity along the central axis and lower velocities to either side.

The nature of the velocity fields may be seen more clearly in Figure 7.14, which presents position-velocity plots in the east-west and north-south directions, centered on the continuum peak and Paα peak, respectively. Along the major axis, the velocity

profile has a very linear segment spanning 250 km s^{-1}, followed by a very flat distribution across the Paα peak. The trailing off to the blue at the very eastern end of the position-velocity diagram is not associated with strong Paα emission, and is possibly contaminated by the presence of an OH airglow line at the wavelength corresponding to $\sim$ 50 km s^{-1}. This noisy region can be seen in the two-dimensional spectra presented in Figure 7.16. Ignoring the blue down-turn to the east, the two-state nature of the east-west position velocity plot as characterized by the two linear segments is certainly real. In the north-south position-velocity plot, the central hump in the velocity field is clearly seen.

The distribution of velocities in IRAS 20046−0623 is not characteristic of any simple mode of motion. The quadratic velocity field to the east, along with the abrupt change in axial orientation presents a challenge to understanding the dynamics of this merging system. Perhaps distinct signatures remain from the progenitor galaxies involved in the merger.

As with IRAS 01521+5224, the placement and velocity of the tidal tail feature in IRAS 20046−0623 can provide some clue to the age and geometry of this merging system. First, the relative shortness and high surface brightness of the tail, together with the distorted appearance of the continuum bar, argue that this system is relatively young, being viewed soon after the first encounter. The projected length of the tail, roughly 7 kpc, is traveled in 3–5$\times 10^7$ yr at typical tail speeds of 150–250 km s^{-1}. The near-straightness of the tail, plus its high recessional velocity—seen as a cluster of points to north in Figure 7.14—would say that the tail's parent galaxy is seen nearly edge-on, from a vantage close to its spin plane. The tail, in fact, should then point at the location of the parent galaxy's nucleus. While there is no prominent continuum peak along the tail centerline, the Paα peak does in fact lie very close to this line.

The rotational axis associated with the western continuum peak is orthogonal to both the kinematic axis of symmetry to the east and the spin plane of the eastern galaxy, inferred from the tidal tail. There are then almost certainly two distinct galaxies overlapping to form the observed configuration. The absence of a continuum peak to the east is at first disconcerting, but the Paα peak gives its presence

away. With $\gtrsim 5$ mag of visual extinction to the line emission, and therefore almost a magnitude of extinction at 2 μm, the absence of a prominent continuum peak is less startling. A foreground screen of dust could simultaneously account for the high extinction to the line emission, and the apparent lack of the eastern galaxy nucleus in continuum light. The western galaxy, which by its elongation appears to be seen nearly edge-on, could provide such a screen.

A picture can be developed that may account for the various observed features. Because of the extinction, the western galaxy is likely in the foreground. The western galaxy is almost edge on, so that we are looking nearly along its spin plane. The eastern galaxy, mostly hidden behind the disk of the western galaxy, is also seen more-or-less from its spin plane, owing to the straightness and recessional velocity of the tidal tail. The eastern galaxy, having a prominent tail developed rather rapidly following the first encounter, is most likely highly prograde. If this is true, then as with IRAS 01521+5224, we are looking nearly in the orbital plane. This puts the western galaxy in a highly inclined orbit, explaining both the lack of a prominent tail and its tardiness at triggering any significant Paα emission in the nuclear region. Figure 7.15 shows a depiction of the geometry of the IRAS 20046−0623 system, with views both onto the orbital plane, and from our vantage point.

The velocity field can also be understood to some degree in this picture. As a result of its prograde geometry, and therefore its efficiency at setting up transport of gas to the nucleus, the eastern galaxy has highly concentrated Paα emission on its nucleus, the shape of which is seen to some extent through the foreground screen. The rotational signature of this nucleus ought to be red to the north and blue to the south, judging by the redshifted tail to the north. Notice in the velocity field of Figure 7.13 that exactly such a gradient is seen on the southern half of the eastern emission. The orientation of the western disk, with a major axis position angle of $\sim 75°$, is placed such that the maximum extinction would be expected just to the north of the Paα peak position. At this position, the diffuse emission in the western disk may dominate the Paα flux, masking the rotation signature of the diminutive background line emission. With this in mind, the position-velocity plot on the right in Figure 7.14

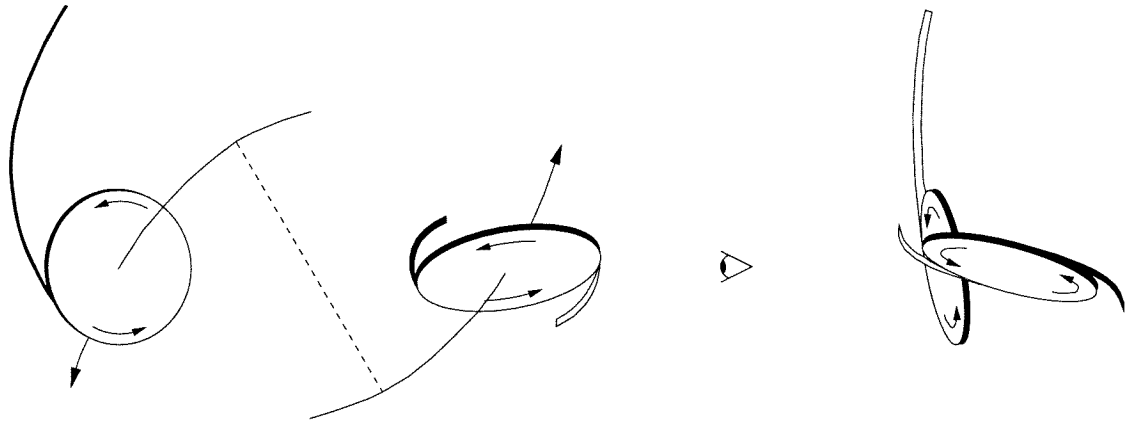

Figure 7.15: The proposed geometry for the IRAS 20046−0623 merger, which is able to reproduce the observed morphology and kinematics. At left is a view more-or-less onto the orbital plane, and at right is the view we have of the system, which is from a vantage point to the right of the left-hand figure, near the plane of the paper. The orbital tracks and time since pericenter are only suggestive here. Note that the galaxy corresponding to the one with the bright tail and nuclear starburst is almost purely prograde in this geometry.

can be understood as a superposition of two components. South of the spatial plot origin, the rotation curve of the background nucleus is seen, but then quickly damped out to the north, where the emission from the diffuse western disk dominates, and the associated extinction suppresses the background flux from the eastern galaxy.

Figure 7.16 displays the two-dimensional spectra of IRAS 20046−0623 along a sequence of spatially descending slit apertures from north to south. In the lower four, or southern, slit apertures, the bright knot of emission associated with the eastern galaxy nucleus can be seen. In the upper three panels, the Paα emission is likely coming only from the western disk. Unfortunately, unlike in Figure 7.20 for IRAS 17574+0629 (see Section 7.4.4), there is a close match in velocities between these two components at the overlapping spatial locations, preventing a clean separation of the two.

With a better understanding of the velocity field in IRAS 20046−0623, a more representative position-velocity plot can be generated for the individual galaxies. Figure 7.17 does this by assuming a 75° position angle for the western galaxy, and by plotting a likely extension of the rotation curve for the eastern galaxy. Besides lying along the major axis of the K_s band continuum emission, the 75° position angle is in good agreement with some of the subtle features of the velocity field in Figure 7.13. In

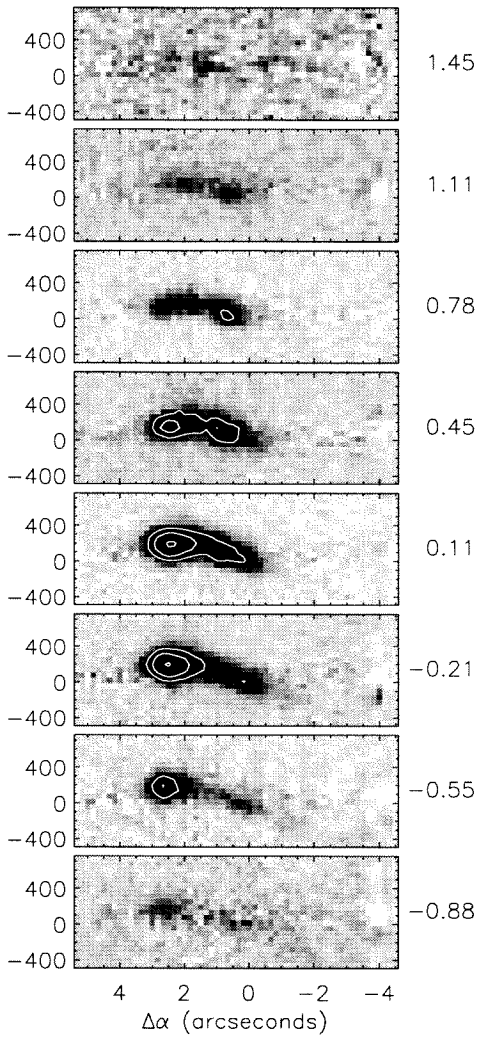

Figure 7.16: A series of two-dimensional Paα spectra of IRAS 20046−0623 along 0.″33 "slits" at a position angle of 90°. Each panel is spatially offset from the adjacent one by 0.″33, with the top-to-bottom progression moving from north to south. The two-dimensional spectra can be understood as a superposition of a compact, bright source to the east (left) and a diffuse, rotating disk of emission extending roughly from the eastern peak position towards the west. The top three panels likely represent only this disk component. Each panel spans 10 arcseconds horizontally and 1250 km s^{-1}vertically. Contours are placed at multiplicative factors of two apart. The spatial coordinates indicated at bottom and right are referenced to the coordinates used in Figure 7.13.

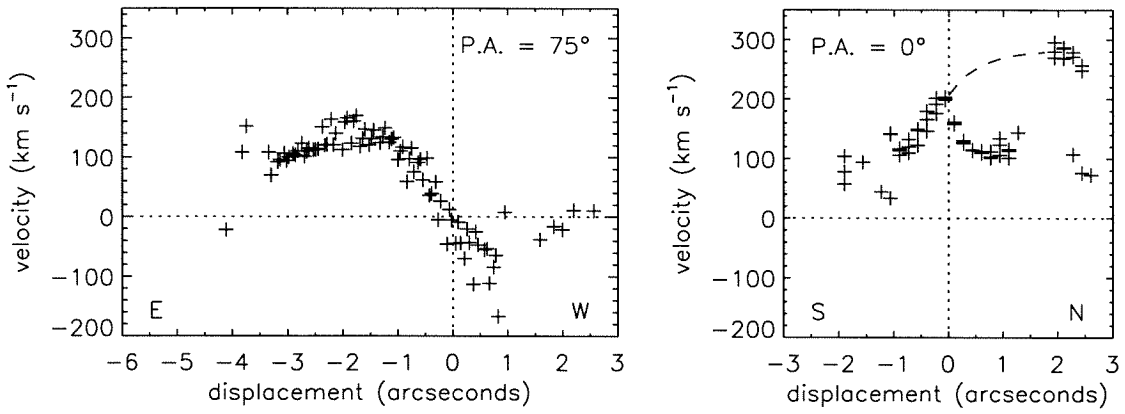

Figure 7.17: Position-velocity plots for IRAS 20046−0623, again along two axes, but this time considering the model that has been developed for the merger geometry. The left-hand plot now shows the rotation curve for the western galaxy, along a position angle of 75°. The right-hand plot shows the likely extension of the rotation curve for the eastern galaxy, which is masked by the dominant emission (plus extinction) from the western disk.

particular, one sees a demarcation between blue and yellow to the SE of the western nucleus that is indeed perpendicular to this position angle. Also, the bluest emission lies to the SW of the nucleus, rather than directly west. The blue-green colored region in the velocity field to the north of the western nucleus does not immediately fit into the scheme, and its nature is unknown.

In the present framework of the geometrical interpretation, IRAS 20046−0623 is a very young interaction, being seen only a few$\times 10^7$ yr after pericenter, during the first encounter. Not only does the tidal tail morphology, velocity, and length support this idea, but the following very simple argument strengthens this interpretation. The eastern galaxy is highly obscured, presumably by the disk of the western galaxy—placing the eastern galaxy in the background. The relative velocities of the eastern and western galaxies is such that the eastern (background) galaxy is receding, as can be seen in Figure 7.17. Therefore, the two galaxies are growing further apart, as would be expected if these galaxies are seen just after a close encounter.

7.4.4 IRAS 17574+0629

7.4.4.1 Morphology of Continuum & Line Emission

The continuum images of IRAS 17574+0629 in Figure 7.18 show a single distorted nucleus with what appear to be two tidal tail features extending to the north and to the east. The Hα+[N II] image shows a prominent emission peak slightly offset from the continuum peak, plus a large region of diffuse emission to the northeast. Figure 7.19 shows the continuum as constructed from the PIFS datacube, along with the appearance of Paα in the system. Similar to the Hα image, a large gaseous nebula is seen in Paα to the northeast, roughly in the direction of the tidal features. The detailed distribution of the Paα nebula does not, however, exactly trace the positions of the diverging tidal features, but rather appears to be shaped like a bubble.

7.4.4.2 Extinction & Star Formation

The Paα distribution can be broken into two regions—the nuclear region, and the extended emission region to the east. The Paα flux in a $3'' \times 3''$ box aperture around the nuclear emission is 4.2×10^{-17} W m^{-2}, while the entire field has $\sim$25% more total flux. Similar apertures on the Hα+[N II] measure 6.7×10^{-17} and 1.3×10^{-16} W m^{-2}, in the same order. A lower limit to the average extinction, using the large aperture measurement, is $A_V > 2.1$ mag, while the nuclear emission gives $A_V > 2.8$ mag. Given the flux ratios, this implies an extinction to the diffuse emission region of $A_V > 0.8$ mag. A ratio of the Paα and Hα+[N II] line images shows the extinction to be separately uniform across both the diffuse region and across the nuclear region, with typical deviations on the order of 0.2 mag.

The total Paα emission, when converted to a global star formation rate in the manner outlined in Section 7.4.1.2, yields 103 $M_\odot$ yr^{-1}, making this the most prodigious star forming galaxy in the sample, assuming that star formation is indeed responsible for the Paα emission. This galaxy is also slightly more infrared-luminous than the other three galaxies in the sample. Applying the measured extinction to the Paα flux results in a total SFR of $\sim$ 150 $M_\odot$ yr^{-1}, with $\sim$ 85% of this coming from the $3'' \times 3''$

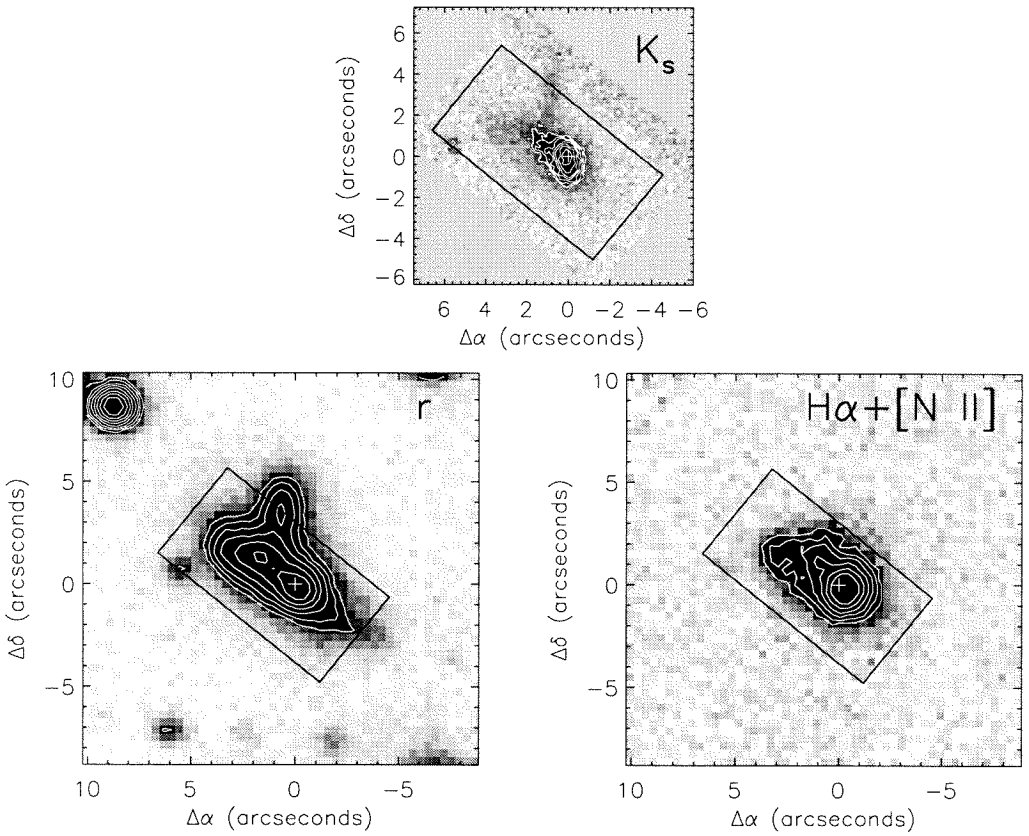

Figure 7.18: Continuum and Hα+[N II] images of IRAS 17574+0629. Two tidal tails are seen extending to the east and north. The Hα morphology indicates the presence of a large, diffuse nebula to the northeast. The rectangular box indicates the position and orientation of the PIFS field. North is up, and east is to the left.

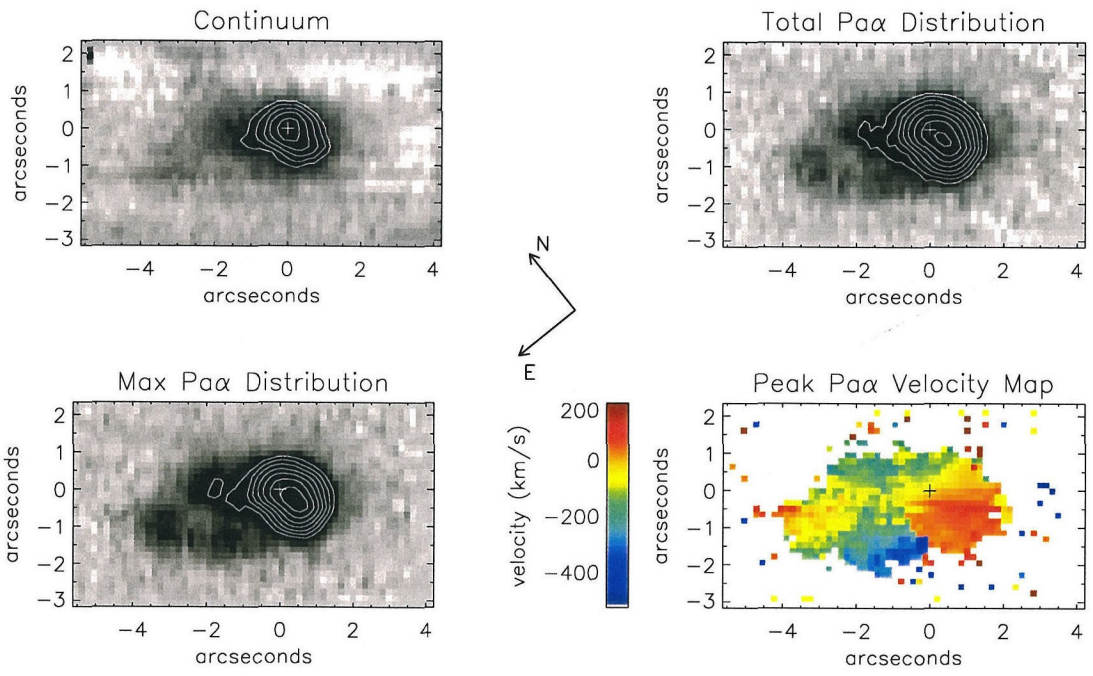

Figure 7.19: Integral field data for IRAS 17574+0629. Description of the four images follows from the Figure 7.2 caption. Field orientation is indicated by the arrows, with "left" corresponding to a position angle of 51°.

aperture around the nuclear region.

7.4.4.3 Merger Geometry

Of this sample, IRAS 17574+0629 is the most difficult to understand in terms of its status as a galactic merger. As mentioned in Section 7.4.4.1, the morphology of the line emission is suggestive of an intense nuclear source accompanied by a large bubble of expanding gas. The kinematic portrayal of the line emission in Figure 7.19 appears quite complex, and does not lend immediate support this picture. An expanding bubble may be expected to display a uniform velocity gradient along the axis of expansion, which would be to the northeast in this case. The velocity field does not show such an orderly trend. The nuclear emission seems to exhibit a rotation signature in the north-south direction, but the velocity field of the diffuse emission is rather twisted and difficult to interpret.

An interesting feature of the IRAS 17574+0629 velocity field is the multi-valued nature to the immediate SE of the nucleus. This can be seen more clearly in the two-

dimensional spectra of Figure 7.20, especially in the three lower left panels. The red nuclear component clearly dominates the emission, and is the component represented in the velocity map of Figure 7.19, concealing the morphology of the blue component.

In attempting to construct a conceptual model accounting for the gas motions, one must take the appearance of the two-dimensional spectra into consideration, as the blue component underlying the brighter red component seen in Figure 7.20 appears to be physically associated with the redder emission to the northeast, owing to the fact that a single, continuous gas component smoothly connects these two regions. Note the consistent appearance of the red-to-blue velocity gradient seen in the faint emission of Figure 7.20 in all of the spatial bins.

In order to isolate this gaseous component of the system, the dominant Paα peak was subtracted from the datacube by fitting and subtracting Gaussian profiles with elliptical cross sections in the individual two-dimensional spectra. This procedure was carried out in the two-dimensional plane represented by Figure 7.20, the result of which is also displayed here. The structure of the Paα nebula with the dominant peak removed appears in Figure 7.21. Judging by the appearance of the modified two-dimensional spectra in the datacube (Figure 7.20), we suggest that the image in Figure 7.21 roughly corresponds to the true morphological character of a physically connected structure in the galaxy.

Figure 7.21 also presents the kinematic structure of the large Paα nebula in the absence of the much brighter nuclear source. Now the velocity field appears more organized, with a distinctive chevron pattern aligned with—and roughly centered on—the nebula's major axis. Such a pattern is consistent with the the bubble description of the nebula., with a smooth gradient along the expansion axis. A trend from blue to red is seen to be present throughout the nebula as one moves away from the galaxy nucleus along the nebula's major axis. If this feature is indeed associated with an expanding bubble, then the observed geometry suggests that material is being ejected towards the observer, and slowing down as it gets farther from its source.

The bubble/outflow picture does not fully satisfy other features of the appearance of IRAS 17574+0629. In particular, the r band morphology in Figure 7.18 is fairly

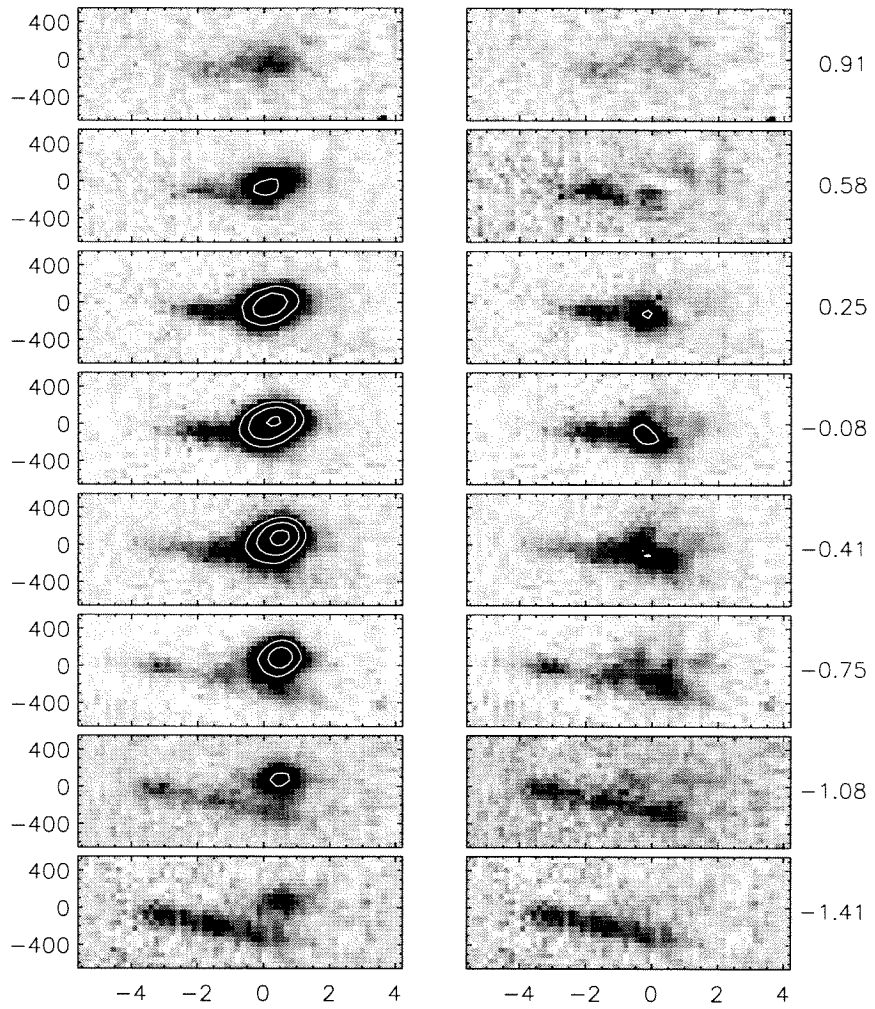

Figure 7.20: A series of two-dimensional Paα spectra of IRAS 17574+0629 along 0.″33 "slits" at a position angle of 51°. Each panel is spatially offset from the adjacent one by 0.″33, with the top-to-bottom progression moving from northwest to southeast. The left column depicts the continuum-subtracted total line emission, while the right hand column displays the same emission with the dominant nuclear Paα component subtracted. Note the multi-valued nature of the Paα emission in the left hand column at the position of the nucleus. The blue component is seen to be physically connected to the red component that appears on the left side of the images in Figure 7.19. Each panel spans 10 arcseconds horizontally and 1250 km s^{-1}vertically. Contours are placed at multiplicative factors of two apart. The spatial coordinates indicated at bottom and right are referenced to the coordinates used in Figure 7.19.

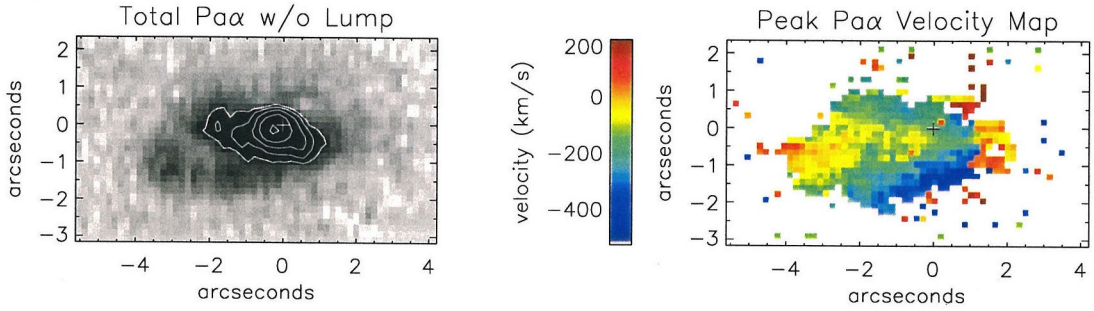

Figure 7.21: Morphology and velocity field of IRAS 17574+0629 after subtracting a mathematical representation of the dominant nuclear Paα component from the two-dimensional spectra comprising the datacube. The underlying velocity field shows an order that is not immediately apparent from Figure 7.19.

similar to that of IRAS 20046−0623 (Figure 7.12, Section 7.4.3). Namely, there is a short stub of a tidal tail extending to the north, and even the little curl at the southeastern edge finds a similar analog in IRAS 20046−0623—which appears to be a very young merger experiencing its first encounter. Indeed, the lack of low surface brightness emission around the perimeter, much like in IRAS 01521+5224, argues that this too is a first encounter ULIRG. Yet there is no obvious second galaxy. It is possible that we are the victim of projection, wherein the second galaxy lies just behind the visible galaxy. In fact, one clue that may support this claim is the offset of the Paα line emission peak from the continuum center by about one arcsecond to the south, corresponding to more than 1.5 kpc. It is hard to imagine the circumstances that might produce an offset this large in a 150 $M_{\odot}$ yr^{-1} starburst. We would expect energy production on this scale to be associated with a mass center capable of gathering the fuel supply.

Another clue in this vein may come from the Paα image with the dominant nuclear emission removed (Figure 7.21). Here, the peak of the Paα emission lies 0.″5 to the NE of the continuum peak, or approximately 1 kpc away. In total, the bright nuclear emission and the less prominent diffuse peak lie at least 2 kpc apart in the plane of the sky. Could these two emission line features point to the locations of the parent galaxies? The continuum shape is not entirely inconsistent with this idea. The K_s image in Figure 7.18 has a north-south extension which could correspond to

the nuclear Paα source—with its north-south velocity gradient—and a spur to the northeast roughly aligned with the Paα feature as seen in the absence of the dominant nuclear component.

If indeed we see two superimposed galaxies, then the tidal features can help distinguish possible configurations. The northern tail is almost certainly associated with the dominant Paα peak, as it is roughly aligned with the rotation axis of this feature. With the sense of rotation—redshifted to the south—then the tail would be blueshifted and in front of the galaxy. In a young encounter, this would put the north-south galaxy in front of the more diffuse galaxy with the northeast-southwest orientation. This arrangement goes against the simple extinction difference between the two, though a high nuclear extinction to the concentrated emission is by itself rather typical in ULIRGs. If this galaxy is relatively well defined in the east-west direction—which the straightness of the tail would support insofar as this indicates we view the galaxy from near the spin plane—then perhaps this arrangement is not too improbable. The extinction to the diffuse line emission region remains low up until the edge of the bright emission line region. The two-dimensional spectra in Figure 7.20 tell a different story, however, namely that the extinction to the diffuse component does not appear to be effected by the presence of the bright nuclear emission. This can be seen in the three lower left panels, which shows no apparent decline in the strength of the diffuse emission at positions that are spatially coincident with the bright component.

Determining an age for the IRAS 17574+0629 encounter is impossible without a clear understanding of its current merger state. Conflicting clues lead to both early and late assessments. The short tails, lack of diffuse emission surrounding the ensemble, possible double nucleus belied by the Paα peaks, and very close resemblance to the IRAS 20046−0623 system would argue for a very early merger. The incompatibility of extinction trends with attempts to reconstruct the merger state based on kinematics, the lack of bright line emission in the northern tidal tail (as seen in IRAS 20046−0623), and the possible interpretation of a large scale outflow bubble argue that this is a late stage, post-merger system.

7.5 Discussion

Ultraluminous infrared galaxies are rare, occupying the extreme tail of the infrared galaxy luminosity function (Soifer et al., 1987; Sanders & Mirabel, 1996). Special circumstances are required to boost the luminosity in these systems by as much as two orders of magnitude over their normal levels. Clearly the merging process is the key, as the overwhelming majority of ULIRGs show evidence for recent or ongoing merger activity. An important question is: where, and in what form is the energy produced that is being radiated in the far-infrared as thermal dust emission? The answer to this question is obscured by the very dust that is producing the infrared flux.

7.5.1 Physical Size & Rate of Star Formation in ULIRGs

A simple calculation of the expected size of the far-infrared radiating region yields a 600 pc diameter under the assumption that the radiation can be characterized as an optically thick concentration of gas and dust radiating as a blackbody at 50 K (60 μm peak wavelength). Whether the emission arises from a single, large concentration of molecular gas and dust or from numerous smaller clouds cannot be directly ascertained given the insufficient resolution of the far-infrared observations. However, if the emission arose from concentrations similar in size to the giant molecular clouds (GMCs) in our Galaxy—typically 50 pc in size—one would require roughly 100 such assemblages. It therefore seems more reasonable to assume that the far-infrared emission arises from a more centrally concentrated collection of gas and dust. Observations of ULIRGs at mid-infrared wavelengths by Soifer et al. (2000) and at millimeter wavelengths by Sakamoto et al. (1999) indeed support this assumption, with typical mid-infrared core sizes of < 200 pc.

In each of the ULIRGs observed in this sample, Paα emission is seen spread over many kiloparsecs, implying widely distributed star formation. But each one of these systems also exhibits a compact source of Paα emission with a flux comparable to—and usually exceeding—the integrated flux of the extended line emission. The

ubiquitous appearance of a bright nuclear Paα feature which dominates the total star formation is an important result. Even these spatially complex ULIRGs, selected for their extended Paα emission, are currently powered by concentrated nuclear starbursts. Also important is the fact that there typically exists at least one magnitude of extinction to the star forming regions at 2 μm, if the total SFR is to account for the high luminosity. The latter point is especially relevant when searching for spectral signatures of active galactic nuclei (AGN) within ULIRGs.

If the far-infrared luminosity in ULIRGs is completely a product of star formation, then it is possible to calculate the rate of star formation required to produce the observed power output. Several such estimates have been made, establishing an order-of-magnitude expectation for ULIRG star formation rates. The first and simplest estimate, from Scoville & Young (1983), computes the rate of mass consumption from O, B, and A stars via the CNO cycle, yielding an expected 77 $M_{\odot}$ yr^{-1} for a total luminosity of $10^{12}L_{\odot}$. This approximation is very nice in its simplicity, though probably an underestimate because some of the mass consumption goes into making lower mass stars that do not contribute significantly to the total luminosity. Hunter et al. (1986) integrate the stellar luminosity with an assumed initial mass function (IMF) to obtain $L_{ir} = 10^{12}L_{\odot}$ with 260 $M_{\odot}$ yr^{-1}, assuming all the luminosity is processed by dust and emitted in the far-infrared. Inoue, Hirishita, & Kamaya (2000) perform a similar, more flexible analysis, arriving at 330 $M_{\odot}$ yr^{-1}, though a rate as low as 200 $M_{\odot}$ yr^{-1} can be obtained by pushing the model to extremes. For our purposes, it is sufficient to say that ULIRGs require an integrated star formation rate of $\sim$ 200 $M_{\odot}$ yr^{-1}.

As pointed out above, each of the ULIRGs in this sample exhibit both widespread and concentrated star formation, as traced by Paα emission. The concentrated Paα emission in each of these four ULIRGs is associated with a galactic nucleus. Comparison of Paα fluxes to Hα fluxes (or 6 cm radio continuum in the case of IRAS 10190+1322) reveals more extinction on the sites of concentrated emission than in the diffuse nebular regions. This is to be expected if the nuclear emission arises from a very large, dense cloud of accumulated gas. The star formation rates in the

extended nebular regions tend to be 10–20 $M_{\odot}$ yr^{-1}—far short of the energy budget required to produce ultraluminous emission. These SFR numbers could be modified upward slightly by extinction corrections, though not by the factor of ten necessary to result in significant far-infrared flux. On the other hand, the nuclear Paα emission translates to typical SFR values of 50–80 $M_{\odot}$ yr^{-1}, after applying extinction corrections measured from Hα. Though this is still a factor of 3–4 short of the ULIRG SFR requirement, it is clear that the bulk of the power comes from the nuclear emission regions. The remaining deficit can then be attributed to high levels of extinction in the interior of the nuclear gas concentration, such that only the outer regions of line emission are seen—even at the wavelength of Paα.

7.5.2 Ages of ULIRGs

The inferred ages of IRAS 01521+5224 and IRAS 20046−0623 of 3–7 $\times$ 10^7 yr, reckoned since closest approach, demand a very fast response to the merger on the part of the gas. In order for the ultraluminous activity to commence so quickly after the first encounter, substantial quantities of disk gas must be very rapidly transported into the central regions. The models by Mihos & Hernquist (1996) show peak star forming activity no sooner than 15 $\times$ 10^7 yr after the first encounter. Similarly, high concentrations of gas do not occur in the models of Barnes & Hernquist (1996) until at least 10^8 yr after closest approach. Additional evidence for very young ULIRGs was found by Mihos & Bothun (1998) via Fabry Perot imaging of four ULIRGs, one of which (IRAS 14348−1447) is believed to be seen just after the first encounter—in this case viewed from well outside the orbital plane.

In addition to the two cases of very young mergers, IRAS 10190+1322 appears to be seen at an intermediate age. The fact that the constituent galaxies appear symmetric and undisturbed (i.e., lacking obvious tidal features) supports this claim. In order to be ultraluminous, it is assumed that galaxies must have undergone at least one close passage—thus stimulating the accumulation of gas to fuel the starburst. When two galaxies in an ultraluminous pair appear close together, then they have

either just passed their first encounter or are closing in for their final collision. Just after first approach, the galaxies appear highly distorted, as seen both in our data and in merger simulations (Barnes & Hernquist, 1996; Mihos & Hernquist, 1996). Thus the IRAS 10190+1322 pair, with its organized morphology, has probably had at least a dynamical timescale to regroup, and is now rapidly approaching the final merger.

As with the young mergers, IRAS 10190+1322 also challenges current models with regard to the time at which merging galaxies produce energy on ultraluminous scales. The model from which the strikingly similar sixth panel in Figure 7.8 is taken (Mihos & Hernquist, 1996) ascribes an increase in SFR relative to the pre-merger level of only a factor of five at the time corresponding to this panel. These models in general predict a significant burst in star formation either following closest approach, or upon final coalescence of the progenitor galaxies, depending on the structure of the galaxy. IRAS 10190+1322 occupies a time in the merger sequence at which models predict a minimum amount of star formation activity. Yet the ultraluminous status of the galaxy pair, plus the directly observed high rates of star formation clearly indicate that the ultraluminous phenomenon can occur even at this stage in the merger sequence.

Careful study of the symmetry of ULIRG pairs in imaging surveys (such as Murphy et al., 1996) suggest that this phenomenon is not entirely rare. Other ULIRGs are seen in states that appear more consistent with a time just prior to final merger than a time shortly after a close approach. Figure 7.22 shows the range of estimated ULIRG ages, performed rather subjectively based on morphological clues provided in imaging surveys by Murphy et al. (1996), Sanders et al. (1988), and Carico et al. (1990). In general, warped isophotes and short, bright tails signal early-stage mergers, while symmetric isophotes and large scale tidal debris signal late-stage mergers. Several ULIRGs were not easily classified by this scheme, thus they appear as unshaded bins on both the early and late sides of the distribution. Details on the time classification and time as a function of nuclear separation are covered in Appendix 7.B.

These results suggest that the ultraluminous phase has a bimodal distribution in time, with some ULIRGs found at very early times, and most seen in the latest stages of the merger process—after the progenitor galaxies have joined. A few ULIRGs are

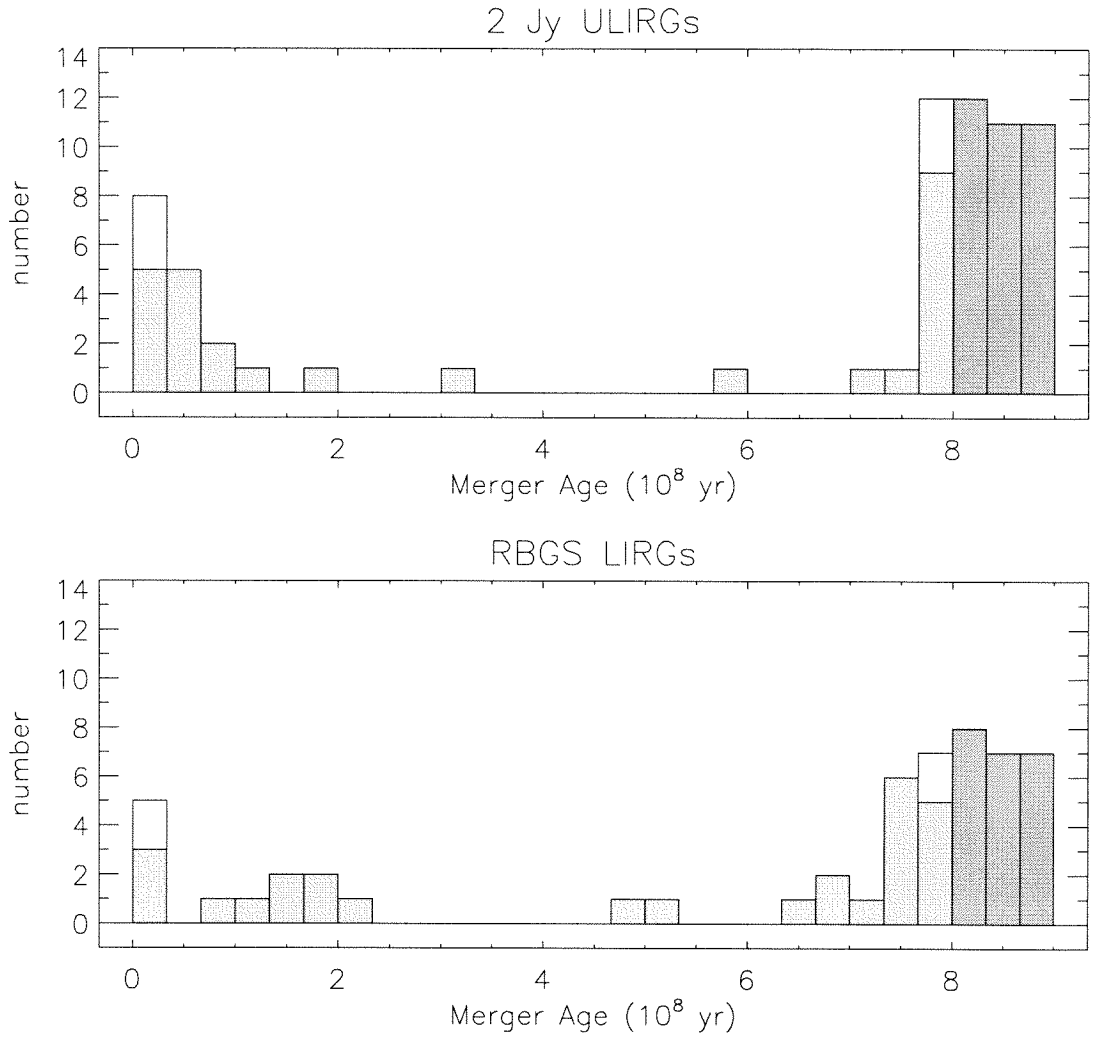

Figure 7.22: Histogram indicating how far ULIRGs are along the merging sequence, as estimated from morphologies in imaging studies. At the very least, ULIRGs appear to have a bimodal time distribution, though wide separation ULIRGs indicate the possibility that the ULIRG phase may occur anywhere along the sequence. Each bin in the histogram represents 3.33×10^7 yr. The final stage ULIRGs have been arbitrarily spread across three bins, for both scaling purposes, and also to reflect the timescale associated with this phase. These post-merger systems are indicated with darker colors. The unshaded boxes represent ambiguous cases that could not easily be classified as early or late interactions, and are accordingly placed at both early and late times. The same information is shown for a similar number of RBGS LIRGs, which exhibit a broader time distribution than ULIRGs. See Appendix 7.B for details on age classification.

also seen at intermediate times. Geometry is likely to play a big role in determining when or if ultraluminous activity occurs along the sequence prior to the final merger. Each of the very early mergers seen in the present sample are believed to have the ultraluminous activity associated with highly prograde galaxies. Tilted disks, such as the northern galaxy in IRAS 01521+5224 and the western galaxy in IRAS 20046−0623, have some star formation activity, mainly away from the nucleus. Perhaps these galaxies are not sufficiently perturbed to organize a central gas concentration, owing to the slower and weaker response of the tilted disks to tidal disruptions. Judging by the time distribution, it appears unlikely that a galaxy will enter an ultraluminous phase during the long interval between initial encounter and final encounter, if not in the first 100 Myr after first encounter.

Though the process of assigning early or late ages to ULIRGs based on morphology has been performed in a somewhat subjective manner, it is interesting to note that there appears to be a significant separation in the infrared luminosity distribution for the early population as compared with the rest of the sample. Figure 7.23 shows this split in histogram form. The late-encounter and post-merger systems are fairly uniformly spread across the luminosity range, while early-encounter ULIRGs are seen clustered near the low luminosity cutoff. At the very least this is an unexpected correlation between morphological character and infrared luminosity. But it also may indicate that the process of judging early or late encounters is not entirely random, and may in fact identify a different type of ultraluminous activity. If the age classification scheme is approximately correct, then this luminosity separation indicates that early ultraluminous activity—usually found occurring on only one nucleus—is accompanied by less intense star formation activity than is typical in final merger events. This could be because the early events do not concentrate the entire gas supply from both galaxies into the nuclear regions in a short period of time—as is likely the case in the final stages of a merger. The early-encounter ultraluminous galaxies may be experiencing rather short, intense bursts brought about by the rapid collection of *some* of the galaxy's gas content into the nuclear regions in response to the sharp tidal perturbation caused by the recent close passage of the companion galaxy.

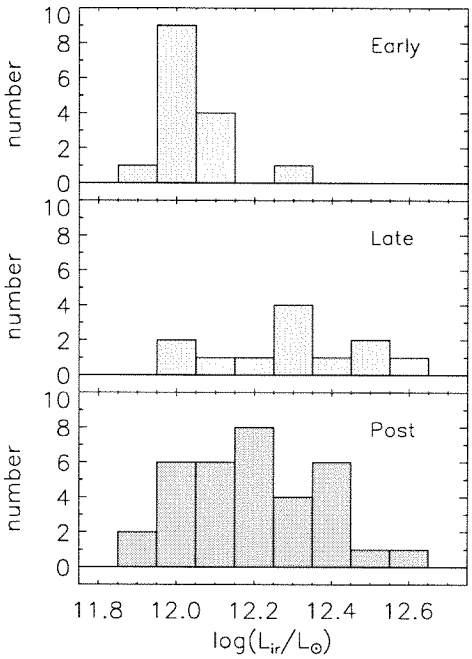

Figure 7.23: The distributions of infrared luminosity for the ULIRGs identified as early-encounter, late-encounter, or post-merger configurations appear to be dramatically different, at least insofar as the early-encounter ULIRGs are tightly clustered around the low luminosity cutoff. No immediate significant difference is seen in the late-encounter or post-merger luminosity distributions.

7.5.3 Proposed Evolutionary Sequence of ULIRGs

One possibility that deserves investigation is that the ULIRG phenomenon is episodic, with punctuated bursts of high intensity possibly occurring more than once along the merger sequence. There exists a fundamental problem in the assumption that merging galaxies can remain ultraluminous throughout the entire merger process, from first encounter to final coalescence. Defined in this way, the merger process takes 5–15 $\times$ 10^8 years to complete, though an ultraluminous starburst, consuming a few hundred solar masses per year, depletes its molecular gas supply of a few$\times 10^{10}$ $M_\odot$ in about 10^8 yr. Clearly then a starburst ULIRG cannot exist throughout the entire merger lifetime. The temporal distribution in Figure 7.22 strongly supports this conclusion, with a significant number of early ULIRGs, very few intermediate-age ULIRGs, and a preponderance of late-stage ULIRGs. The relative timescales of the starburst and merger processes suggest an ultraluminous duty cycle around 10–20%.

It is possible that mergers experience multiple ultraluminous bursts. Three natural time periods can be identified, corresponding to nuclear starbursts in each of the progenitor galaxies separately, plus a final event corresponding to the ultimate merger. Different orbital geometries, physical structures, and gas distributions can act to accelerate, prolong, or prevent the onset of ultraluminous activity in each of the parent galaxies, so that independent bursts do not necessarily happen simultaneously, if at all. As long as some appreciable fraction of the original gas mass is preserved in the disk of at least one of the galaxies, then it is highly likely that a final ultraluminous burst will occur around the time of the final merger. With the possibility of multiple ultraluminous bursts, the duty cycle for the ultraluminous phase may be anywhere from 10–30%.

Early ultraluminous bursts, like the ones seen in the present data, are by no means ubiquitous among ULIRGs. Indeed, since all of the final merger ULIRGs must pass through an initial encounter phase, the early-time peak in the histogram of Figure 7.22 would appear to be much higher if early phase ULIRGs were common. Yet the fact that roughly half of the ULIRGs are seen in separated double nucleus systems, and

that roughly one quarter are early-stage doubles, indicates that a good fraction of the ULIRGs pass through a pre-coalescence ultraluminous burst.

If a galaxy merger experiences an early ultraluminous burst, will there be enough gas left to fuel another burst at the time of final coalescence? Certainly if the companion galaxy has its own fuel supply, yet is not significantly perturbed in the initial encounter, then it can supply the necessary raw materials for a final burst. That possibility aside, in the event that a gas-rich galaxy experiences an early ultraluminous burst, it will not necessarily deplete its entire gas supply in the event. The occurrence of an ultraluminous burst simply indicates that for some period of time, the star formation rate is $\gtrsim$ 100–200 $M_{\odot}$ yr^{-1}. But this phase may last only a few$\times 10^7$ yr, depleting perhaps less than half the available gas supply. The determining factor is the efficiency with which gas throughout the disk is funneled to the nucleus. It is entirely possible that the early bursts in ULIRGs are fueled only by gas from the inner disk. Gas in the outer disk may not have the chance to arrive at the nucleus before the waning tidal disruption is ameliorated by the inherent disk stability. Alternatively, energetic outflow phenomena, namely those produced by supernova winds, may sufficiently disrupt the transient nuclear fueling to bring an early end to the ultraluminous phase.

An important consideration to bear in mind is that ULIRGs do not have to originate from the collision between equally gas-rich galaxies. As long as one galaxy is gas-rich, and the two galaxies are comparable in overall mass, the tidal perturbations can act to fuel a nuclear starburst on the gas-rich galaxy only, or in the final merger if the first encounter is not sufficiently disruptive. Note that each of the ULIRGs observed in the present sample appear to show true ultraluminous activity on only one galaxy nucleus, while the companion is often only moderately active.

With the possibility of brief nuclear starbursts occurring well before the final merger, a natural question is what happens to these systems during the periods when the ultraluminous activity is "turned off?" The observations presented here may provide a relevant clue: very often, there exists extended line emission in the companion galaxy, or surrounding the nuclear starburst. The conditions for extended disk star

formation only require moderate tidal disturbances, leading to crossing orbits and therefore relatively low-velocity cloud-cloud collisions within the disk. The resulting star formation process would be expected to have a significantly longer lifetime than the nuclear starburst phenomenon—probably on the order of the disk's dynamical timescale of a few$\times 10^8$ yr. The star formation rates measured in the extended emission nebulae of this sample are non-trivial, often at 10–20 $M_\odot$ yr^{-1}. As such, these galaxies may qualify as luminous infrared galaxies (LIRGs) in the absence of an ultraluminous nuclear starburst. LIRGs are defined as galaxies with $10^{11.3} L_\odot < L_{ir} < 10^{12.0} L_\odot$. Needless to say, the evolution of luminosity in ULIRGs must occur in such a manner that some time is spent in the so-called "luminous" phase.

7.5.4 Can LIRGs Be "Resting" ULIRGs?

The distinction between LIRGs and ULIRGs is an artificial boundary in luminosity. Merging galaxies may alternate between luminous and ultraluminous states with some non-trivial duty cycle. The problem reduces to one of luminosity evolution during the merging process. Clearly ULIRGs pass through the "luminous" state during their normal course of development. Figure 7.24 depicts an example scenario of luminosity evolution for a major merger. This diagram is merely suggestive, but roughly speaking, is capable of reproducing luminosity functions for luminous infrared galaxies, as well as integrated gas depletion via star formation.

Indeed LIRGs are frequently found in merging pairs, with the fraction of LIRGs classified as strongly interacting rising from 40% at the lower luminosity cutoff to $\sim$ 100% at the high end (Sanders, 1992). LIRGs are more abundant than ULIRGs in a given volume of space by at least a factor of 20–30 (Soifer et al., 1987). If $\sim$ 60% of LIRGs are associated with major mergers, then there are at least ten times as many major mergers classified as LIRGs than mergers that are ultraluminous. If indeed these two classes of galaxies represent different phases of the same phenomenon, then the ultraluminous duty cycle would be around 10% of the luminous phase in galactic encounters.

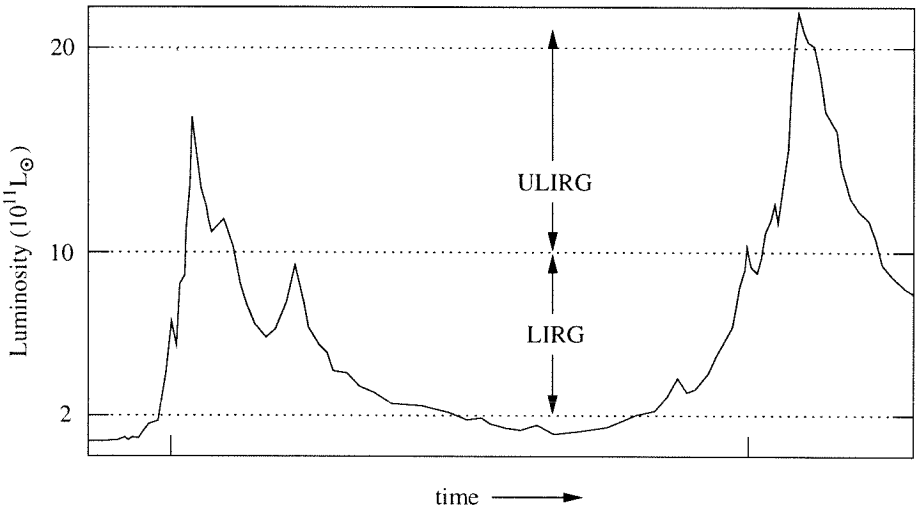

Figure 7.24: Cartoon representation of a possible luminosity evolution sequence as a function of time during the merger process. This particular example shows three principal peaks in luminosity, corresponding to the two progenitor galaxies reacting to the first encounter, followed later by the burst corresponding to the final merger. In this representation, a significant portion of the merger lifetime is spent in the "luminous" phase, and the ultraluminous phases are much like islands poking above the luminosity floor. The ticks along the time axis signify the epochs of the first and final encounters. The fine structure in the light curve is simply intended to indicate that critical processes associated with rates at which fuel is made available or can collapse into stars may vary on timescales of a few million years or less.

Obviously this connection between LIRGs and ULIRGs is an oversimplification. Surely some LIRGs will never reach ultraluminous status due to the lack of raw materials. Yet CO measurements in interacting LIRGs and ULIRGs in similar merger states (double nucleus systems) presented by Gao & Solomon (1999) indicate that LIRGs have similar amounts of molecular gas compared to ULIRGs, with median CO luminosities of 5.8×10^9 and 9.0×10^9 respectively, in units of K km s^{-1} pc^{-2}. Yet the median luminosities of the LIRGs and ULIRGs in their sample differ by a factor of four. Moreover, carefully examining the Gao & Solomon data, one finds no dramatic trend of CO luminosity with L_{ir} across the LIRG sample. Figure 7.25 illustrates this point. Therefore, it seems that LIRGs and ULIRGs share similar quantities of molecular gas, and experience the same close interactions.

To be strictly consistent in terms of molecular gas content, one may wish to remove the LIRG data points in Figure 7.25 with less CO content than ULIRGs, taking only those galaxies with CO luminosities greater than 6×10^9 K km s^{-1} pc^{-2}. This leaves half of the LIRGs, moving the estimated ultraluminous duty cycle from 10% to 20% based on relative number densities. The estimates of duty cycles in this way are consistent with the duty cycles estimated from comparing timescales of mergers and ultraluminous starbursts.

Again, the companion galaxies to the ULIRGs seen in this sample provide *in situ* examples of what the ULIRGs might look like in the non-ultraluminous state. Just as observed for some LIRGs, these galaxies host extended star formation across large portions of their disks. With modest star formation rates of a few$\times 10$ $M_\odot$ yr^{-1}, these galaxies may still preserve enough fuel supply for a final burst, yet have enough activity to classify as LIRGs for a substantial fraction of the encounter event.

Though highly speculative, the slight decrement in CO luminosity from ULIRGs to LIRGs may be due in part to partial consumption of the fuel supply in the ULIRGs that experience an early ultraluminous burst. It is evident that early bursts exist in ULIRGs. If these last a few $\times 10^7$ yr, consuming fuel at 200 $M_\odot$ yr^{-1}, then a significant fraction of the few$\times 10^{10}$ $M_\odot$ of molecular fuel is consumed, though perhaps not all of it. The LIRGs are left with enough fuel to continue moderate star formation, and

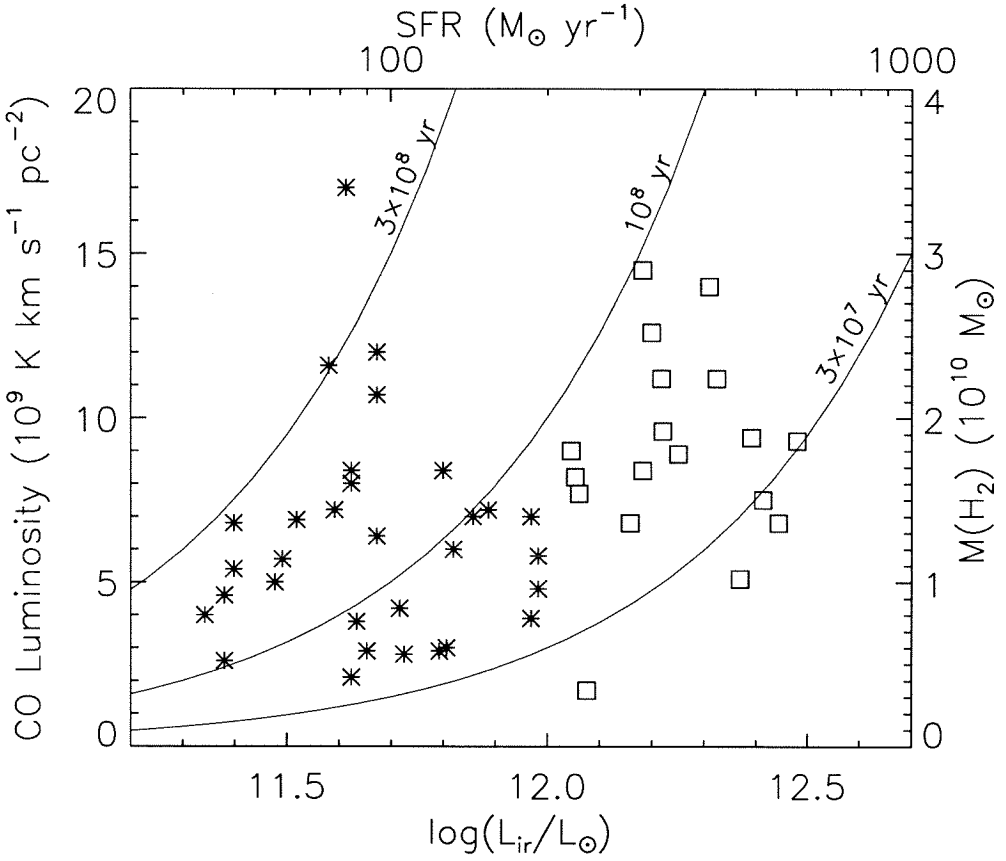

Figure 7.25: CO luminosity as a function of far-infrared luminosity for the sample of interacting galaxies studied by Gao & Solomon (1999). Despite an order-of-magnitude increase in infrared luminosity, the CO luminosity is hardly different between the LIRGs and the ULIRGs. Note the linear vertical scale. Also indicated is the approximate molecular gas mass, as well as the star formation rate required to produce the observed luminosity. Curves are drawn to indicate the timescales over which a given luminosity can be sustained given the current fuel supply. Uncertainties in conversions between CO luminosity and gas mass, as well as the luminosity-SFR conversion can move these age curves by at least a factor of two.

may hold on to enough for the final merger burst.

A preliminary characterization of the morphological properties of strongly interacting LIRGs in the Revised Bright Galaxy Sample (RBGS) (Mazzerella et al., 2000) indicates that the proposed ULIRG-LIRG evolutionary connection does hold some merit. If LIRGs were simply weaker versions of ULIRGs, then they would be found in similar states of merging. Yet both the mean and median separations for double nucleus LIRGs in the RBGS are roughly twice that found in the 2 Jy ULIRG sample from Murphy et al. (1996). This applies for both the samples as a whole, as well as for subsets containing only double galaxies. These figures are summarized in Table 7.5.

The apparent difference in galaxy separations may have an evolutionary origin. But varying merger geometries may also play a role. Weaker interactions between massive galaxies produce a diminished tidal disturbance, which one would expect to result in less star formation, and thus lower infrared luminosity. These same weak interactions would naturally be associated with greater galactic separations. But weaker interactions would have two other measurable consequences that are not supported by the imaging studies. First, weaker interactions would obviously produce less dramatic distortions, such as tidal tails and warped isophotes. No immediate difference in these morphological features is discernible in the imaging data. Second, wider approaches would assume more purely parabolic trajectories, with apocenter occurring much further for the weaker interactions. This can also be thought of in

Table 7.5. LIRG & ULIRG Separations

Sample	Number	Mean Separation (kpc)	Median Separation (kpc)	Separation Range (kpc)	Mean L_{ir} ($10^x L_\odot$)
LIRGs: all	51	10.3	4.9		11.54
doubles	28	18.7	12.3	3.6–49	11.55
ULIRGs: all	64	5.4	0.15		12.16
doubles	32	10.8	6.4	0.3–48	12.13

terms of less significant dynamical friction in the weaker interactions. The observed range in separations among LIRGs and ULIRGs is almost identical, so that both consequences of weaker interactions are not directly reflected in the imaging data.

The same early/late age classification that was performed on the 2 Jy ULIRG sample was also performed on the RBGS LIRGs, the histogram for which is presented in Figure 7.22 along with the ULIRG data. The age distributions are markedly different from that of ULIRGs, with more LIRGs found at times far from the critical encounter times (at 0 and 8×10^8 yr on the histogram scale). Put in the context of luminosity evolution, the age classification data are consistent with the notion that LIRGs represent the tail of the first-encounter ULIRG burst, and also appear as a precursor to the final merger. It should be pointed out that the post-merger LIRGs and ULIRGs are placed into the last three bins of the histograms in Figure 7.22. In reality, there could be a radical difference in the age distribution for post-merger LIRGs and ULIRGs. ULIRGs are still somewhat confined temporally due to the fact that they cannot produce ultraluminous power levels via starbursts for more than a few$\times 10^8$ yr. LIRGs are not quite as restricted in this regard. Studying the morphologies of post-merger ULIRGs and LIRGs may be a way to probe the time since merger, based on the extent to which the system has relaxed from the violent process of coalescence. Such analysis is not attempted here. If the LIRGs are indeed found to exist at later post-merger times than ULIRGs after the final merger, then just as above, these LIRGs could simply be the fading embers of ULIRGs.

As pointed out earlier, it would be naive to think that all major galactic mergers have gone through or will go through an ultraluminous phase. Certainly the wide range of possible encounter geometries, molecular gas content, galactic structure, etc. limit the peak power output of some systems to something less than ultraluminous. However, it seems plausible that a significant fraction of the major mergers currently seen in less luminous states have or will experience at least one ultraluminous burst during the course of the merging process.

7.6 Conclusions

Merging galactic systems are by their very nature complex, rapidly evolving entities. Integral field spectroscopy offers an ideal way in which to capture this complexity across the entire two-dimensional spatial extent. Often the added dimension of information allows one to reconstruct the full merger geometry.

The integral field ULIRG observations presented here allow us to determine the approximate time at which we view these merging systems relative to the first close encounter. The surprising result that many ULIRGs appear to be quite young brings into question the nature of luminosity evolution for major galactic mergers. We suggest that many of the major galactic mergers currently seen in less luminous states have gone through or will eventually pass through an ultraluminous phase, depending on the efficiency and rapidity with which molecular gas can be funneled into the nuclear regions. Almost all ULIRGs seem to go through an ultraluminous state during the final merger, but some also experience early bursts. The very early bursts observed in the present sample are associated with highly prograde encounter geometries. These galaxies may be able to preserve enough fuel to sustain a second ultraluminous burst, or alternatively, the companion galaxy may supply the raw materials for this final event.

Among the more direct results of this work are the following findings:

1. Ultraluminous galaxies may be found at very early times in the merger sequence, perhaps $\lesssim 5 \times 10^7$ yr after the first close encounter.

2. Even the very early events produce their ultraluminous emission from a highly concentrated nuclear starburst.

3. There exists significant extinction to the nuclear line emission region, generally greater than 1 magnitude at 2 μm. Thus a hidden AGN would be difficult to detect, even at these wavelengths.

4. ULIRGs may also be found at intermediate times, well after the first close encounter, and just prior to the final merger. Current models for merging galaxies

do not predict significant amounts of star formation at these awkward times. However, the models simply follow local gas densities, and do not treat subtleties of star formation or gas distributions at small scales.

5. Young tidal tails often host appreciable star formation at rates of several solar masses per year, perhaps related to the existence of crossing orbits at early stages of tail formation.

We are very grateful for the generosity of Joe Mazzarella, who allowed us to access the pre-publication images of the RBGS catalog. Eiichi Egami assisted with some of the observations. We thank Michael Strauss for his role in the early stages of the Caltech effort in studying ULIRGs. We also thank Gerry Neugebauer, Christopher Mihos, Lars Hernquist, and Andreas Eckart for helpful discussions. We thank the night assistants at Palomar, Rick Burruss, and Karl Dunscombe. for their assistance in the observations. This research has made use of the NASA/IPAC Extragalactic Database (NED), which is operated by the Jet Propulsion Laboratory, Caltech under contract with NASA. T.W.M. is supported by the NASA Graduate Student Researchers Program, and the Lewis Kingsley Foundation. This research is supported by a grant from the National Science Foundation.

Appendix 7.A Galaxy Merger Geometries

7.A.1 Basic Geometries

Galactic encounters between two disk galaxies can happen in a multitude of different ways. Choosing the orbital plane of the galactic centers (as determined by the cross product of the initial velocity vectors), one needs four parameters to define initial positions and velocities of the galaxy centers relative to each other. Additionally, the orientation of the spin axis of each galaxy relative to the orbital plane requires two angles apiece. Additional parameters, of course, are needed to describe the mass distributions, distribution of angular momentum, etc. Obviously a vast expanse of parameter space is needed to specify all possible encounter geometries. Focusing on the disk orientation angles, both an inclination and an "argument of nodes" are needed to specify the geometry. The inclination can be negative, signifying a spin in the opposite sense from a positive inclination.

Merger geometries break up into two main classes, one being prograde, and the other retrograde. Each galaxy has its own associated geometry, so that merging galaxy pairs may be found in any combination of prograde and retrograde geometries. A configuration is prograde if the spin axis of a galaxy and the angular momentum vector of the same galaxy *(relative to* the other galaxy) generally point in the same direction—i.e., the two vectors have a positive dot product. An analogous motion is that of the Moon around the Earth, or the Earth around the Sun. In both cases, the sense of rotation is the same as that of revolution. In the case of the Moon, the rotation rate is in resonance with the revolution about the Earth, such that the same face is always presented to the Earth. Venus and Uranus, on the other hand, exhibit retrograde motions, with rotations opposing the orbital motions.

In a merging context, a prograde geometry is more tidally disruptive than a retrograde one, because the perturbing galaxy moves slowly in the rotating frame of the prograde galaxy, exposing a region of the galaxy to the gravitational disturbance for

a longer period of time. A retrograde galaxy, on the other hand, sees the perturbing galaxy move around rather rapidly in the rotating frame, such that tidal disturbances are averaged out.

7.A.2 Tidal Tail Formation

Following careful study of the figures in Toomre & Toomre (1972) depicting tidal tails strewn from prograde disks, it is seen that the velocity fields of tails are such that material moves perpendicular to the tail extent. Also clear is that the formation of tails can be understood in terms of simple mechanics. The material on the far side of the disk from the tidally disruptive companion does not feel as much acceleration from the companion as does the host galaxy nucleus, owing to its greater distance from the perturbing mass. The host galaxy's nucleus is, in effect, pulled away from the outboard disk material. The disk material then follows a nearly straight-line course having a velocity vector roughly equal in magnitude to the circular velocity of the disk plus the velocity of the galaxy's center of mass at the time of closest approach. Thus the maximum velocity available to the tidal material in the merger center of mass frame is the sum of these two velocities.

Because the tail velocity stems from both rotational and orbital motion, it is not surprising that the tail resides in a plane somewhere between the spin plane and the orbital plane, though the tail may be somewhat warped, not lying purely in a plane. Toomre & Toomre (1972) showed that the tail tends to exist in a plane closer to the spin plane than the orbital plane. In a pure prograde orbit, these planes coincide, and the tail, of course, lies in this plane.

Appendix 7.B Merger Age Classification

The age of a merger, as determined from imaging data, is guided by two principles. The first is that tidal tails and related debris take time to grow to large scales. When the tidal extensions are much larger than the nuclear separation between galaxies, it

may be assumed that the galaxy pair is seen well after the initial encounter. There is, of course, the possibility that multiple close encounters occur before the final coalescence of nuclei. The implicit assumption in this analysis is that only two encounters occur—an initial passage followed by a final merger. The very presence of tidal tails indicates a short-lived and intense disturbance in the recent past. Slow, spiralling approaches to merging would not produce these striking features. Even collisionless encounters drain energy and angular momentum from the core galaxies through dynamical friction and by throwing off tidal material to great distances. The high-class simulations of galaxy mergers (e.g., Mihos & Hernquist, 1996; Barnes & Hernquist, 1996) suggest that even previously unbound (or critically bound) galaxies with a 10 kpc first-encounter pericentric distance undergo a single subsequent large separation before plunging back together for the final merger. Thus any obvious and vastly extended tidal debris is assumed to have been generated in a previous close encounter, with the galaxies presently on the verge of permanently joining each other. Conversely, short, high-surface-brightness tidal tails are assumed to be recent formations, indicating a young encounter.

The second guiding morphological clue deals with the inner morphologies of the galaxies. Because the galaxies probably spend a few dynamical timescales between the time of first encounter and the final collision, the galaxies have a chance to reorganize themselves, ameliorating any structural perturbations caused by the encounter. Thus highly distorted inner morphologies, such as obvious bar modes and warped disks likely indicate a young merger. Often, the warped features correspond to the stubby beginnings of a tidal tail.

Large scale tidal features take precedence over the more subjective assessment of distorted inner isophotes in assessing the age of the merger. The absence of apparent large scale tidal structures presents an ambiguity between their true absence or their low surface brightness. In these cases, either the presence of a short tail-like extension or obviously warped inner structure flags the ULIRG as an early merger. But without these additional clues, the age of the merger cannot be easily determined. This population is indicated in Figure 7.22 by the un-shaded bins, and these bins are doubly

represented at both early and late times.

Conversion of galaxy separation to time along the merger sequence is not performed in any sophisticated manner. The galaxies are simply assumed to experience a parabolic separation profile in time, i.e., constant acceleration. It is easy to justify this behavior when the galaxies are at apocenter, because at this time, the highly eccentric orbits are very nearly parabolic. As the distance between the galaxies diminishes, the acceleration would increase if the galaxies were point masses. But the vast dark matter halos of the galaxies act to soften the interaction. Representing the dominant mass component, the dark halos begin to overlap, resulting in a diminished net acceleration. These two effects roughly cancel each other, leading to a nearly parabolic time-separation relation. Numerical integration of halo mass interactions, using halo distribution functions like those detailed in Mihos & Hernquist (1996), show little departure from this behavior.

The parameters of the parabolic separation function are chosen to approximately represent the situation found in ULIRGs. The maximum separation observed in the 2 Jy ULIRG sample is 48 kpc (Murphy et al., 1996), so we will adopt 50 kpc as the nominal maximum separation for each encounter. The timescale for the encounter is chosen to be 8×10^8 yr, which results in a maximum relative velocity of 250 km s^{-1}, closely matching observed velocity differences in close pairs. The resulting time stretch has the dramatic effect of putting virtually all observed ULIRGs at either very early or very late times. A few objects appear at intermediate times, demonstrating that the ultraluminous phenomenon can be rather delayed. But by-and-large, the ULIRG temporal distribution appears to be bimodal.

Table 7.6 presents the somewhat subjective age classifications for the double nucleus galaxies in the complete 2 Jy sample, as defined in Murphy et al. (1996). Most of the classifications are based on the images found in Murphy et al., though supplemental data were obtained from Surace et al. (1998) and Surace, Sanders, & Evans (2000). Note the tendency for the galaxies classified as early interactions to have luminosities at the low end of the ultraluminous range. This is displayed graphically in Figure 7.23, and suggests that this scheme of classification is less than random.

Table 7.6. Merger Age Classification

Galaxy	Separation (kpc)	$\log \frac{L_{IR}}{L_\odot}$	Age Category	Comments
IRAS 00153+5454	8.1	12.10	early	distorted disks, confined debris
IRAS 01521+5224[a]	7.7	11.95	early	short, bright tails, distorted
IRAS 05246+0103	9.6	12.05	early	distorted, short tail?
IRAS 09061−1248	6.4	11.97	early	distorted disks, confined debris
IRAS 09111−1007	36.0	11.98	early	distortion, bars?—both disks
IRAS 09583+4714	13.0	11.98	early	distortion, bars—both disks
IRAS 10035+4852	11.4	11.93	early	two bright, relatively short tails
IRAS 10565+2448	20.2	11.98	early	tail length similar to separation
IRAS 14348−1447	4.8	12.28	early	short, bright tail
IRAS 14394+5332	48.0	12.04	early	near apogee—early/late irrelevant
IRAS 16474+3430	6.5	12.12	early	short, bright tail, distorted
IRAS 17028+5817	22.5	12.11	early	distorted, short tidal features
IRAS 18470+3233	9.4	12.02	early	two very distorted disks
IRAS 20046−0623[a]	3.6	12.02	early	short, bright tail
IRAS 23327+2913	21.7	12.03	early	distorted, young bridge/tail
IRAS 00091−0738	2.3	12.21	late	tidal debris much larger than sep.
IRAS 00188−0856	14.1	12.33	late	symmetric, no bright tidal extensions
IRAS 03158+4227	40.0	12.55	late	both symmetric
IRAS 03521+0028	3.6	12.48	late	large, diffuse tidal features
IRAS 10190+1322[a]	5.3	11.98	late	symmetric, no bright tidal extensions
IRAS 12071−0444	1.8	12.31	late	tidal tail much larger than separation
IRAS 12112+0305	3.7	12.27	late	mature tidal features
IRAS 12540+5708	2.8	12.50	late	large scale tidal debris
IRAS 13451+1232	3.9	12.27	late	symmetric, large scale tidal debris
IRAS 15245+1019	3.4	11.96	late	large scale tidal tail
IRAS 21396+3623	15.4[b]	12.40[b]	late	symmetric, no bright tidal extensions
IRAS 22491−1808	2.1	12.12	late	large, diffuse tidal features
IRAS 08572+3915	5.8	12.08	unknown	ambiguous tidal structure
IRAS 13539+2920	7.2	12.04	unknown	some distortion, could be early
IRAS 16487+5447	5.3	12.12	unknown	diffuse tidal fuzz, could be late

[a]Member of the present sample

[b]Revised redshift from Strauss et al. (1992) value: $cz = 44750$ km s^{-1}

Bibliography

Barnes, J. E., & Hernquist, L. 1992, *Nature*, 360, 715

Barnes, J. E., & Hernquist, L. 1996, *Astrophysical Journal*, 471, 115

Barton, E. J., Geller, M. J., & Kenyon, S. J. 2000, in preparation

Binney, J. & Merrifield, M. 1998, *Galactic Astronomy*, (Princeton, NJ: Princeton University Press), p. 514

Borne, K. D., Bushouse, J., Lucas, R. A., & Colina, L. 2000, *Astrophysical Journal*, 529, L77

Carico, D. P., Graham, J. R., Matthews, K., Wilson, T. D., Soifer, B. T., Neugebauer, G., & Sanders, D. B. 1990, *Astrophysical Journal*, 349, L39

Chromey, F. R., Elmegreen, D. M., Mandell, A., & McDermott, J. 1998, *Astronomical Journal*, 115, 2331

Clements, D. L., Sutherland, W. J., McMahon, R. G., & Saunders, W. 1996, *Monthly Notices of the Royal Astron. Soc.*, 279, 477

Crawford, T., Marr, J., Partridge, B., & Strauss, M. A. 1996, *Astrophysical Journal*, 460, 225

Downes, D., Solomon, P. M., & Radford, S. J. E. 1993, *Astrophysical Journal*, 414, L13

Duc, P.-A., & Mirabel, I. F. 1998, *Astronomy & Astrophysics*, 333, 813

Duc, P.-A, et al. 2000, *Astronomical Journal*, submitted

Elmegreen, B. G., Kaufman, M., & Thomasson, M. 1993, *Astrophysical Journal*, 412, 90

Gao, Y., & Solomon, P. M. 1999, *Astrophysical Journal*, 512, L99

Hibbard, J. E., & van Gorkom, J. H. 1996, *Astronomical Journal*, 111, 655

Hibbard, J. E., & Yun, M. S. 1999, *Astronomical Journal*, 118, 162

Hunter, D. A., & Gallagher, J. S. III 1985, *Astrophysical Journal Supp. Series*, 58, 533

Hunter, D. A., Gillett, F. C., Gallagher, J. S., Rice, W. L., & Low, F. J. 1986, *Astrophysical Journal*, 303, 171

Inoue, A. K., Hirishita, H., & Kamaya, H. 2000, *Publ. of the Astron. Soc. of Japan*, in press (astro-ph/0003318)

Larkin, J. E., Knop, R. A., Lin, S. Matthews, K., & Soifer, B. T. 1996, *Publ. of the Astron. Soc. of the Pacific*, 108, 211

Kennicutt, R. C. 1983, *Astrophysical Journal*, 272, 54

Kulessa, A. S., & Lynden-Bell, D. 1992, *Monthly Notices of the Royal Astron. Soc.*, 255, 105

Mazzeralla, J. M., Sanders, D. B., Kim, D. -C., & Jenson, J. B. 2000, in preparation

Mihos, J. C., & Hernquist, L. 1994, *Astrophysical Journal*, 431, L9

Mihos, J. C., & Hernquist, L. 1996, *Astrophysical Journal*, 464, 641

Mihos, J. C., & Bothun, G. D. 1997, *Astrophysical Journal*, 481, 741

Mihos, J. C., & Bothun, G. D. 1998, *Astrophysical Journal*, 500, 619

Mihos, J. C. 2000, 195th AAS Conference, 19.03

Mirabel, I. F., Dottori, H., & Lutz, D. 1992, *Astronomy & Astrophysics*, 256, L19

Murphy, T. W., Armus, L., Matthews, K., Soifer, B. T., Mazzarella, J. M., Shupe, D. L., Strauss, M. A., & Neugebauer, G. 1996, *Astronomical Journal*, 111, 1025

Murphy, T. W., Matthews, K., & Soifer, B. T. 1999, *Publ. of the Astron. Soc. of the Pacific*, 111, 1176, Chapter 5, this thesis

Murphy, T. W., Soifer, B. T., Matthews, K., Kiger, J. R., & Armus, L. 1999, *Astrophysical Journal*, 525, L85, Chapter 3, this thesis

Murphy, T. W., Soifer, B. T., Matthews, K. et al. 2000, in preparation, Chapter 2, this thesis

Reshetnikov, V. P. 1998, *Astronomy Letters*, 24, 153

Rieke, G. H., & Lebofsky, M. J. 1985, *Astrophysical Journal*, 288, 618

Oke, J. B., & Gunn, J. E. 1983, *Astrophysical Journal*, 266, 713

Osterbrock, D. E. 1989, *Astrophysics of Gaseous Nebulae and Active Galactic Nuclei* (Mill Valley, CA: University Science)

Persson, S. E., Murphy, D. C., Krzemenski, W., Roth, M., & Rieke, M. J. 1998, *Astronomical Journal*, 116, 2475

Sakamoto, K., Scoville, N. Z., Yun, M. S., Crosas, M., Genzel, R., & Tacconi, L. J. 1999, *Astrophysical Journal*, 514, 68

Sanders, D. B., Soifer, B. T., Elias, J. H., Madore, B. F., Matthews, K., Neugebauer, G., & Scoville, N. Z. 1988, *Astrophysical Journal*, 325, 74

Sanders, D. B., Scoville, N. Z., & Soifer, B. T. 1991, *Astrophysical Journal*, 370, 158

Sanders, D. B. 1992, in ASP Conference Series, Vol. 31, *Relationships between Active Galactic Nuclei and Starburst Galaxies*, ed. A. Filippenko (San Francisco: ASP), 303

Sanders, D. B., & Mirabel, I. F. 1996, *Annual Review of Astron. & Astrophys.*, 34, 749

Schlegel, D. J., Finkbeiner, D. P., \& Davis, M. 1998, *Astrophysical Journal*, 500, 525

Schweizer, F. 1978, in IAU Symposium 77, *The Structure and Properties of Nearby Galaxies*, ed. E. M. Berkhuijsen & R. Wielebinski (Dordrecht: Reidel), 279

Scoville, N. Z., & Young, J. S. 1983, *Astrophysical Journal*, 265, 148

Soifer, B. T., Neugebauer, G., Matthews, K., Egami, E., Becklin, E. E., Weinberger, A. J., et al. 2000, *Astronomical Journal*, 119, 509

Soifer, B. T., Sanders, D. B., Madore, B. F., Neugebauer, G., Danielson, G. E., et al. 1987, *Astrophysical Journal*, 320, 238

Solomon, P. M., Downes, D., Radford, S. J. E., & Barrett, J. W. 1997, *Astrophysical Journal*, 478, 144

Strauss, M. A., Davis, M., Yahil, A., & Huchra, J. P. 1990, *Astrophysical Journal*, 361, 49

Strauss, M. A., Huchra, J. P., Davis, M., Yahil, A., Fisher, K. B., & Tonry, J. 1992, *Astrophysical Journal Supp. Series*, 83, 29

Surace, J. A., Sanders, D. B., Vacca, W. D., Veilleux, S., & Mazzarella, J. M. 1998, *Astrophysical Journal*, 492, 116

Surace, J. A., Sanders, D. B., & Evans, A. S. 2000, *Astrophysical Journal*, 529, 170

Thuan, T. X., Lipovetsky, V. A., Martin, J. M., & Pustilnik, S. A. 1999, *Astronomy & Astrophysics Supplements*, 139, 1

Toomre, A., & Toomre, J. 1972, *Astrophysical Journal*, 178, 623

Trimble, V. 1999, in Allen's *Astrophysical Quantities*, ed. A. N. Cox, (New York: Springer Verlag; AIP Press), 569

Tyson, J. T., Fischer, P., Guhathakurta, P., McIlroy, P. et al. 1998, *Astronomical Journal*, 116, 102

Yoshii, Y. & Takahara, F. 1988, *Astrophysical Journal*, 326, 1

Zwicky, F. 1956, *Ergebnisse der Exakten Naturwissenschaften*, 29, 344

Chapter 8 Conclusions

This thesis has presented a variety of observations of ultraluminous infrared galaxies (ULIRGs). The observations had different aims, with the common theme of understanding the circumstances responsible for the extreme far-infrared luminosity in these galaxies. The briefest summary of what has been learned is stated as follows. Ultraluminous infrared galaxies are predominantly powered by dense nuclear starbursts brought about by the disruption and funneling of gas into the nuclear regions in response to the galaxy interaction process. A few active galactic nuclei (AGN) are seen in the sample, which are thought to be indicators of super-massive black holes at the centers of the galaxies, fueled by the interaction-induced nuclear gas concentrations. Some ULIRGs appear to be experiencing their first close encounter with their companion galaxies, introducing the notion that the ultraluminous phenomenon may be episodic in nature.

The statement that ULIRGs are predominantly powered by starbursts is consistent with the findings of a number of other investigators from radio, mid-infrared, near-infrared, visible light, and X-ray studies (Crawford et al., 1996; Smith, Lonsdale, & Lonsdale, 1998; Genzel et al., 1998; Rigopoulou et al., 1999; Veilleux, Sanders, & Kim, 1999; Rieke, 1988; Nakagawa et al., 1999). The present data add the highest sensitivity, highest resolution near-infrared spectra presented to date on a reasonably large sample of ULIRGs. At this level of sensitivity and resolution the vast majority of ULIRGs show no signs that anything other than starbursts are responsible for the luminosity. It is important to note, however, that the extinction estimated from this same set of data is very high—a few orders of magnitude—in some galaxies, even at the wavelength of Paα. Such extinctions could easily conceal AGN in the interiors of these galaxies. In this regard, even the lower extinctions that we estimate for some ULIRGs are based only on the line emission we see. This emission could emanate from outer regions where the extinction is relatively low, allowing a more highly obscured

concentration of gas and dust deep within the nuclear regions.

Of the two ULIRGs showing signs of AGN activity in the sample of 33 galaxies, one has been studied with the Palomar Integral Field Spectrograph (PIFS). Because IRAS 08311−2459 does not exhibit a classically defined broad line region with a width of several thousand km s^{-1}, but rather shows a seemingly asymmetric base to the Paα line profile characterized by a 1000 km s^{-1} width, it is not immediately obvious from the near-infrared spectrum that this galaxy hosts a bona-fide AGN. The PIFS data illustrate the power of the integral field approach in elucidating subtle features of the spatial character of various line emitting regions. In this case, the red and blue wings of the Paα line are seen to be spatially unresolved and co-located. In addition, the apparently asymmetric line profile is understood to be due to the presence of He I emission—a fact that is verified in the spatial extent of the line. Similarly, the very high excitation [Si VI] line is spatially unresolved and symmetric—in contrast to the neighboring molecular hydrogen line which shows an extended, elongated spatial character. The most natural explanation for these observations is that an AGN, or buried quasar, exists in the nucleus, with outflow and shock phenomena less likely scenarios for producing the observed spectral features. Additionally, the velocity-resolving capability of the integral field observations shows that the narrow component of the Paα emission and the H_2 emission share the same rotational motion, and can be associated with a disk of star formation activity surrounding the central AGN. The star formation by itself accounts for a significant fraction of the total infrared luminosity, though it appears that the AGN is still the dominant component.

Finally, the integral field spectrograph was used to look at a selection of morphologically complex ULIRGs, with the rather open-ended goal of seeing what kinds of motions exist in their gas distributions. Rotation seems to be the dominant mode of gas motion in the observed sample, with the possibility of a large-scale outflow in IRAS 17574+0629. The rotational senses and relative radial velocities of the individual galaxies in the sample often allowed a reconstruction of the merger geometry, by which it was found that some ULIRGs have only very recently experienced a very disruptive encounter. Judging by the presence of short, massive, rapidly expanding

tidal tails, the recent encounters are likely the very first major encounters experienced by the galaxy pairs. The very young encounter ages demand very rapid and efficient transport of gaseous material into the nucleus of at least one of the galaxy nuclei, where the dominant line emission source is observed to exist. It is very likely that the currently inactive galaxy in these systems will maintain a substantial fraction of its gas to fuel a second ultraluminous burst at the time of final merger. In addition, the early and rapid star formation process in the active galaxy may be curtailed by a number of processes before the fuel supply is entirely converted into stars, again leaving substantial quantities of gas for a future ultraluminous burst. Such disruptive processes may include moderation by supernova winds, the disappearance of the bar potential as the galaxy dynamically relaxes from the sharp tidal disturbance, or simply a failure to transport gas at large radii into the center. With the realization that galaxy encounters may undergo ultraluminous phases at a variety of times during the merging process, the notion arises that ULIRGs and the less luminous LIRGs (luminous infrared galaxies) represent different evolutionary phases of the same physical process. Clearly not all galaxy mergers will experience an ultraluminous phase, but a substantial fraction of the interacting systems observed in the luminous phase have undergone or will undergo an ultraluminous burst at some time during the merger process.

Stepping back from the scientific results of the thesis, I will say a few words about my perspective on the future and utility of integral field spectroscopy. Although I recognized early on that integral field spectroscopy was "the right way" to go about studying astronomical sources as complex as ULIRGs, I was skeptical that the increased information would lead to tractable solutions of merger dynamics. Upon first confronting the data, my suspicions were confirmed: while the data were marvelously rich in information, it was often not clear what could be learned. However, the more I delved into analysis, the more impressed I was with what the integral field data had to offer. I am now convinced that in many cases the simultaneous added dimension over longslit or Fabry Perot techniques is worth much more than the 50% gain one might attribute to the simple increase in dimensionality. This is perhaps most appar-

ent in Chapter 6, in which very subtle line morphologies and spatial positions could be compared without being hampered by gross systematic errors, as would exist in sequential datasets built up by traditional means. I believe that integral field techniques, especially once coupled with adaptive optics systems, will continue to mature, and will ultimately be rather commonplace at astronomical facilities.

Bibliography

Crawford, T., Marr, J., Partridge, B., & Strauss, M. A. 1996, *Astrophysical Journal*, 460, 225

Genzel, R., et al. 1998, *Astrophysical Journal*, 498, 579

Nakagawa, T. et al. 1999, Kyoto IAU Symposium 186, abstract S186-103T

Rieke, G. H. 1988, *Astrophysical Journal*, 331, L5

Rigopoulou, D., Spoon, H. W. W., Genzel, G., Lutz, D., Moorwood, A. F. M., & Tran, Q. D. 1999, *Astronomical Journal*, 118, 2625

Smith H. E., Lonsdale C. J., & Lonsdale, C. J. 1998, *Astrophysical Journal*, 492, 137

Veilleux, S., Sanders, D. B., & Kim, D.-C. 1999, *Astrophysical Journal*, 522, 139